Table 9.3 Synopsis of the work area classification at CERN [456]

Classification	Ambient dose equivalent rate limit		Annual effective dose limit
	Permanent workplaces	Low-occupancy areas	
Non-designated	0.5 μSv/h	2.5 μSv/h	1 mSv
Supervised	3 μSv/h	15 μSv/h	6 mSv
Simple controlled	10 μSv/h	50 μSv/h	20 mSv
Limited stay	not permitted	2 mSv/h	20 mSv
High radiation	not permitted	100 mSv/h	20 mSv
Prohibited	not permitted	-	20 mSv

All these systems need to be connected to the secure power network (see Sect. 9.4.1) or have an autonomy of at least 120 minutes to guarantee the life safety of occupants. They also need to be designed to ensure an overall system fire-rated integrity of at least 90 minutes (E90).

Moreover, robotic systems can be deployed to guide the occupants in their evacuation, by providing an indication of the safe direction to evacuate (projecting arrows on the floor of the transport zone) [453] and providing audio assistance to the emergency response team. Evacuation signs will also be visible on the compartment doors.

9.4.2 Occupational hazards during nominal conditions

While the facility is in operation, the occupants are exposed to the hazards that are present under nominal conditions. The hazards and safety requirements during nominal operation are mentioned here, whereas the accident scenarios are discussed in Sect. 9.4.3.

Ionising radiation For mitigating risks associated with ionising radiation, the standard prescriptive methods outlined in the existing CERN radiation protection rules and procedures are employed. However, optimisation of the design of civil engineering infrastructure is more assimilated in a performance-based approach, where the proposed design has to be evaluated to see whether it will comply with the radiation protection objectives.

Radiological hazards High-energy particle beams interact with each other in the experiments or with beamline components in the accelerator, creating secondary particles that may pose radiological risks during operation (prompt radiation). This interaction also produces residual radioactivity that will present a potential hazard during maintenance (residual radiation). Workers may be exposed to ionising radiation from activated equipment, gases, or fluids by external exposure. The radioactive contamination hazards and the resulting internal exposure from incorporation are expected to be negligible.

The FCC-ee will operate in four phases, with beam energies rising from 45 GeV in Z mode to 182.5 GeV in $t\bar{t}$ mode, and beam currents dropping from 1.27 A to 4.9 mA. Thus, radiological risks vary with the phase and the most conservative scenarios have been used for their assessments.

At the stage of the feasibility study, detailed integration, such as routing ventilation ducts and water pipes, has not yet been completed. Infrastructure integration will be optimised in later design phases. The same is valid for the material moved from the accelerator to storage areas or workshops for maintenance and repair or for elimination. As in other industrial facilities, radioactive sources and X-ray generators may be used for various purposes. These activities will follow standard prescriptive methods, as already commonly applied at CERN or in industry.

All results of the radiation transport simulations presented here were obtained using the FLUKA code [330] with FLAIR [454].

Radiation area classification Dose constraints for the design of the infrastructure as well as active radiation monitoring will ensure that radiation doses received by personnel working on site remain below the regulatory limits [455] under nominal and accident operating conditions.

The radiation area classification scheme [456] allows radiation risks to be managed and ensures that optimisation processes, training, access control, and collective and personal protection means for personnel intervening in the respective areas are adequate for the expected risks. A summary of the radiological area classification adopted at CERN is provided in Table 9.3.

Protection objectives The risks resulting from ionising radiation are analysed very early in the design phase among others, with the objective of developing mitigation approaches that ensure that accessibility requirements are met for each area.

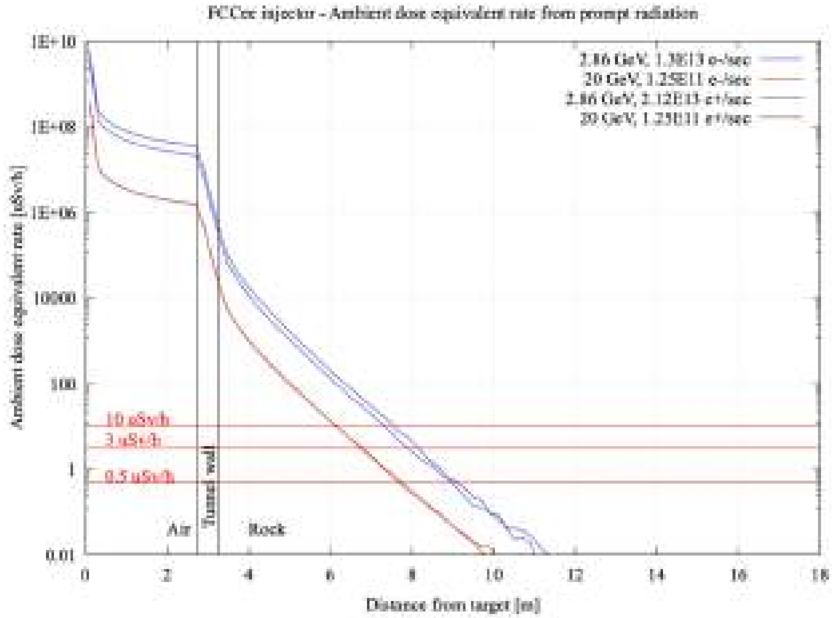

Fig. 9.6 Ambient dose equivalent rate through rock (from 3.25 m distance onwards), resulting from a continuous beam loss in the FCC-ee injector complex based on initial assumptions for potential beam losses

Areas with unacceptably high radiation levels from prompt radiation (high radiation and prohibited radiation areas) are inaccessible during operation, and essential risk control measures are employed as described above. The access control system prevents entry to such hazardous areas, whereas an interlock system halts beam operation if unauthorised access occurs. An emergency stop system ensures the rapid and controlled termination of beam operation if necessary.

Where feasible, areas accessible during beam operation will generally be designed to allow a classification as a non-designated area, avoiding any radiation protection restrictions. The planned civil engineering infrastructure complies with the radiation protection requirements for the operation of FCC-ee. However, the present infrastructure may not necessarily be ready in all parts for FCC-hh, especially where compliance can only be reached by significant costs at the current stage or where infrastructure is only required for FCC-hh. The required infrastructure modifications or additions will need to be implemented after the operation of FCC-ee. One example is the dedicated beam dump caverns that will be only needed for FCC-hh and would not be used by the FCC-ee.

Residual dose rates in the accelerator tunnel have been estimated for several areas, and these will allow a first evaluation of potential constraints on the operation of the facility and maintainability, as well as the related optimisation of the design of beamline components.

Injector complex The injector complex injects electron and positron beams alternately into the booster. Radiological hazards during nominal operation come mainly from prompt radiation from the positron source, beam dumps, and loss locations in the linear accelerators and the damping ring. It is necessary to determine the minimum soil thickness needed to contain the prompt radiation, aiming to keep the klystron hall above the accelerators as a non-designated area.

An initial set of beam parameters and assumed loss terms has been used to estimate the shielding thickness required above the injector complex. Figure 9.6 shows the ambient dose equivalent rates at 90° through shielding from a beam loss on a thin long target, indicating the thickness required to achieve the dose rate objectives. Approximately 6 m of soil cover is deemed adequate for the specified loss term.

A conventional fixed target, where 2.86 GeV electrons interact in a tungsten rod, is used to produce the positrons. The target station will have specific shielding. Activation of the target and downstream accelerator elements also generates sources of radiation which have an impact on workers during maintenance work. These residual radiation levels are reduced by local shielding and optimisation of the elements concerned during the technical design phase.

The highest levels of activation in the injector complex will occur at the positron production target, and initial studies show that these levels will impose strict restrictions on access and maintenance, with extended cool-down times. Remote handling and shielding are indicated, aligned with intervention and maintenance protocols.

Underground infrastructure The collider will be housed in the tunnel with a limited number of access points and connection tunnels, minimising the interfaces between accessible and inaccessible areas that need to be studied and adapted in the design to meet radiation protection objectives. The lateral shielding of 10 m rock effectively contains stray radiation during nominal operation and accident events for both FCC-ee and FCC-hh. More penetrating radiation from loss points in the forward direction is effectively shielded by hundreds of metres of rock, ensuring protection for other potential underground infrastructures.

The general design assumptions taken for the underground infrastructure are as follows.

- The accelerator tunnel and experiment caverns are not accessible during beam operation.
- The service caverns and klystron galleries must be accessible during beam operation for both FCC-ee and FCC-hh. The minimum shielding between the accelerator tunnel and accessible areas is about 10 m, as required by FCC-hh and also driven by stability considerations from civil engineering. Connection tunnels should be long (∼ hundreds of metres) or, if short (∼ tens of metres), include chicanes and/or shielded doors. Chicanes are preferred over shielded doors which have a risk of failure and because chicanes have fewer maintenance issues.
- Service caverns should be non-designated areas (see Table 9.3) for unrestricted access.
- Klystron galleries will be classified as non-designated areas or supervised radiation areas.
- Access to the arcs must be possible without requiring passage through high-radiation areas.
- Alcoves, i.e., technical areas attached to the accelerator tunnel, must be shielded to prevent activation of the installed equipment and are inaccessible during beam operation.
- Areas with high radiation and activation levels must be separated from low activation areas in terms of ventilation and cooling systems (compartments) and personnel access (bypass routes, local shielding).
- The FCC-ee booster will be located on top of the collider ring. As it will operate at about only 10% of the collider current and at varying energies, the studies conducted so far were limited to the collider itself.

The items identified in the collider that will likely show higher activation levels and hence higher residual dose rates are:

- The beamstrahlung dumps next to the interaction points; two dumps on each side of each experiment in points PA, PD, PG, and PJ;
- collimators and absorbers installed in a dedicated insertion region in point PF and next to the interaction points;
- the matching regions next to the interaction points impacted by scattered radiation from the beam collisions in the experiments;
- the main beam dumps in point PB;
- the inner detectors in the interaction points;
- the EM separators installed at point PH.

The following sections highlight some results of the radiation protection studies conducted during the feasibility study phase.

Arc sections The arc sections make up the largest part of the accelerator. Activation and average residual dose rate levels can have a potential impact on personnel, depending on the time it takes in the tunnel to reach a particular workplace.

The main relevant source terms are beam interactions with the residual gas molecules in the vacuum chamber and the synchrotron radiation. The latter contributes only significantly to activation in the $t\bar{t}$ mode, where synchrotron radiation is energetic enough to produce relevant photoneutron fluence and, thus, induced activity.

Figure 9.7 illustrates the expected residual dose rates after $t\bar{t}$ operation. The dose rate levels induced by the other modes are two to three orders of magnitude lower. In the $t\bar{t}$ mode, some waiting time may be required before performing interventions in the tunnel to reduce the dose to personnel. However, the decay is relatively fast, and within a few days, it is down to very low levels acceptable for long interventions. These figures show dose rates without any shielding installed around the photon absorbers. It is now planned to install this shielding. It will have an important mitigating effect so that dose rates will be considerably lower in the $t\bar{t}$ phase.

The ventilation system is designed to recycle air, limiting the release of short-lived radioisotopes during operation. Inhalation and immersion doses were calculated for interventions immediately after the beam stop without air renewal (worst case), with insignificant doses in all modes, except for $t\bar{t}$, where a few µSv per hour of stay could be expected. However, flushing is always required for safety before entering the tunnel.

In conclusion, the FCC-ee arcs will exhibit some activation, but the low dose rates should not lead to significant doses to individuals passing or intervening in the arc sections.

Connection tunnels between experiment and service caverns Colliding beams at interaction points create secondary particles that spread throughout the experiment cavern. Although the detector absorbs much of this radiation, some can reach areas such as the service cavern, which must remain accessible during operation. It has been assessed whether accessing the service cavern is feasible during operation with measures such as shielding and chicanes in the connection tunnels.

This study is for FCC-hh, as proton-proton collisions produce higher dose rates than the electron-positron collisions in FCC-ee. A layout compatible with FCC-hh will, therefore, be compliant with FCC-ee. This approach is justified because the caverns and connection tunnels will not change between the two colliders.

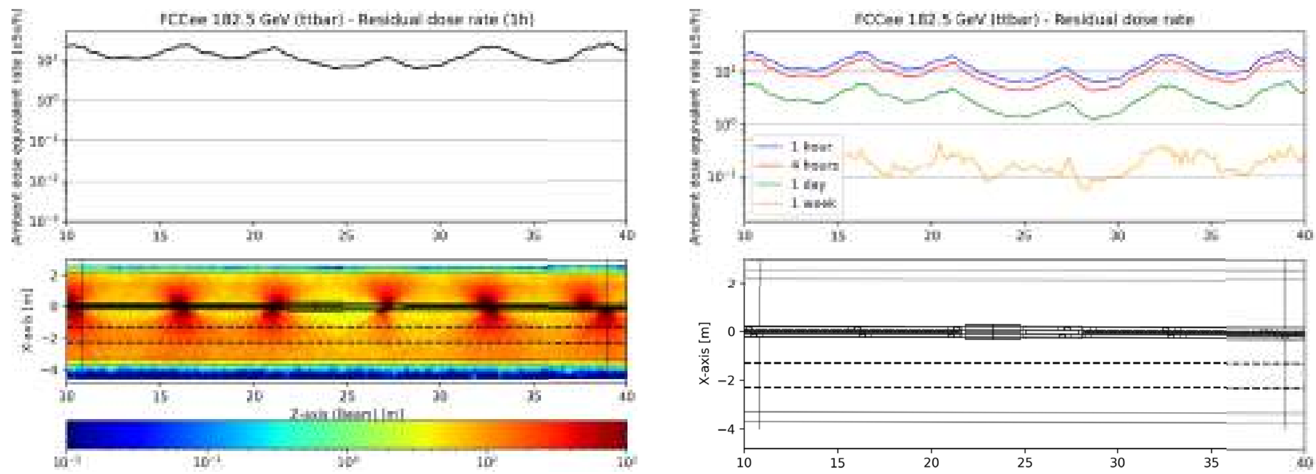

(a) (b)

Fig. 9.7 The graphs represent the distribution of the ambient dose equivalent rate (µSv/h) in the arcs after the $t\bar{t}$ operation phase, averaged over the y-axis from -50 cm to +50 cm, approximately 1 m above the floor. (a): with a decay time of 1 hour, (b): Average values after various decay times: 1 hour, 4 hours, 1 day, and 1 week. The irradiation profile considers all years of $t\bar{t}$ operation phase, taking into account shutdown periods

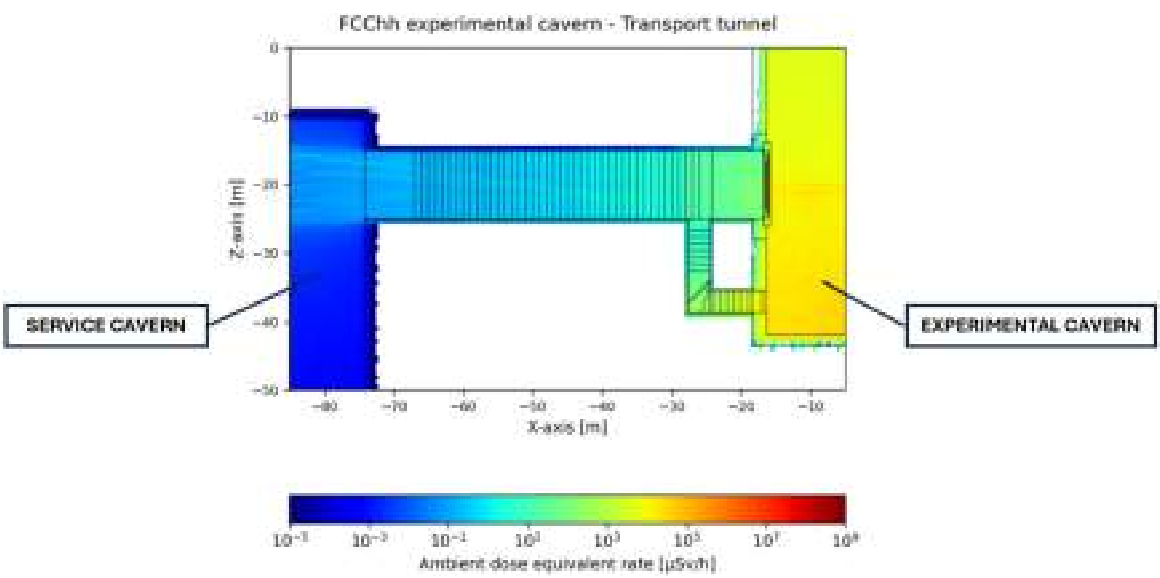

Fig. 9.8 The plot shows the ambient dose equivalent rate averaged over 3 m in height at the FCC experiment points from pp collisions along the transport tunnel between the service and experiment caverns. At the tunnel-experiment cavern interface, a 1 m shielding wall and a two-legged chicane for personnel passage are implemented

Radiation transport simulations were performed for the entire geometry, including the experiment cavern, the connection tunnels, and the service cavern. The assessment considered the most conservative operational FCC-hh scenario ('ultimate'), with a collision rate of 3.24×10^{10} p/s.[19]

The spatial distribution of the dose rate through the service tunnel and within the service gallery is shown in Fig. 9.8. The results demonstrate that the proposed design will meet the target ambient dose equivalent rate limit, i.e., <0.5 µSv/h inside the service cavern, allowing access during operation with permanent occupancy (non-designated area classification).

The feasibility of designing and building the following mitigation measures was confirmed by integration and civil engineering: (1) mobile shielded doors with a thickness of 1 m at the entrance of the transport tunnel and (2)

[19] Based on a peak luminosity of 30×10^{34} cm^{-2}s^{-1}.

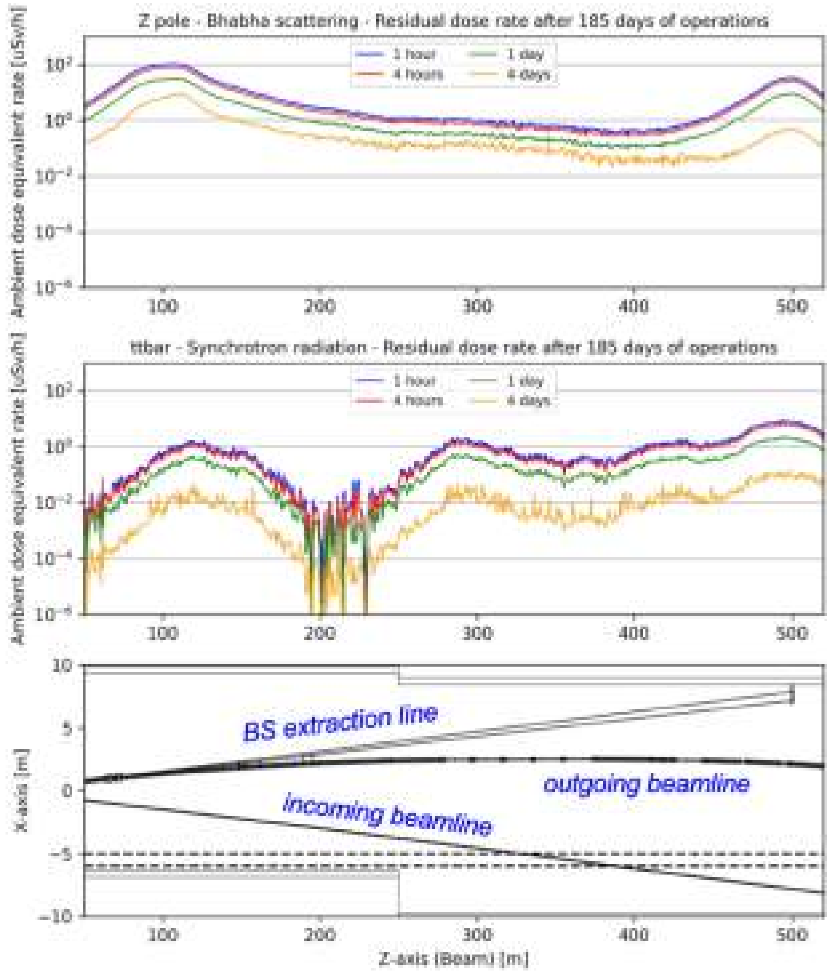

Fig. 9.9 The top and centre plots show residual dose rates averaged within the dashed lines in the straight section geometry next to the FCC-ee IP (bottom plot, distance from the IP). These were computed for two radiation sources: (1) radiative Bhabha during Z pole and (2) synchrotron radiation during $t\bar{t}$, assuming one year of operation (185 days)

a two-legged chicane for the access tunnels for personnel. Additionally, the current design includes a three-legged chicane (not included in the simulation studies shown here), for connecting the main accelerator tunnel with the experiment service area, to minimise the dose rate contribution from the accelerator tunnel. The schematic layout proposed by civil engineering and integration includes chicanes for direct access tunnels. This will ensure that the radiation protection objectives for the service cavern are met.

Bypass tunnels Bypass tunnels allow access from the service cavern to the accelerator tunnel, bypassing the experiment caverns. Bypass tunnels can be designed to allow access to areas with low activation levels while avoiding passing through areas of increased residual radiation risk. The bypass tunnels must reduce prompt radiation streaming towards the service cavern down to acceptable levels, ideally without the need for additional mobile shielding walls for easier access.

Two bypass tunnels are planned at each experiment point to connect the service cavern with the accelerator tunnel. FCC-ee and FCC-hh feature different radiation sources near the interaction regions, with radiological hazards that must be considered when designing the layout of bypass tunnels and their junctions with the accelerator tunnel. The constraints must be assessed for both accelerators:

- *FCC-ee*. Beamstrahlung, synchrotron radiation (SR), and radiative Bhabha (RBB) electrons increase the residual radiation levels in the straight sections next to the interaction points. Residual dose rate levels in the personnel and transport passage are in the range between 0.1 and 100 µSv/h after decay times of 1 to 4 days, as determined in some preliminary simulation studies (see Fig. 9.9). The integration of SR and RBB shielding on the outgoing beamline, which is still pending, will further help to reduce residual dose rates. The beamstrahlung dump must be shielded so that the impact on the personnel and transport passage is reduced to sufficiently low levels in the passageway, located on the opposite side of the tunnel.
- *FCC-hh*. Residual radiation levels are increased in the straight sections next to the IPs, from collision debris in the IP. The ambient dose equivalent rate levels in the personnel and transport passage range between 0.1 and 10 mSv/h after decay times of 1 day to 1 week (see Fig. 9.10). The area has to be considered as a high radiation

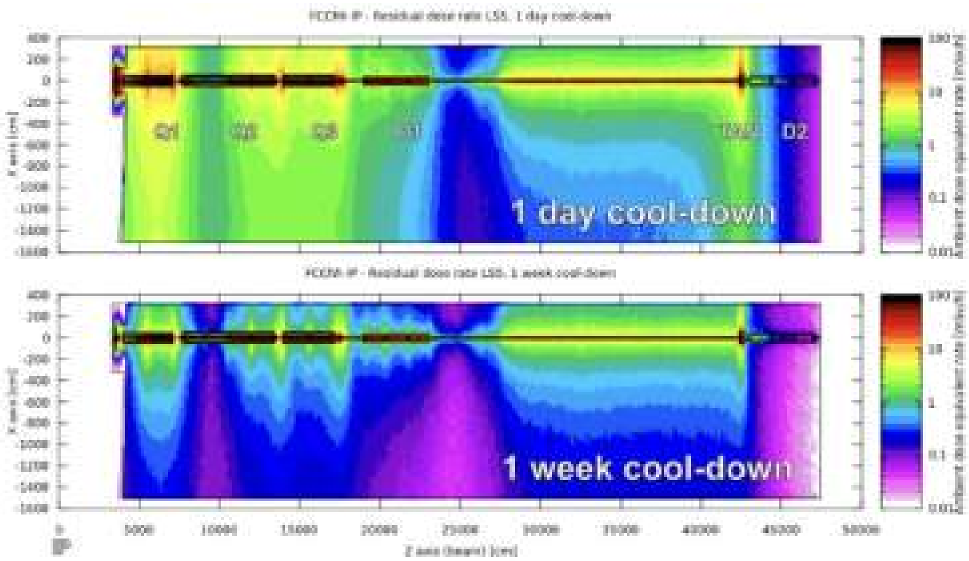

Fig. 9.10 Results showing residual dose rate at FCC-hh IP straight sections after an irradiation of 25 y, with an average collision rate of 5.4×10^{9} p/sec (10 y) + 3.2×10^{10} p/sec (15y). Acceptable positions for the connection of the bypass tunnel are at ∼200 m and at ∼450-500 m

area. Given the enlarged tunnel cross section, it seems feasible to integrate additional shielding along the beam line, effectively reducing residual dose rates to acceptable levels in the personnel and transport passage. Alternatively, the bypass tunnels could be extended before the operation of the FCC-hh.

Beam dump The beam dumps will receive a rather small fraction of the accelerated particles, considering the top-op operation mode and approximately only one dump per day, and will therefore become radioactive to a level that will likely not require a compartmentalisation of the area for separate ventilation. The dumps are shielded and placed in a section where the tunnel cross-section is increased. The passage for transport and personnel in the straight section is sufficiently far from the dumps to achieve acceptable dose rate levels at the passage. Dedicated dump caverns and extraction beam lines will need to be added for FCC-hh.

The radiological study of the beam dumps examines the residual radiation levels next to the beam dumps and is based on a preliminary dump proposal that still lacks a detailed technical design. The study was done for the Z pole scenario, which is considered to be the most conservative. Each beam dump is composed of a cylindrical graphite structure of a length of 600 cm. The structure consists of three layers of graphite with varying densities of 1.1 g/cm^3 and 1.8 g/cm^3. An additional layer consisting of a high-density absorber made of CuCrZr is integrated at the end of the structure. The dump is encapsulated with a 1 cm thick layer of titanium alloy. The extraction line is equipped with three successive cylindrical spoilers made of graphite (with densities ranging from 1.7 to 1.8 g/cm^3) and 3 cm thick. A first dump shielding was implemented, consisting of a first layer of iron (20 cm) and a second layer of concrete (40 cm). Although this is still a conceptual shielding design, it illustrates the expected effects of potential shielding.

FLUKA Monte Carlo simulations were performed in order to assess the residual dose rate after one year of operation (185 days), considering one beam dump per day, where all particles stored in the collider are discharged. The number of particles dumped annually is 4.44×10^{17}p/y (Z pole). The results show that the residual dose rate reaches values around 45-50 µSv/h, at a distance of 1-2 m from the shielded dump, after 185 days of operation (one dump per day) and 1 hour of cool-down; after 1 day, it reduces to 15 µSv/h. The dose rate values are relatively low, indicating that even a minimal shielding around the dumps effectively reduces residual radiation to almost acceptable levels.

Beamstrahlung dump The radiological impact of the beamstrahlung dump using liquid lead as an absorber was assessed. FLUKA Monte Carlo simulations were performed for the Z pole operation mode, as it generates the highest beamstrahlung power among all operational modes. Initial simulations at $t\bar{t}$ mode indicate as well considerable dose rates and more important activation due to the higher energetic beamstrahlung spectrum.

The model considered an inclined beam dump with a layer of liquid lead. An initial shielding design was tested to mitigate the risks associated with residual radiation. The shielding is 1 m thick in all directions and extends 5 m upstream around the vacuum chamber to mitigate backscattering.

Figure 9.11 shows the average dose rate values in the transverse plane across the tunnel, at the level of the beamstrahlung dump, considering an irradiation profile of 1 year at Z pole operation (185 days). Residual dose rate values, after 1 hour of cool-down time, may reach 7 Sv/h inside the shielding. Approximately 3 m away from the shielding, the dose rates decrease to below 100 µSv/h.

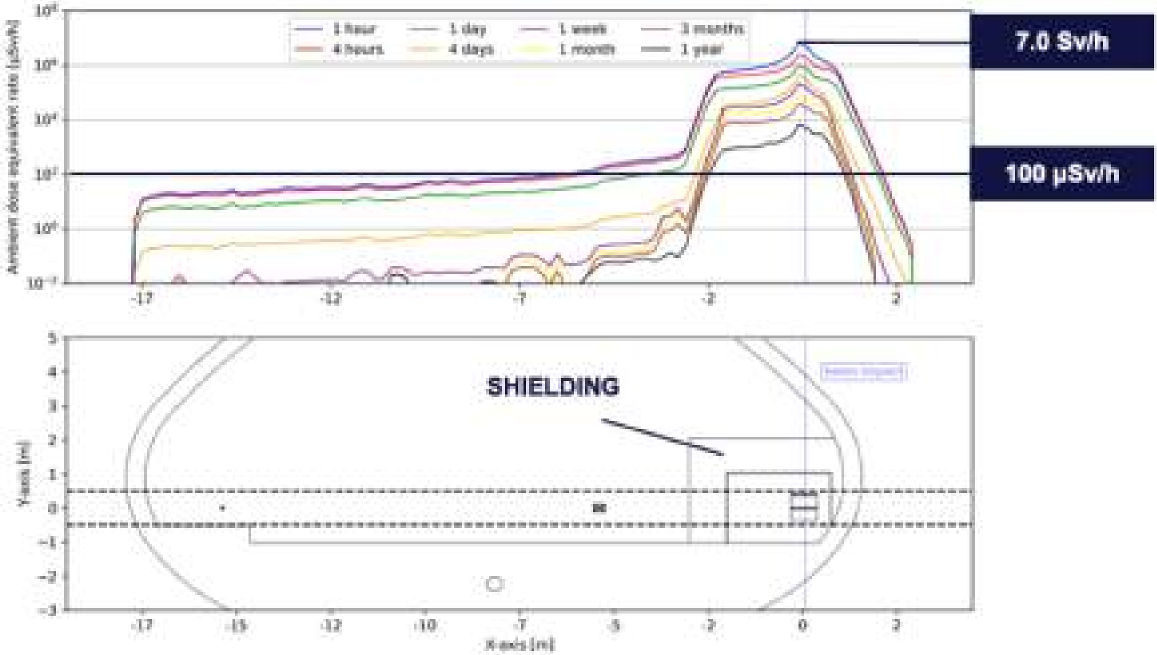

Fig. 9.11 Residual ambient dose equivalent rate profile at the FCC-ee beamstrahlung dump, after 185 days of Z pole operation, for different cool-down times. The profiles are averaged in the volume enclosed by the two dashed lines, which extends 1 m on Y-axis and Z-axis

At these very high dose rates, optimised shielding is mandatory to contain the residual dose rate at an acceptable level outside the dump. The current shielding must be enlarged and optimised to reduce the dose rate to 1−10 μSv/h in the passage area after 4 hours of cool-down time. Appropriate shielding will certainly be more massive, but can be integrated. The dose rate from activated lead in the pumping circuit and reservoir will be further assessed and included inside a shielded casing. Waiting times before manual interventions on the dump will be considerable (days/weeks), and remote operation will be used to minimise doses to personnel while handling components and performing maintenance. The activation of the lead absorber will require particular attention and a dedicated study during the technical design phase to assess the radiological risks and implications for handling and elimination.

Collimation FLUKA Monte Carlo simulations were conducted to evaluate residual radiation in the collimation section (PF) and the potential impact on the design, integration, civil engineering and cooling/ventilation. The model encompasses the positron betatron collimation section, including 12 quadrupole magnets, 6 collimators (both primary / secondary and horizontal / vertical) and 2 shower absorbers. A standard tunnel cross section is used without detailed integration of additional infrastructure, such as ducts, cables, and piping.

The Z pole is considered the operational mode with the highest loss rate of 8.5×10^{11} p/s, based on a beam lifetime of 30 minutes.

Figure 9.12 presents the residual dose rate profiles along the straight section of the positron betatron collimation after 185 days at Z pole operation, evaluated for different cool-down times (ranging from 1 hour to 1 year). The results indicate the highest peak occurring in front of the secondary horizontal collimator. The high dose rates span several tens to hundreds of metres, with maximum residual dose rate values reaching 1 mSv/h after one week of cool-down.

Based on the parameters provided, the collimation section exhibits very high dose rates, making immediate hands-on maintenance in this part of the tunnel impossible. Evaluating and improving collimator shielding could help reduce activation levels in the surrounding infrastructure. With further optimisation of design parameters, the implementation of appropriate bypass tunnels, and a hybrid maintenance approach (combining personnel and robotics), it appears feasible to allow access after one day of cool-down. This time frame is also essential to ensure the decay of short-lived radioactive isotopes in the air, enabling safe ventilation and the controlled release of air into the environment through flushing.

Surface sites Radiological hazards at surface sites during nominal beam operation are potentially induced by prompt radiation that can propagate from the experiment cavern up through the shaft.

The same parameters and radiation sources used to calculate the prompt radiation in the connection tunnels, described above, are applied to calculate the propagation of the prompt radiation from the experiment cavern to

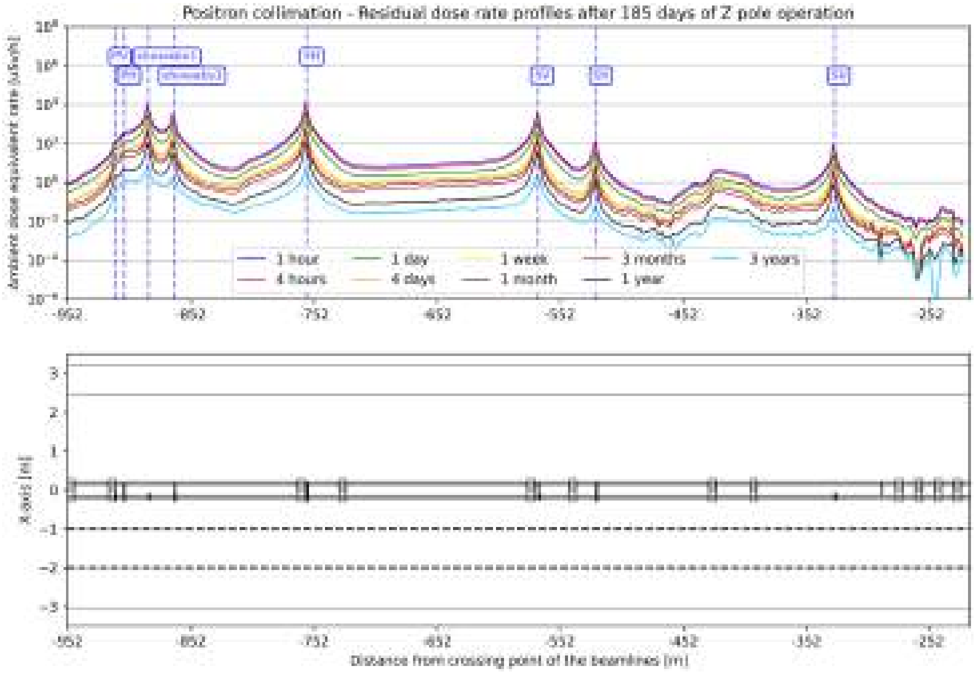

Fig. 9.12 The plot displays the residual dose rate profiles along the positron betatron collimation straight section after 185 days of Z pole operation, evaluated for different cool-down times (ranging from 1 hour to 1 year). The labels correspond to the components on the beamline: PV (primary vertical), PH (primary horizontal), showabs1 (first shower absorber), showabs2 (second shower absorber), SV (secondary vertical), and SH (secondary horizontal)

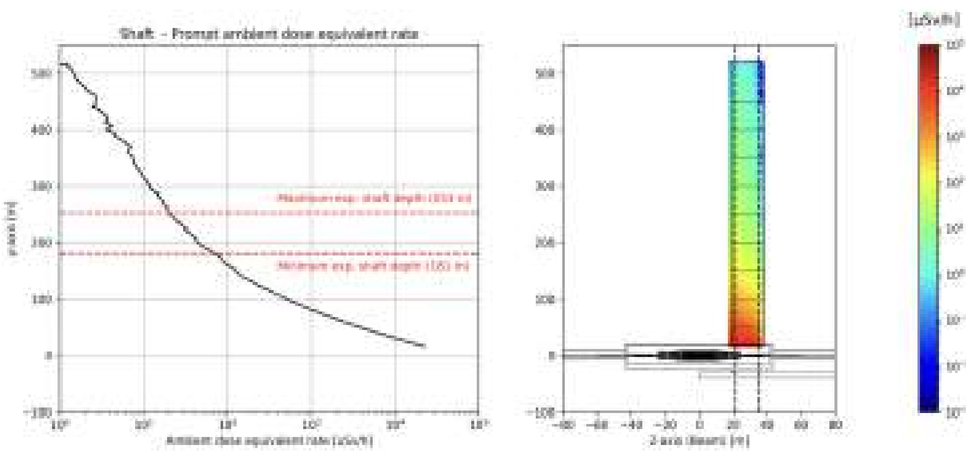

Fig. 9.13 Ambient dose equivalent rate through the shaft resulting from pp collisions in the experiment cavern

the surface along the shaft. The study considers FCC-hh, where proton-proton collisions ('ultimate' scenario, with a collision rate of 3.24×10^{10} p/s) produce a dose rate higher than that of electron-positron collisions in FCC-ee.

The results are shown in Fig. 9.13. The colour map on the right displays the values of the ambient dose equivalent rate along the shaft using a colour gradient (in µSv/h). The left graph depicts the profile of the ambient dose equivalent rate, with values averaged over the volume defined by the two dashed lines in the colour map on the right. The two horizontal red dashed lines represent the minimum and maximum depths of the shafts for the four experimental points. This allows visualisation of the range of ambient dose equivalent rates at the different surface sites.

The plot shows surface dose rates ranging from 10 to 70 µSv/h. Shielding installed at the machine-detector interface, and a 1-metre thick concrete shielding at the top of the shaft are adequate mitigation measures.

Other radiological hazards at the surface site may arise from the handling of activated material that has been removed from the tunnel. Standard prescriptive methods are used to limit the radiological risk to personnel by having dedicated areas to store and work on radioactive items. Buffer zones are established at the border between areas where activation can occur and non-activation areas to control the flow of material and to guarantee the correct classification of items removed from the accelerator areas.

The release of radioactive air and water from the accelerator tunnel and the experiment cavern poses a negligible risk. This is mitigated by recycling the air during operation and having dedicated water handling installations to avoid any potential contamination or uncontrolled releases.

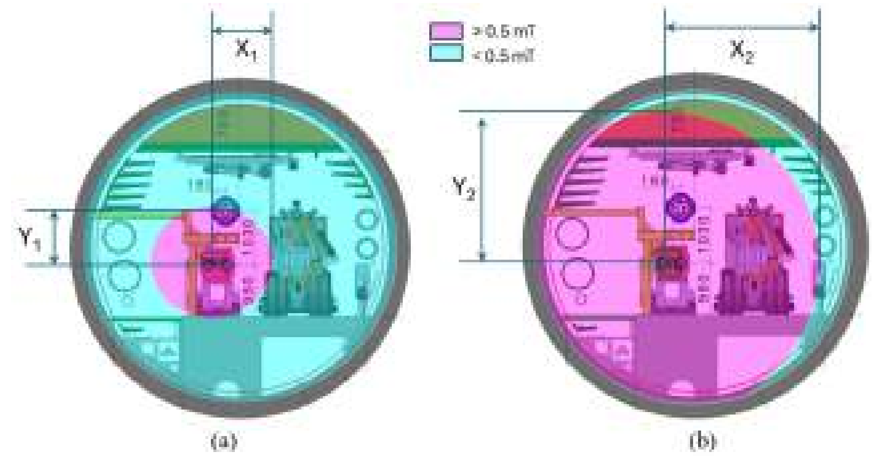

Fig. 9.14 Simulation of stray field envelope at 0.5 mT for the FCC-ee collider arc. a) Dipole: $(X_1, Y_1) = (1070, 980)$ mm; b) Quadrupole: $(X_2, Y_2) = (2690, 2720)$ mm

The use of radioactive sources and X-ray-generating devices in surface facilities may occasionally occur during the construction and operation phases. These common practices are covered by standard prescriptive methods and rigorous regulations that have been widely applied at CERN and in industry.

Non-ionising radiation (NIR) Risk of non-ionising radiation includes exposure to static magnetic fields, time-varying electromagnetic fields (e.g., RF), lasers and non-coherent light sources (e.g., UV & Infrared, light, LED). These risks are currently addressed by standard practices, namely by European Directives [457, 458]. It is possible, at this stage, to conclude that the design of NIR-generating accelerator and detector components will respect the exposure limit values of the directives.

For static magnetic fields (e.g., from permanent or electro-magnets), the exposure limit values (ELV) and action levels (AL) are given by CERN's General Safety Instruction GSI-NIR-1 [459].

Stray magnetic field from experiment detectors A study was performed simulating typical fringe fields from the experiment cavern housing an FCC-hh detector representing a worst-case scenario and concluded that the residual magnetic field at the surface of experiment points is well below current limits. At a distance of 200 m above the detector, the stray field is of the order of 0.1 mT, whereas the limit for wearers of active medical devices is 0.5 mT [460].

Stray magnetic field from the collider A study was performed simulating the extent of stray fields for evaluation against the ELVs and ALs. All stray field envelopes at the ELVs stay within 1 m from the magnet's centre, except for the quadrupole, which emits a stray field envelope at 0.5 mT to most of the cross-section of the tunnel (Fig. 9.14). This is due to the fact that the quadrupole has substantial field strength (≈ 0.45 T at the aperture) and an open iron yoke. In comparison, the dipole yoke is also open but with low field in the aperture (60 mT), while the sextupole also has a relatively high field (0.5 T) but confined within a closed iron yoke. Since quadrupoles will be spread throughout the arc, people with active implantable medical devices (AIMD) would not be able to access the tunnel, without a valid medical certificate [459]. Even when the magnets are not powered, there is still a residual risk of remanent fields stemming from magnetised metal in the surroundings. Occasional access in specific areas may be granted, based on a risk assessment and fenced off from any individual 0.5 mT sources.

Access is possible for the public and workers without any particular risk[20] ($B < 40$ mT). Any work near the dipoles and quadrupoles when the magnetic source is on would require a specific workplace risk assessment and training.

Lasers for beam polarisation Fixed laser installations are planned in some alcoves for beam polarisation and energy calibration. The laser installation will be installed within a dedicated laser area (DLA), with interlocks to cut off the source in case of unauthorised access. The classification of the laser systems, as well as the engineering control measures, will follow the applicable International Standards, i.e., IEC 60825 series [461].

Optical fibre network The infrastructure will deploy an optical fibre network (OFN) for internal communication and data transmission. Depending on the maximum output power of the transmitter (dBm), the OFN will be classified within a given hazard level in accordance with IEC 60825 [461]. For any given hazard level, a set of engineering control measures are required.

[20] Such as wearers of passive metal implants and pregnant workers.

Electrical safety The electrical infrastructure will cover everything from low voltages (e.g., lighting) to high voltages (e.g., power transmission). Despite this wide range, electrical safety may still be covered by standard practices. Most of the electrical equipment will be housed in surface buildings, in the service caverns, and the alcoves. The FCC accelerator and experiment detectors are expected to be designed according to the appropriate international standards (IEC) where they obey the safety by design principle, i.e., ensuring a proper degree of inherent protection (e.g., IPx rating according to the IEC 60529 standard [462]) preventing live parts being accessible. Any non-standard equipment will be subject to a rigorous risk assessment design process to ensure conformity with the applicable legislation. The electrical network will be designed according to national and international standards for all voltage levels (low, medium, and high). A secure power network is foreseen as mentioned in Sect. 9.4.1. The location of cable trays in the tunnel arc and the alcoves is chosen to minimise interference with the occupants.

Occupants and emergency teams will be authorised and required to activate an emergency stop in case of an unsafe situation or incident, cutting off the electrical power to the general (non-safety-related) services. In the LHC, this is achieved by a spatial distribution of general emergency stop (AUG) buttons along the tunnels and caverns. The exact technical solution for the FCC will be studied in the next phases, during the detailed design of the electrical network.

For works or activities in which the protection elements are temporally removed, there are a set of technical and administrative procedures to ensure the safe execution of such activities. For example, lock-out, tag-out and electrical work permits to ensure safety during interventions on electrical equipment. A safety-by-design approach is enforced, considerably reducing the technical and administrative burden of specific safety prescriptions.

Chemical safety Only a few chemicals are required for the operation of the FCC infrastructure. Most of them will be used in the closed circuits of the cooling water network:

- Biocides - chlorine dioxide, produced from hydrochloric acid and sodium chloride.
- Corrosion inhibitors - mainly sulphuric acid.

Significant quantities of synthetic lubricants (e.g., BREOX) are expected on the surface sites for the cryogenic compressors. Cooling refrigerants (coolants) are also needed for the fan coils in the tunnels and chillers on the surface. Some traces of oil are expected underground, but these will be in minimal quantities (e.g., vacuum pumps, motors, and other machinery).

At this stage, only standard chemicals are intended to be used, hence standard practices and regulations are applicable when handling these chemicals. For each chemical product, the supplier must deliver a safety data sheet (SDS) or an extended safety data sheet (eSDS) and a technical data sheet (TDS) with information on product usage, on hazards during use and during emergency procedures.

Mechanical safety The feasibility study focused on the technical infrastructure at large and its possible impact on the civil engineering layout. The mechanical design of the beamlines and equipment inside the infrastructure will be detailed in the next phases of the project. The necessary safety studies and assessments will be performed in parallel.

The use of robotics (both overhead and floor-driven) will be widely present in the FCC infrastructure. The cohabitation of robots and personnel poses a safety hazard that will be dealt with during the design phase, where the robotic systems are designed and manufactured according to the EU Regulation 2023/1230/EU on machinery [463] and associated harmonised standards.

Indoor air quality The indoor air quality in the underground infrastructure is guaranteed by the ventilation system described in Sect. 9.4.1. During access mode, the air renewal for hygienic purposes is guaranteed by the air exchange in the concerned sector. The values of the flow rates and air velocities in the tunnel are shown in Table 9.4. In the technical points (PB and PF), the supply flow rate for the service caverns and connection tunnels is 20,000 $m^3\ h^{-1}$. For the experiment points (PA, PD, PG and PJ), the supply flow rate for the service caverns and connection tunnels is also 20,000 $m^3\ h^{-1}$, whereas the experiment caverns are supplied with 50,000 to 70,000 $m^3\ h^{-1}$. The RF points (L and H), are supplied with 20,000 $m^3\ h^{-1}$ in the service areas (cavern and connections) and 30,000 $m^3\ h^{-1}$ in the RF sector in the tunnel [438].

The ventilation of the underground infrastructure is a pre-condition for access. Hence the correct functioning of the ventilation system must be ensured before granting access to personnel.

Noise As far as reasonably possible, the owners of noise-generating equipment installed both in the underground areas or surface sites must apply technical solutions to achieve a daily exposure level below 80 dB(A) [464]. These limits are considered state-of-the-art and would avoid the mandatory use of personal protective equipment (e.g., earplugs). In the case of specific equipment emitting higher sound levels (e.g., cryogenic compressor building at the surface), specific engineering and personal protective measures must be put in place.

Table 9.4 Metrics of the ventilation system in the accelerator tunnel during access mode [438]

Scheme	Flow rate [$m^3\,h^{-1}$]	Velocity [$m\,s^{-1}$]	ACH[a] [h^{-1}]
Semi-transverse	27,000 (per half arc) *(54,000 per sector)*	0.25 *from 0 (midpoint) to 0.5*	0.3 *in a sector*
Longitudinal	54,000 per sector	1	0.3

[a] Air changes per hour

Workplace ergonomics Despite the fact that there are no permanent workplaces in the underground infrastructure, occupants may be requested to spend considerable amounts of time performing repetitive tasks therein. The integration of the tunnel arc, as well as the experiment and services caverns, must take into account the requirements to ensure proper workplace ergonomics.

In the tunnel arc, the passage from the transport area towards the opposite side of the accelerator(s), i.e., the external side, passes underneath the beamline in between two beam elements (e.g., dipoles, corrector magnets, etc.). Such a passage must take into account the ergonomics of occupants crossing from one side to the other several times a day. Standard practices as used in industrial installations are available in EN 547 [465] to cover this occupational hazard. If passage underneath the beamline remains the baseline approach, the minimum vertical clearance from the floor to the vertical obstacle (i.e., the beam pipe) is 1123 mm.[21]

9.4.3 Occupational hazards during accident scenarios

During the feasibility study phase, only some selected accident scenarios were analysed, mainly those deemed to have an impact on the layout and civil engineering structure of the underground infrastructure. Additional accident scenarios will be assessed during the next phases of the study.

Ionising radiation Accident scenarios that may be relevant in terms of radiological protection will not produce different hazards from those described for nominal operation, i.e., external exposure from prompt or residual radiation or internal exposure from the incorporation of radioactive contamination. The relevant scenarios considered are the following.

- Beam losses: refers to the inadvertent deviation or depletion of particle beams from their intended trajectory within the accelerator, leading to secondary radiation from interactions with accelerator components. A machine protection system must ensure that such events are detected and the beam will be directed either to the beam dumps or absorbed by the collimation system or protection devices.
- Fire: fire can release radioactivity from combustible activated materials, with smoke that carries radioactive isotopes. As it spreads and settles, contamination may occur. The radioactivity content in combustible materials is low and will not lead to a relevant exposure of the intervening personnel. The radiological risk to workers or emergency responders is negligible, given the greater risks that such emergency situations present, such as oxygen deficiency, smoke toxicity, and fire.
- Leakages: leaks from water circuits can release large amounts of water that may contain radioactive isotopes. The radioactive concentration of the water circuits is low and will not lead to any relevant exposure scenarios.

The main accident scenario considered is an accidental beam loss, where the civil engineering infrastructure is critical to contain prompt radiation and protect workers in adjacent areas. Although unlikely and mitigated by the machine protection system, such scenarios are considered in the design. Beam loss scenarios are assessed at critical locations, that are, the injector complex, bypass tunnels, and RF klystron galleries. The dose objective of 1 mSv per incident[22] is respected in the following loss cases studied.

Injector complex Dose equivalents from secondary radiation during full beam loss scenarios of one-hour duration remain largely inferior to those of the continuous loss scenario with a limited loss rate, as described above.

The doses behind 6 m of soil will be less than 100 µSv as shown in Fig. 9.15. Therefore, the constraining scenario is determined by a sustained, limited beam loss rate.

[21] Based on the tallest population in CERN's members states, with a wrist to shoulder blade distance of 823 mm (95^{th} percentile) and an additional 300 mm allowance covering the helmet, and head movement clearances.

[22] Design target values for a non-designated area. It refers to the maximum effective dose per event with a probability <0.01 per year.

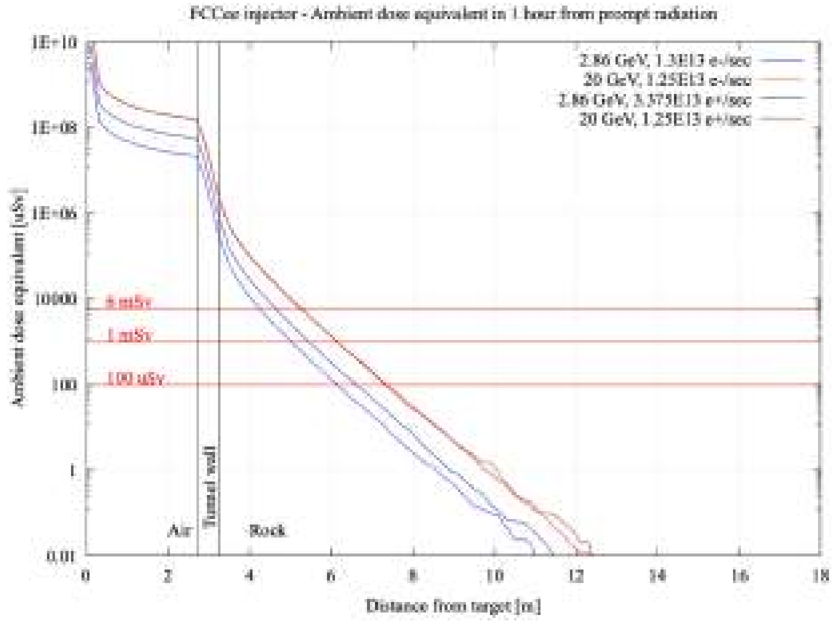

Fig. 9.15 Ambient dose equivalent through the shielding at the FCC-ee injector complex, resulting from a 1-hour beam loss scenario

Klystron gallery During the operation of the collider and booster, the klystron galleries remain accessible. Given that radiation can propagate through waveguide ducts and emergency exit staircases, prompt radiation propagation was assessed in the event of an accident scenario, i.e., beam loss.

In the absence of well-defined beam loss scenarios, the study considers the most conservative case, which is the complete beam loss, where all the particles stored in the ring (both electrons and positrons) impinge on a single cryomodule located below the waveguide duct. Although this scenario is highly improbable, it can serve as an upper limit for the analysis of a catastrophic event. Radiation transport simulations were performed to determine the ambient dose equivalent in the klystron gallery.

The beam loss scenario is analysed for the Z mode (beam energy 45 GeV) as it has the highest beam intensity of all operational modes, which is not compensated for by the higher energy at $t\bar{t}$ mode. The resulting dose was normalised using the total number of particles stored in the ring, that is, 15,800 bunches of 1.51×10^{11} particles per bunch, for 2 beams giving 4.8×10^{15} particles in total.

The results, shown in Fig. 9.16 and Fig. 9.17, include two types of plots: a 2D colour map illustrating the dose distribution within a specific tunnel subcell, highlighting the transverse cut used in the simulation model, and a 1D profile averaging the values from the colour map along the waveguide duct profile.

The results show that, during a full beam loss scenario in Z mode, the dose in the klystron gallery is of the order of 10 µSv. This value is well below the annual dose limit of 1 mSv for a non-designated area, as indicated in Table 9.3.

The access requirement to the klystron gallery during FCC-hh operation still needs to be decided. If the gallery remains accessible, the radiological conditions must be compatible with the radiation source presented by the FCC-hh.

Bypass tunnels The S-shaped bypass tunnels at the experiment points, approximately 100 m in length, were evaluated for their compatibility to ensure low doses in the service cavern during catastrophic beam losses in the accelerator tunnel. In the absence of defined beam loss scenarios, the study assumes the most conservative case: a full beam loss of all stored particles of both beams impinging on an accelerator component in front of the junction with the bypass tunnels. Figure 9.18 shows the results of the radiation transport simulations, where the service cavern is connected to the bottom left, and the accelerator tunnel is running at the top of the plot. Ambient dose equivalents remain below 1 µSv for FCC-ee in Z mode and at about 10 µSv for FCC-hh for a catastrophic full beam loss in the collider. The results demonstrate compliance with the design objectives.

Fire and smoke Fire and smoke propagation pose a significant risk to the FCC infrastructure, particularly in underground areas. The likelihood of a fire can vary based on factors such as location, activity, layout, fire load, and occupancy levels. However, fires in confined spaces are especially dangerous due to the accelerated growth caused by thermal radiation feedback and the rapid spread of smoke.

As an outcome of the initial hazard registry analysis, the following list describes possible ignition sources or fire-specific hazards across FCC areas:

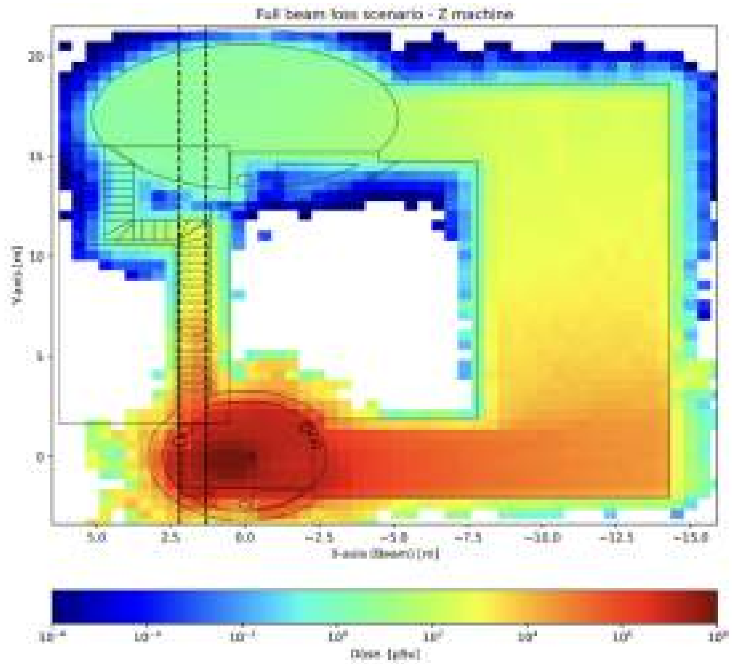

Fig. 9.16 The ambient dose equivalent is calculated for a catastrophic accident scenario, considering that all particles stored in the FCC-ee collider are lost against an RF cryomodule in a single event. The colour map illustrates that the estimated ambient dose equivalent inside the klystron gallery is approximately 10 µSv

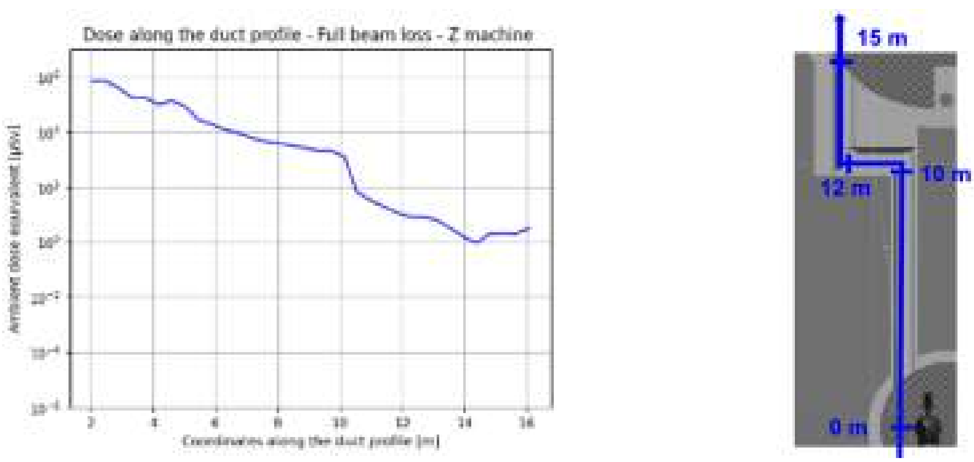

(a) (b)

Fig. 9.17 The plot presents the dose projected along the duct during a complete beam loss scenario at the FCC-ee RF section. Prior to the second leg (at x = 10 m), the ambient dose equivalent reaches 2 mSv. Then, the values decrease down to 1 µSv, due to the presence of the chicane. At the far end, the dose increases again as a result of the contribution of radiation coming from the staircase

1. High and low voltage installation, including cables and power wet/dry transformers (overheat, short-circuit, arc) (For LHC, the frequency of an electrical fire was estimated as $\approx 4 \times 10^{-3}$/year [466])
2. Transport vehicles (accident, battery malfunction)
3. Hot works (welding, grinding)
4. Cryogenic systems (oxygen enrichment of air, condensed air dripping on combustible materials)
5. Pumps and mechanical devices (overheat)
6. Flammable and explosive atmospheres (in surface building only)
7. Glowing cigarette
8. Arsonist (considered as unlikely for underground areas due to access control and active surveillance)

These hazards are mitigated by means of a fire safety concept that describes the coordinated set of civil-engineering, technical and organisational measures to reduce fire risk to the level that meets safety objectives (see Sect. 9.2.2).

The fire safety concept follows two strategies:

- *prescriptive approaches* based on Host States laws: this *deem-to-satisfy* solution ensures that at least life safety criteria are met, and safety measures are commensurate with standard industrial fire risks. This will be the default strategy for surface buildings.

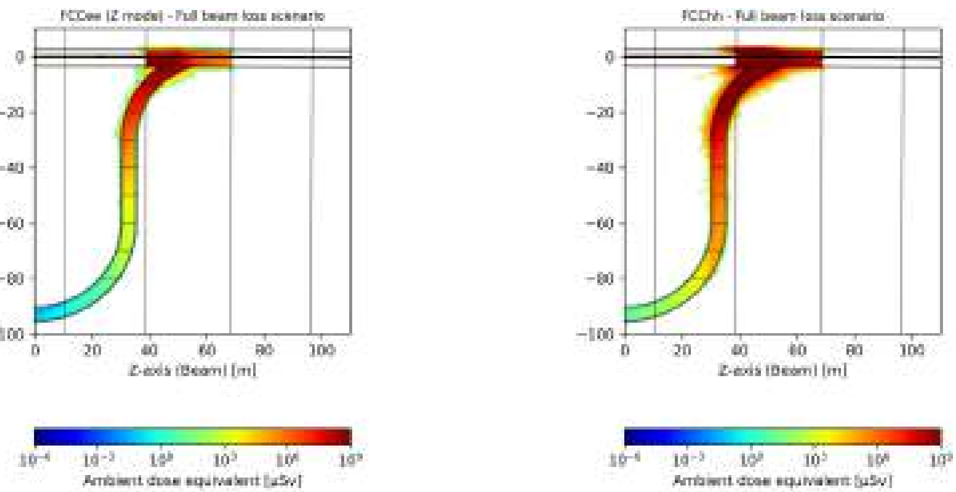

(a) (b)

Fig. 9.18 These plots show the stray radiation scattering along a bypass tunnel from a full beam loss of both beams in FCC-ee, Z-mode (beam energy 45 GeV) (a) and FCC-hh (b)

- *performance-based design*: as explained in Sect. 9.3.3, whenever the technical prescriptions cannot be implemented, are not appropriate or simply out of scope, the safety objectives need to be ensured by guaranteeing the safety performance of the facility in case of accidental scenarios.

The following subsections summarise the safety studies to characterise fire hazards in FCC and describe the prevention and mitigation measures included in the main areas of the infrastructure. Fire resistance, reaction to fire and organisational measures to ensure fire safety are discussed at the end of the chapter. The proposed fire safety concept will be refined in the subsequent phases of the study and updated to reflect any future changes to the baseline used in the feasibility study.

Tunnel arcs The accelerator tunnel represents the largest volume and floor area of the entire facility. Thus, specific attention has been devoted to studying how a fire will impact the evacuation and the life safety of the occupants. The entire analysis is available in a technical report [467], with a summary of the main assumptions and outcomes below.

To verify that the proposed compartmentalisation and smoke extraction strategies ensure life safety objectives, computational fluid dynamics (CFD) simulations using the NIST's Fire Dynamics Simulator (FDS) (v6.8.0) [468] have been performed for a complete 400 m long compartment.

The tenability limits below (based on ISO 13571 [469]) define the performance criteria used throughout the study:

- Visibility of the evacuation path (at 2 m height) < 10 m
- Fractional Effective Dose (FED) > 0.3
- Temperature > 60 °C

Additional criteria are analysed for further comparison among trial designs such as: FED> 0.1, hot smoke layer temperature of 200 °C, smoke layer spread velocity and heat flux > 2.5 kW m^{-2}.

The time to reach these untenable conditions constitutes the 'Available Safe Egress Time' (ASET). The 'Required Safe Egress Time' (RSET) is defined as the time required for the occupants to leave the compartment. The comparison of both times provides the safety margin used for the analysis of life safety criteria, as illustrated in Fig. 9.19. The ASET $>$ RSET condition is a safety requirement for all scenarios studied.

The baseline pre-movement time and walking speed are taken from BS PD 7974-6 [470] and set as 30 s and 1.2 m s^{-1}, respectively. The 90$^{\text{th}}$ (pre-movement) and 10$^{\text{th}}$ (walking) percentiles of the standard distribution associated to those values (i.e., 120 s and 0.8 m s^{-1}, respectively) have also been used to explore slower responses. Table 9.5 summarises the list of input parameters required to perform the evaluation.

Several design fire scenarios were developed during the conceptual study phase, during brainstorming sessions conducted with accelerator safety experts and using reference data from the literature [471]. Among these, a fire developing from a transport vehicle loaded with pallets was shown to be the worst-credible scenario with respect to life safety in the tunnel. The heat release rate (HRR) curve obtained shows a medium-fast growing phase that reaches a first peak of 4 MW in 8 min. After a short dip, the HRR continues to grow up to a 8 MW peak reached after 17 min, as shown in Fig. 9.20.

The study also investigated the two main ventilation strategies proposed above as well as the impact on the final available safety margin time (ASET − RSET) of several different design criteria such as: smoke extraction

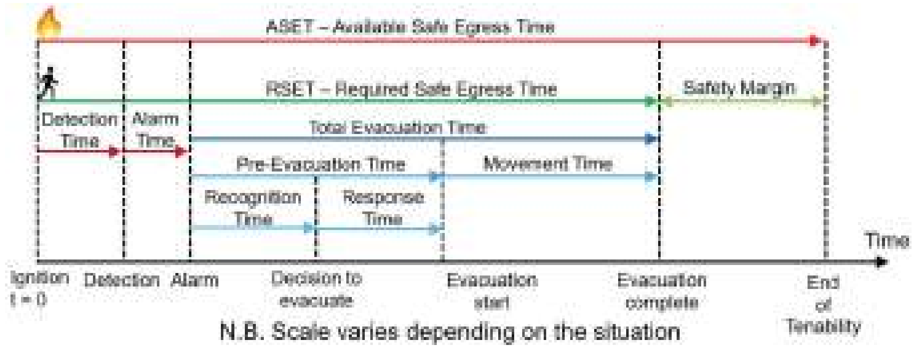

Fig. 9.19 Illustration of the different time stamps and input parameters to evaluate the ASET and RSET, starting at the ignition ($t = 0$)

Table 9.5 Input values to perform the ASET-RSET analysis. Occupants are considered to be awake and familiar with the premises - Cat. A, and assumed to be trained to a high level of safety management - level M1 (ensured by appropriate training before access to underground facilities is granted (see Sect. 9.4.5). Whilst the complexity of the building is considerable, having a wayfinding system (see Sect. 9.4.1) and only two possible routes (left or right) allow the selection of a building level B2. Level A1 is considered since a robust detection system is to be installed across underground premises. The occupants' location is relative to the location of the fire

Parameter	Value	Justification
Detection time	120 s	Performance requirement for such fire
Pre-movement time	30 s (120 s)	BS PD 7974-6 [470]
Ventilation ramp up	0 - 60 s	Ventilation design [438]
Walking speed	1.2 $\mathrm{m\,s^{-1}}$ (0.8 $\mathrm{m\,s^{-1}}$)	BS PD 7974-6 [470]
Occupant's location	−100 m / 0 m / +150 m	Credible scenarios

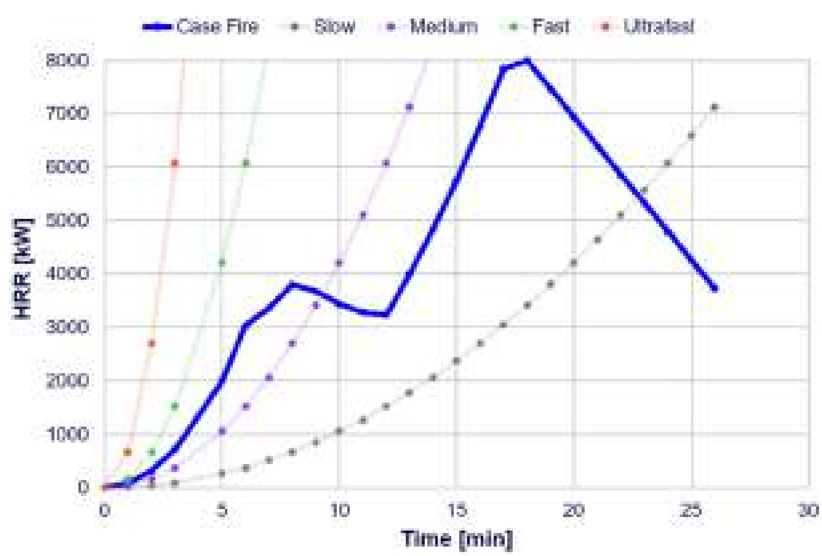

Fig. 9.20 Fire scenario of transport vehicle considered for PBD assessment against the life safety objective in the tunnel arc. Standard t^2-curves (ISO 16733-1 [472]) are also depicted for comparison (from slow to ultra-fast growth). The analysis is stopped after 27 min to match the simulated time relevant for life safety

flow, fresh air supply, door behaviour, delay times, background initial flow. All the cases (nominal and degraded) are described in a specific technical report [467].

The performance criteria are examined using time-position plots for all scenarios studied, as illustrated in Figs. 9.21 and 9.22. The evacuation time-position profiles (extensively used in tunnel fire safety [473, 474]) allow the ASET > RSET condition to be verified as well as quantifying the safety margin when the occupants reach the end of the compartment.

The analysis of all scenarios confirmed that both of the proposed smoke extraction concepts allow enough time to safely evacuate the compartment under nominal conditions. Some degraded modes (i.e., no detection, and therefore no automatic activation of any action) do not meet ASET > RSET condition.

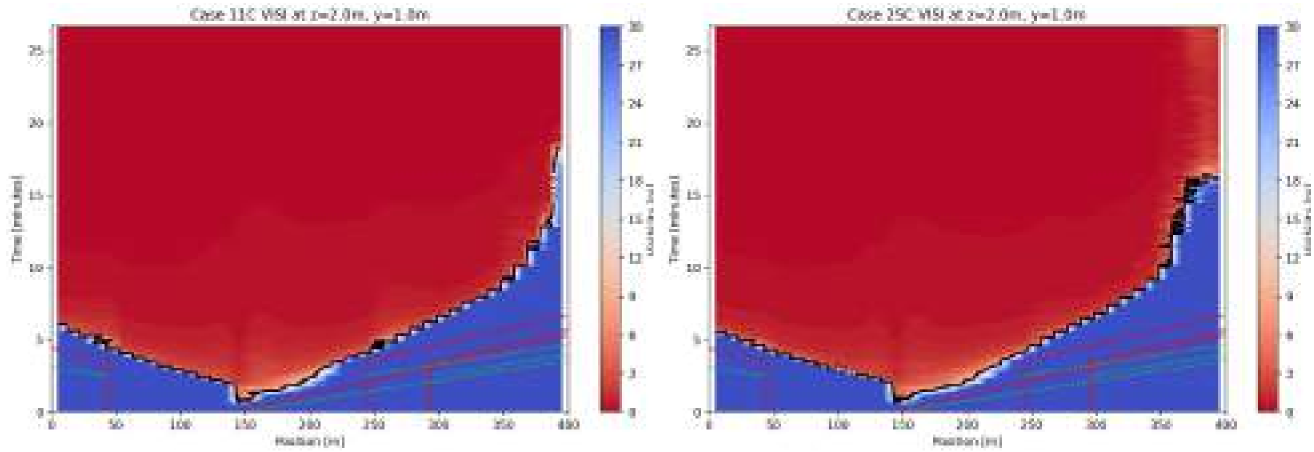

(a) Semi-transverse Case 11C [468]

(b) Longitudinal Case 25C [468]

Fig. 9.21 Visibility time-position plot for semi-transverse (ST) and longitudinal ventilation (LT) strategies. The 10 m visibility threshold is clearly depicted as well as different possible evacuation pathways (shown as dashed lines) for reduced and nominal human behavioural cases. Ventilation vector: left-to-right. Both strategies ensure that occupants can evacuate before reaching untenable visibility conditions; ST is the most performant option, namely downstream the seat of the fire

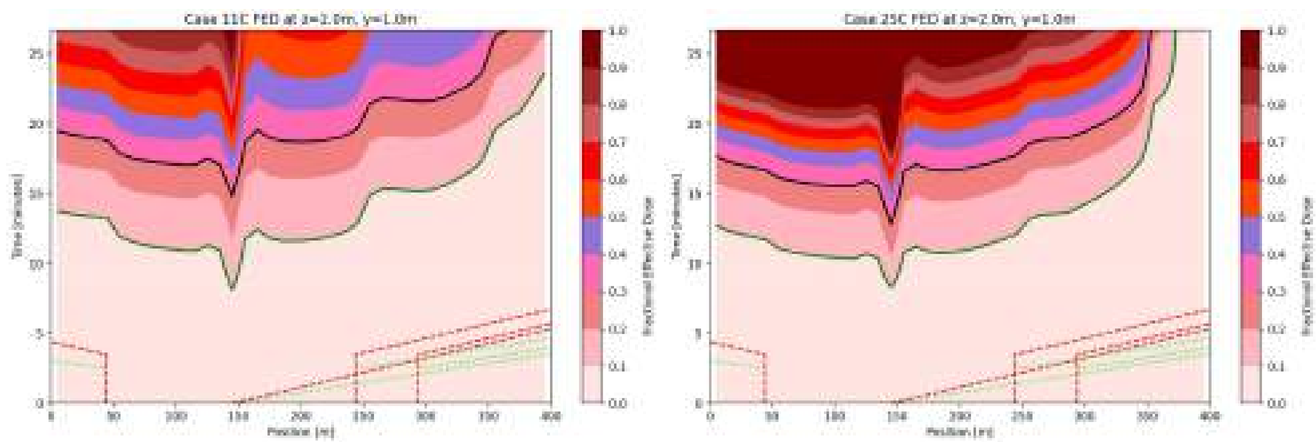

(a) Semi-transverse Case 11C [468]

(b) Longitudinal Case 25C [468]

Fig. 9.22 Fractional effective dose (FED) plot for semi-transverse (ST)and longitudinal (LT) ventilation strategies. Ventilation vector: left-to-right. The FED 0.1 and 0.3 thresholds are clearly depicted, as well as evacuation lines for reduced and nominal human behavioural cases

Finally, the safety margin for nominal and reduced speed evacuees provided by nominal conditions (no degraded modes) of cross-sectional and longitudinal smoke extraction strategies are compared in Fig. 9.23. Several extraction capacities from 0 to 25,000 m^3/h are also explored. The semi-transverse solution shows better smoke-sweeping capacity, providing a better margin for the same extracted flow. The comparison also demonstrates that the absence of smoke extraction induces a negative safety margin, i.e., the occupants are unable to reach the compartment due to the lack of visibility.

In conclusion, from a safety point of view, the dynamic confinement offered by the semi-transverse scheme is found to be more efficient and robust (including degraded modes) for the safe evacuation of occupants in case of an incident. Thus, for this feasibility study phase, the semi-transverse option is considered as the baseline for the FCC tunnel.

Shafts and safe areas Within the shaft and their waiting areas (see Sect. 9.4.4), the fire risk will be limited to fire loads stemming from the safety systems themselves. These areas are critical for safe evacuation and must not be compromised; hence, no storage of combustibles is allowed. As mentioned above, the pressurised volume and an EI120 compartment ensure that these areas are free of smoke at all times.

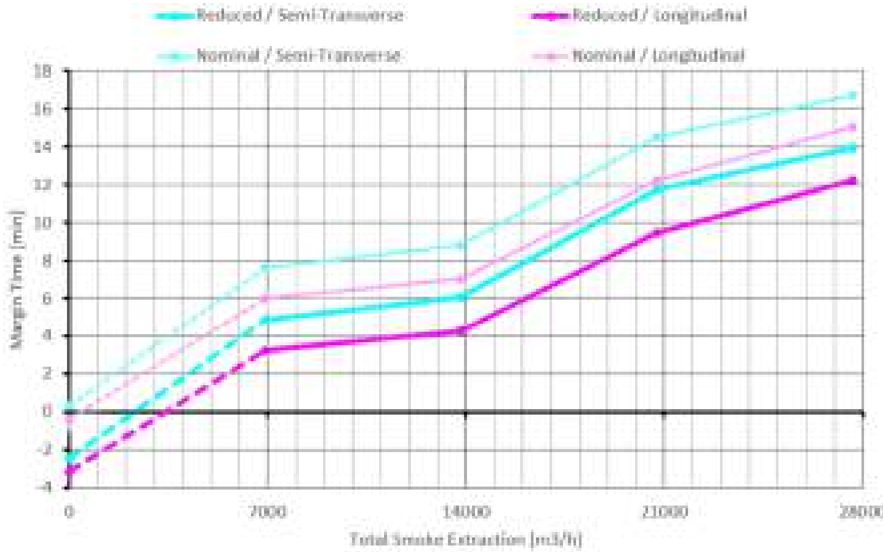

Fig. 9.23 Safety margin (ASET-RSET) available for reduced (120 s pre-movement time and $0.8\ \mathrm{m\,s^{-1}}$) and nominal (30 s pre-movement time and $1.2\ \mathrm{m\,s^{-1}}$) evacuees and different smoke extraction (and supply) flows

Conversely, the transport zone of the vertical shaft poses a significant fire risk. Due to its chimney-type configuration, a fire at the bottom of the shaft will quickly propagate upwards, making it difficult to reach and extinguish. To mitigate this, additional fire safety measures should be considered, such as cable enclosures, fire protective barriers at regular intervals, etc. Although this scenario does not pose a major threat to life safety (since the transport zone is separated from the lift shaft), it is important to consider how safety systems are protected at the surface. In a later stage of the study, the impact on property protection and continuity of operation of such scenarios will be considered in a cost-benefit analysis to identify the most appropriate measures.

Experiment caverns Fire risk in experiment caverns is primarily associated with the large quantity of data and power cables feeding the detector and the ignition sources and combustibles integrated within its sub-systems.

The reaction to the fire of cables will be controlled to limit the energy, smoke, and acidity production and all the cable trays exiting in the experiment caverns (via the connection galleries) must be sealed and covered with intumescent paint to prevent propagation. In localised areas with vertical dense cable tray arrangements, automatic extinguishing systems (e.g., water mist) will be considered as a compensatory measure for property protection and business continuity.

Regarding the detector, a dedicated risk assessment will be conducted for each detector sub-system, identifying the most appropriate compensatory measures to maintain the fire risk within acceptable limits. The LHC detectors currently employ several effective safety measures to mitigate the fire risks, including:

- **Inert nitrogen atmosphere**: the inner detector volumes are filled with nitrogen to eliminate ignition sources in combustible areas.
- **Inert gas extinguishing systems**: flooding systems are in place to suppress potential fires in outer layers, with manual activation available from the control room.
- **Dedicated detection systems**: localised detection systems monitor for anomalies and can trigger power cuts to prevent malfunctions. These systems utilise inner temperature monitoring and multi-parameter gas sampling to ensure precise oversight within the detector.
- **Over flooding foam system**: a water-based foam system allows flooding of the cavern in case of extensive fire. This system is not aimed at life safety and might be destructive to the detector electronics. Technical and cost-benefit analyses are required to evaluate the appropriateness for the FCC detectors.

From a life safety standpoint, the lower-level safe-passage connections to protected areas in the service cavern (purple galleries in Fig. 9.24) allow quick evacuation in case of fire. Due to the volume of the FCC-ee detector compared to the large dimensions of the cavern and its shaft (Fig. 9.24), smoke extraction is not required for life safety. This was closely studied for ATLAS and CMS in the LHC [439, 440] and remains valid for the FCC experiment caverns at this stage. A smoke extraction system is still necessary to ensure safe and efficient fire-fighting intervention, as well as to reduce potential property loss in case of fire.

Service caverns The service caverns house the majority of the technical infrastructure to feed the underground facilities. They are areas with significant fire loads and ignition sources, such as power transformers, electrical racks, and computing rooms, which must be enclosed within equipment-specific EI120-rated fire compartments.

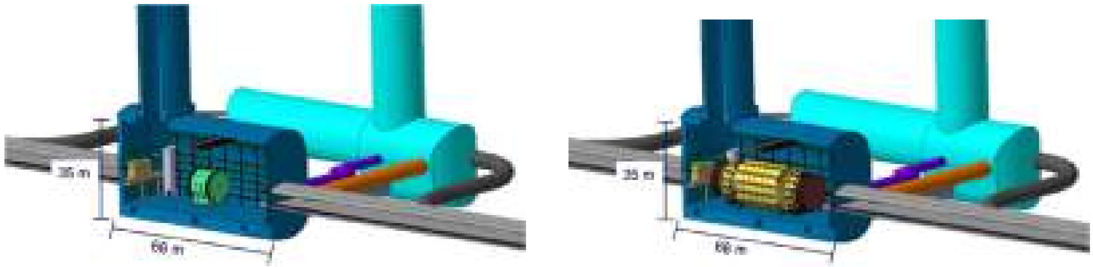

(a) FCC-ee (b) FCC-hh

Fig. 9.24 Illustration of the FCC detectors at the experiment point PG

The proximity to pressurised safe areas and the efficient vertical means of evacuation (shafts) ensure the life safety of the occupants, as verified by the studies performed for the LHC [439, 440].

The evacuation passages from the experiment area and the main tunnel are also completely enclosed within an EI120 fire-rated over-pressurised compartment and will not be impacted by any fire in the service cavern.

A cost-benefit analysis will determine if dedicated extinguishing systems, such as inert gases or water mist, will be needed to protect property in critical areas such as computing rooms or power transformer zones.

Klystron galleries The klystron galleries concentrate high electrical energy and combustible loads comprising power cables and the klystrons themselves. While dry technologies exist, the infrastructure is being designed for the possibility of hosting oil-filled klystrons. These galleries are equipped with a ceiling-mounted emergency extraction system, similar to the main tunnel, and evacuation distances are limited < 200 m (i.e., 400 m in between two exits). Several pressurised connection staircases to the main tunnel, are distributed along the gallery, ensuring the evacuation of occupants in case of fire (see below).

Alcoves Alcoves will contain large amounts of active equipment needed for the operation of the accelerator in a small volume: transformers, control and power racks, electrical components, etc. They are considered as high fire risk areas due to the combination of fire load with multiple electrical ignition sources. Hence, they must be compartmentalised with respect to the accelerator tunnel, with a fire door, fire dampers and sealing of all services which cross.

The maximum combustion time of a 1 MW fire in the alcoves is $\approx$1 h 30 min. This is considering the relatively small and enclosed volume ($\leq$40 m^3) and the fact that fire cannot be sustained below 13%[23] O_2 concentration [475]. Hence, the fire rating for the alcove compartments is EI120, considering that flashover conditions cannot be discarded at this stage.

The racks and services feeding the safety systems of the tunnel arc will be installed in the alcoves. This equipment will be contained in separate volumes within the alcoves, protected with a dedicated fire compartment. This limits the risk of compromising those safety systems in case of a fire inside the alcove.

The evacuation distance to reach the fire door at the entrance of the alcove remains limited (below 40 m), so the occupants can quickly reach the adjacent compartment in the main tunnel.

The smoke extraction ducts installed in the alcoves are connected to the tunnel smoke extraction system with fire-rated dampers. As mentioned above, smoke extraction from the alcoves is deemed not necessary for life safety but is important for the emergency intervention teams, property protection and business continuity in case of a fire.

In some specific alcoves, oil-filled transformers might be installed. In these cases, localised extinguishing systems (e.g., CO_2, inert gas, automatic powder extinguisher, water mist) will be considered case by case to mitigate the impact on property protection and continuity of operations to an acceptable level. Moreover, the rail-mounted robotic intervention solution that is planned for the tunnel areas might not be suited to the alcove geometry and justifies further study for automatic extinguishing of high-fire risk-specific equipment.

Surface buildings The surface buildings will house most of the underground technical systems. The fire load is considered to be present in the form of electrical cables, racks, power transformers, and other industrial equipment (oil compressors, pumps, fans, etc.). Prescriptive approaches for industrial facilities as per Swiss AEAI [442] and French Code du Travail [441] provide the design requirements to ensure life safety goals. In addition to the minimum host state requirements, areas considered as high-risk (with high fuel load density or ignition sources) will be equipped with automatic fire detection systems, enabling the prompt detection and activation of first responders. In such cases, the evacuation alarms will also be automatically triggered.

[23] Conservative value to account for hydrocarbon fuels.

Reaction to fire The underground inner lining will be made of non-combustible materials (A1/A2 as per EN 13501-1 [476]) and will not increase the fire load in the facility. Partitions must also be non-combustible (including sandwich panels, false ceilings/floors, and finishing). This is in line with the requirements for underground transport tunnels [432, 477, 478].

The combustibility of material contained in the premises will be strictly controlled to limit combustibility and the consequences of any ignition. CERN Safety Instruction IS 41 [479] limits the spread of flames, droplets behaviour and smoke production of all materials to a minimum or low contribution to fire (i.e., A, B and C Euroclasses [476]) and prevents the use of halogenated materials. Whenever these provisions cannot be met, a dedicated risk analysis is performed to determine compensatory measures to limit such materials.

Specific attention is to be paid to the reaction to fire of cables. CERN Specific Safety Instruction SSI-FS-2-1 [480] already requires the installation of cables that are certified to, at least, Cca-s1,a2,d1 class or equivalent. Cca-s1,a2,d1 [451] must be retained as the minimum class for cables in the FCC, as it implies:

- Limited self-propagation.
- Low thermal energy released.
- Low smoke production.
- Limited fire growth rate.
- Non-acidity of gases (i.e., halogen-free).
- No sustained flaming droplets (>10 s).

Fire resistance In the event of fire, the integrity of the underground structure must be maintained for the period of time required to:

- Ensure self-rescue and complete evacuation of occupants.
- Allow safe intervention of emergency responders.
- Limit tunnel damage and recovery time.

This fire-resistant requirement must be applied to the civil structures as well as to the technical systems that need to operate in case of fire (e.g., cables, cables trays, ventilation ducts). It will be evaluated using natural curves[24] and engineering methods. Natural curves will be developed with the worst possible scenarios impacting the infrastructure (localised and distributed fires) and will consider all phases (growth, developed fire and decay). It is important to note that these natural curves might not be the same as used in Sect. 9.4.3 for life safety assessment due to the main safety objective being assessed: a critical scenario for evacuation (a rapid growing fire) is not necessarily the most critical scenario for structural resistance (long-lasting fire). The resistance assessment must consider the serviceability limits for the load bearing and spalling requirements to ensure that the above-mentioned objectives are met, despite the absence of extended collapse of the structure. For convenience, the final resistance can be expressed as per ISO 834 [429] using a time-temperature equivalent method as available in [481] and [482].

Table 9.6 highlights the minimum prescriptive requirements for fire resistance used in the Host States, as well as in other particle accelerator infrastructures. The risk levels N1, N2, and N3 for French road tunnels are determined by the potential impact of structural collapse on both the infrastructure and its surroundings [483]. In particular, risk level N3 is indicated for immersed tunnels and when the risk of local collapse can represent a major risk of flooding. While the corresponding prescriptive fire resistance (R240 + HCM120) appears disproportionate for FCC due to the lack of comparable fire loads, the risk of water intake as a consequence in case of local collapse will be studied in the next phases of the project.

As indicated above, the proposed fire resistance for underground infrastructure expressed as per ISO 834 is:

- R90 for tunnel and experiment caverns.
- R120 for alcoves, service caverns and areas with specific fire load.
- R120 for safe areas and protected shafts.

The different fire scenarios studied in the tunnel areas show that even in degraded mode, temperatures remain below 300 °C for a large part of the tunnel (Fig. 9.25b). Close to the seat of the fire, the maximum recorded air temperatures for most unfavourable scenarios remain below 600 °C. This is substantially below the ISO 834 curve (Fig. 9.25b), demonstrating that the proposed fire resistance ensures the life safety of occupants during the evacuation phase. The next phase of the study will evaluate whether greater resistance is needed to ensure the objective of property protection and business continuity.

[24] Temperature-time curve that describes the behaviour of a fire in an uncontrolled or natural environment, without external intervention or standardised conditions. This curve is derived from real fire scenarios and reflects the actual growth, peak and decay phases of a fire.

Table 9.6 Overview of minimum fire resistance prescribed in underground tunnels. R refers to fire resistance as per ISO 834 curve and EN 13501-2 [430]. RWS/HCM refer to the normalised hydrocarbon time-temperature curves with faster growth and higher temperatures than the ISO-834 curve as depicted in Fig. 9.25a. q stands for fire load density. Clearance is the maximum allowable height of the tunnel

Source	Fire Resistance [m]	Comment
FR road tunnels [477]	R60	If clearance $<$ 3.5 m for all risk levels
	R120	If clearance $>$ 3.5 m for risk levels N1
	HCM120	If clearance $>$ 3.5 m for risk levels N2
	R240 + HCM120	If clearance $>$ 3.5 m for risk level N3
FR railway urban tunnels [484]	R120	for public transportation
CH Industrial Building [485]	R60 (R90)	Height $>$ 11 m $<$ 30 m (if $q > 1200$ MJ/m^2)
	R90 (R120)	Height $>$ 30 m $<$ 100 m (if $q > 1200$ MJ/m^2)
CH road tunnels [486]	R60	For lightweight vehicles
	RWS/HCM 120	If heavy goods
CH railway tunnels [487]	HCM 120	If submerged or below water tables
	R120 (RWS/HCM 120)	For unstable tunnel (if >trains/day)
	R120	For stable ground
XFEL [435]	R90	For shaft and underground infrastructure
HL-LHC [488]	R60	tunnel
	R120	safe areas and protected shaft

Organisational measures for fire prevention The following general requirements to prevent fires and limit their consequences will be implemented:

- All hot works are to be conducted under a fire permit approval stipulating preventive and compensatory measures to be put in place (most of them are already implemented in the current CERN safety policy);
- Smoking will be strictly forbidden in all buildings at CERN, including underground areas.
- Fire safety awareness must be part of the access training ranks. This shall include instructions on prompt manual alarm triggering, behavioural reflex, and first response training.
- Maintenance and control. Patrol (automated) will check for unusual cues (hot spots, improperly placed material).
- Regular tests and fire drills. Fire safety systems must be permanently monitored and checked. Unplanned evacuation drills will regularly verify that the global safety concept is successfully implemented and if there are discrepancies, propose actions and update the concept.

Oxygen deficiency hazard (ODH) The SRF cryomodules of the FCC-ee rely on liquid helium to reach their superconducting state. The 400 MHz cavity cryomodule will be cooled using 115 kg of helium at 4.5 K (He-I), whereas the 800 MHz cryomodule will use 55 kg of superfluid helium (He-II) at 2 K. Following a risk assessment [489], a few accident scenarios were identified as potential sources of helium release in the FCC tunnel. Such a release poses considerable risks for people working underground. The helium gas released into the environment would displace the air (i.e., the oxygen) and lead to a possible asphyxiation of occupants underground; this is referred to as an Oxygen Deficiency Hazard (ODH). Moreover, low-temperature helium flow can also cause severe internal/external cold burns. A performance-based design approach, using numerical simulations in the form of computational fluid dynamics (CFD), provided an analysis of the ODH in the RF section of the FCC-ee accelerators. The outcome of the safety studies is summarised below, based on a series of reports that contain the full details [490, 491].

For simulations, a full fire compartment (400 m) in the RF sector at point PH was selected as the control volume. The CFD simulations were performed in two dedicated batches, corresponding to the two accident scenarios chosen for the analysis: 1) sustained RF quench and 2) loss of beamline vacuum. The FCC-ee SRF system will be designed to avoid a sustained RF quench, leaving the loss of beamline vacuum to be considered as the most credible incident (MCI) at this stage, with a mass flow rate of 20 kg s^{-1} [489]. The scenarios studied are summarised in Table 9.7. The case and mesh settings for the CFD solver are detailed in [490, 491].

Fig. 9.25 Temperature profiles in the case of a fire in the tunnel

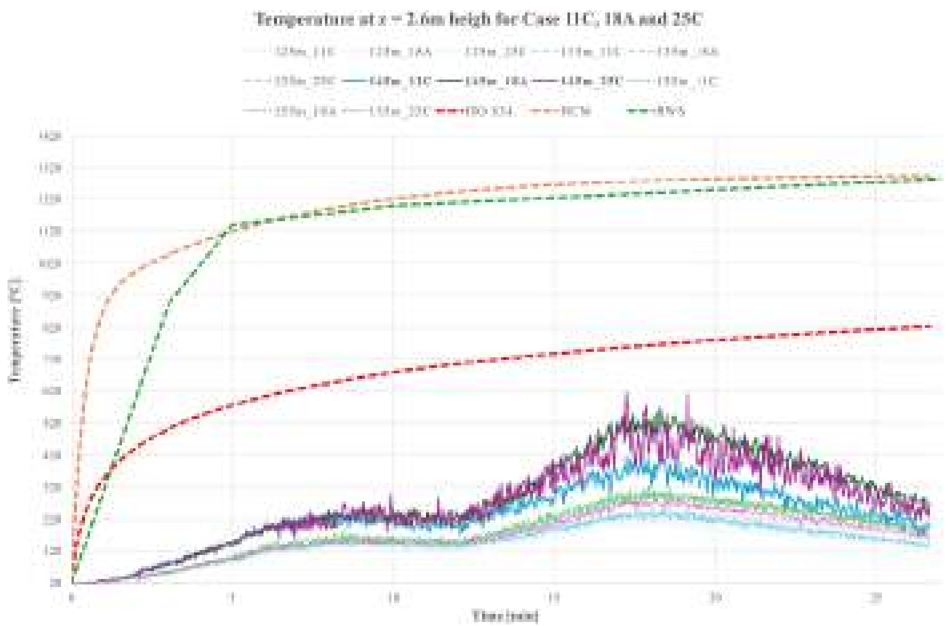

(a) Temperature evolution for transport vehicle fire with three different ventilation conditions [468].

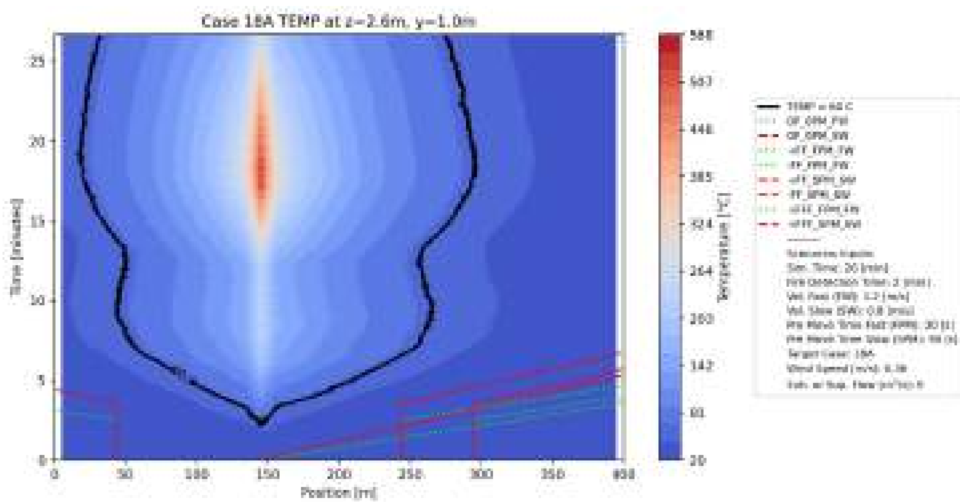

(b) Temperature time-position plot for case 18A [468]. Ventilation vector: left-to-right. Air/smoke temperature is measured at 2.6 m from the ground. This case represents a failure of the smoke extraction system and maximises the thermal impact to the tunnel for the vehicle fire design. The black line corresponds to the 200 °C threshold. The red and green dashed/dotted lines are evacuation trajectories for worst and nominal human behaviour cases.

The simulations were run on CERN's HPC cluster and post-processed, focussing on analysing the following results:

- Comparison between input scenarios.
- Dynamic behaviour of the oxygen levels in the cross-section of the tunnel.
- Time needed to reach ODH conditions in the evacuation path.
- Propagation speed of the Helium cloud front.
- Propagation speed of the Helium Plug.[25]

[25] Area of the tunnel that is completely filled with helium gas.

Table 9.7 List of simulation scenarios and the main input parameters

Ref.	Scenario	Relief points [per CM]	Burst disc ϕ [mm]	Mass flow [kg s^{-1}]	Pressure & temperature [bar(a)]/[K]	Sim time [s]
SC1	Sustained RF quench	1	100	2.9	2.0 / 5.32	57
SC2		2	100			
SC3		4	50			
SRF01	Loss of Beamline Vacuum	1	100	20		26
SRF02		2	100			

Table 9.8 Results of the CFD simulations with the scenarios described in Table 9.7

Ref.	Time to reach 18% O_2 [s]	Propagation speed [m/s]			He plug size [m]
		Cloud front	He plug ($\dot{m}_{He} \neq 0$)	He plug ($\dot{m}_{He} = 0$)	
SC1	7	1.52	0.66	0.58	32
SC2	10	1.33	0.57	0.7	29
SC3	15	1.66	0.63	0.81	35
SRF01	4	3.3	5.3	3.3	73
SRF02	2	2.57	3.8	2.57	53

- Longitudinal size of the Helium Plug.

The findings are summarised in Table 9.8, showing the time at which untenable conditions are reached in the transport/evacuation zone (i.e., $O_2 \leq 18\%$), the propagation speed of the helium cloud front, and the behaviour of the helium plug formed in the tunnel. This includes scenarios where gas is still being relieved from the burst disk ($\dot{m}_{He} \neq 0$) and when the inventory is empty ($\dot{m}_{He} = 0$), along with the size of the corresponding plug at the end of the simulation. Figure 9.26 illustrates the results of the cross-section and longitudinal propagation of the helium cloud.

The simulations confirm the turbulent flow effects observed in real-life scenarios [492]. Untenable conditions are reached as soon as 2 seconds after the opening of the pressure relief device, and after an additional 4 seconds the cloud has propagated another 12 m downstream. The turbulent flow leads to the creation of a helium plug, which was observed in all 5 scenarios, right next to the release point and extending up to 70 m in length within 26 seconds (Table 9.8). The plug can obstruct the entirety of the transport zone, posing a heavy constraint for the evacuation of the occupants towards the adjacent compartment where they would retrieve the transport vehicle to evacuate from the underground area.

Given these observations, with the cryomodules at nominal conditions (i.e., maximum inventory), access to the RF section of the tunnel must be blocked when the risk of such accident events is present. Access to the klystron gallery is allowed, however, the bore holes for the wave guides need to be leak tight. Additional future studies may determine if there is a minimum inventory where access to the RF sector would be possible. In this case, occasional access may be granted with prior approval (i.e., through established procedures) and by requesting the use of personal protective equipment (PPE), such as self-rescue masks. It is intended to extend these studies, for the further design of the FCC study to include the use of the emergency (smoke) extraction duct and measure the impact on the extent of the helium plug and cloud propagation, in view of iterating on the access conditions to the RF sector.

It is also preferable to have a cryomodule design with multiple release points, although a single release point might still be studied in more detail to improve the outcome compared to SRF01.

The ODH assessment for the experiment caverns will be performed in the next phase of the study, when the detector technologies are chosen and which cryogenic gas will be utilised (if any).

Seismic hazard The region is characterised by a moderate seismic level. With 11 earthquakes of magnitude > 5 estimated to have occurred within a radius of 100 km around Geneva in the last 500 years the hazard is considered and analysed. At least two seismically active faults stretch about 10 and 30 km southwest of Geneva, within the area of the current reference implementation scenario. In order to provide suitable seismic safety requirements for the design of the civil and mechanical structures, equipment, and installations foreseen in the underground facilities, subsequent preparatory phases need to assess seismic hazards at the depths concerned. To do so, a

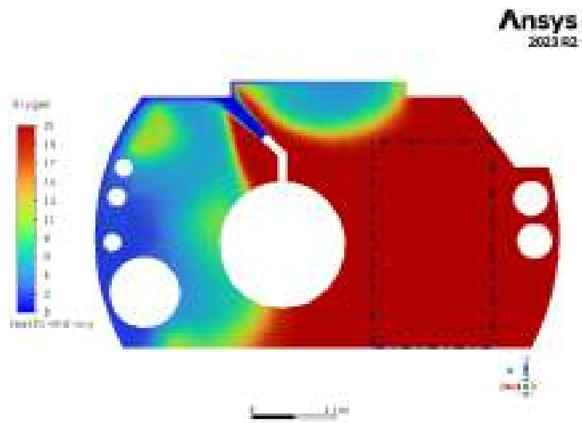

(a) $t = 1$ s

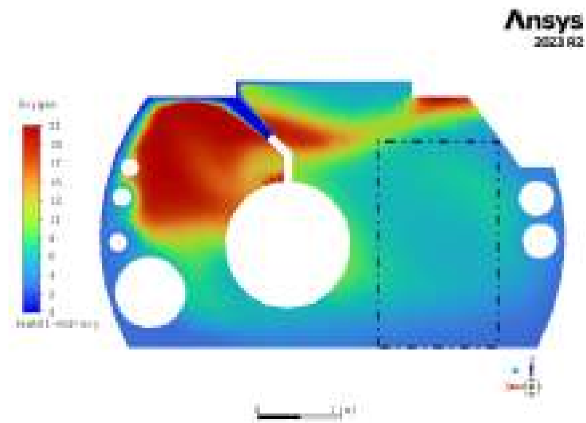

(b) $t = 3$ s

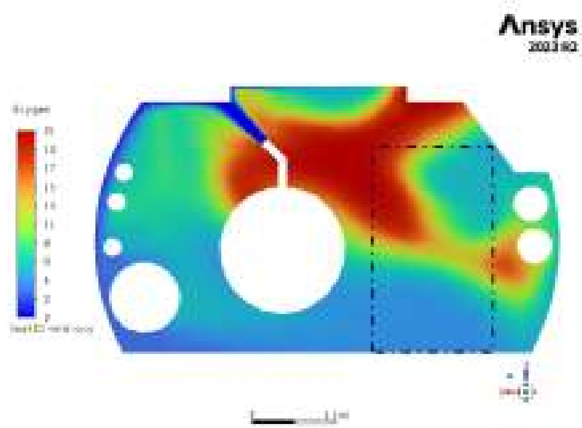

(c) $t = 6$ s

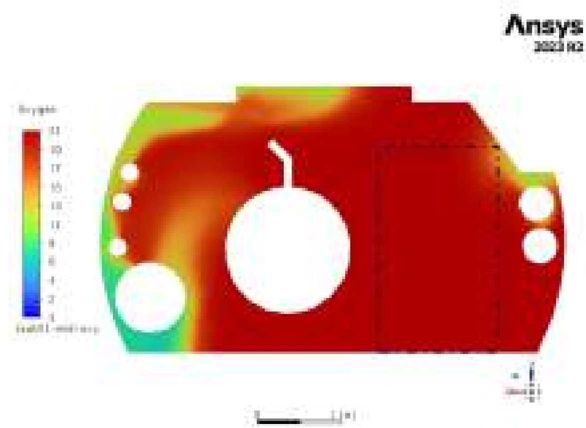

(d) $t = 26$ s

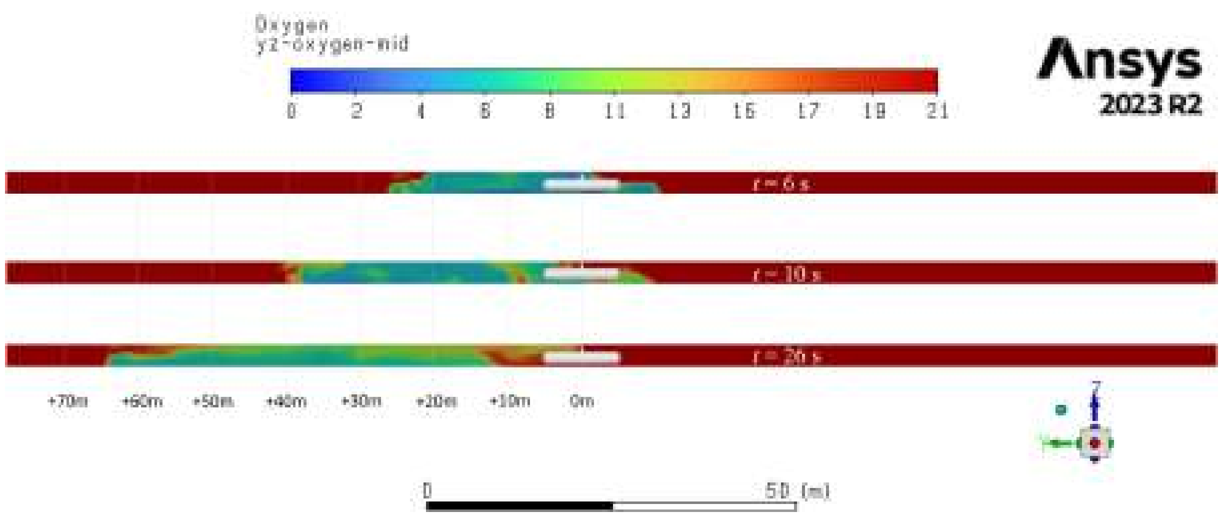

(e) He plug propagation at $t = 6, 10, 26$ s

Fig. 9.26 Results for of the CFD simulations of scenario SRF02 at a time t, following the opening of the burst disk. a) - d): Cross-section view just 1 m away from the burst disk. e): longitudinal view of the helium propagation. Colour scale shows the oxygen content in the 2D plane (passage from red to orange: the transition to 18% and below). Ventilation flows right-to-left collaboration with the Swiss Seismological Service (SED), hosted by the Swiss Federal Institute of Technology Zurich (ETHZ), the University of Geneva (UNIGE), and the French Université Grenoble Alpes (UGA) is proposed for further studies. So far, a simplified approach based on the adaptation of the legal seismic safety requirements for ordinary surface buildings on French territory was used to design and assess new mechanical structures and equipment in the Large Hadron Collider (LHC) and Super Proton Synchrotron (SPS) complexes, meaning that the structural elements could be over- or under-sized to resist the required earthquake loads. This proposal will build upon a project to draw a probabilistic-seismic-hazard-oriented and tailor-made assessment for the proposed underground facilities. The main products of the projects are:

- Seismic Hazard Curves: a family of seismic hazard curves that represent the annual frequency of exceeding different levels of ground motion, essential for designing earthquake-resistant structures and assessing the safety of existing facilities.
- Site Response Analyses: uniform hazard spectra (UHS) and scenario earthquakes, including acceleration time-histories, for seismic design and safety evaluations of the civil infrastructure and the equipment structures hosted there.

The overall study is planned for a 3-year period (2025 - 2028).[26]

9.4.4 Evacuation

A series of evacuation studies were undertaken for the underground infrastructure.

General requirements and considerations The following list summarises the minimal requirements for all FCC areas, in line with the prescriptive requirements in France's Code du Travail [441] and Switzerland's Norme de Protection Incendie [442] used for standard facilities:

- At any given point, occupants must be able to choose at least two distinct evacuation paths. The maximum dead-end evacuation distance is ≤ 40 m (e.g., in alcoves).
- The width of any evacuation doors must be ≥ 0.9 m.
- The maximum evacuation distance:
  - for surface buildings: in accordance with [441, 442];
  - for underground installations: in accordance with performance-based design and inline with best practices in other underground tunnel infrastructures.
- Emergency shelters (refuges) without safe escape routes connecting to the surface are not considered in the safety concept for the operation phase. This is in line with the provisions of Directive 2004/54/EC for road tunnels [431].

Tunnel arc: evacuation modelling The evacuation from the underground infrastructure will rely on both horizontal and vertical means. Personal transport vehicles will ensure the horizontal evacuation from the nearest alcove to the safe area at the bottom of the access shaft. Vertical evacuation will be ensured via pressurised lift shafts equipped with a secured set of lifts (composed of 2 lifts for redundancy and availability), to bring occupants to the assembly points at the surface.

At the bottom of every lift shaft a fire-, smoke- and gas-proof safe area is needed to ensure that occupants can safely wait for the arrival of the lift. Defining the size (surface area) of the safe area and its impact on tunnel occupancy is crucial to verify the safety concept during evacuation processes, ultimately defining the maximum number of occupants allowed underground at the same time. For a safe evacuation, maximum admissible crowding in safe areas should be under 3 occupants/m^2 [495].

Many conditions with different probabilities (e.g., occupancy distribution in the tunnel, walking speed or transportation speed) need to be evaluated in order to define the required surface area and reserve enough space near the shaft in the integration drawings. At this phase of the study these parameters are not exhaustively known; hence a stochastic approach with random variables (in a given set ranges) is more suitable. Therefore, to determine the size of the safe area, an evacuation model was developed using plain Monte Carlo simulations.

Depending on the location of the fire, one or more sectors of the tunnel arc will need to be evacuated. A worst-case scenario is assumed where the fire is just next to the connection to a service cavern, blocking access from one sector only, which means that all occupants of an entire sector must evacuate via the other access shaft (10 – 11 km away). In addition, it is a common practice to also evacuate the adjacent sectors that are not affected by the fire (as in the LHC scenario). To summarise, occupants from one and a half sector (1.5 sectors) will be evacuating through a single shaft (Fig. 9.27).

[26] Note that the French and Swiss seismic hazard model currently in force for surface buildings will be superseded by the new European Seismic Hazard Model (ESHM 2020) [493] that will be incorporated in the second generation of the Eurocode 8 [494].

Fig. 9.27 Simplified schematic of the evacuation model

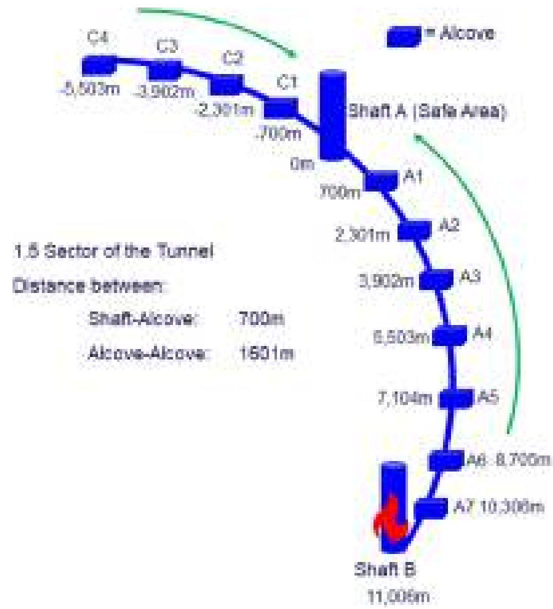

Table 9.9 Evacuation scenario parameters

Scenario Number	Vehicle occupant capacity	Occupancy distribution	N. of alcoves (per Sector)	Vehicle Parking Capacity (Alcove/Shaft)	Occupants / 1.5 Sector	Occupants / Sector
1	2	Binomial	7	10/20	260	**174**
2	3	Binomial	7	10/20	390	**260**
3	4	Uniform	7	4/4	192	**128**
4	4	Uniform	9	4/4	240	**160**

In this model, the number and location of the alcoves are important, indicating the total parking capacity. For the feasibility study, the baseline number of alcoves is 7 per sector, but alternative studies were carried out assuming 9 alcoves.

It is assumed that all occupants inside the tunnel will have access to a transport vehicle. Therefore, the maximum number of occupants allowed inside the sector is limited depending on the capacity of the transport vehicles and the parking space in the sector. A total of 4 different simulation scenarios were created (see Table 9.9) with 2 different distribution methods for the occupancy distribution in the tunnel. The number of occupants per sector is comparable to a scale-up (factor 3) of the maximum number of occupants seen during Long-Shutdown 2 (LS2) in the LHC [496].

The distribution of occupants in the tunnel is an important variable in determining the size of the safe area. Since lone working is not allowed by default, it is assumed that occupants are working in groups. The number of occupants per group and their position is treated as random. They are placed either in between two adjacent alcoves or between the service cavern (Shaft A) and the nearest alcove. After the evacuation alarm, both the occupants between Shaft A and Shaft B and the occupants in the half sector on the other side of Shaft A start to evacuate to the safe area in Shaft A (Fig. 9.27). To do this, occupants between the two alcoves must first walk to the alcove where they parked their vehicles and then travel to the safe area of Shaft A with their vehicles. Occupants in the area between Shaft A and the nearest alcove will walk directly. Two different occupancy distributions (Fig. 9.28) were used to indicate the initial positions of groups.

The simulations consist of 50 different random occupancy distribution scenarios, each run with Monte-Carlo (1000 samples). The results are shown in Fig. 9.29, with an occupant walking velocity as a normal distribution (mean(SD) of 1.2(0.3) $\mathrm{m\,s^{-1}}$) and a transport velocity as a uniform distribution ($[20-30]\ \mathrm{km\,h^{-1}}$). The maximum number of occupants that reached the safe area at the end of each simulation (50,000 in total) is recorded and is also shown in Fig. 9.29. Scenarios 3 and 4 require the smallest safe area size. This is mainly due to the uniform distribution of the occupant groups in the tunnel, meaning that they will all arrive at the safe area in a distributed fashion, thus crowding is limited by the travel time of the lift. Scenarios 1 and 2 have a binomial distribution with an agglomeration of occupants in the middle of the arc (this could be the case during a major repair or

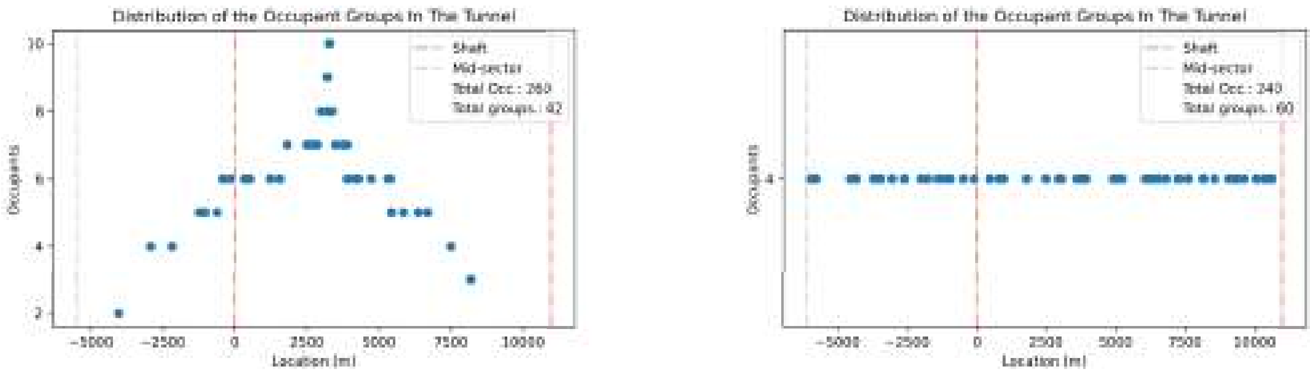

(a) (b)

Fig. 9.28 Example of occupant group distribution along 1.5 sectors. Shaft A location at position 0 m. a) Binomial distribution, restricted to 2 and 10 occupants per group; b) Uniform random distribution, restricted to groups of 4 occupants

maintenance in a particular arc cell). This would lead to a higher crowding at the safe area once these occupants reach the lift, hence a larger safe area is required to maintain a density below 3 occupants/m^2. The results show that having a minimum safe area of 50 m^2 would be suitable safety. It is feasible to implement such an area near the lifts of all eight service caverns. Additional details are available in the technical report [396].

Technical points: service caverns The service caverns at the technical points are connected to the accelerator tunnel via compartmentalised passages that will be used as emergency escape routes. In some points (such as PF), the service shaft is not directly connected to the service cavern. Therefore, an additional horizontal connection tunnel is required. It will also be used as a safe evacuation path.

The service shafts at the technical points are equipped with one set of lifts to ensure the vertical evacuation to the surface. Each set consists of two lifts for redundancy and increased availability. Lifts have a dedicated pressurised fire-resistant compartment (lift shaft), separating the air volume from the surrounding environment (i.e., service cavern) to protect the integrity of the evacuation to the surface in case of emergency. The pressurised compartment is extended to the safe area, with its size as determined above.

Experiment points: experiment and service caverns The experiment points will enable independent dedicated flows of occupants up to the surface, separating those evacuating from the experiment and service caverns from those evacuating from the accelerator tunnel.

The experiment cavern is connected to the service cavern through three separate personnel passages that can be used as emergency escape routes: two at the level of the beamline and one at the ground floor. These personnel passages will contain little or no combustible material. Additional bypass chicanes are integrated whenever a personnel passage requires heavy mobile shielding for radiation protection purposes. A second connection tunnel on the ground floor is only for the passage of material and will not be considered a safe evacuation path.

The main tunnel is connected to the service cavern by two bypass tunnels about 100 m from the interaction point and two connection tunnels at the end of the long straight section close to the experiment cavern (Fig. 9.30).

Airlocks are planned in the connections between the tunnel/experiment cavern and the bypass tunnels/service cavern, separating and isolating the ventilation volumes to prevent the mixing of radioactive air with accessible areas.

Similar to the other points, the occupants rely on lifts for vertical evacuation to the surface site, which will be done by a single shaft located in the service cavern. This is a new concept, different from the experiment points at LEP/LHC, which profited from more than one shaft. However, the separation of the flow from the accelerator tunnel and the experiment cavern is still ensured by having two sets of two lifts (four in total), in the shaft: one set to house the occupants evacuating from the experiment and one set for occupants evacuating from the accelerator (Fig. 9.30). Each set is composed of 2 lifts for redundancy and availability. Each set of lifts has a pressurised fire-resistant compartment, separating the air volume from the surrounding environment (i.e., shaft and service cavern) to protect the integrity of evacuation to the surface. The pressurised compartment is extended to the dedicated experiment and accelerator (machine) safe areas (Fig. 9.30). The safe area is where the occupants wait for the lift to evacuate to the surface. The size of the accelerator safe area, as previously mentioned, is a minimum of 50 m^2, while the exact footprint of the experiment safe area is yet to be integrated and will dictate the maximum occupancy allowed in the experiment cavern (3 occupants / m^2).

Fig. 9.29 Simulation results of the evacuation study. a) results of one simulation run of scenario 2, with the occupancy density (crowding) in the safe area over time; b) Maximum number of occupants (crowding) in the safe area for each scenario

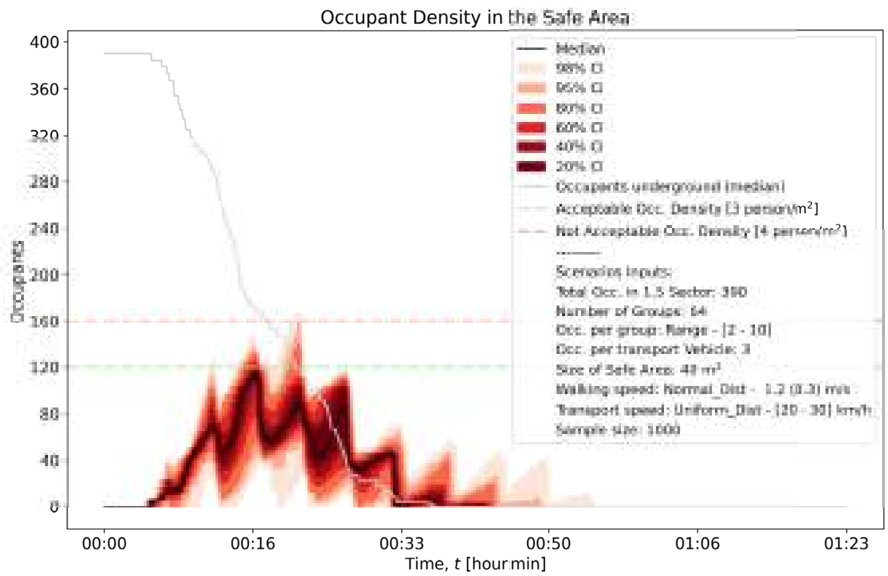

(a) Result of one simulation for scenario 2

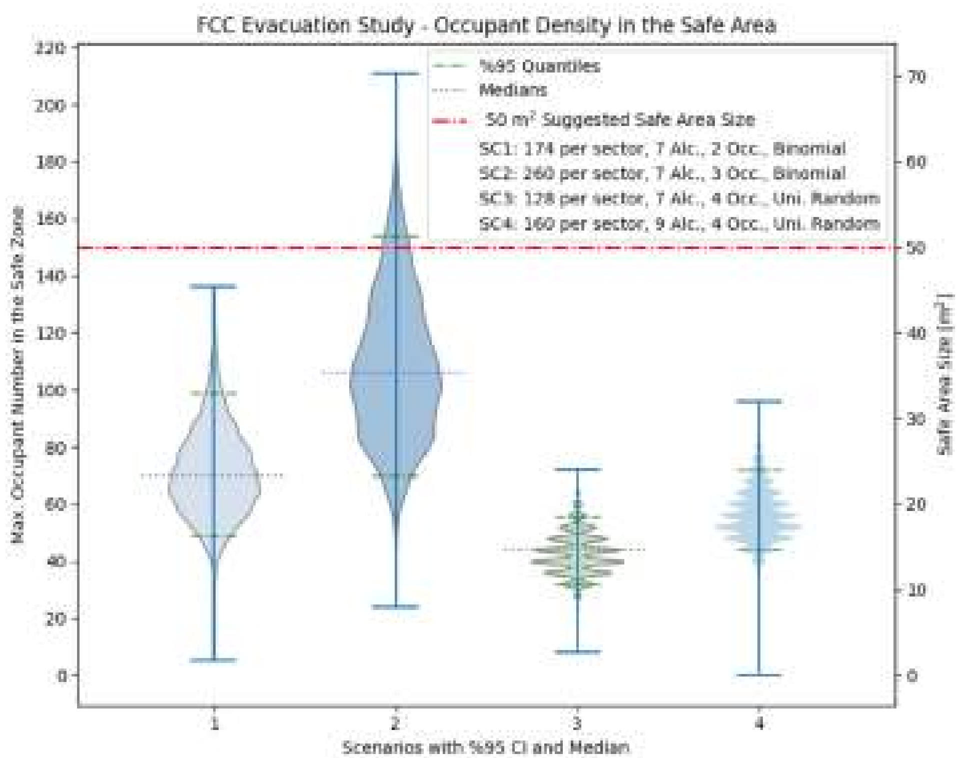

(b) Result of 50 000 simulation runs for each scenario.

Klystron galleries The superconducting RF (SRF) cavities in the RF sections will be fed by waveguides coming from klystron galleries located above the main tunnel. The length of these klystron galleries is roughly 2010 m in point PH and 1445 m in point PL. A series of connections to the main accelerator tunnel via staircases are available at regular intervals and at both extremities, providing the necessary means of evacuation from the klystron galleries in case of emergency (e.g., fire in the modulators) and thus avoiding dead ends. These connections are shown on Fig. 9.31 and are distributed as follows:

- At PH, there are a total of 6 tunnel connection staircases, one every 341 m.
- At PL, there are a total of 4 tunnel connections, one every 354 m.

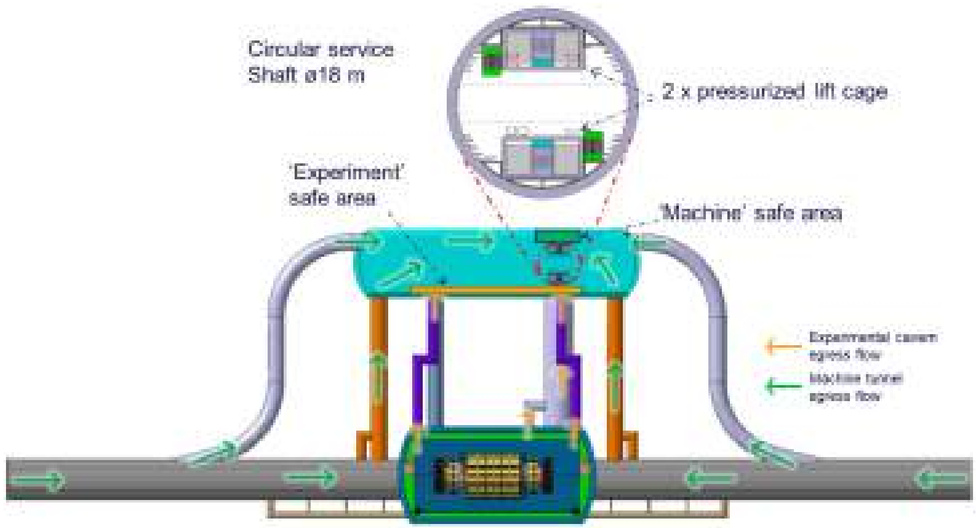

Fig. 9.30 Integration of the evacuation flow of occupants in an experiment point. The illustration shows the example of the experiment cavern housing an FCC-hh detector

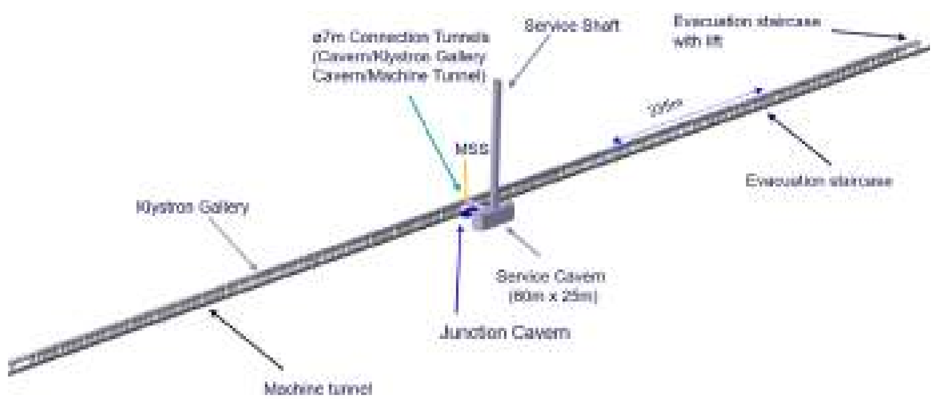

(a) Point PH - 341 m in between staircases

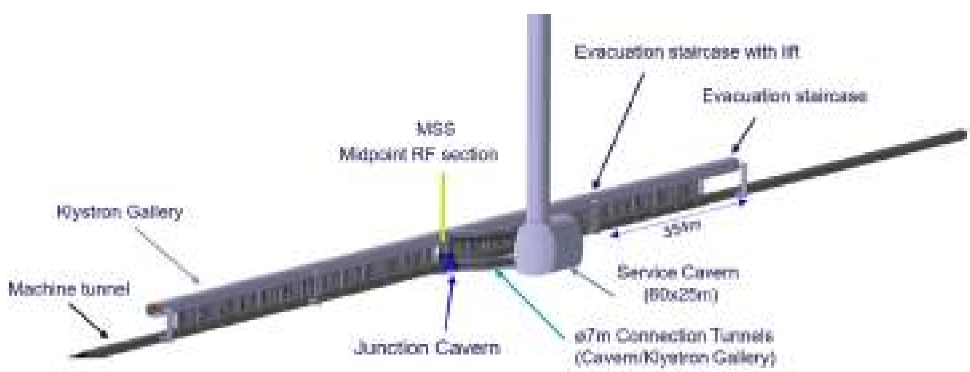

(b) Point PL- 354 m in between staircases

Fig. 9.31 Klystron galleries and their evacuation connections in point PH (a) and PL (b)

The frequency of these connections helps to minimise the distance that any occupant would need to walk to reach another fire compartment in the main tunnel. Each staircase will be equipped with fire doors at both ends (tunnel and gallery). In addition to the static confinement properties, each connection will also be pressurised, ensuring a dynamic confinement between the main tunnel and the gallery. A more in-depth risk analysis will be conducted for this area during ta subsequent design phase to assess if the distance and number of staircases are sufficient.

In addition to the staircases, at the two ends of each klystron gallery, lifts are available for transporting personnel and material, avoiding having to pass through the RF section to work in the arc. These lifts will not be used in an emergency (e.g., fire). Access to the Klystron gallery is also possible from the service cavern in the middle of the RF sector.

Alcoves Alcoves will be spread along the accelerator tunnel (minimum 7 alcoves per sector): two big alcoves and five small alcoves. These alcoves house electrical racks and equipment and will form a dedicated EI120 fire-rated compartment, separated from the main tunnel. They will have a single access (in and out), through a fire door connecting to the main tunnel, creating a dead-end in terms of evacuation. The maximum allowable distance from the end of the alcove to the fire door must not exceed 40 m. This is based on the maximum evacuation distance to reach a protected staircase in France [441], ensuring that the adjacent fire compartment (i.e., the main tunnel, relatively free from smoke) can be reached safely in time.

In the baseline layout, all the alcoves comply with this maximum distance. The layout also includes two mezzanines, one on each side of the alcove. Staircase connections from the mezzanine to the ground floor will be installed at both extremities of the alcove to ensure that the evacuation length is not doubled and to avoid being trapped on the mezzanine.

Surface buildings The surface buildings will rely on applicable national and international standard practices for the evacuation requirements applicable to industrial infrastructures within the Host States. For PB the Swiss AEAI Directives 15-15 [485] and 16-15 [497] will apply. For all the other sites, the French Labour codes are applicable [498].

9.4.5 Emergency preparedness and intervention concept

An underground particle accelerator of 91 km in circumference presents unique challenges in terms of emergency response. The threefold size increase compared to the LHC presents challenges, including much larger distances between access points (11 km) and surface distance between shafts. Hence, a new emergency preparedness and intervention concept is required.

The emergency response concept proposed is divided into four distinct phases, starting from a confirmed accident event (e.g., fire) [499]:

- First Response: trained personnel or contractors at the accident site are responsible to raise an alarm, provide first aid, deliver first response (e.g., fire extinguishers) and initiate evacuation procedures.
- Robotic Intervention: remote-operated robotic vehicles gather situational data and conduct preliminary firefighting actions before human intervention. Ceiling-mounted and floor-based robots can fulfil these tasks, for example.
- Local Fire Services: on-site support from local emergency services, primarily for surface-level interventions.
- CERN Fire & Rescue Service (CFRS): CFRS to coordinate emergency interventions, if relevant with other emergency services, with the use of equipment stored both in surface and underground locations. This includes for instance foam-based firefighting systems and compressed air foam (CAFS) units. Rapid-deployment solutions are required to ensure a quick intervention to all eight surface sites.

Support infrastructure for emergency response The concept will also rely on a robust support infrastructure for an efficient emergency response:

- Surface site: landing zone in the vicinity for airborne emergency intervention, a command post, a casualty room, and a logistical hub for storing specialised intervention vehicles, firefighting robots, and extinguishing agents.
- Underground: compartments with designated safe waiting areas, compartmentalisation, smoke extraction (with CFRS override and remote control), priority intervention vehicles and robotic assistance units. A reliable communication system, vertical dry risers connecting the surface and service cavern, and underground water reservoirs will ensure adequate firefighting resupply.

Unlike current baseline practice in the LHC, the use of robots will play a critical role in the emergency response for the FCC by enabling the possibility of quick fire response within the underground infrastructure, where human access may be restricted during accelerator operations.

Training and implementation strategy To fulfill the concept, all underground personnel will be trained in emergency response and first aid. A structured transition plan will be developed to align with this new approach. CERN has already begun testing robotic solutions to validate their potential in real emergency scenarios. Further technical details will be made available in the relevant reports [499].

Given the critical partnership with the local fire services in fulfilling the concept, we emphasize the importance of CFRS being actively involved in the joint work with these key partners. This includes the establishment of joint training programmes, workshops, and drills building on the current practices.

By implementing these measures, the FCC will enhance its ability to manage emergency situations efficiently while prioritising the safety of personnel and infrastructure.

9.5 Safety during the construction and installation phases

9.5.1 Safety coordination

The baseline concept for safety coordination is based on French legislation, as 7 out of the 8 surface sites are located within French territory. For the surface site PB in Switzerland, Swiss legislation applies. The detailed design will include a proposal to harmonise processes across all worksites to increase efficiency.

In accordance with French law [500], the project owner is responsible for safety coordination throughout all phases of the project [422].

Specialised external service providers (i.e., safety coordinators) will assist the project owner in this safety coordination mission.

Safety coordinators are responsible for preparing coordination plans and the PGCSPS (Plan Général de Coordination en matière de Sécurité et de Protection de la Santé) for the relevant worksite(s). These plans must be provided to contractors during the tendering phase to clearly outline their safety obligations and expectations, as well as to specify the applicable laws and regulations governing the project. All worksite-related safety documents, procedures, and methods must be written in French to ensure compliance with national regulations. Each contractor remains responsible for the safety of their own employees, according to their operating methods. Any accident or incident occurring within the worksites must be reported by the contractors using a form-based system. Today, at CERN, this reporting is governed by CERN's safety rule SR-SIM [501].

9.5.2 Construction phase

During the construction phase, civil engineering works on the surface and underground are executed by specialised firms under contract with CERN. It ends with the handover of the buildings and underground structures to CERN from the contractor.

The evacuation plan and emergency procedures in the event of incidents within the worksite(s), will be included in the PGCSPS. Such procedures are developed in consultation with CERN, the contractor and the local emergency services. It indicates, among others, the assembly points for emergency services, access conditions to the various zones means to evacuate victims and the need for specific firefighting / response equipment. Joint training, reconnaissance and drills should be organised with the CFRS to ensure a tailored response and strengthen the collaboration with the local services.

9.5.3 Installation phase

The installation phase begins with the handover of the surface buildings and underground structures from the civil engineering contractor to CERN.

This will happen at different moments for each access point and the associated tunnel sectors: in the underground area of an access point, the installation phase can start after the total or partial release of the adjacent tunnel sectors leading to the neighbouring access point with lift facilities. In a tunnel sector, installation activities are allowed as long as there are two adjacent access points from which the occupants can reach safely to evacuate. These rules will guarantee a two-way evacuation possibility, with secured horizontal and vertical means of escape at all times. The technical and organisational details of safety during the installation phase will be engineered in the project preparatory phase.

Two sub-phases of installation can be distinguished: the service installation (electricity, lighting, ventilation, cooling, detection and alarm systems, and transport system) and the accelerator installation (beamline elements, magnets, RF cavities, cryogenic systems, power converters, and control systems).

Service installation Service installation begins after the release (handover) of the civil engineering (CE) structures from the contractor to CERN. The temporary lighting, ventilation, lifts and other services installed by the civil engineering contractor could potentially be taken over and used by CERN for the initial phases of the service installation. Obviously, no work can be executed by CERN and its contractors without these essential services. It is therefore advisable to foresee the transfer of these assets to CERN at the time of handover, saving the time and cost of CERN installing essential services in a provisional manner. The transfer should include the assets, as well as the technical documentation and maintenance procedures. Similarly, robust construction site access control devices (e.g., turnstiles) could be transferred from the contractor and connected to the CERN access control system. This would allow verification of CERN imposed training, etc., access control and the enforcement of work coordination.

Safety organisation during service installation The services mentioned above are largely installed by contractors mandated by CERN. In order to coordinate work and occupational safety coherently, experience from the High Luminosity LHC shows that the work of a pairing (*binome*) consisting of an activity coordinator employed by CERN and an independent safety coordinator (see Sect. 9.5.1) is very effective. The FCC project should adopt the same approach. Given the geographical span of the facility and the unavailability of most of the safety and automation systems in this early phase of the installation works, each of the access point sites will be permanently manned by guards. Their primary role will be to ensure smooth material entry without compromising access control procedures. In addition, during working hours, a site supervisor will ensure the respect of safety procedures and act as a liaison with service and equipment groups at CERN in case behavioural or technical anomalies are observed.

Installation order during service installation The underground ventilation system is essential for the well-being and safety of workers, especially in the 11.4 km long tunnel sectors. The definitive ventilation system will be installed with priority. This includes cooling water, which is required for the air-handling units along the tunnel. Once the smoke extraction duct is equipped, the dampers and extractors are powered and commissioned, local control of smoke development is possible. At the same time, while avoiding co-activities, the definitive electrical supply and lighting will be installed. This includes the installation of detection systems' control and indicating equipment (CIE) racks in the alcoves, high-voltage cables to the alcoves and transformers. Cable trays will be installed to guide the numerous cables in an orderly manner.

The installation of definitive detection systems can proceed with lower priority. If smoke detection is performed by aspiration tubes, then this system can only be made operational after the accelerator installation, because of its sensitivity to dust and welding fumes, which would raise numerous false alarms. Manual call points distribution and a dedicated procedure will ensure prompt alarm activation during this degraded phase.

For the FCC, the transport system has a safety role during evacuation, it is also indispensable for the next phase in which the accelerator is installed. As described in Sect. 9.4.1, the transport system is based on autonomous vehicles, both for the transport of personnel and for large and heavy loads. All infrastructure to allow autonomous movement of the vehicles must be available at the end of the service installation phase.

Emergency response during service installation During the service installation, a provisional alarm system is required since the automatic fire detection would not yet be available. Manual call points (break-the-glass devices) and provisional evacuation sirens will be installed and cabled to the CIE racks. Provisional communication infrastructure is necessary to transmit the alarms to the central emergency coordination team.

Due to the large distances in the tunnel, and on the surface between the surface sites and a CERN site, where the emergency coordination takes place, the possibility for timely intervention of trained emergency services has to be implemented before the installation phase starts. Consequently, early development of the integrated emergency concept is needed.

Occupational safety during service installation During service installation the safety systems may not be installed or not be fully operational, and strict measures for occupational safety must be implemented. According to preliminary estimates, up to 200 occupants per sector are expected during the installation phase. This is significant but less than in the worst-case scenario during the operation phase that was studied (Sect. 9.4.4).

The focus is on the self-protection of the workers:

- Access is only granted to trained personnel.
- All workers must be trained in the use of the self-rescue mask (for use in case of fire or smoke), and the use of the transport vehicles for evacuation.
- A sufficient number of certified first-aiders at the workplace[27] must be trained.
- All workers must also be trained in raising an alarm by pressing the alarm button if there is a fire or smoke development and to react correctly to the evacuation sirens.
- The installation schedule and planning must have shifts dedicated to high-risk activities where the human presence is limited to the absolute minimum. For example, using night shifts for heavy transport activities, such as cable drums or other bulky loads, where the access to the sector concerned is restricted to the transport team only.
- The underground worksites must be kept clear of combustible materials at all times. Any such material (packaging, cable drums) must be evacuated to the surface immediately after its use.
- The transport zone of about 2.5 m width must be kept free of stored material throughout the tunnel to permit evacuation.

[27] A first-aid qualification with a focus on the most frequent types of personal accidents at industrial workplaces. The training lasts two days and is concluded by a proficiency test.

Accelerator installation Once the basic services - ventilation, lighting, electricity, smoke extraction, detection, and alarm systems and transport - are commissioned, the sub-phase of accelerator installation may begin.

Safety organisation during accelerator installation The same concept as the previous phase is assumed, with an update of the existing PGCSPS, if necessary.

Installation order during accelerator installation Drawing on experience from LHC, the accelerator will be installed in a sequence of

- Transporting the magnets and other beamline elements like collimators, and RF cavities to their designated location.
- Making provisional geometrical alignment.
- Connecting the beamlines with each other.
- Connecting the electrical supply and the controls to the magnets.
- Concluding with a final geometrical alignment.

The partition walls separating the tunnel into 400 m long fire compartments can be installed as soon as the magnets are placed. A phased approach, where only certain partitions are initially installed or where the partitions leave openings for the installation of further cables and services, allows the flexibility needed during installation while improving the safety of degraded modes. Passive protections in the form of partition walls are the most reliable system for this phase. Finally, the automatic detection and alarm system can be commissioned.

Similar to the service installation sub-phase, the planning will include shifts dedicated to high-risk activities, such as magnet transport, and avoid co-activity by restricting access to only the teams concerned.

Transport during accelerator installation Magnets will be lowered underground with overhead cranes through the large shafts of the service caverns at sites PA, PD, PG and PJ. Then, a magnet transport vehicle will move them past the already installed magnets to their final location. During this journey, the magnet transport vehicle effectively blocks the transport zone of 2.20 m width, thus blocking the evacuation exit. Access during transport to a sector will be restricted to the transport team, reducing the number of occupants underground during this period. Once the magnet transport has passed the midpoint of the sector, a returning vehicle can pass an arriving one in the extended lay-by area at the central alcove. The same rule applies to the transport of other large items which are wider than 80 cm and thus cannot be bypassed by a personnel vehicle.

From the moment when all magnets are positioned in a sector, the transport, and evacuation rules applicable during normal operation become valid, because only the transport zone is available. In particular, special, narrow personnel transport vehicles must be used for personnel and light loads.

Emergency response during accelerator installation The provisional alarm system with break-glass push buttons installed during the service installation sub-phase remains active until the automatic detection and alarm system has been commissioned. If the detection technology chosen is aspiration smoke detectors, this can only be done after all dust and fume generating works are concluded. The alarm system must be configured to trigger the evacuation alarm (sirens or voice messages) and alert the central emergency coordination team, which will analyse the situation and engage the most appropriate emergency response with the different emergency services.

Occupational safety during accelerator installation The type of work during accelerator installation is mostly of a mechanical and electro-mechanical nature. This includes hot work (grinding, welding and brazing), which is a potential ignition source. The compartment walls, installed after magnet placement, may have a higher leakage rate for smoke than in their final configuration because some openings for cables and other services cannot be tightened before all installation work is finished. The mitigating measures personnel have to apply to take account of this are identical to those in the service installation sub-phase: minimisation of combustible material, rigorous training of workers performing hot work in extinguishing and alarm procedures, self-rescue mask and evacuation training for all workers.

9.6 Conclusion

The safety concept outlined in this report emphasises a comprehensive and integrated approach to safety throughout all phases of the proposed facility. From the initial construction and installation phases to the long-term operation of the collider, safety systems to manage risks associated with both normal and accident scenarios have been studied.

This concept demonstrates the feasibility, in terms of life safety, of the current baseline layout and design for the FCC-ee. However, any modification of the proposed baseline will require an update of the concept and the reassessment of its safety effectiveness.

Moving forward, a continuous risk assessment and iterative enhancement of the concept are essential for the evolving nature of the project. Additionally, it is crucial to address the remaining open points and research gaps identified during the concept's development.

As the effort progresses, the safety concept will incorporate other safety objectives, maintaining a strong safety-oriented approach in the design of this unprecedented facility.

Chapter 10

FCC-hh collider design and performance

10.1 Design and performance

The Future Circular Collider (FCC) integrated programme offers the most powerful post-LHC experimental infrastructure proposed to address key open questions in particle physics. It envisions an initial electron-positron collider phase, FCC-ee, which will later be followed by a proton-proton collider, both of which will be installed in the same tunnel of approximately 91 km in circumference, close to CERN.

The hadron collider, FCC-hh, would operate at a centre-of-mass energy of about 85 TeV (or above), extending the energy frontier by almost an order of magnitude compared with the LHC, and providing a 5- to 10-times higher integrated luminosity than the upcoming High-Luminosity LHC. The mass reach for direct discovery at FCC-hh will amount to several tens of TeV, and it will allow, for example, the direct production of new particles, whose existence could already be indirectly exposed by precision measurements at FCC-ee. The FCC-hh hadron collider can also accommodate ion and lepton-hadron collision options, allowing complementary physics explorations.

The FCC-hh accelerator configuration described in this chapter, including its layout and injector options, preserves the rich potential for a diverse physics programme, ranging from heavy ion collisions to a dedicated flavour or forward physics programmes, as are familiar from the LHC. Examples of this potential were amply discussed in the CDR and are briefly reviewed in Sect. 1.2 of Volume 1. Furthermore, it is expected that the 4-fold symmetry of the interaction regions will add flexibility and boost performance to the exploitation of the two lower-luminosity interaction points.

The FCC integrated programme follows the successful example of the past Large Electron Positron Collider (LEP) and Large Hadron Collider (LHC) projects at CERN, which used one and the same infrastructure for successively realising two large collider projects. Inspired by the sequence of LEP and LHC, the comprehensive long-term FCC programme maximises the opportunities of physics. The lepton and hadron colliders, FCC-ee and FCC-hh, would profit from common civil engineering and also from sharing much of the technical infrastructure. The updated baseline layout of the FCC-ee electron-positron collider and its injector design are fully compatible with the demands of the future hadron collider (FCC-hh), and do not compromise the latter's performance. The main ring optics and RF configurations for both colliders were refined to simplify operation across the energy range of FCC-ee and to enable a smooth transition to FCC-hh after the completion of the FCC-ee research programme.

The FCC-hh baseline assumes 14 T Nb_3Sn magnets, that are compatible with a collision centre-of-mass energy of 85 TeV. An R&D path towards HTS magnets would enable higher collision energies. The present design allows four collision points and experiments. The experience gained from the Phase II upgrades of the LHC detectors for the HL-LHC, developments for further exploitation of the LHC and ongoing detector R&D for future Higgs factories will be important stepping stones for the development of the FCC-hh experiments.

In the next sections, the layout for the collider, the injector options, and the injection lines will be described. Following this, Sect. 10.4 describes the pathway to developing the key technology required for the FCC-hh: the development of high-field magnets based on both the 14 T Nb_3Sn technology and higher-field HTS, that could enable higher collision energies and/or cost savings. Teams around the world are pursuing the development of the requisite magnet technology. The primary regions involved in the advancement of magnet technology include the US, Europe, Japan, and China. In each region, there are growing efforts to coordinate and integrate research internally among universities, laboratories, and, to some degree, industry.

An R&D plan is outlined which shall close the gap between the near- to medium-term scope (5–10 years) of the European High Field Magnet (HFM) Programme and the US Magnet Development Programme on the one hand, and the long-term needs of the FCC integrated programme on the other hand. It complements the bottom-up, technology-driven approach of the HFM Programme with a top-down, long-term strategic roadmap derived from the requirements of the FCC-hh. Moreover, this plan will provide a framework for the coordination of R&D efforts on a global scale and over a sustained period of time.

Finally, this chapter closes with a discussion of some other accelerator systems that would be required for the FCC-hh, including cryogenic plants and their distribution.

10.2 FCC-hh layout and optics

10.2.1 Layout of the FCC-hh ring

Since the publication of the Conceptual Design Report (CDR) [10] several studies have been carried out to provide a revised and improved version of the ring layout. The key concepts that have been used to determine the main properties of the new layout can be summarised as follows: the outcome of the placement studies; the proposal to equip the new layout of the FCC-ee ring with four experiment points; the considerations on the harmonic number of the FCC-hh ring that should be made compatible with that of its injector.

The placement studies provided strong indications that the length of the FCC-hh ring had to be shortened to satisfy the multiple constraints that emerged during the investigations. Most of the reduction compared with the CDR was achieved by reducing the lengths of the arcs, keeping the total length of the straight sections constant. However, a final adjustment also reduced the length of the straight sections.

The FCC-ee design introduced the important constraint that the ring should assume a four-fold symmetry and four-fold superperiodicity, to enable four experiment insertions with optimum luminosity performance. This feature, which must also be fulfilled by – and may similarly benefit – the FCC-hh ring, radically changes the configuration with respect to what was presented in the CDR [10]. The functions of the various technical insertions had to be reviewed and different functions to be combined differently, which resulted in a modified layout and optics design for most of the insertions. Another major change in the layout is the radial displacement of the interaction points (IP) of the FCC-hh ring to align with the IP positions of the FCC-ee ring. This geometric modification has a significant impact, as the dispersion suppressor is employed to control the new ring geometry. This adjustment must be implemented while ensuring the feasibility of the optics, particularly maintaining proper dispersion matching. This change has an important side effect on the optimisation of size and layout of the experiment caverns, with the option of sharing the detector's services, infrastructure, and possibly components between the lepton and the hadron FCC colliders [502]. A further major modification to the ring layout is the reduction of the number of surface sites from twelve to eight, which is beneficial in terms of overall costs and which also facilitated the placement. The last, but certainly not least, change with respect to the original baseline configuration is the proposal to locate the last part of the transfer lines inside the ring tunnel. This choice has the benefit of reducing the length of the tunnel needed for the transfer lines from the injector to the FCC-hh.

The proposed layout of the FCC-hh ring is shown in Fig. 10.1. The circumference is 90.66 km, with 2032 m long technical insertions and experiment insertions accommodated in a straight tunnel of length of 1400 m, with approximately 965 m distance between the last dipole magnets on either side of the IP. The experiment insertions are located in Point A (PA), Point D (PD), Point G (PG), and Point J (PJ). The IPs of the hadron and lepton rings are superimposed within a few millimetres.

Figure 10.2 shows a comparison of the three rings on the right side of an experiment insertion. The crossing angle between the two FCC-ee rings is clearly visible, with the FCC-hh straight section in between the two rings. Further away from the IP, the three rings converge and are fully compatible with a single tunnel. Detailed studies of the geometry of the hadron ring optimised the current layout so as to reduce the radial distance between the three rings, with a beneficial impact on the integration. This important result was achieved by carefully displacing the main dipoles in the region of the dispersion suppressors (see the next section). Applying the same recipe, also in the technical insertions the geometries of the hadron and lepton rings were matched as closely as possible, with a radial distance between the rings of approximately 30 cm).

The merging of secondary experiments with injection systems, which resembles the concept implemented in the LHC, was abandoned because it would have generated transfer lines that were too long. The injection of the clockwise beam is performed in PB, and it is combined with the momentum collimation, whereas the injection of the counter-clockwise beam is performed in PL, and it is combined with the RF system. The beam is always injected into the outer beam channel of the FCC-hh accelerator. The two other technical insertions, points PF and PH, each have a single role: to house the beam dump and the betatron collimation systems.

A review of the FCC-hh quadrupole families, including their magnetic properties and the mechanical apertures, has been carried out. The list of magnet families used in the current layout of the FCC-hh ring is presented in Table 10.1. Several of the proposed families in the insertions could still be further optimised as discussed below.

Before entering the details of the discussion of the design of the magnetic lattices of the new layout of the FCC-hh, it is important to mention a crucial change with respect to the CDR. The nominal field of the main dipoles is 14 T, which corresponds to the centre-of-mass energies of 84.6 TeV. The geometry of the proposed layout is fully compatible with the new ranges of dipole field and centre-of-mass energy. In the rest of the document, the strength of the quadrupoles is expressed for a beam energy of 45 TeV, which amounts to adding a 6% safety margin to the available magnetic strength. When citing minimum magnet strengths, an injection energy of 3.3 TeV is considered, as had been adopted by the CDR. These values could be scaled linearly to alternative lower injection energies of 1.7 or 1.3 TeV.

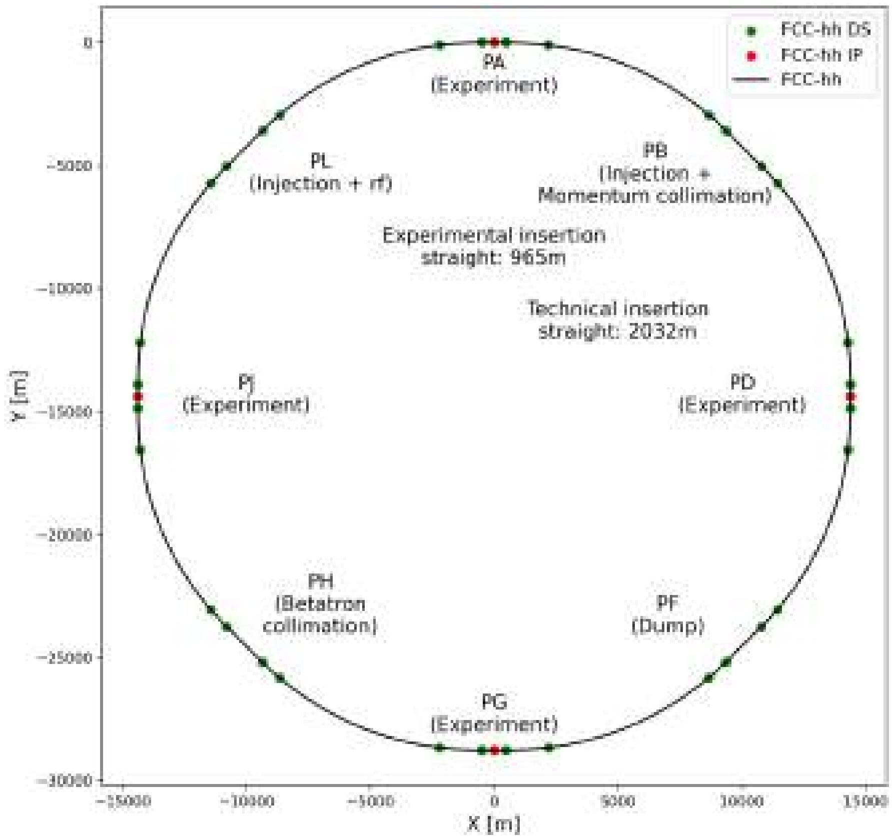

Fig. 10.1 Overall view of the layout of the new FCC-hh ring configuration. The functions of the various insertion regions are mentioned. The experiment straight sections are located with respect to the four-fold symmetry of the ring. The length of the straight sections is also mentioned

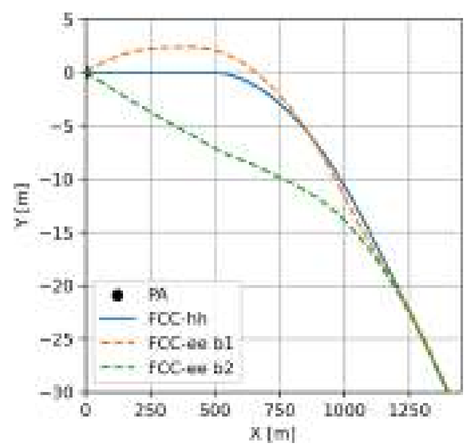

Fig. 10.2 Comparison of the geometry of the FCC-hh ring and for the two FCC-ee rings in the vicinity of PA. The same situation occurs in the other three experiment insertions

10.2.2 Design of regular arcs and dispersion suppressors

The review of the FCC-hh lattice imposed by the placement studies was used to reassess some of the principal assumptions made for the former CDR layout [10]. This is the case for the choice of regular arc cell length. For highest-energy hadron accelerators, designing the lattice with a longer regular cell offers one clear advantage. Namely, the longer cell leads to an increase in the dipole filling factor (for the FCC-hh, this factor was increased from 0.8 as in the CDR to 0.82 at present), with an accompanying increase in the values of beta-functions and dispersion. The larger optical functions enhance the efficiency of the correction systems, such as the chromatic sextupoles and Landau octupoles, but they also render the beam more sensitive to magnetic field errors, in particular at injection, putting additional demands on the magnet design and the correction systems. An obvious upper limit to the cell length is set by the physical dimensions of the vacuum chamber, the injected beam emittance, and the required beam aperture. In Ref. [503], the target aperture values are given as 13.4 σ at injection energy and 15.5 σ at collision energy, where σ denotes the nominal rms beam size computed for a normalised rms emittance of 2.2 μm).

Table 10.1 Main parameters of the dipole and quadrupole families used in the entire ring. All fields are referred to 45 TeV to include a safety margin on the required magnetic strength. Note that the orientation of the various aperture types might change according to the polarity of the quadrupole, in order to optimise the beam aperture

NAME	Magnetic[1] length [m]	Nominal field [T]	Nominal gradient [T/m]	Aperture cross section	Aperture dimensions [mm]	Coil aperture diameter [mm]	Number of magnets
MB	14.187	14	NA	Beamscreen[2]	–	50	4464
MBX	10.0	14.6	NA	Octagon[3]	33.1/33.1/13.5/76.5	116	8
MBR	13.0	5.6	NA	Octagon	33.1/33.1/13.5/76.5	80	24
MBW	14.0	1.7	NA	Ellipse[4]	29.5/22.0		20
MQ	6.4	NA	375.0	Beamscreen	–	50	536
MQ	9.6	NA	375.0	Beamscreen	–	50	8
MQ	10.0	NA	375.0	Beamscreen	–	50	8
MQ	12.0	NA	375.0	Beamscreen	–	50	24
MQM	6.0	NA	375.0	Rectellipse[5]	15.0/13.2, 15.0/15.0	50	17
MQ1	14.3	NA	130.0	Circle	36.49	164	16
MQ2	12.5	NA	105.0	Circle	58.24	210	32
MQ3	14.3	NA	105.0	Circle	58.24	210	16
MQ4	12.0	NA	175.0	Rectellipse	28.9/24.0, 28.9/28.9	70	8
MQ5	12.0	NA	260.0	Rectellipse	20.0/18.2, 20.0/20.0	60	8
MQR	6.4	NA	280.0	Rectellipse	20.0/18.2, 20.0/20.0	60	8
MQY	6.0	NA	200.0	Rectellipse	28.9/24.0 - 28.9/28.9	60	2
MQY	9.1	NA	200.0	Rectellipse	28.9/24.0, 28.9/28.9	60	14
MQYL	12.8	NA	200.0	Rectellipse	28.9/24.0, 28.9/28.9	60	6
MQW	4.0	NA	40.0	Ellipse	26.1/15.3		44

[1] The specified magnetic length corresponds to an individual magnet. Multiple magnets may be concatenated to form a longer structure if necessary.

[2] This cross-section corresponds to the shape depicted in Fig. 10.3 (right) and is defined by points.

[3] An octagon is defined by four numbers: the half width and half height along main axes, two angles sustaining the cut corner in the first quadrant, given in radians and in order of increasing values.

[4] An ellipse is defined by two numbers specifying the horizontal a_h and vertical a_v semi-axes, given in the form a_h/a_v.

[5] A rectellipse is a shape obtained by the intersection of a rectangle and an ellipse [116, 210] and is defined by four numbers specifying the half-width r_w and half-height r_h of the rectangle, horizontal a_h and vertical a_v semi-axes of the ellipse, given in the form r_w/r_h, a_h/a_v. Note that, in general, the ellipse is replaced by a circle.

In Fig. 10.3, the regular cell with optical parameters and available beam aperture is shown for the current layout. The number of main dipoles per cell has increased from 12 in the CDR [10] to 16. The overall cell layout with the dipole (blue) and quadrupole (red) magnets is indicated at the top. The phase advance per cell was kept at 90°. The cell length is about 275.8 m, to be compared with about 213.0 m for the CDR. The change in the arc cell results in a larger value of the beta-functions and dispersion, which has several positive and also a few negative side effects. Even for this longer cell, two cryo-jumpers, connected to the quadrupole cryostats, are sufficient to feed all superconducting magnets from the cryogenic line [504]. The beneficial increase in cell length and the induced increase in the values of optical parameters require a small adaptation of the dimensions of the beamscreen. Figure 10.3 shows the cross section of the beam screen from the CDR [10] (dotted line) and a proposed new version with larger horizontal aperture (continuous line). These changes in the beamscreen dimensions will require a more detailed design validation in the next study phase.

The performance of the corrector systems that are present in the arc was also evaluated and reviewed [505], and the new layout of a short straight section of a periodic FODO cell is shown in Fig. 10.4. As a direct consequence of the cell lengthening, each arc consists of fewer cells, reducing the number of available slots for installing the required correctors. However, the larger beta-functions and dispersion enhance the effectiveness of some correctors in their roles. The properties of the correction circuits in the arcs are listed in Table 10.2, where N_c represents

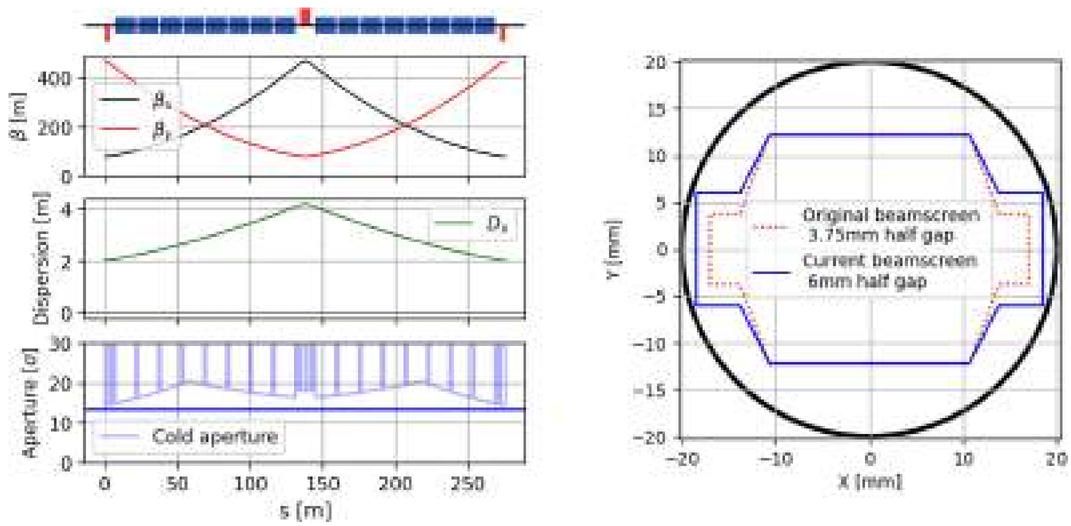

Fig. 10.3 Layout, optical parameters, and dispersion of the 16-dipole periodic FODO cell design (left) and cross section of the beamscreen compatible with the aperture requirements of the arc cell (right). The horizontal line in the aperture plot represents the minimum value acceptable

Table 10.2 Correctors circuits properties and capabilities for the FCC-hh Ring. For the correction of the linear coupling, the resonance strength indicated by C^- is defined as $C^- = \frac{1}{2\pi}\int \sqrt{\beta_x\beta_y}k_s e^{i(\mu_x-\mu_y)}\mathrm{d}s$, where $\beta_{x,y}$, k_s and $\mu_{x,y}$ are the beta functions, skew quadrupole gradient, and phase advances, respectively

	Length [m]	Strength [Tm^{-n}]	Integral strength [Tm^{1-n}]	N_c	N_m	Correctors capabilities
Dipole orbit correctors MCB	1.2	4.5	5.4	61	1	residual rms orbit ≤ 0.3 mm
Trim quadrupoles MQT	0.5	220	110	2	8	up to 0.15 tune shift with β-beating $\leq 1\%$
Skew quadrupoles MQS	0.5	220	110	2	2	$C^- < 10^{-4}$
Chromatic sextupoles MCS	1.2	7000	8400	2	28	control around $Q' = 10$ with squeezed optics
Landau octupoles MO	0.5	2.2×10^5	1.1×10^5	2	18	Same amplitude detuning as in CDR

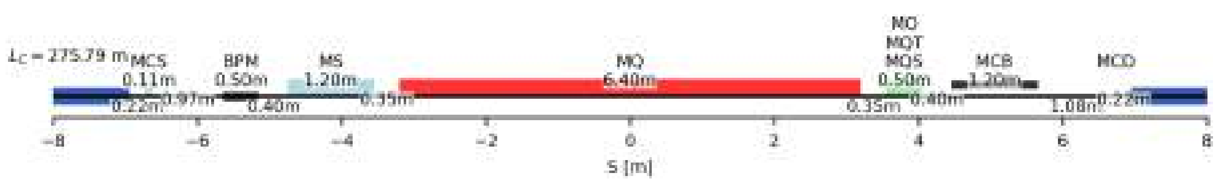

Fig. 10.4 Layout of the periodic FODO cell short straight section (left to right: sextupole spool piece MCS, beam position monitor BPM, chromatic sextupole MS, main quadrupole MQ, Landau octupole MO, trim quadrupole MQT, skew quadrupole MQS, orbit corrector MCB, and decapole spool piece MCD)

the number of circuits per arc, while N_m stands for the number of magnets per circuit. The symbol n in the units represents the order of the magnetic multipole, which is 0 for a dipole.

The analysis of corrector efficiencies has identified several additional optimisations that can be applied to the layout of the Short Straight Sections (SSS). These improvements will enhance the dipole filling factor of the collider and will be incorporated into the next iteration of the FCC-hh ring lattice. In general, a shortening of each SSS of about 4 m can be envisaged. Another possible source of gains in the energy reach of FCC-hh can come from increasing the length of the main dipole. Even for this aspect, the change in the design of the periodic FODO cell will be part of the next version of the magnetic lattice.

The dispersion suppressors (DS) were reviewed starting from the CDR design [10]. The presently proposed layouts are shown in Fig. 10.5, where the DS for the transition between the regular arc and experiment insertion is displayed at the top, and the one connecting the regular arc and a technical insertion at the bottom.

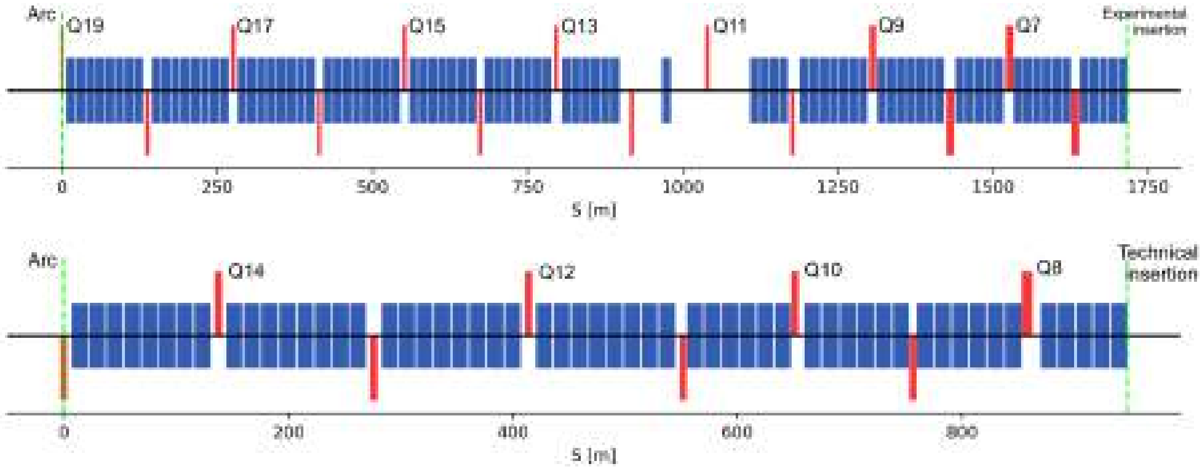

Fig. 10.5 Layout of the dispersion suppressor on the left of an experiment insertion (top) and technical insertion (bottom)

The complexity of the design of the DS for the experiment insertions resides in the need to control the whole geometry and to radially displace the IP position. The control of the geometry is achieved by selectively displacing blocks of the main dipoles, whereas the quadrupoles are kept in regular positions to ensure control of the optics and dispersion. The DS starts just behind Q19 and ends with Q6, and its extent is an essential parameter to ensure optimal geometry control. The quadrupoles in the DS are assumed to have independent powering, which ensures enough optical flexibility. In practice, this can be achieved with main quadrupoles, powered in series with the other main quadrupoles in the regular part of the arc, and trim quadrupoles to ensure independent control of the gradient generated at a given ring location. This scheme has been successfully implemented in the LHC [116] and provides optimised hardware use (quadrupoles and power converters). However, on most occasions, these trim quadrupoles must be set to the opposite polarity of that of the main quadrupole they accompany, trading efficiency for space and simplicity. The details of the quadrupole families and their powering will be studied in more detail at a later stage.

The DS for the technical insertions is shorter, running between, but not including, Q15 and Q7. In this case, the main role of the DS is to control the dispersion since the ring geometry does not need to be changed in the technical insertions. It should also provide enough optical flexibility to enable the matching of the optical parameters of the regular arc with those of the various technical insertions.

Both types of DS have short gaps (of the order of 2 m) to allow the installation of collimators, the so-called TCLD collimators, which should absorb particles that have lost energy in interactions with the primary and secondary collimators.

10.2.3 Experiment straight sections

The experiment insertions are the core of the FCC-hh ring design, both for the complex geometry needed to match the radial position of the IPs with those of the FCC-ee and for the requirement to achieve the low β^* value needed to reach the target luminosity performance. At injection energy, $\beta^* = 10\ m$ (like the LHC case [116]), which is then reduced to $\beta^* = 30\ cm$ at collision energy. The squeeze of β^* will take place, at least partially, during the energy ramp, based on considerations of the available aperture that indicate the minimum value β^* for a given beam energy.

The layout of the four experimental insertions is identical to maintain consistent optics. However, the polarity of the separation dipoles varies, as both beams change between outer and inner magnet aperture at the different insertions. This causes a slight variation in the horizontal dispersion function, which manifests itself in two distinct forms. Two important differences with respect to the layout presented in Ref. [10] were implemented: the strictly straight beam-line section is about 965 m instead of 1400 m as a consequence of the radial displacement of the IP. Furthermore, the separation (MBX type) and recombination (MBR type) dipoles are superconducting to reduce their total length, which is important given the reduced length of the straight section. This set up resembles what is being implemented for the HL-LHC [8, 9], where the normal-conducting D1 of the LHC will be replaced by a superconducting one. The D2 recombination dipole is already superconducting in the LHC and will remain so in the HL-LHC, although with an increased coil aperture.

In terms of the magnetic field, the integrated strength of the separation and recombination dipoles is 146 T m at 45 TeV, and the nominal fields of the D1 and D2 magnets are 14.6 T for and 5.6 T, respectively. The radius of

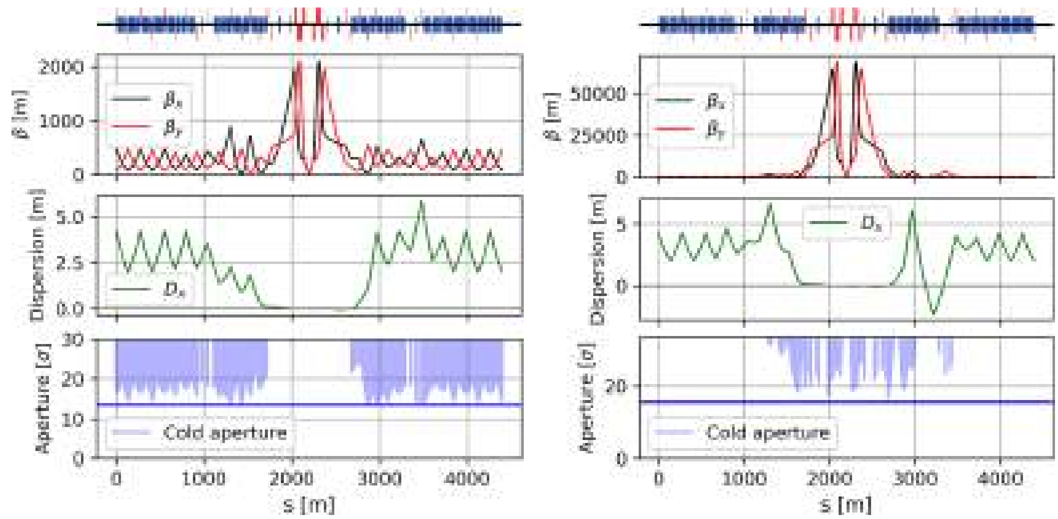

Fig. 10.6 Optical parameters, dispersion, and beam aperture for the injection optics of the experiment insertion at PA (left, $\beta^* = 10$ m) and the collision optics (right, $\beta^* = 30$ cm) including crossing angle. The horizontal line in the aperture plot represents the minimum value acceptable

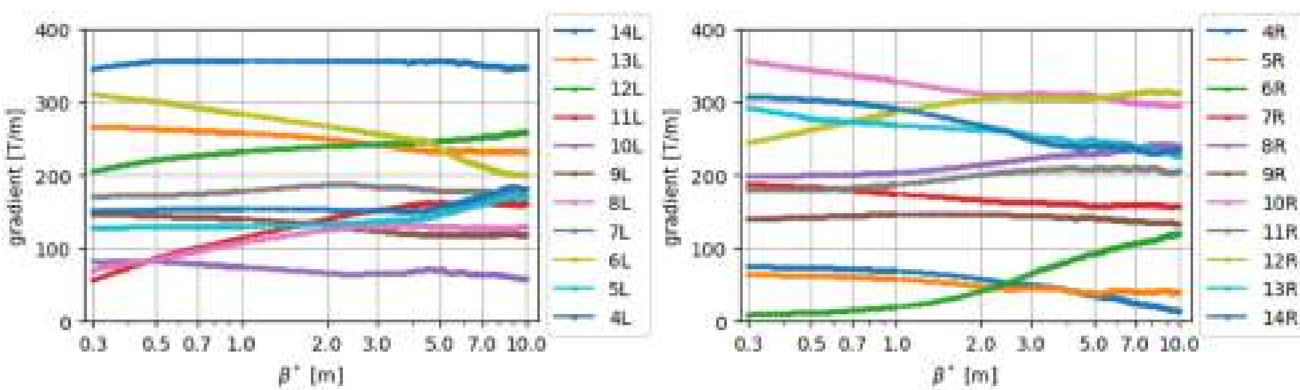

Fig. 10.7 Quadrupole strength during the β^* squeeze for the left and right sides of the experiment insertion (left and right plots, respectively)

the coil aperture has been determined and found to be 58 mm for D1 and 40 mm D2. For comparison purposes, the coil radius of the HL-LHC D1 and D2 separation and recombination dipoles is 75 mm and 52.2 mm, respectively.

The optical parameters, dispersion, and beam aperture for the layout of the PD experiment insertion are shown in Fig. 10.6 for the solution with $\beta^* = 10\ m$ for the injection energy (left) and $\beta^* = 30\ cm$ for collision energy. The most striking difference is the maximum value of the beta-functions that reaches about 2000 m and 70,000 m for injection and collision optics, respectively. The target aperture values for the two cases differ and so do the bottleneck locations. For the injection optics, aperture limits appear in the dispersion suppressors surrounding the straight section. Conversely, for the collision optics, including the orbit from the crossing angle, the aperture limit is first reached in the separation dipole (D1), followed by the inner triplet, while the rest of the insertion provides aperture values that largely exceed the target. This suggests that, in the future, the aperture of the D1 separation dipole should be increased. On the positive side, in view the available aperture margin in Q1, a further reduction of β^* could be envisaged.

Note that the ring chromaticity varies during the squeeze due to the contribution of the experimental insertions to the overall ring chromaticity. The strength of the chromatic sextupoles needed to obtain $Q' = 10$ when $\beta^* = 10$ m is approximately 19% of that required to obtain the same Q' when $\beta^* = 30$ cm.

A solution has been found for the squeeze from $\beta^* = 10$ m to $\beta^* = 30$ cm and the corresponding quadrupole strengths are shown in Fig. 10.7. The starting point for this transition is not compatible with the aperture requirements at injection energy. Therefore, the transformation of the nominal injection optics to the starting

Table 10.3 Strength of the insertion quadrupoles for the injection optics of the experiment insertion at PA (second column, $\beta^* = 10$ m) and the collision optics (third column, $\beta^* = 30$ cm). All the gradients correspond to 45 TeV

NAME	Gradient [T/m]	Gradient [T/m]	Gradient [T/m]	Gradient [T/m]	Maximum gradient [T/m]
MQ.14L	−127.9	−172.3	−127.9	−172.3	375.0
MQ.13L	119.9	133.1	119.9	133.1	375.0
MQ.12L	−114.1	−102.9	−114.1	−102.9	375.0
MQ.11L	94.9	28.2	94.9	28.2	375.0
MQ.10L	−116.6	−40.9	−116.6	−40.9	375.0
MQ.9L	190.9	146.5	190.9	146.5	375.0
MQ.8L	−176.4	−70.1	−176.4	−70.1	375.0
MQ.7L	222.7	170.6	222.7	170.6	375.0
MQ.6L	−129.1	−311.2	−129.1	−311.2	375.0
MQY.5L	149.3	127.8	155.1	128.0	260.0
MQY.4L	−88.0	−151.7	−90.9	−151.6	175.0
MQXE.3L	94.8	94.8	94.8	94.8	105.0
MQXD.2L	−92.9	−92.9	−92.9	−92.9	105.0
MQXC.1L	114.1	114.1	114.1	114.1	130.0
MQXC.1R	−114.1	−114.1	−114.1	−114.1	130.0
MQXD.2R	92.9	92.9	92.9	92.9	105.0
MQXE.3R	−94.8	−94.8	−94.8	−94.8	105.0
MQY.4R	60.0	75.8	60.0	74.6	175.0
MQY.5R	−72.7	−64.8	−70.0	−63.5	260.0
MQ.6R	124.4	8.6	124.4	8.6	375.0
MQ.7R	−149.2	−187.9	−149.2	−187.9	375.0
MQ.8R	166.7	198.9	166.7	198.9	375.0
MQ.9R	−117.2	−140.0	−117.2	−140.0	375.0
MQ.10R	85.4	178.1	85.4	178.1	375.0
MQ.11R	−101.2	−90.3	−101.2	−90.3	375.0
MQ.12R	108.2	122.7	108.2	122.7	375.0
MQ.13R	−120.8	−146.0	−120.8	−146.0	375.0
MQ.14R	107.2	153.9	107.2	153.9	375.0

point of the squeeze sequence is envisioned during the energy ramp,[28] as the squeeze sequence satisfies the aperture requirements when the beam energy reaches 10 TeV or higher.

The strength values of the quadrupoles that generate the two optical configurations of the experiment insertions are summarised in Table 10.3.

A cornerstone feature for the performance of the experiment insertions is the crossing scheme. A set of correctors generates a local orbit bump around the IP to mitigate the effect of long-range beam-beam interactions [10]. The orbit also separates the beams, preventing collisions until the beams are at top energy and the optics is squeezed. Although the bump is fully corrected and, therefore, transparent to the rest of the ring, the horizontal and vertical dispersion generated must be taken into account. The strategy followed is similar to that employed in the LHC [116]. At injection, the quadrupoles in the dispersion suppressors are used to rematch the horizontal dispersion to the neighbouring arcs, while the standing vertical dispersion is small enough that it does not necessitate countermeasures. When transitioning to collision optics, a set of orbit correctors in the arc is used to create a closed-orbit bump that exploits the field of the chromatic sextupoles to cancel the vertical dispersion. This is illustrated in Fig. 10.8, where the crossing and separation bumps are presented at injection energy (top) and at top energy (bottom) for the nominal value of the half-crossing angle and half-separation that are 100 µrad and 1.5 mm, respectively.

[28]The duration of the energy ramp is approximately 20 min.

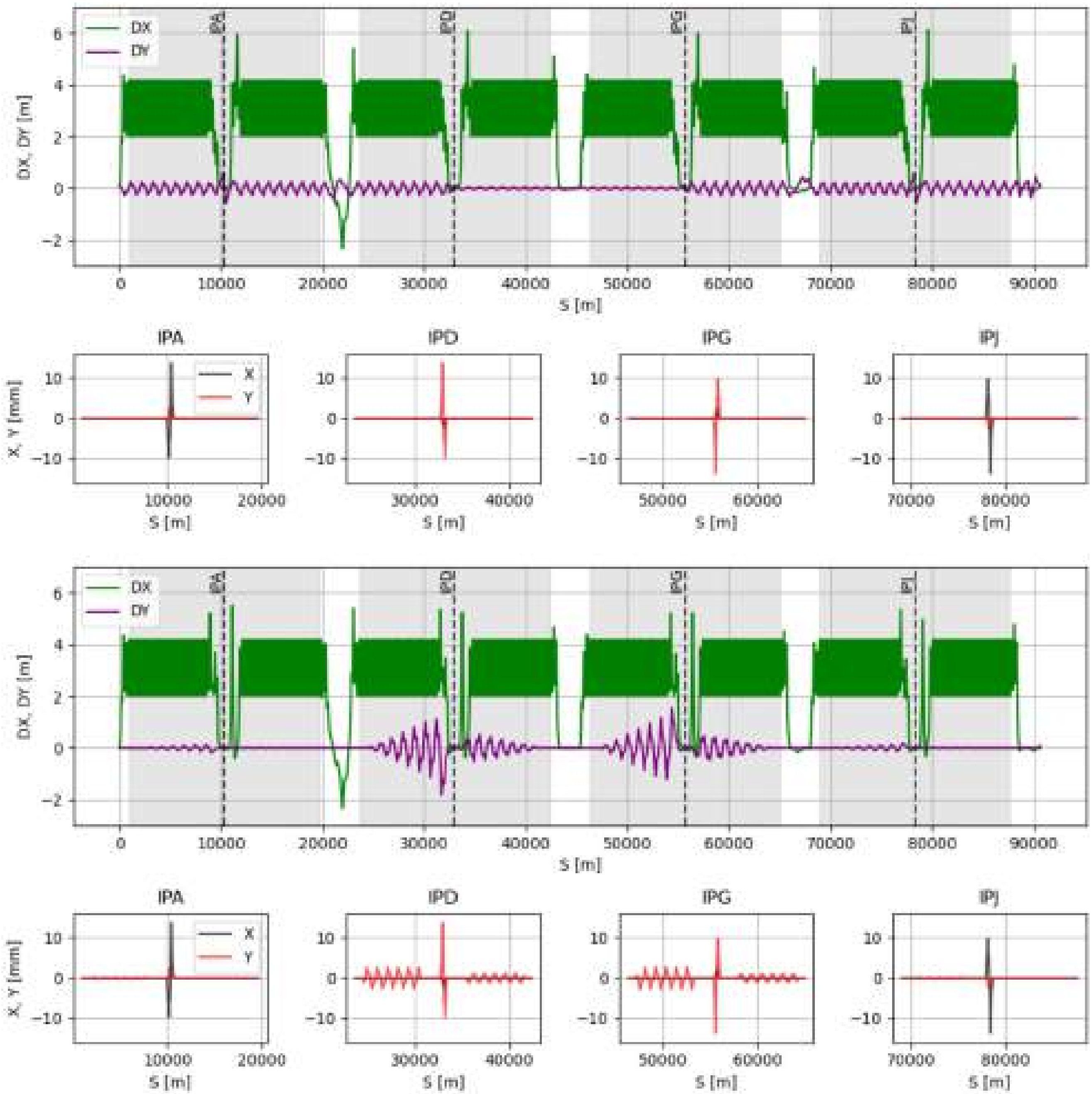

Fig. 10.8 Closed dispersion and orbit with crossing angle and separation at injection (top) and collision (bottom) energies with a closer look at the experimental insertions

The orbit bump at top energy that created the dispersion bump is clearly visible, and the overall correction of the spurious vertical dispersion is good. The primary constraint is the alternating crossing plane between PA and PG. The crossing and separation schemes in all experimental insertions are designed to accommodate all possible combinations of crossing and separation planes while ensuring compatibility with this constraint.

10.2.4 Beam dump

As described above, changes in the ring layout with respect to CDR [10] reduced the length of the technical straight sections from 2800 m to 2032 m. The new layout accommodates the dump systems for both beams at PF, as a result of civil engineering considerations. At an intermediate stage [506], the possibility of merging the dump

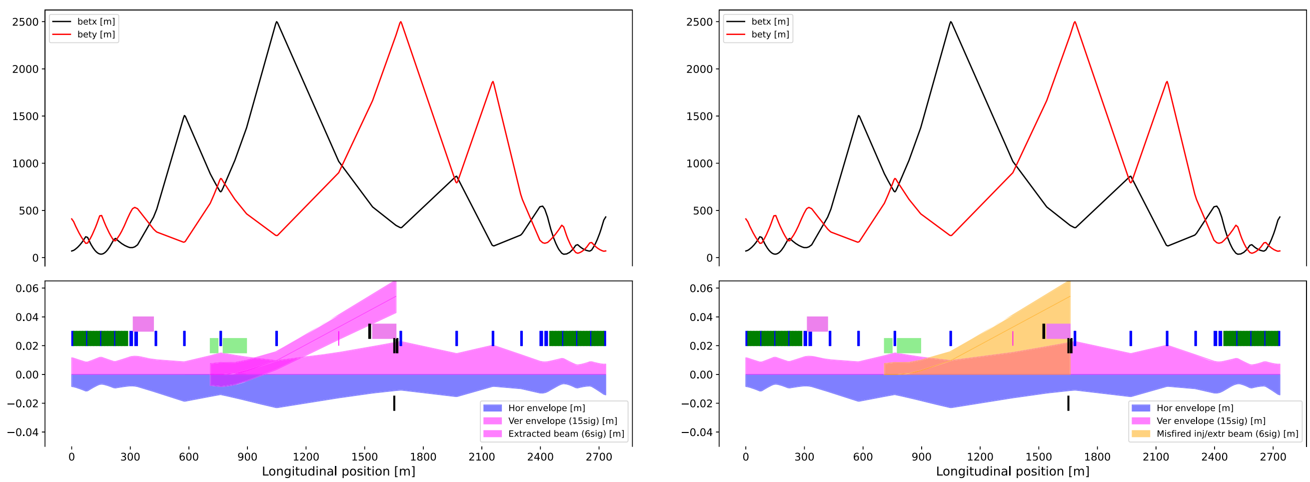

Fig. 10.9 Left: Optics (top) and beam envelopes and active elements (bottom) for the extraction straight section around PF. Right: Dump system failure scenario: asynchronous beam dump. The configurations shown refer to collision energy

and injection systems for the clockwise beam in PB was considered. However, this option was deemed unfeasible, primarily due to machine protection concerns arising from the complexities of handling combined failure scenarios for the injection and dump systems. The necessary layout modifications could only be resolved by dedicating a technical insertion exclusively to the beam dump. The system is illustrated in Fig. 10.9 (left), where the circulating and extracted beam envelopes are shown for the nominal extraction case, ensuring sufficient clearance.

The externally activated dumping system has the function to extract and dilute the beam, and to dispose the entire extracted beam onto an external absorber located 2.5 km from the extraction point in a dedicated cavern. The design of the complete dump system is driven both conceptually and hardware-wise by machine protection considerations [507].

The extraction system design had to be adapted to the reduced length of the straight section, leading to an increased length of the superconducting extraction septa (utilising superconducting shield and truncated cosine-theta technologies), as well as higher switch voltage and an extended system length for the extraction kickers. At this stage, it is challenging to predict the switch technology that will be available on the FCC-hh timescale. However, if significant difficulties arise in achieving the required hardware parameters, an alternative approach could allow the extracted beam to pass through an aperture in the cryostat of the downstream quadrupole, reducing the required septum deflection angle by approximately one-third of its nominal strength.

The design of systems involving fast pulsed devices acting in a single turn on a beam with unprecedented power, such as that of the FCC-hh, is driven by their failure scenarios. A relevant failure scenario concerning the asynchronous beam dump is shown in Fig. 10.9 (right), where the misfiring of an extraction or dilution kicker leads to an immediate trigger of the full system that, however, is not synchronised with the beam abort gap. Dedicated protection absorbers are expected to protect the downstream machine from particle spray. The damage limit of the absorbers drives the extraction kicker rise time. This limit is most critical for global machine protection, in particular in the case that a beam abort occurs with the full beam at top energy. For this specific failure scenario, only a single dumped beam is shown. The systems for the other beam are arranged symmetrically around the centre of the straight section.

The general optical parameters and the beam aperture are shown in Fig. 10.10.

The strength and aperture values for the quadrupoles that generate the optical configuration of the beam dump are summarised in Table 10.4.

10.2.5 RF and injection straight section

The technical insertion at PL is used to accommodate the RF system and the injection of the counter-clockwise beam. The main constraints imposed by the RF system are the increased inter-beam distance, which must reach 420 mm to accommodate the accelerating cavities, and the cancellation of dispersion in the straight section where the cavities are located to minimise synchro-betatron coupling. These constraints are met by introducing two doglegs that both increase the inter-beam distance and ensure that the dispersion and its derivative are zero in the central part of the insertion.

The beam is injected in the vertical direction, as the transfer line will run above the main ring magnets, just on top of the external aperture of the circulating beam. Optimal injection conditions require a phase advance of

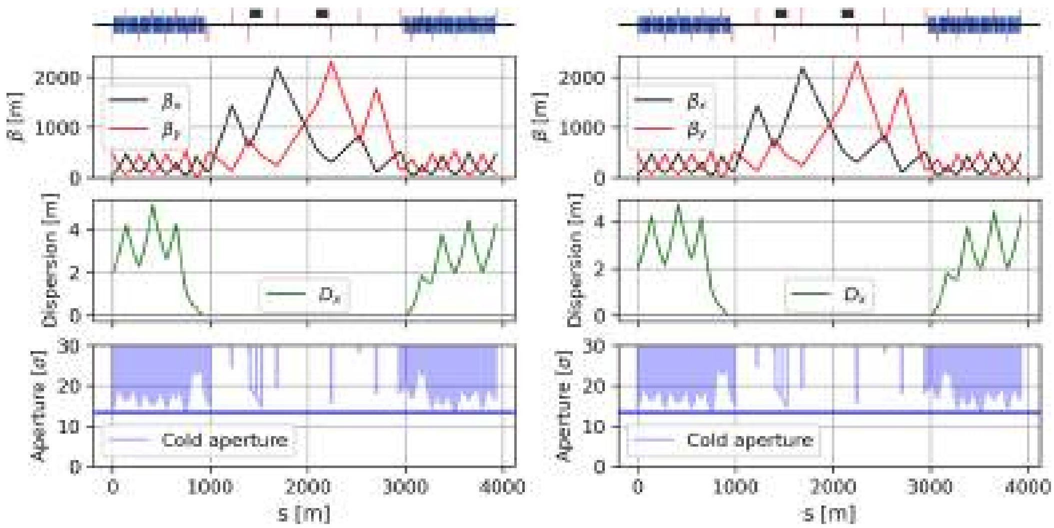

Fig. 10.10 Optical parameters, dispersion, and beam aperture at injection of two configurations of the dump insertion with different settings in the dispersion suppressors to match the ring to injection (left) and collision (right) tunes. MKD and MSD positions are highlighted in black. The horizontal line in the aperture plot represents the minimum value acceptable

Table 10.4 Strength of the insertion quadrupoles for the optics of the technical insertion at PF (beam dump) and its dispersion suppressors. All the gradients correspond to 45 TeV

NAME	Gradient [T/m]	Maximum gradient [T/m]
MQ.14LF.B1	116.47	375.0
MQ.13LF.B1	−120.36	375.0
MQ.12LF.B1	116.72	375.0
MQ.11LF.B1	−115.10	375.0
MQ.10LF.B1	155.11	375.0
MQ.9LF.B1	−160.22	375.0
MQ.8LF.B1	62.91	375.0
MQM.B7LF.B1	−151.48	375.0
MQM.A7LF.B1	−151.48	375.0
MQY.6LF.B1	43.49	200.0
MQY.5LF.B1	−47.69	200.0
MQY.4LF.B1	24.98	200.0
MQY.4RF.B1	−24.98	200.0
MQY.5RF.B1	47.69	200.0
MQY.6RF.B1	−43.49	200.0
MQM.A7RF.B1	136.32	375.0
MQM.B7RF.B1	136.32	375.0
MQ.8RF.B1	−49.48	375.0
MQ.9RF.B1	169.34	375.0
MQ.10RF.B1	−127.26	375.0
MQ.11RF.B1	142.57	375.0
MQ.12RF.B1	−116.81	375.0
MQ.13RF.B1	125.28	375.0
MQ.14RF.B1	−131.00	375.0

90° between the kicker and the injection protection dump, and maximising the value of $\sqrt{\beta_x\beta_y}$ at the location of the injection protection dump. An additional constraint in the design of the injection of the counter-clockwise

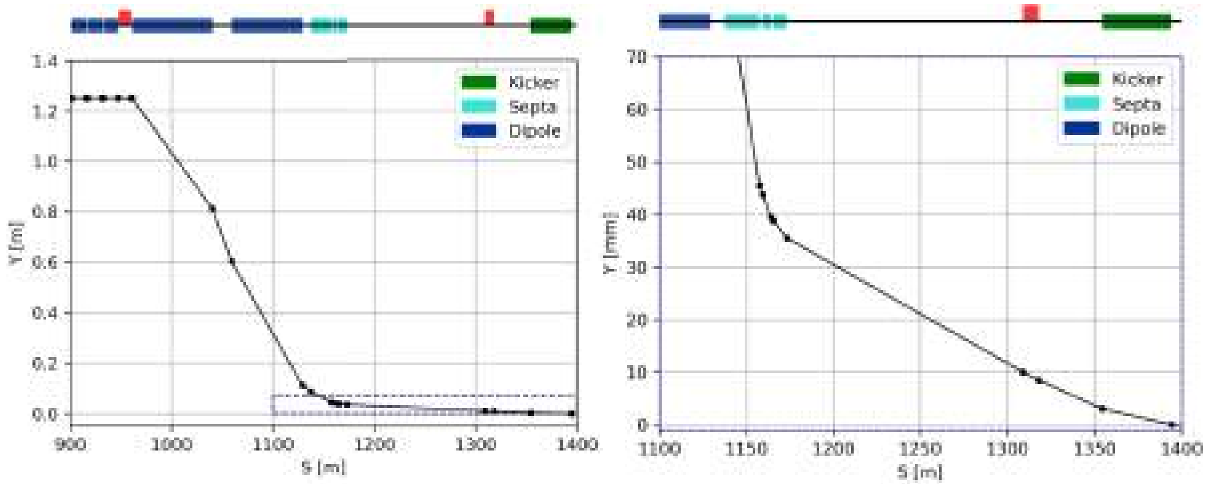

Fig. 10.11 Trajectory in the vertical plane of the injected counter-clockwise beam from the transfer line arc to the injection kicker (left) and a detailed view of the path through the septa (right). Exceptionally, the description of the layout is made using the counter-clockwise beam as a reference

Table 10.5 Electromagnetic and aperture parameters of the septa, dipole, and kickers assumed for the injection of the counter-clockwise beam

NAME	Active length [m]	Blade thickness [mm]	Magnetic field [T]	Aperture cross section	Aperture dimensions [mm]
MSI1	8.0	8	0.7	Ellipse	12.0 / 11.0
MSI2	5.0	12	1.0	Circle	16.0
MSI3	20.0	18	1.2	Circle	16.0
MBWI	70.0	NA	1.4	Circle	16.0
MKI	40.0	NA	0.024	Circle	18.3

beam is to use the same hardware as installed in PB for the injection of the clockwise beam: this does not pose any serious challenge for the overall design of the insertion.

Figure 10.11 shows the vertical trajectory of the injected beam, assuming a difference in height between the circulating and injected beams of 1250 mm. This first block of bending magnets represents the end of the transfer line, followed by a downward bending dipole, a second dipole that starts to deflect the trajectory to become parallel with the plane of the collider and then the septa, with a field that decreases with the reduction of the thickness of the septum blade (the details are given in Table 10.5). The last block of bending magnets represents the kickers that cancel the residual angle of the injected beam. The second dipole is a recent addition to the magnetic sequence that helps to reduce the longitudinal footprint of the insertion dedicated to the injection elements and is labelled MBWI in Table 10.5. It is installed in a region where the injected and the circulating beams are separated enough that a conventional dipole can be used rather than a septa-type magnet. This allows using a stronger magnetic field of 1.4 T to accelerate the geometrical transition between the plane of the transfer line to that of the collider.

Note that the quadrupole located in between the two groups of bending devices is used to provide an additional dipole kick exploiting the off-axis traversal of the beam.

Figure 10.12 shows the optical parameters, dispersion, and beam aperture at injection, corresponding to the most critical configuration. The part of the insertion close to the DS on the right-hand side (light-blue box in the figure) is where the injection system is located: it is left empty here, as the injection elements are inactive for the circulating beam, and they do not affect the beam whose optics are shown here. The section envisaged for the RF system (green box in the figure) has a length of approximately 870 m.

Table 10.6 summarises the strength of the quadrupoles that generate the optical configuration of RF and injection insertion.

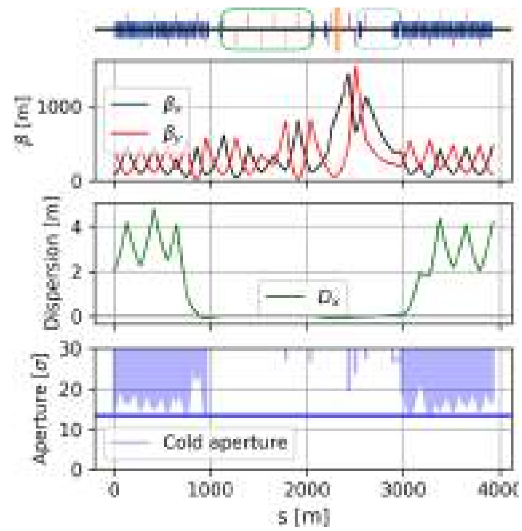

Fig. 10.12 Optical parameters, dispersion and beam aperture at injection, corresponding to the most critical configuration for the optics of the RF and injection insertion for the anti-clockwise beam. Sections dedicated to a specific function are highlighted: the area where the RF cavities may be located (green), injection protection devices (orange) and injection elements (light blue). The horizontal line in the aperture plot represents the minimum value acceptable

10.2.6 Betatron collimation

The collimation system is meant to clean the betatron halo and off-momentum particles surrounding the main beam. These two functions are performed by two subsystems located in two insertions to allow for dedicated optical conditions. Cleaning of the betatron halo requires small values of the dispersion function and appropriate phase advances between the various collimation stages. Cleaning off-momentum particles requires large normalised dispersion[29] values and is discussed in further detail in Sect. 10.2.7.

A side effect of the collimation system is the beam impedance originating from the jaws that are close to the beam edge. Recently, for the HL-LHC, mitigation measures for the beam impedance based on local changes to the beam optics were proposed (see Ref. [508, 509] and references therein), which aim at increasing the beta functions at the collimators. This novel concept has also already been incorporated into the optics design of the FCC-hh betatron collimation insertion.

Two additional novel features were implemented in the layout of the collimation insertions, both related to the geometry of the doglegs that are part of the insertions. The main function of doglegs in the LHC collimation insertions is to filter out the neutral particles generated by the beam-matter interaction in the jaws of the collimators [510]. Thanks to the doglegs, the neutrals are prevented from depositing energy in the coils of the first superconducting dipole on the opposite side of the insertion, i.e., at the beginning of the DS. Hence, the LHC collimation geometry need not be exported to the FCC-hh, by rescaling it to the higher beam energy. Instead, it is sufficient to introduce the minimum deflection that brings the neutrals out of the cross-section of the coils of the first superconducting dipole at the beginning of the downstream DS. This approach simplifies the layout of the doglegs and relaxes the requirements in terms of dipole strength needed to generate the doglegs. Based on these considerations, each of the two doglegs of the PH insertion is made of two dipole blocks (composed of two MBW-type dipoles) with opposite polarities, and each block generates 46.0 T m at collision energy.

The second change is keeping the inter-beam distance constant along the whole straight insertion. In fact, in the LHC, the arc inter-beam distance of 194 mm is increased in the collimation insertions to 224 mm by the geometry of the doglegs of the two counter-rotating beams. In the layout of the FCC-hh collimation insertions, the inter-beam distance remains constant and has the same value as in the arcs, namely 250 mm. This choice has a fundamental consequence, as in this case, not only the optical parameters are the same for the counter-rotating beams, but also the dispersion functions are the same. Hence, this design choice facilitates having exactly identical layouts and optics for the two beams.

The Q6 quadrupoles, previously composed of six MQTLH magnets as in the LHC [116], have been replaced in the new layouts by a single MQY quadrupole. This change optimises the beam aperture, eliminating an unnecessary bottleneck.

Additionally, to maximise the available beam aperture, the orientation of the elliptical beam pipe in the MQW quadrupoles is adjusted according to the quadrupole polarity.

The betatron collimation subsystem is located in PH, and the corresponding layout and optical functions are shown in Fig. 10.13. As discussed above, a novel optical configuration featuring high-beta values has been designed to mitigate the beam impedance generated by the collimators. However, this optics is not suitable for the injection

[29] The normalised dispersion is defined as $D_x/\sqrt{\beta_x}$.

Table 10.6 Strength of the insertion quadrupoles for the RF insertion at PL and its dispersion suppressors. All the gradients correspond to 45 TeV

NAME	Gradient [T/m]	Maximum gradient [T/m]
MQ.14LL.B1	117.49	375.0
MQ.13LL.B1	−115.18	375.0
MQ.12LL.B1	115.75	375.0
MQ.11LL.B1	−110.70	375.0
MQ.10LL.B1	158.84	375.0
MQ.9LL.B1	−170.55	375.0
MQ.8LL.B1	75.86	375.0
MQM.7LL.B1	−353.09	375.0
MQR.6LL.B1	261.98	280.0
MQR.5LL.B1	−252.75	280.0
MQR.4LL.B1	274.79	280.0
MQR.3LL.B1	−180.75	280.0
MQR.2LL.B1	187.29	280.0
MQR.1LL.B1	−274.64	280.0
MQR.01LL.B1	233.43	280.0
MQR.1RL.B1	−259.94	280.0
MQY.2RL.B1	−78.80	200.0
MQY.3RL.B1	71.95	200.0
MQYL.4RL.B1	87.58	200.0
MQYL.5RL.B1	−132.28	200.0
MQY.6RL.B1	67.81	200.0
MQYL.7RL.B1	96.84	200.0
MQ.8RL.B1	−48.36	375.0
MQ.9RL.B1	150.32	375.0
MQ.10RL.B1	−113.83	375.0
MQ.11RL.B1	139.02	375.0
MQ.12RL.B1	−100.32	375.0
MQ.13RL.B1	116.73	375.0
MQ.14RL.B1	−116.30	375.0

energy because here it would violate the aperture requirements. Furthermore, cleaning performance is essential at collision energy and much less important at injection. Therefore, two optical configurations were designed: one with mid-range values of the beta-function to be used at injection, and one with large values of the beta-functions that should be used at collision energy. These two configurations are those shown in Fig. 10.10 (left, for the injection configuration and right, for the collision configuration). An optical transition between the two configurations is envisioned during the energy ramp. This same type of transition will first be tested at the LHC during Run 3, with the goal of becoming operational for the HL-LHC. Consequently, the FCC-hh will benefit from existing operational experience with dynamic optical changes in the collimation insertions. It is important to highlight that, in both LHC and FCC-hh, the target aperture differs between the two configurations, and, in all cases, the aperture requirements are satisfied.

Table 10.7 summarises the strength and aperture values for the quadrupoles generating the two optical configurations of the insertion for betatron collimation.

10.2.7 Momentum collimation and injection

The technical insertion at PB serves two functions, namely injection of the clockwise circulating beam and momentum collimation. A transition region of approximately 530 m (from the kicker to the primary collimator) is used to match the optics between these two systems, while also providing shielding between the kickers and momentum collimation debris, particularly in the event of injection losses.

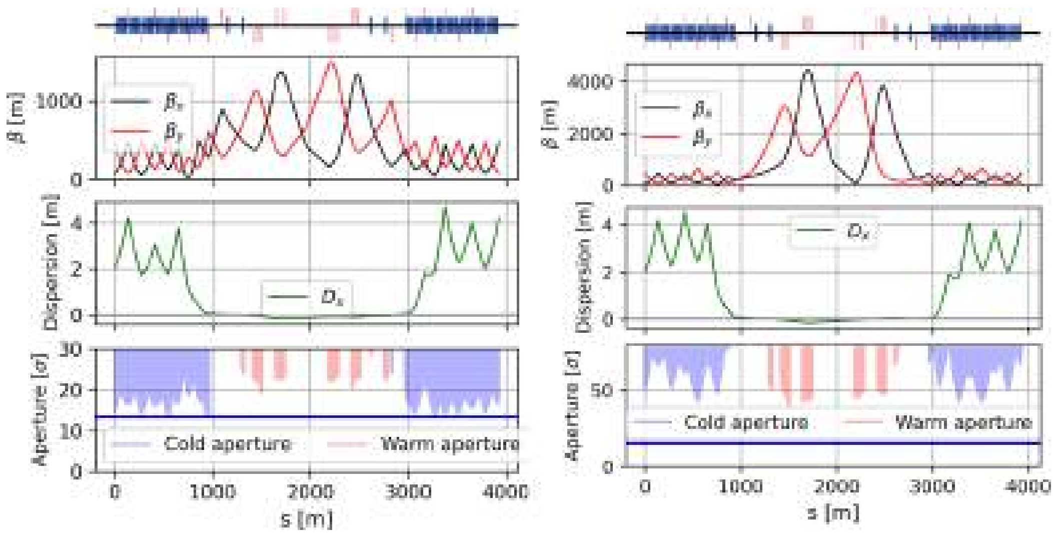

Fig. 10.13 Optical parameters, dispersion and beam aperture for the low-beta optics (for injection) of the betatron collimation insertion PH (left) and the high-beta (for collision) variant (right). The blue and the red aperture regions indicate superconducting and normal-conducting magnets, respectively. The horizontal line in the aperture plot represents the minimum value acceptable

Table 10.7 Strength of the insertion quadrupoles for the betatron insertion at PH (second column, low-beta, third column, high-beta) and its dispersion suppressors. All the gradients correspond to 45 TeV

NAME	Gradient [T/m]	Gradient [T/m]	Maximum gradient [T/m]
MQ.14LH.B1	117.3	127.6	375.0
MQ.13LH.B1	−103.8	−110.4	375.0
MQ.12LH.B1	113.2	116.3	375.0
MQ.11LH.B1	−105.7	−124.0	375.0
MQ.10LH.B1	152.8	168.7	375.0
MQ.9LH.B1	−115.9	−108.8	375.0
MQ.8LH.B1	52.4	61.4	375.0
MQM.7LH.B1	−57.5	−206.0	375.0
MQY.6LH.B1	28.3	79.3	200.0
MQW.5LH.B1	−25.5	−28.5	44.0
MQW.4LH.B1	38.6	34.8	44.0
MQW.4RH.B1	−33.2	−31.9	44.0
MQW.5RH.B1	38.2	34.8	44.0
MQY.6RH.B1	−154.3	−83.9	200.0
MQM.7RH.B1	215.7	207.8	375.0
MQ.8RH.B1	−58.2	−36.7	375.0
MQ.9RH.B1	159.5	142.6	375.0
MQ.10RH.B1	−114.2	−114.5	375.0
MQ.11RH.B1	139.5	140.0	375.0
MQ.12RH.B1	−88.9	−97.3	375.0
MQ.13RH.B1	114.6	113.5	375.0
MQ.14RH.B1	−103.9	−113.2	375.0

This insertion presents two main challenges from a beam optics perspective. First, the optimal beam properties for maximising the performance of each system individually are conflicting. Ideally, the injection region should have zero dispersion to prevent the need for very tight injection protection absorber settings, which must otherwise account for momentum offsets while maintaining alignment with the collimation hierarchy.

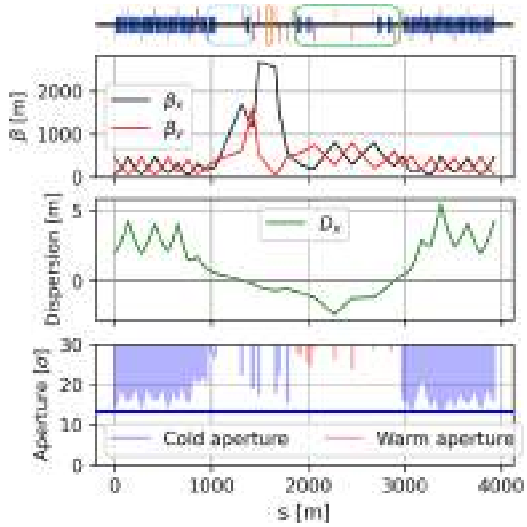

Fig. 10.14 Optical parameters, dispersion and beam aperture at injection for the momentum collimation and injection insertion PB for the clockwise beam. Sections dedicated to a specific function are highlighted: injection elements (light blue), injection protection devices (orange) and momentum collimation elements (green). The horizontal line in the aperture plot represents the minimum value acceptable

Conversely, a large value of the normalised dispersion is necessary for the momentum collimation systems to function effectively. Additionally, to protect each system from potential losses originating from the other, the longitudinal footprint of each subsystem must be carefully allocated, including a buffer area with shielding between them.

The first challenge is addressed by fine-tuning the upstream dispersion suppressor to ensure that the residual dispersion from the arc meets these constraints. The second challenge is managed by optimising the injected beam trajectory, as discussed in the previous section.

In this insertion, the optics of the two beams can differ if necessary since the counter-clockwise beam is not subject to injection constraints. This flexibility allows its optics to be configured in a way that minimises the impact of momentum collimation losses on the injection elements.

Doglegs are also needed for the momentum collimation system, and each block of dipoles (composed of three MBW-type dipoles) generates 69.0 T m at collision energy.

The layout and hardware configuration of the injection system are identical, but mirror reflected, of that shown in Fig. 10.11 and Table 10.5.

Figure 10.14 shows the optical parameters, dispersion, and beam aperture at injection that corresponds to the most critical configuration. The dispersion is matched so that it is small as the beam reaches the injection kicker and then grows as the beam reaches the dogleg where the primary collimator is located.

The strength values for the quadrupoles that generate the optical configuration of the insertion for the off-momentum collimation are summarised in Table 10.8.

10.2.8 Impedance considerations

Beam-coupling impedance remains largely unchanged with respect to the CDR [10, Sect. 2.4.7]). The main implications from the change of layout are related to a shorter ring circumference, which implies a slightly larger revolution frequency and a reduced total length of beam screens and vacuum pipe, along with lower maximum beam energy, a lower magnetic field on the beam screen at top energy, and possibly a higher operating temperature of the beamscreen. The vertical dimension of the beam screen remains unchanged from the CDR, with a half height of 12.2 mm.

The reduction in tunnel length results in an 8% increase in the revolution frequency, shifting the first unstable betatron line to higher frequencies. However, this has no significant impact on stability, as the associated rigid-mode instability is effectively suppressed by the transverse feedback damper [10]. Additionally, the reduced tunnel length decreases the resistive-wall impedance of the vacuum structure—particularly of the beam screens—by the same 8%. The reduction of the magnetic field from 16 T to 14 T also leads to a reduction of the resistivity of the copper beam screens, through magnetoresistance, of about 8% (assuming a residual resistivity ratio of 70 as in the LHC beam screens [511], and standard copper properties for magnetoresistance [512] and temperature dependency [513], as implemented in XWAKES [514]), which leads to a reduction of their resistive-wall impedance by 4%.[30] By contrast, the lower flat-top energy (42.3 TeV instead of 50 TeV) has a more pronounced effect, as both tune shifts and growth rates are inversely proportional to γ, leading to an 18% increase.

[30] If the beam screens were operated at 70 K instead of 50 K, their resistive-wall impedance would increase by 21% with respect to the CDR configuration (50 K, 16 T). At injection energy (corresponding to a dipole field of 1.09 T, almost unchanged with

Table 10.8 Strength of the insertion quadrupoles for the momentum collimation insertion at PB and its dispersion suppressors. All the gradients correspond to 45 TeV

NAME	Gradient [T/m]	Maximum gradient [T/m]
MQ.14LB.B1	123.6	375
MQ.13LB.B1	−124.0	375
MQ.12LB.B1	118.1	375
MQ.11LB.B1	−125.3	375
MQ.10LB.B1	150.5	375
MQ.9LB.B1	−129.6	375
MQ.8LB.B1	57.9	375
MQYL.7LB.B1	−20.1	200
MQY.6LB.B1	67.8	200
MQYL.5LB.B1	−122.6	200
MQYL.4LB.B1	68.8	200
MQY.3LB.B1	103.2	200
MQY.2LB.B1	−56.8	200
MQM.1LB.B1	−131.8	375
MQY.1RB.B1	1.6	200
MQW.2RB.B1	−20.2	44
MQW.3RB.B1	32.2	44
MQW.4RB.B1	−31.3	44
MQW.5RB.B1	27.8	44
MQY.6RB.B1	−169.8	200
MQM.7RB.B1	231.0	375
MQ.8RB.B1	−40.5	375
MQ.9RB.B1	129.9	375
MQ.10RB.B1	−111.3	375
MQ.11RB.B1	131.8	375
MQ.12RB.B1	−103.3	375
MQ.13RB.B1	110.2	375
MQ.14RB.B1	−115.6	375

Since at top energy, the resistive-wall impedance of the beam screens accounts for only 10% of the total impedance [10], the stability at the flat top is degraded with respect to the CDR by approximately 20%, primarily due to the lower beam energy. At injection energy, where the beam screen contributes 50% of the total impedance, stability improves by 4% if the beam screen temperature remains unchanged. Even in a worst-case scenario, the increase in instability growth rates and tune shifts remains manageable at both injection and flat top [10]. If the injection energy is lowered to 1.3 TeV, the multi-bunch instability growth times decrease by a factor of almost three to 20–25 turns [10]. Also, here, a safety margin still exists since even faster multi-bunch instabilities, e.g. with rise times about 10 turns, could be damped by an LHC-type feedback system along with Landau octupoles and non-zero chromaticity [515].

10.2.9 Ongoing studies

The cell magnet layout and the number of dipoles per cell are already optimised for maximum beam energy. An even higher dipole filling factor might still be achieved by optimising the length of the main dipoles, which is subject to various constraints, such as the size of the shaft used to lower the dipoles.

A non-standard option for the FCC-hh ring configuration utilises combined-function magnets [516]. Further investigations of this approach (see, e.g., Ref. [517]), including corrector systems and refined length of the combined-

respect to the CDR), the corresponding increase due to temperature would be of 48%, as the temperature effect is more pronounced at low values of the magnetic field.

function magnets, is essential for determining whether if this setup could serve as a viable alternative to the present baseline lattice.

10.3 FCC-hh injection

10.3.1 Hadron injectors in the SPS or LHC tunnel

Machines located in three different tunnels were initially considered as potential hadron injectors: a booster within the collider tunnel, a modified LHC or a new superconducting machine in the LHC tunnel, and a superconducting SPS (scSPS) in the SPS tunnel. The option of placing a booster in the collider tunnel, using superferric magnets at 1.1 T with a 70% filling factor, was discarded at an early stage due to the need for long bypass tunnels —approximately 15 km in length—around the experiment caverns.

The remaining options, involving a machine in either the LHC or SPS tunnel, differ in their achievable injection energy for the collider. An scSPS limits the injection energy to 1.3 TeV, whereas a machine in the LHC tunnel could exceed the collider's baseline injection energy of 3.3 TeV.

In addition to the injection energy of 3.3 TeV the main requirements of the hadron injector are the delivery of the beam parameters in intensity, emittance and bunch spacing, as well as a fill duration of around 30 min.

A detailed study was carried out to evaluate the feasibility of modifying the existing LHC into a fast-ramping 3.3 TeV injector. This analysis included assessing layout modifications in the straight sections, optimising the powering segmentation to enable faster ramping, and developing a simplified optics design [518]. The FCC-hh Conceptual Design Report [10] concluded that, at 3.3 TeV, the threshold for FCC-hh injection absorbers to survive beam impact requires a burst-mode transfer of 130 batches from the modified LHC to the FCC-hh, each batch consisting of 80 bunches. This configuration would allow the full LHC beam to be transferred within a few seconds.

Alternatively, the LHC could be replaced by a 4 T superconducting machine based on magnet designs from RHIC, Tevatron, or FAIR (SIS200/300). To avoid excessively long transfer lines, this machine would require either polarity reversal or a twin-aperture magnet design. The RF system is assumed to limit the ramp-up time to no more than 50 s, resulting in a total collider filling time of 39 minutes. Additionally, this option would necessitate a burst-mode injection transfer lasting several seconds.

Another approach to replacing the current LHC within its tunnel involves a superferric, iron-dominated machine operating at 2T, capable of achieving a transfer energy of approximately 1.75 TeV. However, neither of these options has been studied in further detail at this stage.

If the collider can accommodate an injection energy of 1.3 TeV, a superconducting machine in the SPS presents an intriguing option. This possibility has been explored at the conceptual level and is documented in Ref. [519].

This study considered following the present SPS lattice, which naturally is well-matched to the existing tunnel geometry, using missing bend dispersion suppressors. A collimation system needs to be integrated into the straight-section layout. The beam transfer from the scSPS to the collider is limited to 640 bunches per transfer due to absorber limits. In this case, no burst-mode transfer is required. The filling time considered in Ref. [519] needs to be revised in view of the reduced number of collider bunches and a possibly higher ramp rate.

Overall, the feasibility of an scSPS is mainly determined by the design of large aperture, fast ramping dipoles, and quadrupoles. The design study compares 2D designs of main dipoles and quadrupoles for both single- and double-layer coil configurations. Among these, the 4.2 K-compatible double-layer coil design emerges as the most promising. The study also evaluated a challenging 80 mm aperture, primarily motivated by also allowing a slow-extraction based fixed-target programme reaching up to 1.3 TeV. Recent advancements in crystal-assisted slow extraction provide confidence that the current spiral step of 20 mm could be reduced to approximately 5 mm, directly impacting the required magnet aperture.

The initial magnet study also highlights the significant benefits of doubling the injection energy in the SPS to 50 GeV, as this would reduce the critical energy/field swing and AC losses. In addition, this approach could eliminate the current need for transition crossing. Given that the PS will be more than 100 years old at the time of FCC-hh, one might consider replacing the PS with a 50 GeV machine - a superconducting machine in the PS tunnel or a normal conducting PS2 (studied as an option to renovate the LHC injector chain).

Injector option summary and outlook The three options for an FCC hadron injector are summarised in Table 10.9. All options can deliver the main beam parameters required, such as intensity, emittance, and bunch spacing. The main difference is the implied FCC-hh injection energy. The modified LHC option stands out for the filling time, in particular, since the filling time of the scSPS was calculated with a rather conservative ramp rate. The LHC would also need a large effort in continuous consolidation over decades before being repurposed as an FCC hadron injector.

If the collider injection energy stays above the reach of an scSPS, an attractive option seems to be a new 4 T machine in the LHC tunnel. Another possibility, with an intermediate beam energy, is a 2-T superferric machine.

Table 10.9 Comparison of high-energy booster options, a superconducting machine in the SPS tunnel (scSPS), a modified faster-ramping LHC and a new 4 T machine in the LHC tunnel. A further option (not shown) with an intermediate energy of 1.75 TeV would be a superferric machine in the LHC tunnel

	Unit	scSPS	mod. LHC	4 T LHC
Circumference	km	6.9	26.7	26.7
Apertures		1	2	1
Injection energy	GeV	26	450	450
Extraction energy	TeV	1.3	3.3	3.3
Injection field	T	0.12	0.6	0.6
Maximum field	T	6	4	4
Energy/field swing		50	7	7
Individual dipole length	m	12	14.3	14.3
Dipole filling factor		0.65	0.66	0.66
Number of dipoles		372	1232	1232
Number of quadrupoles		216	480	480
Number of bunches		640	2600	2600
Stored energy	MJ	15	167	167
Booster filling time	min	0.5	7.5	3.8
Ramp rate	T/s	0.4	0.026	0.08
Cycle length	min	1.1	12	4.9
Booster cycles per FCC fill		34	4	8
Collider filling time	min	37	46	39

Table 10.10 Lengths of transfer lines and tunnels from the LHC with the required magnet fields in the connection tunnel and inside the collider tunnel, respectively

	TL length [km]	Tunnel length [km]	Dipole fields [T]
LHC P8 to PB	9.5	1.9	6.6/1
LHC P8 to PL	7.5	3.8	4.7/1

If 1.3 TeV is acceptable for the collider, an scSPS becomes appealing, also in view of a possible synergy of beam transfer tunnels.

Given the timescale for all options, it seems valid to consider renovating the entire injector chain, allowing the removal of certain bottlenecks in beam production.

For the next study steps, it is planned to establish a parametric model for the main cost drivers of a 3.3 TeV superconducting machine and a 1.75 TeV superferric machine in the LHC tunnel, and a 1.3 TeV superconducting machine in the SPS tunnel.

10.3.2 Layout of the FCC-hh injection

In the case of using the present LHC or a new 4 T machine in the LHC tunnel as the FCC hadron injector, the beam would be transferred at 3.3 TeV, which, in Ref. [10], was considered the baseline injection energy.

With the new geometry of the lepton transfer lines from the surface to the collider tunnel (see Sect. 7.7), there is no longer a synergy between the lepton and hadron transfer tunnels to simplify the civil engineering work for the lepton tunnels.

For hadron beams from the LHC tunnel, it is proposed that both beams be extracted from P8, as illustrated in Fig. 10.15. Compared to the current LHC dump system, designed for 7 TeV and operated at 6.8 TeV, an extraction system for FCC beams would require only half the deflection while benefiting from at least 50 years of technological advancements. Additionally, such an extraction system could be designed with a simpler triggering logic compared to a fail-safe dump system.

Transfer lines from LHC P8 to the collider tunnel require superconducting magnets well within the reach of current Nb-Ti technology (see Table 10.10). As soon as the transfer lines join the collider tunnel, the magnetic field required drops to the injection field of the collider magnets, as described in detail in Sect. 10.3.1.

In case a lower injection energy into the collider is attainable, the option of a super-ferric iron-dominated machine in the LHC tunnel allows a beam transfer at around 1.75 TeV. This option could use the same extraction

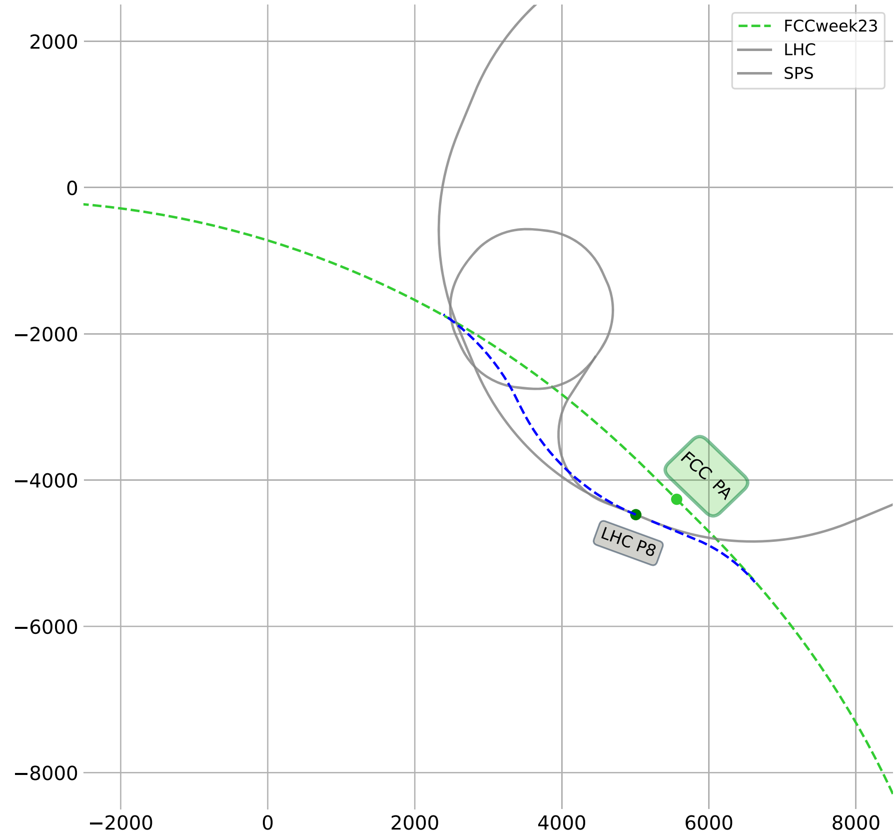

Fig. 10.15 Transfer tunnels (blue dashed) for 3.3 TeV hadron beams from LHC P8 to the collider. The transfer lines continue inside the collider tunnel for several km to reach the injection straights PB and PL

Table 10.11 Lengths of transfer lines and tunnels from the scSPS with the required magnet fields in the connection tunnel and inside the collider tunnel, respectively

	TL length [km]	Tunnel length [km]	Dipole fields [T]
SPS-LSS4 to PB	12.9	1.6	7.4/0.44
SPS-LSS6 to PL	6.9	0.9	4.2/0.44

system layout as described above. The reduced transfer energy would be beneficial for the system design. Also, the transfer line geometry could be the same as described above, with lower fields in the transfer dipoles.

10.3.3 Layout of the FCC-hh injection lines from a superconducting SPS

For a superconducting SPS, based on ~ 6 T magnets, the transfer energy is limited to 1.3 TeV. At this energy, the use of the existing TI8 tunnel for hadron transfer is within reach of the current technology, which reduces the new tunnelling for the clockwise beam injected in PB by 3 km (see Fig. 10.16 and Table 10.11). The dipole fields required amount to 5.9, 2.3 and 7.4 T for the different arcs, respectively. As soon as the transfer line is in the collider tunnel, a field of 0.44 T is required.

For the anti-clockwise beam injected in PL, the straight Sect. 6 (LSS6) of the SPS is favoured to have a short connection of less than 1 km to the collider tunnel with dipole fields of 4.2 T.

10.3.4 Transfer lines in the ring tunnel

Two sections of the FCC-hh transfer lines are inside the collider tunnel, in the arcs that join PA and PB (for the clockwise beam) and PA and PL (for the counter-clockwise beam). The design of the transfer line will inherit the features of the regular arcs of the ring over this length. It is assumed that periodic cells of the transfer line will be copies of those in the hadron collider, with each containing 16 dipole magnets. Furthermore, the focusing structure will also be applied to the part of the transfer lines outside the ring tunnel, whereas the geometry will impose a different choice of dipole magnets.

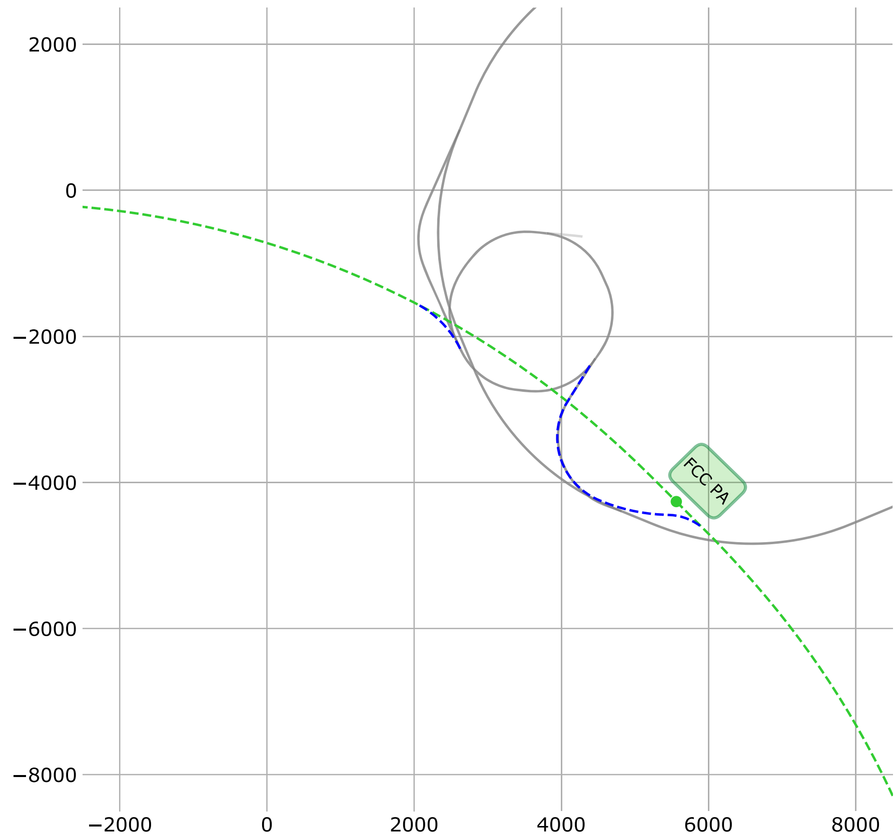

Fig. 10.16 Transfer tunnels (blue dashed) for 1.3 TeV hadrons from SPS LSS4 to the collider in clockwise direction, and from SPS LSS6 to the collider in anticlockwise direction. The transfer line continues inside the collider tunnel for several km to reach the injection straights PB and PL

Table 10.12 FCC-hh transfer line magnets parameters for injection energy of 3.3 TeV and for the section located inside the ring tunnel. The total length of the tunnel section of the two transfer lines is 19.6 km. Such an estimate is an upper bound based on the FCC-hh arc length. The FCC-hh ring regular cell is 276 m long

		Electromagnet	Permanent magnet
Interconnections	Longitudinal gap (mm)	550	50
Aperture and field quality	Beam pipe inner diameter (mm)	30	
	Good field region (GFR) diameter (mm)	20	
	Field linearity in GFR (units)	2	
Dipoles	Integrated dipole field per cell (T m)	230	230.4
	Dipole magnet field strength (T)	1	
	Magnet magnetic length (m)	5	1.2
	Number of magnets per cell	46	192
	Total dipole length (km)	8.51	8.52
Quadrupoles	Integrated quadrupole gradient per cell (T)	118	
	Quadrupole magnet gradient (T/m)	20	25
	Magnet magnetic length (m)	3	1.2
	Number of magnets per cell	4	8
	Total quadrupole length (m)	444	355.2

Two injection energies have been considered, 3.3 TeV, which is the baseline assuming the LHC as an injector, and an alternative of 1.3 TeV, assuming a superconducting SPS. The higher injection energy is considered for the magnet design parameters in Table 10.12).

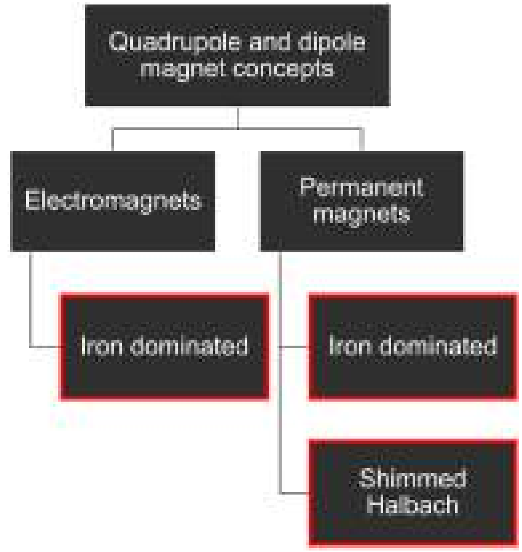

Fig. 10.17 Sketch of the possible conceptual designs for the transfer line magnets. The three magnet design concepts highlighted in red were selected

Fig. 10.18 Photograph of a 6.3 m long dipole magnet (HCMBI_001) used in the LHC transfer line

In view of the large scale of production for the transfer line magnets, assembly and manufacturing will be a key focus of future development efforts.

The aim of the following preliminary assessment was to consider existing magnets at CERN and elsewhere, firstly to generate multiple design concepts and secondly to make an initial assessment of whether these could satisfy the transfer line requirements. Ultimately, three concepts, highlighted in Fig. 10.17, were selected for further development. These three concepts will be developed until the most suitable design can be identified, also taking into account resource effectiveness. Typically, this assessment will be based on lifetime cost, but it will also consider other factors, such as climate impact and ethical issues regarding where raw materials are sourced.

Electromagnet design concepts Iron-dominated normal-conducting accelerator magnets are a mature and well-understood technology. Furthermore, the field strength required is compatible with the normal-conducting magnet capabilities, making them suitable for this application. The volume of the yoke will be optimised to reduce weight and material cost while retaining sufficient torsional rigidity and magnetic performance. The most critical optimisation involves determining the optimal size of the coil cross-section to minimise the total lifetime cost. This requires balancing capital investment costs, primarily driven by the conductor, with overhead expenses, mainly related to electrical power consumption.

One dipole magnet design provides a 1.2 T field in the 30 mm aperture and is largely inspired by the TI2/TI8 transfer line magnets that connect the SPS ring to the LHC (see Fig. 10.18). An H-shaped yoke geometry was selected because it has better torsional rigidity and saturation performance compared to other options. This minimises the dipole cross-section dimensions, particularly the height. The exact length of each magnet unit has not yet been determined, but a 5 m dipole would weigh 4600 kg.

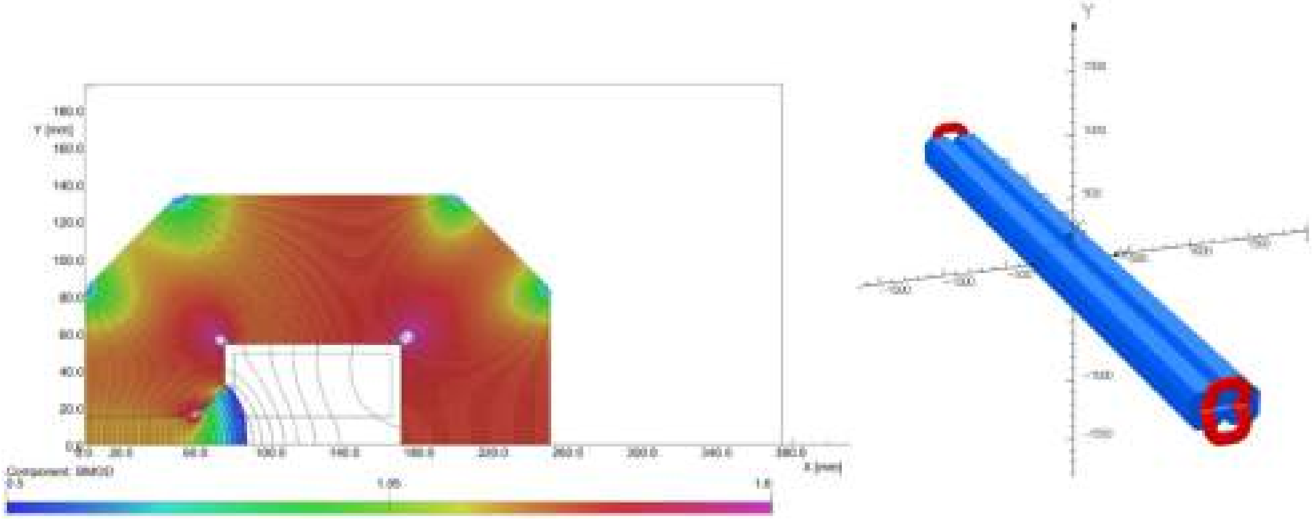

Fig. 10.19 Left: Normal conducting dipole magnet 2D field distribution (four-fold symmetry). Right: Normal conducting dipole magnet 3D model

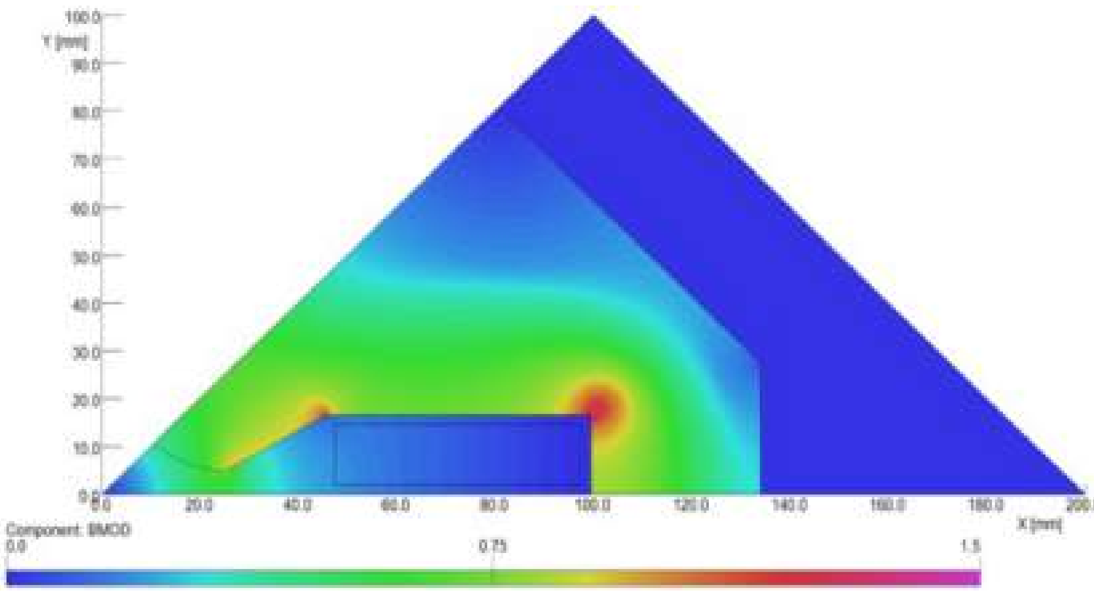

Fig. 10.20 Normal conducting quadrupole magnet 2D field distribution (eight-fold symmetry)

The yoke is made of laminated electrical steel. The laminations are punched and then stacked together, which is the most cost-effective assembly method for producing a large series of long magnets. This configuration also minimises eddy current losses when the magnets are ramped, reducing running costs.

The 58 kA turns required are provided by two bedstead coils. This coil shape reduces the interconnection length between magnets, thus maximising the longitudinal filling factor. The coils are wound with a hollow copper conductor and cooled with demineralised water. Figure 10.19 (left) shows the 2D field distribution in the yoke cross-section, while the 3D magnet geometry is visible in the right plot of the same figure. Note the length of the magnet relative to its cross-section.

The quadrupole concept is also inspired by the TI2/TI8 transfer line magnets. It would be an assembly of laminated steel quadrants with water-cooled coils. Each of the four coils provides 7.4 kA turns, which produces a 25 T/m gradient in the 30 mm diameter aperture, with a 1.5 m long quadrupole weighing 1000 kg. The 2D field distribution in the yoke cross-section is shown in Fig. 10.20.

Fig. 10.21 Samarium Cobalt permanent magnet wedge used in the FASER Halbach magnet at CERN

Permanent magnet solutions Permanent magnets (PM) for accelerators are especially well suited to the transfer line specifications. As the FCC-hh beam will always be injected at the same energy, the magnet strength does not need to be varied. Additionally, the field quality requirements are less stringent than those in the collider ring because the beam only makes a single pass. It is worth mentioning that PMs are already used in accelerators, albeit on a much smaller scale. For instance, at CERN, there are permanent accelerator magnets in Linac4 [520] and the beamline of the FASER [521] experiment. At Fermilab, the 3.4 km recycler ring is entirely based on PMs [522, 523]. Furthermore, PMs can also be found in insertion device magnets for electron synchrotrons around the world (see Ref. [524] for a review).

Note that PM blocks/wedges are the magnetised elements that are assembled to create an accelerator magnet (see Fig. 10.21). During their manufacture, they should gain homogeneous magnetisation (magnitude and direction) oriented relative to an external mechanical datum surface. However, manufacturing tolerances introduce magnetisation errors that must be monitored through quality assurance testing and mitigated by the accelerator magnet designs.

Magnetic forces between PM elements make it challenging to assemble them in a precise and safe way. However, the design concepts presented here are not novel, and multiple assembly techniques are already available. More research is needed to determine whether these approaches are suitable for the industrial scale required by the FCC-hh or whether new techniques will need to be developed.

The design of the transfer line will also include active correctors, i.e., normal-conducting magnets that are meant to compensate for, e.g., trajectory errors in the transfer lines due to the extraction conditions in the FCC-hh injector or magnetic-field errors from the PMs of the transfer line.

Risks associated with permanent magnets PMs have two key weaknesses: the magnetic field they produce is susceptible to radiation dose and variations in temperature, both of which will affect the transfer lines. Therefore, it is important to examine these vulnerabilities and make an initial assessment of whether realistic operating conditions could prevent the transfer line magnets from functioning adequately.

The first vulnerability is the temperature dependence of PMs, which could cause a drift in magnetic field strength as the ambient temperature varies. Annual temperature data from the LHC tunnel [525], which is assumed to behave similarly to the FCC-hh ring tunnel, and PM material data were used to calculate the maximum possible integrated dipole error per cell (see Table 10.13). The magnitude is small enough to be managed using active corrector magnets.

The second vulnerability is PM demagnetisation due to irradiation. Demagnetisation mechanisms are complex, but damage is primarily a function of dose and energy [526], with different levels of PM having different susceptibilities. For this initial assessment, it is assumed that the PM elements of the transfer line receive a uniform dose indirectly (i.e., from the collider beam). Moreover, the direct dose from the transfer line beam is neglected, and it is assumed that there is no realistic failure scenario where the beam could be lost and dumped into the transfer line. This assumption will be reviewed when the details of the machine protection configuration are discussed.

Table 10.13 Permanent magnet temperature dependence parameters with annual LHC tunnel temperature variation

	Unit	SmCo	NdFeB
Temperature dependence	%/°C	0.035	−0.120
Temperature variation (annual)	°C	±0.87	
Integrated dipole field per cell	T m	235	
Correction field magnitude per cell	T m	0.716	2.435

Table 10.14 Radiation dose rate parameters for the assessment of the FCC-hh transfer line magnet

	Unit	Value
Commissioning dose rate	Gy/year	200
Commissioning duration	year	5
Operation dose rate	Gy/year	20
Operations duration	year	35
Total lifetime	year	40
Lifetime dose	kGy	1.7

Table 10.15 Permanent magnet material need and forecast supply

		Unit	
NdFeB global supply	2019	k-tonnes/year	130
	Forecast for 2030	k-tonnes/year	200
Required volume of NdFeB magnet blocks/wedges for concepts	Iron-dominated concept designs	tonnes	950
	Shimmed Halbach concept designs	tonnes	625

Another aspect that will be reviewed in later studies is the possible impact of localised losses occurring in the collider ring, such as the so-called unidentified falling object (UFO) events that have been observed and studied in detail in the LHC (see, e.g., Ref. [527] and references therein for a review of this topic). Losses from these events are typically on the order of 1×10^8 protons. While they could potentially trigger a quench in a superconducting magnet, they may also impact the PMs. This possibility will be investigated further in future studies.

There are significant uncertainties in calculating an estimate for the accumulated lifetime dose. Three key variables are: residual gas density in the collider vacuum tube; longitudinal position (dose rate is higher between collider magnets); and number of years spent in commissioning vs. in operation (dose rate is lower in the latter phase). Using the FCC-hh particle transport simulation studies [528] and taking conservative assumptions, a lifetime dose of 1.7 kGy was calculated (see Table 10.14). For SmCo or NdFeB magnets, this dose should not alter the magnetic field on the axis by more than 1 unit (factor of 10^{-4}) so the transfer line requirements would still be satisfied. In conclusion, whilst radiation damage can be considered a low risk, this assertion will need to be rigorously tested before committing to a PM transfer line design. In addition, a comprehensive literature search will be conducted to understand the resistance of PMs to radiation. Potentially, the FCC will need to conduct its own PM irradiation test campaign.

An additional risk of using a PM design is insufficient supply from manufacturers. For that reason, although they are more sensitive to temperature and less resistant to radiation [529], NdFeB PMs were selected because they are produced at a lower cost and on a larger scale than SmCo PMs [530]. Table 10.15 shows that the forecast global supply of NdFeB should be sufficient to cover the required volume for both PMs concepts. Note that the iron-dominated permanent magnet design has not yet been optimised, so this value represents an upper limit.

Iron-dominated permanent magnet design concepts Iron-dominated permanent accelerator magnets generate a magnetic field using PM elements and function similarly to conventional iron-dominated electromagnets. The iron yoke serves as a low-reluctance path, enhancing magnetic flux density. The pole helps shape the magnetic field distribution within the aperture and can be shimmed to improve field quality. This is particularly beneficial in PM accelerator designs, where magnetisation and assembly errors pose significant challenges. The iron also helps homogenise the magnetic field, mitigating these errors.

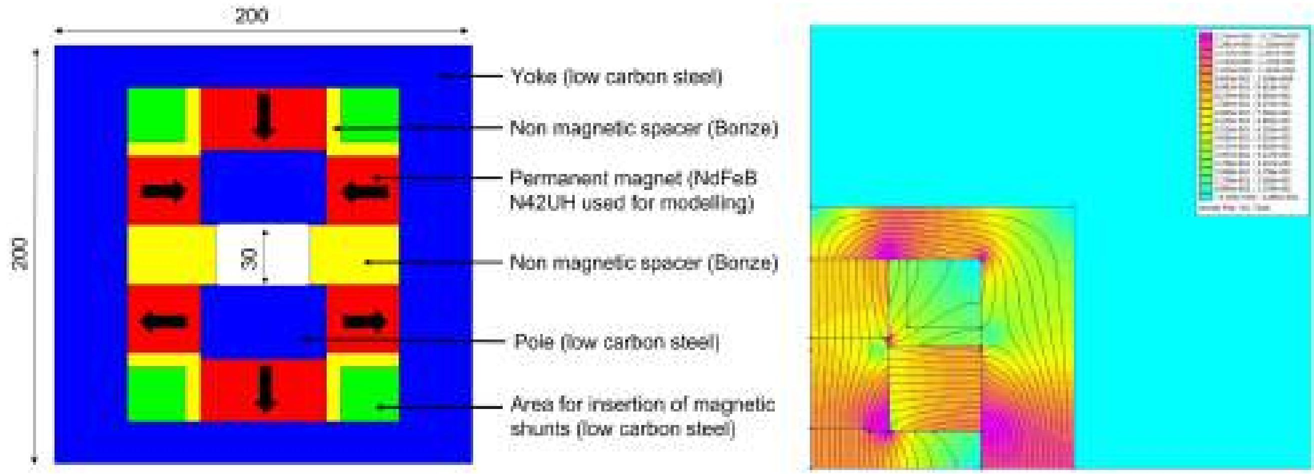

Fig. 10.22 Left: Iron-dominated permanent dipole magnet cross-section. Right: Iron-dominated permanent dipole magnet 2D field distribution (four-fold symmetry)

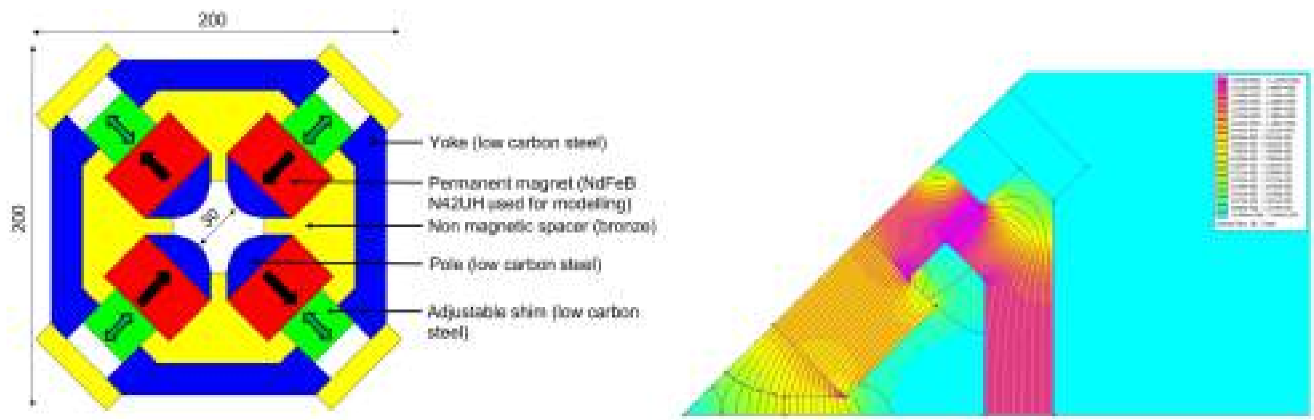

Fig. 10.23 Left: Iron-dominated permanent quadrupole magnet cross-section. Right: Iron-dominated permanent quadrupole magnet cross-section (four-fold symmetry)

The dipole and quadrupole design concepts both feature parallelepiped-shaped PM blocks. These are easier to produce and have better magnetisation direction tolerances compared to other geometries. First, the low-carbon steel yokes and non-magnetic components are assembled, and then the PM blocks are added one by one into the assembly. The blocks are inserted into cavities where some low-carbon steel material is present on either side. This reduces magnetic forces, making the assembly process simpler and faster.

The dipole design concept has an iron length of 1.2 m and an overall cross-section dimension of 0.2×0.2 m, it provides a field of 1 T in the aperture of 30 mm. The field integral can be adjusted by a few percent by inserting magnetic shunts at the magnetic measurement stage, mainly to compensate for irregularities of PM blocks. The dipole magnet cross section is presented in Fig. 10.22 (left), and the 2D magnetic field distribution is shown in the right part of the same figure.

The quadrupole concept design has an iron length of 1.1 m and an overall cross-section dimension of 0.2×0.2 m. The gradient in the aperture diameter of 30 mm can be adjusted from 25–30 T/m using radially adjustable shims. This operation is performed in the magnetic measurement stage. The cross section is presented in Fig. 10.23 (left) and the 2D magnetic-field distribution is shown in the right part of the same figure.

The price of PM material will be a significant factor in the overall accelerator magnet cost. It is, therefore, crucial to minimise the PM volume in each design, first by shimming/narrowing the poles, and secondly by optimising the working point of the PM elements on their magnetic hysteresis curves.

Shimmed Halbach magnet design concepts In Halbach arrays, PM elements are arranged to minimise the magnetic field on one side of the array whilst maximising it on the other. Indeed, cylindrical Halbach arrays are an exceedingly compact configuration of permanent multipole accelerator magnets, i.e., they require minimal PM element volume

Fig. 10.24 Left: Performing rotating coil magnetic field quality measurements on an unshimmed Halbach magnet. Right: Shimmed Halbach magnet. Note the iron shimming rods of varying lengths (black) that have been assembled and glued to the plastic collar (white)

to produce a given field strength over a circular aperture [531]. However, the absence of iron to homogenise the magnetic field means that manufactured Halbach magnets are highly sensitive to PM magnetisation and assembly errors. Consequently, significant resources are typically invested in the manufacture and assembly of Halbach accelerator magnets to ensure satisfactory field qualities. This can include a range of measures: first, it requires extensive quality assurance, measuring the magnetic field of PM wedges (either individually or as a representative sample). Second, it may be necessary to match problematic PM wedges around the circumference of the cylinder to partially cancel field errors [531]. Finally, when assembling PM wedges, a mechanical structure may be needed to guide them in position; or mechanical shims might be used for small adjustments [532]. Both of these options reduce the PM packing factor, which affects magnetic performance. Even with these expensive mitigation measures, the field quality that can realistically be achieved is limited. Based on CERN experience building Halbach accelerator magnets, it is anticipated that a standard design would not satisfy the current FCC-hh transfer line requirements for field uniformity of about ± 2 units.

Fortunately, cylindrical Halbach accelerator magnets can be shimmed to substantially decrease harmonic field errors. This technique was successfully developed and implemented in the CBETA 500 MeV electron energy recovery linac at Cornell University [533]. Initially, conventional Halbach magnets were manufactured with a slightly increased bore size to accommodate the shim assembly. Following that, standard rotating coil measurements are used to evaluate the magnetic field error harmonics (see Fig. 10.24 (left)).

An automated code was subsequently developed to optimise the distribution of magnetic shims around the bore circumference. These shims become magnetised, functioning as small dipole sources. Finally, the optimisation code determines the required length for each iron shimming rod before insertion into the magnetically transparent collar (see Fig. 10.24 (right)).

Working with suppliers to create suitable processes, the CBETA team produced an initial production run of 216 magnets. Initially, the magnets had a relative field error of 18.2 units on average, which decreased to 2.2 units after shimming. This gives confidence that by making the manufacturing tolerances less stringent during the initial build phase, the overall cost of production can be reduced without impacting the quality of the magnetic field [533] (see Fig. 10.25).

Figure 10.26 shows a cross section of the cylindrical FCC-hh transfer line Halbach dipole and quadrupole magnet concepts, respectively. Note that the inner bores of the magnets have been increased beyond what is required for the beam pipe to accommodate the shim assembly. The designs demonstrate that the required field strengths can be achieved using sensible PM wedge geometries and volumes. However, it is more challenging to determine what level of field quality can realistically be achieved because this is a function of manufacturing tolerances that are not yet known. Currently, extrapolating from the initial production run of CBETA indicates that the FCC-hh field quality requirements can be met. More research and development will be needed to confirm this statement. There are two main avenues of investigation that need not be mutually exclusive. A prototyping campaign would have the joint benefits of expanding knowledge of manufacturing processes and tolerances in the real world. Alternatively, stochastic modelling tools could be used to assess the sensitivity of the unshimmed Halbach field quality to different manufacturing tolerances, including PM wedge magnetisation magnitude/directional errors and wedge

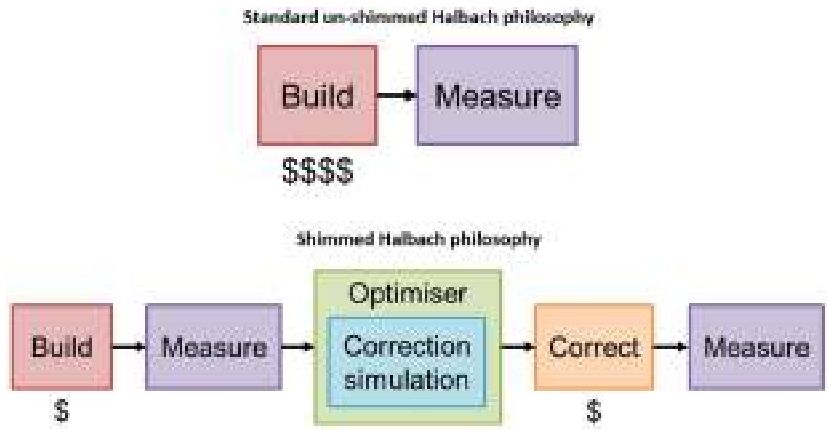

Fig. 10.25 Flow chart describing the production of conventional and shimmed cylindrical Halbach magnets, respectively

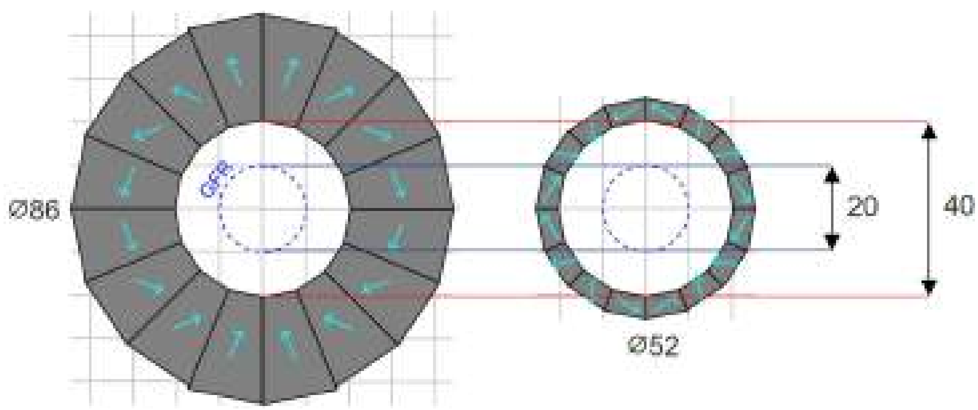

Fig. 10.26 Halbach dipole (left) and quadrupole (right) for the FCC-hh transfer line magnet concepts

radial/azimuthal positional errors. For example, the ROXIE 2D magnetic modelling package [534] has a tool to perform randomised error studies. It is primarily used to investigate the effect of varying the azimuthal position of conductors in superconducting magnets but could also be used to study a range of Halbach parameters.

Conclusions on FCC-hh transfer line magnets and future work An initial assessment resulted in three viable candidate magnet concepts. The next phase of investigation will develop these designs to a level where the most suitable can be evaluated. Given the large scale of FCC-hh compared to existing accelerators, a significant focus of this work will be on manufacturing and assembly challenges.

Obtaining accurate lifetime cost estimates will be key to making an informed choice. Currently, there are too many uncertainties to perform reliable calculations. However, it is still useful to begin considering how the contribution of different capital and overhead costs will affect the final total, which is qualitatively shown in Fig. 10.27. Although it should not be used as a tool to evaluate each concept, this information is useful to compare costs within each category.

A permanent magnet research and development programme has the potential for significant benefits for accelerator engineering and beyond. Collaboration agreements can also accelerate progress, with different partners contributing various expertise and capabilities. Collaborators at other research institutes could offer valuable contributions to the electromagnetic design of accelerator magnets. Meanwhile, private-sector manufacturers are well-placed to develop new industrial-scale production processes.

Integration of the transfer lines in the FCC-hh tunnel was studied, considering the various options for the magnet design. The result of these studies is shown in Fig. 10.28, where the normal-conducting (left) and PM (right) solutions are presented. In both cases, the nominal tunnel size does not need to be increased to allow the installation of the transfer lines. However, it is evident how the smaller size of the cross-section of the PMs renders this concept highly interesting, also with regard to integration.

10.4 High-field magnets

The following is organised in four sections. Section 10.4.1 provides an update to the baseline magnet parameters for FCC-hh dipoles, and outlines the changes with respect to the 2019 conceptual design report. Section 10.4.2

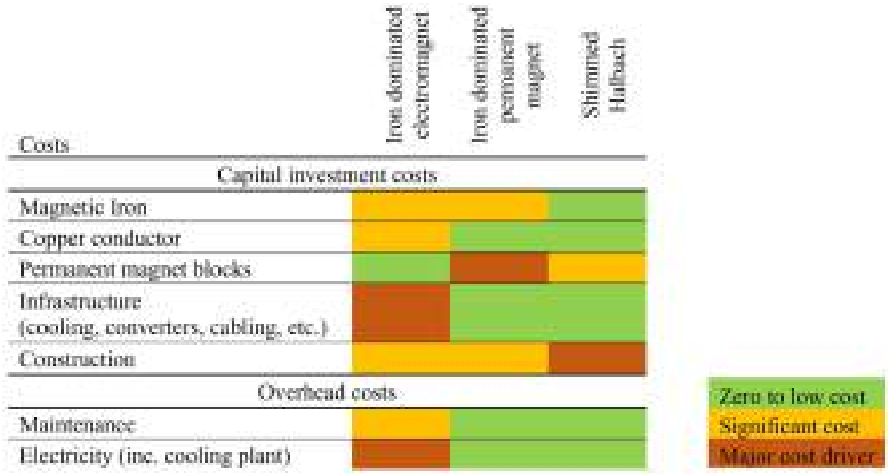

Fig. 10.27 Qualitative considerations on the magnet costs for the various concepts considered

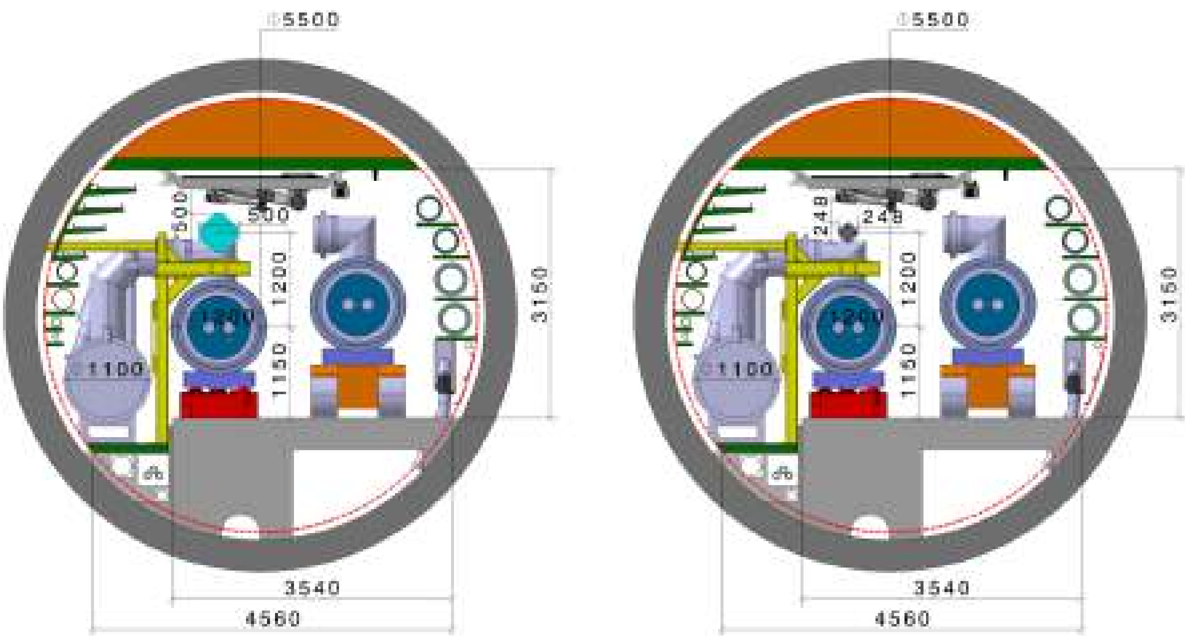

Fig. 10.28 Cross-section of the FCC-hh ring tunnel with a sketch of the integration of the transfer lines for the two options under study, namely with normal conducting magnets (left) and permanent magnets (right). Integration of the transfer lines into the ring tunnel does not require any increase in the tunnel cross-section

mentions alternative choices for the magnet system and how they would affect other accelerator subsystems; Sect. 10.4.3 presents design options that will validate key magnet parameters, places them in the context of past and present projects, and provides key figures for a block-coil design; finally, opportunities and challenges of HTS options for FCC-hh dipole magnets are discussed in Sect. 10.4.4. Considerations of cost and timeline are not given here, but will be addressed by FCC and the HFM Programme in the input to the update of the European Strategy for Particle Physics.

10.4.1 Baseline with Nb_3Sn magnets

Evolution of main parameters The main parameters of the FCC-hh with Nb_3Sn main dipoles and its evolution with respect to the design report [10] is given in Table 10.16. As discussed in Sect. 10.2.1, from the point of view of the conceptual layout and optics, the main change is the 7% reduction of the accelerator circumference, from 97.76 km to 90.66 km. The relevant parameter for the energy reach, i.e., the length of the arcs, is reduced by 5%. However, an iteration on the optics layout, thanks in particular to the use of longer cells, allows for an increase of the arc filling factor by 4% from 0.80 to 0.83 [517].

Table 10.16 Parameters of the FCC-hh lattice, 2019 and 2025 values

Parameter	Unit	CDR 2019	2025 Nb_3Sn
Dipole field	(T)	16.0	14.0
Dipole aperture	(mm)	50	50
Dipole magnetic length	(m)	14.3	14.3
Operational temperature	(K)	1.9	1.9
Tunnel length	(km)	97.76	90.66
Arc length	(km)	81.0	76.9
Arc filling factor	-	0.80	0.83
C.m. energy	(TeV)	50 + 50	42.5 + 42.5
Loadline fraction	-	0.86	0.80
jc at 16 T and 4.2 K	(A/mm^2)	1500	1200
Number of dipoles	-	4587	4463
Number of quadrupoles	-	760	520

For the magnet baseline parameters, the main change is the reduction of the operational field from 16 T [535] to 14 T [536]. This choice enables the following accompanying measures, which together provide a consistent baseline with high confidence level based on HL-LHC experience:

- An increased margin for magnet operation: the loadline fraction (nominal current divided by maximum theoretical current) is decreased from 86% [535] (the same value as for the LHC Nb-Ti dipoles at 7 TeV [537, 538], but considered risky for the production of more than 4000 Nb_3Sn dipoles) to 80% (2% above the baseline for the HL-LHC Nb_3Sn triplet). A discussion of the margins associated to this loadline fraction is given in Sect. 10.4.1;
- It is assumed that the conductor critical non-copper current density required to produce 14 T at 80% loadline fraction can be attained with the best Nb_3Sn conductor available today, corresponding to 1200 A/mm^2 at 16 T, 4.22 K; see Sect. 10.4.2 for the fit and expected values at other fields and temperatures. The target defined for an FCC-hh conductor in 2015 of 1500 A/mm^2 at 16 T, 4.22 K [539] has been achieved and exceeded in laboratory samples. Development of usable wires for magnets, based on this technology, is under way, but efforts have not yet started to industrialise the technology.
- EuroCirCol studies showed that the design of 16 T magnets is marginal with respect to the target of maximum 200 MPa of stress in the coil [535];[31] for a classical magnet design, the 12.5% reduction in field from 16 T to 14 T corresponds to a 25% reduction in stress, and therefore the 14 T magnet design can satisfy a condition of maximum stress of 150 MPa, which is more appropriate for a large scale production.

Other relevant parameters such as operational temperature, aperture, inter-beam distance, maximum size of the magnet, are unchanged. With the reduction of the magnetic field and of the arc length, and the increase of the arc filling factor, the centre of mass (c.m.) energy is 84.6 TeV.

Filling factor, cell quadrupoles Cell quadrupoles in the LHC lattice have a magnetic length of 3.15 m, and a gradient of 220 T/m, thus providing ∼700 T of integrated gradient [537]. The cell contains six dipoles, whose magnetic length is 14.3 m, and total cell length is 107 m: the ratio between total magnetic length of the dipoles and cell length is the filling factor of the arc: $14.3 \times 6/107 = 0.80$. The remaining 20% is left for interconnections and spool pieces (occupying 1.35 m for each dipole, i.e., about 10%), cell quadrupoles (5.9%) and other magnets.

For the FCC-hh, the seven-fold increase in energy compared with the LHC would require a seven times larger integrated gradient, i.e., ∼5000 T, and, using the same technology and cell layout, one would need 22.5-m-long quadrupoles occupying nearly 50% of the arcs. To avoid this adverse effect on the filling factor, one has to choose longer cells; this makes not only more space for dipoles because quadrupoles are more spaced, but also shortens the quadrupoles since the integrated gradient is inversely proportional to the cell length [536].

In the first version of the FCC-hh optics the number of dipoles per cell has been doubled w.r.t. the LHC from six to twelve, with a total cell length of 210 m [10]. A recent further step brought the number of dipoles to 16, with a total cell length of 276 m [540]: the 1600 T of integrated gradient can be achieved by 4.2-m-long quadrupoles giving 375 T/m [10], occupying 3% of the cell. In this way the filling factor is increased to 0.83, and the resulting energy with 14 T dipoles is 85 TeV COM; see Table 10.16, fourth column. Further optimisations could give filling

[31] Note that the peak stress in the magnet coil is not a direct observable of the magnet; here, as in all the previous literature, peak stresses in the finite element model are referred to, with some assumptions on magnet preload, etc.

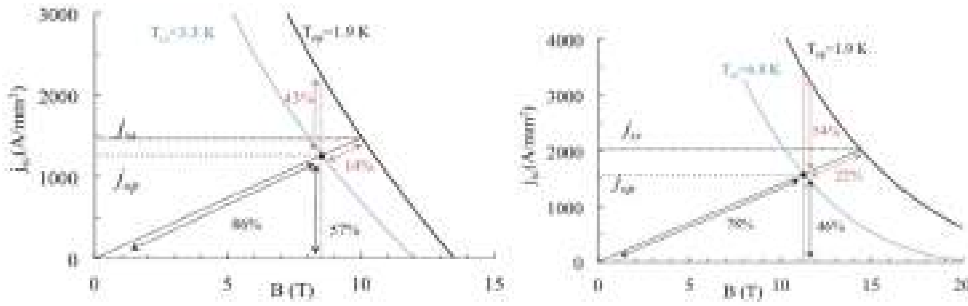

Fig. 10.29 Margins for Nb-Ti LHC dipoles at 7 TeV and 1.9 K (left) and for the HL-LHC quadrupoles at 7 TeV and 1.9 K (right)

factors up to 0.87, thus reaching 90 TeV; this can be considered an upper limit, since the assumption for the distance between the magnetic lengths of two consecutive dipoles is 1.5 m (10% larger than in the LHC, requiring more massive end supports for the coil ends of 14 T magnets) and it appears difficult to reduce.

Injection energy and magnet aperture A possible FCC-hh injection energy is 3.3 TeV as in the Conceptual Design Report [10]; this gives an energy increase by a factor 14.2 between injection and collision energy, slightly smaller than in the LHC, where this factor is 15.6. The larger injection energy compensates for the larger beta functions due to the longer cell length, and facilitates fitting the beam within a 50 mm aperture, and leaving space for a beam screen to intercept the synchrotron radiation.[32] Since the beam size is proportional to the square root of cell length divided by the injection energy, compared to the LHC injection, the beam size in the FCC is reduced by 30%. Differently the LHC dipoles, thanks for the much larger bending radius, the FCC-hh dipoles do not require a curved geometry since the aperture gain would be negligible (of the order of 1 mm). Protons at 3.3 TeV for injection into the FCC-hh could be provided either from a modified LHC or from a new 4 T machine in the LHC tunnel.

Alternative FCC-hh injector options with 1.75 TeV and 1.3 TeV injection energy based on a superferric ring in the LHC tunnel or a faster cycling superconducting machine in the SPS tunnel are also being considered [10, Chap. 6.4]. However, these would pose major challenges for the accelerator and magnet systems, with an unprecedented energy increase for a high-energy hadron collider (factors of 25 or 33 from injection to top energy, respectively, to be compared with a record energy swing by a factor of 23 for the HERA proton ring), which would require a renegotiation of requirements on the control of field quality and magnet reproducibility at injection. Moreover, these could also require a larger magnet aperture (thus increasing the mass of the conductor), or a shorter cell length (thus reducing the filling factor and the energy reach). Further studies are needed to converge on the choice of the optimum injector for the FCC-ee.

Main dipole margins The short sample condition is defined as the combination of the peak field in the coil and the current density in the superconductor that corresponds to the measured critical surface of a strand short sample at the operational temperature: this is the maximum theoretical field achievable in the magnet. Superconducting magnets operate at a fraction of this value, called *loadline fraction*. The loadline margin is defined as one minus the loadline fraction. The *current fraction* is the ratio between the maximum theoretical current that can be carried at the operational field and the operational current. The current sharing temperature is the temperature where the pair of nominal field and current density lie on the critical surface. The *temperature margin* is the difference between the current sharing temperature and the operational temperature.

Figure 10.29 presents a visualisation of these margins for (HL-)LHC magnets based on two different types of Low Temperature Superconductor (LTS), namely for the LHC arc dipoles operating at 7 TeV, and for the HL-LHC triplet quadrupoles at 7 TeV. LHC Nb-Ti dipoles have 14% loadline margin, 43% current margin and 1.3 K temperature margin [537, 538, 541]. The HL-LHC Nb_3Sn quadrupole production is proving that a 22% loadline margin can be achieved systematically, with very limited training and no retraining after a thermal cycle [542, 543]; the current margin is 54%, and the temperature margin is 4.9 K, i.e., about three times larger than in the LHC dipoles. All quadrupoles systematically reach operational current at 4.5 K, thus proving the existence of a temperature margin larger than 2.6 K.

Margins for the 2019 and 2025 baseline for the FCC-hh dipoles are shown in Fig. 10.30. The 2025 baseline for FCC-hh guarantees a 4.6 K temperature margin, cf. the previous value of 3.3 K, and a 60% current margin. Margins for the 2019 and 2025 FCC-hh Nb_3Sn dipoles are compared with those for the LHC Nb-Ti arc dipoles and for the HL-LHC Nb_3Sn triplet magnets in Table 10.17.

[32] Note that the beam screen presented in the baseline [10] corresponds to 100 TeV c.m. energy, with double the synchrotron radiation at 85 TeV.

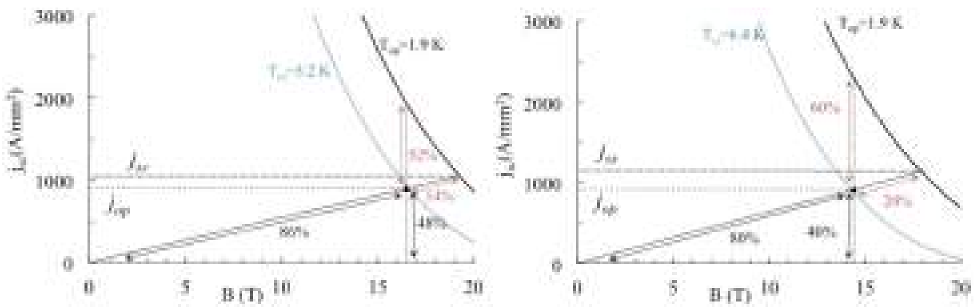

Fig. 10.30 Margins for FCC-hh Nb_3Sn dipoles at 1.9 K: baseline of 2019 (left) and of 2025 (right)

Table 10.17 Margins for LHC dipoles at 7.0 TeV, HL-LHC triplet, FCC-hh dipoles, all operating at 1.9 K

	Energy (TeV)	Bore field (T)	Peak field (T)	Loadline margin (%)	Current margin (%)	Temperature margin (K)
LHC dipole	7.0	8.3	8.7	14%	43%	1.3
HL-LHC triplet	7.0	9.9†	11.3	22%	54%	4.9
FCC-hh dipole 2019	50	16	16.5	14%	52%	3.3
FCC-hh dipole 2025	42.5	14	14.5	20%	60%	4.5

† The quadrupole gradient times the aperture radius is given here.

Hypothesis on hysteresis losses In the case of the FCC-hh Nb_3Sn dipoles, the main source of the so-called AC losses are the hysteresis losses due to the magnetisation of the superconductor (also called persistent currents); they are peculiar to superconductors, and they are proportional to the filament size. The energy dissipated over a full cycle is independent of the ramp rate, and therefore the power losses scale with the ramp rate $\mathrm{d}B/\mathrm{d}t$. Note that other sources of AC losses as currents induced in loops that are partially resistive through the inter-strand resistance in cables, or the inter-filament resistance are proportional to $\mathrm{d}^2B/\mathrm{d}t^2$. Losses are dissipated in the magnet coil during the ramp, and the cryogenic power needed to deal with them is related to the magnet temperature: higher operational temperatures imply lower power consumption for cryogenics. On the other hand, the magnet temperature has little influence on the power needed to deal with synchrotron radiation, since this is intercepted on the beam screen at or above 50 K; see Table 10.20.

For the FCC-hh magnet, a target of 5 kJ/m over the ramp (i.e., 10 kJ/m for the complete cycle) has been set in the CDR [10]. With the present status of technology for Nb_3Sn conductors, having filaments of the order of 50 µm, Nb_3Sn dipoles at 14 T have about twice this, i.e., 20 kJ/m for the full cycle [544]. Several paths are possible to close this gap between targets and technology:

- Reducing the filament size; the drawback in this option is that it requires R&D on the conductor. The need was identified [539, 545] and attempts in this direction were carried out. The resulting technology should clearly not increase cost or decrease critical current, which is not granted;
- Using artificial pinning centre (APC) technology [546], that gives lower critical current density at low field, and therefore lower hysteresis losses, satisfies the 10 kJ/m target. APC also have the potential of giving larger current densities in the 14 T-18 T range, see next section;
- Increasing the cooling power of the cryogenic system, that only has to absorb these losses during the ramp;
- Provide additional temperature margins so the magnet cold mass can buffer the energy deposited during the ramp; superfluid helium in the cold mass plays an important role in the buffering mechanism;
- Doubling the ramping time, with a corresponding reduction of the integrated luminosity.

10.4.2 Alternative choices for the LTS magnet system

Several alternative choices and how they would impact other accelerator subsystems are described below. They are: (i) operation at 4.5 K, (ii) a combined function lattice, (iii) longer dipoles and (iv) a lower operational field of 12 T. More design options that meet the above baseline parameters and do not affect other accelerator subsystems are discussed in Sect. 10.4.3.

4.5 K operation The data of HL-LHC Nb_3Sn quadrupole magnets shows that they can all operate at 4.5 K [542, 543]. Moreover, instabilities limiting performance are more severe at 1.9 K than at 4.5 K. This could open

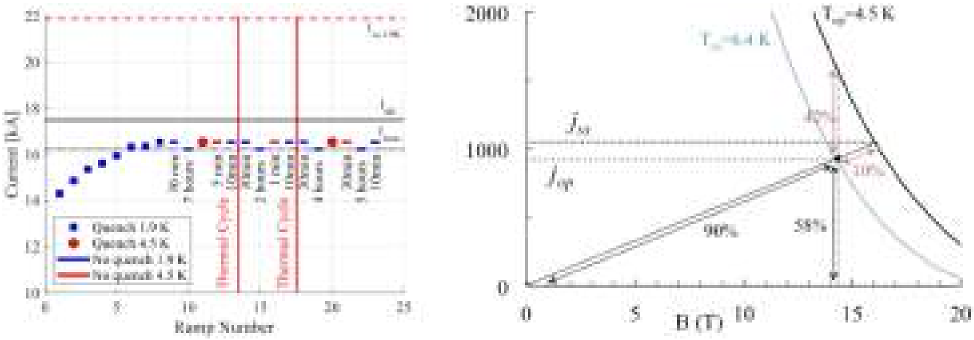

Fig. 10.31 A typical HL-LHC Nb_3Sn quadrupole magnet training, reaching nominal current also at 4.5 K (left) and margins for an option of FCC-hh Nb_3Sn dipoles designed for 1.9 K operating at 4.5 K (right)

the possibility of operating at 4.5 K. Keeping the same magnets with 20% loadline margin at 1.9 K would imply a reduced loadline margin of 10% at 4.5 K, and a current density margin of 42% and a temperature margin of 1.9 K; see Fig. 10.31. Even though the HL-LHC magnets are routinely reaching this condition in individual tests, this baseline for the FCC-hh appears promising but extremely daring, given that the magnet system must also be robust against beam-induced effects that may be more severe than in the LHC due to the increased beam energy. The 4.5 K option is under study, and would present the following advantages: (i) Reduced complexity of the cryogenic system and its cost; (ii) Reduction of the cryogenic power to remove heat from the cold mass of a factor two to three; since about half of the heat has to be removed from the cold mass (the other half on the beam screen), this would imply a reduction of the cryogenic power by 30%.

The 4.5 K option could rely on dry magnets (cold mass not filled with liquid helium (LHe)); this would reduce the He inventory; however, it would imply challenges to magnet cooling during the ramp, and to magnet insulation (LHe is a much more reliable insulator than vacuum because the Paschen effect in residual gas could lead to a dielectric breakdown during a quench). To prove the viability of this option it is necessary to develop a baseline for the cooling at 4.5 K, and determine whether the theoretical temperature margin of ∼2 K and ∼40% in current density is sufficient to operate the ∼4400 magnets in the FCC, or whether to increase the margins. Note that in case of a 4.5 K baseline it is quite probable that all magnets should be individually tested at 1.9 K before installation, since training is much faster at 1.9 K, because during training at 4.5 K performance plateaus (that can be overcome at 1.9 K) may appear.

Combined function lattice A combined function lattice relies on removing the main quadrupoles and having a systematic quadrupole component (b_2) in the dipoles. This layout reduces the flexibility of operation, but it is used in some low-energy accelerators. The main advantage is to remove the need for two families of quadrupole magnets, even if their number (500) is fairly moderate with respect to that of the dipoles. The combined function lattice implies more stringent requirements on dipole alignment, since it contains the quadrupolar component; the option was considered, but eventually discarded for the LHC [547]. If the conductor peak field is kept constant, the combined function option would allow a further increase in beam energy of approximately 0.5%. The reason is that the larger filling factor would be partially compensated by the need to lower the main dipole field because part of the peak field would be created by the quadrupolar component [548].

20 m long magnets In the late 2000s, the US LARP programme achieved the scaling of a Nb_3Sn quadrupole from 1.5 m to 3.4 m long magnets [549]; HL-LHC quadrupoles at CERN prove the scaling to 7.5 m [543]. Scaling in length of FCC-hh dipoles is currently planned in two steps, first to 5 m (with the possibility of vertical testing of the magnet) and a second to 14.3 m.

The limit in magnetic length for LHC and FCC of 14.3 m is related to the European Union regulations for standard transport. For the SSC project, 17.5 m-long Nb-Ti dipoles were planned for the lattice and 15 were built and reached requirements [550]. Having 20 m-long magnets would have three positive consequences:

- A reduction of the total number of magnets to manufacture from ∼4400 to ∼3200 units, with, possibly, a 30% shorter production (about two years), or 30% fewer production lines (see Table 10.16);
- A reduction of the magnet cost; assuming 25% of the total cost is due to manufacturing and a reduction of 30% in the magnet number, the total cost of the dipoles would be reduced by 8%;
- An increase of the filling factor of 3.5%, either used to increase the energy to 88 TeV COM, or to reduce the dipole cost (via a 0.5 T field reduction and less conductor).

In case this route is further pursued, detailed studies are required to assess the impact of 20 m long magnets on several other areas, such as transport and integration.

Table 10.18 Assumptions for critical current density of Nb_3Sn superconductor

Critical current density in superconductor (A/mm^2)	12 T	15 T	18 T
1.9 K	3655	2170	1185
4.22 K	2800	1515	705

12 T magnets A layout based on a 12 T operational field would provide 73 TeV COM energy, with the same hypothesis on the filling factor as in the baseline shown in Table 10.16. Using the same loadline margin as for the 14 T baseline, 12 T dipoles would have a similar current and temperature margin, but require 30% less conductor. 12 T dipole short models are planned in the HFM programme, manufactured by INFN [551], as well as at CERN and PSI.

10.4.3 Nb_3Sn dipole designs

Requirements Based on the experience of the HL-LHC triplet quadrupole magnets, the following targets have been set:

- *Field*: To provide an operational field in the aperture of 14 T, short models must be able to systematically reach 15 T (so-called ultimate field). For the operational field of 12 T, an ultimate field of at least 13 T is required.[33]
- *Loadline and temperature margin*: The dipoles operated at 1.9 K should provide a loadline margin of at least 20%, and a temperature margin larger than 2.6 K at operational field to reach operational field also at 4.5 K.
- *Mechanics*: The structure must be able to withstand forces corresponding to the ultimate field. The coil, in the case of a design including a coil preload, must be not in tension at nominal field.[34] The target maximum stress must not exceed 150 MPa in all phases (assembly, cool-down, and powering to nominal).
- *Protection*: the hotspot temperature for the protection system in the nominal scenario (without failures) must not exceed ∼270 K. The system should guarantee a maximum hotspot temperature of 350 K in case of realistic and conservative failure scenarios.

Conductor properties The parametrisation used for the Nb_3Sn conductor is the following

$$J_{\mathrm{sc}}(T,B)=\frac{C_0}{B}\left(1-\left[\frac{T}{T_{\mathrm{c0}}}\right]^{1.52}\right)^{0.96}\left(1-\left[\frac{T}{T_{\mathrm{c0}}}\right]^{2}\right)^{0.96}\left(\frac{B}{B_{\mathrm{c20}}\left(1-[T/T_{\mathrm{c0}}]^{1.52}\right)}\right)^{2.5} \tag{10.1}$$

with $T_{\mathrm{c0}} = 16$ K, $B_{\mathrm{c20}} = 29.38$ T, and C_0 is the variable parameter to scale the conductor performance: $C_0 = 214\,000$ AT/mm^2 for the improved HL-LHC considered as the baseline. The specification for HL-LHC has been given at 12 T and at 15 T. For an FCC-hh dipole at 14 T, specifications should be given at 15 T and at 18 T (at 0.5 T larger than peak field in operational condition and at short sample field, respectively). The critical current densities at different fields and temperatures are given in Table 10.18.

Quantity of conductor The driving term of the magnet cost is the quantity of conductor: it accounts for about one third of the cost for the LHC dipoles, and half of the cost for the HL-LHC magnets. The quantity of conductor is parametrised via the equivalent coil width w_{eq}, i.e., the width of the 60° sector coil having the same surface area as the insulated coil, see Fig. 10.32, left. This quantity has the advantage of being related to the field and to the current density via the approximated expression

$$B\ [\mathrm{T}] \approx 0.007 J\ [\mathrm{A/mm^2}] w_{\mathrm{eq}}\ [\mathrm{mm}]. \tag{10.2}$$

The volume of the insulated conductor is given by

$$V \approx \frac{4\pi l_{\mathrm{m}}}{3}\left[(r+w_{\mathrm{eq}})^2 - r^2\right] = \frac{4\pi l_{\mathrm{m}}}{3}\left[2rw_{\mathrm{eq}} + w_{\mathrm{eq}}^2\right] \tag{10.3}$$

[33]Note that LHC dipoles, operating at 8.1 T in the LHC at an equivalent energy of 6.8 TeV, had short models systematically reaching 9.5 T.

[34]Note that this is a less stringent requirement than previously used (10 MPa of compression at nominal or at ultimate field); this is justified on the grounds that many experimental data show that partial unloading does not prevent reaching nominal field.

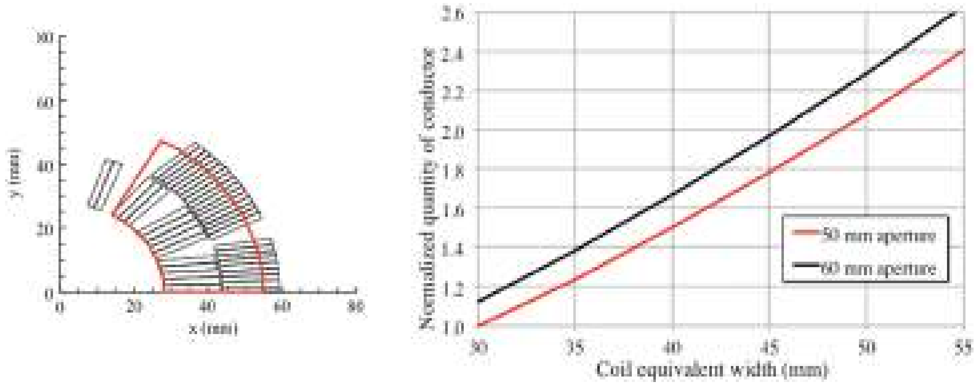

Fig. 10.32 Coil layout for the LHC dipole, and equivalent coil width (width of the red sector, left) and quantity of conductor versus equivalent coil width (right)

where l_m is the magnet length, and r is the magnet aperture radius (see also Fig. 10.32, right). For FCC-hh, a coil width of up to 55 mm is considered, thus giving a quantity of conductor 2.5 times larger than in the LHC dipoles.

Previous achievements in bore field Nb_3Sn accelerator dipole models have been developed since the late 80's. A short summary of the achievements is given below. All cases refer to 1 to 2 m long magnets (usually called short models), except for the HL LHC magnets (11 T dipoles and final triplet quadrupole).

In 1990 the CERN-Elin dipole reached 9.5 T at 4.3 K in a 50 mm aperture, with a two-layer coil based on $\cos(\theta)$ geometry and grading [540]. This option was not retained for the LHC due to the higher cost with respect to the Nb-Ti option at 1.9 K and the complexity of the technology.

In the 1990s the MSUT dipole reached 11.3 T at 4.5 K in a 50 mm aperture, with a two-layer coil based on $\cos(\theta)$ geometry and grading [552]. The magnet was tested again in 2020 at 1.9 K, achieving the power converter limit (11.8 T bore field).

In the 1990s the D20 LBNL dipole reached 13.4 T at 1.9 K in a 50 mm aperture, with a four-layer coil based on $\cos(\theta)$ geometry and strong grading [553, 554].

In the 2000s the HD2 LBNL dipole reached 13.8 T at 4.5 K, with a novel coil configuration based on a two-layer block design. Unlike to previous models, which all had an aperture of 50 mm, this magnet has a free bore of 36/43 mm diameter [555].

In the second half of the 2010s, the Fresca2 CERN-CEA dipole reached 14.6 T at 1.9 K, with a coil configuration based on a four-layer block design. This magnet, conceived as a cable test station operating at 13 T, has a free bore of 100 mm diameter [556, 557]. All of its features conform to accelerator requirements, except for the very large coil width (80 mm, see Fig. 10.33) that makes it unaffordable.

In the second half of the 2010s, some 11 T dipoles short models reached 12.0 T [558, 559] both at CERN and in FNAL in a 60 mm aperture at 1.9 K.[35] Note that the coil has the same width as the LHC dipoles, and therefore the higher field is obtained by higher current density (540 A/mm^2 rather than 360/440 A/mm^2 at nominal current), see Fig. 10.33. The scaling to 5 m showed degradation of performance after thermal cycles in the long magnets; nevertheless, the programme achieved two significant results: (i) the first double aperture Nb_3Sn dipole magnet, fully compatible with machine operation and (ii) the first scaling of Nb_3Sn coils to 5 m lengths, reaching a bore field above 11 T.

In the second half of the 2010s, MDPCT1 dipole reached 14.5 T at 1.9 K in a 60 mm aperture. This magnet, made at FNAL, is a four-layer $\cos(\theta)$ dipole with grading. This is the first dipole to reach fields above 14 T at 4.5 K [560], and also the first to reach more than 14 T with a coil width of the order of 50 mm (as compared to 80 mm of Fresca2). After reassembly and after a thermal cycle the performance degraded irreversibly by more than 10% [560].

Since 2015, the HL-LHC interaction region triplet quadrupoles [542, 543, 561] showed very good reproducibility of performance (11.3 T peak field in nominal conditions), nominal currents were also achieved at 4.5 K in all models, 13 T was achieved in many short models, scaling to 7.15 m lengths, and there was no degradation of performance after thermal cycle. The project is halfway through production at the moment of writing.

Magnet designs: $\cos(\theta)$*, block coil, common coil* As shown during the EuroCirCol studies [535], the target magnetic field can be achieved with different designs, each one presenting opportunities and challenges. The more classical way is to follow the $\cos(\theta)$ configuration; a two-layer design can give 12 T dipoles [551] with a coil width of the order of 35-40 mm, and a third and fourth layer are needed to reach 14 T operational fields as in MDPCT1. The

[35] Note the possible confusion between the magnet name (11 T) and the maximum achieved field (12.0 T).

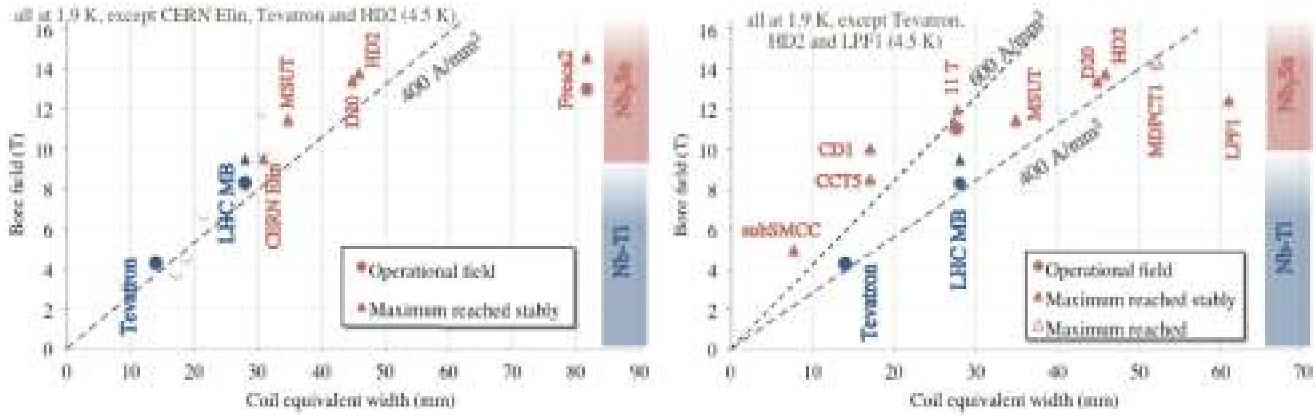

Fig. 10.33 Operational and achieved field versus coil width in LHC and Tevatron colliders, and in Nb_3Sn short models (left), and 11 T, MDPCT1 dipoles, and in common coil and CCT demonstrators (right)

Fig. 10.34 Conceptual design of 14 T and 12 T magnets: BOND (left), FalconD (centre left), SMACC1 (centre right), F2D2 (right)

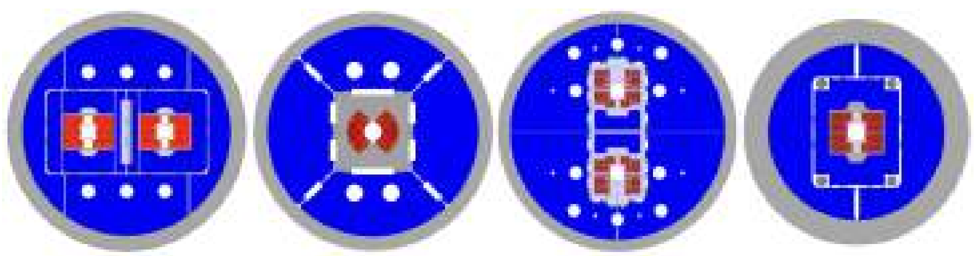

first option is being developed in INFN and at CERN (FalconD) and a proposal for a four layer coil was put forward by INFN for EuroCirCol [562].

The design based on block coils holds the record in field today and therefore is a natural alternative to the cos(θ) design. This option is being pursued by CERN, with a two-layer coil and a 25 mm wide cable (BOND [563]), and by CEA-Saclay with a four-layer coil including grading (F2D2 [564]) and an intermediary step with flat racetrack coils (R2D2 [565]). As an example, the cross-section and the main parameters of the BOND magnet are given in Fig. 10.34 and Table 10.19. The coil width, as for other designs, is of the order of 50-55 mm. This is a first list of parameters of a design that could be further optimised to reduce the conductor mass.

The main differences with respect to the designs presented in 2019 [535], are (i) 20% lower stored energy due to the lower field, (ii) a maximum hotspot temperature of 270 K in case of a quench with nominal protection, and (iii) a coil stress below 150 MPa. The conductor mass is 10% lower, and current densities of the 2025 baseline are very similar to the current densities of the 2019 baseline in the inner layer (all 2019 designs use grading).

A third option is the common coil design, which is an intrinsically double aperture magnet, based on racetrack coils plus non-planar correction coils; the idea has been proposed in the 90's [566], and today is the design that has been adopted for the Chinese SppC dipole. In 2022, IHEP built a hybrid Nb_3Sn/Nb-Ti technology demonstrator magnet called LFP1-U that reached 12.5 T in two small 14 mm diameter apertures [567], and 90% of short sample at 4.5 K; see Fig. 10.33. The next step for IHEP is LFP3, aiming to produce 16 T, with 13 T obtained from Nb_3Sn plus 3 T from HTS [568]. The common coil path is being followed by CIEMAT, aiming at a 14 T operational field with Nb_3Sn, based on a common coil design in a 50 mm aperture ([569] and DAISY design [570]. Recently, the PSI team has made a significant improvement in the design, finding an asymmetric configuration of the coil that allows having planar correction coils of the same type as the common coils [571]. This design will be applied to CIEMAT magnets.

Magnet designs based on stress management A stress managed magnet [572] design can be defined as a design where the supporting structure is not external, as in the cos(θ) layout, or external and internal, as in the block and common coil designs, but it is spread within the coil as a metallic winding former. The advantage is twofold: (i) the structure can intercept forces and avoid stress accumulation and (ii) the winding former acts as a winding, reaction and impregnation tooling, thus, accelerating manufacturing processes. This can allow the use of higher current densities in the windings, though this advantage is compensated by the winding former, which dilutes the effective current density. A disadvantage could be that after epoxy impregnation, bonded interfaces are loaded in tension and may break, leading to long training. Alternatives to epoxy impregnation are being studied.

Table 10.19 Parameters for possible designs of 12 T and 14 T, scaled to 14.3 m magnetic length

		FalconD	SMACC1	BOND	F2D2	DAISY
Coil type		$\cos(\theta)$	Stress-Managed Common Coil	Block Coil	Block Coil Graded	Common Coil
Field	(T)	12	12	14	14	14
Current	(kA)	19.9	12.7	19.3	9.2	15.4
Peak field	(T)	12.5	12.6	14.8	14.6	14.6
Loadline margin	(%)	25	23	18	24	19
Equivalent coil width	(mm)	37.4	20.1 + 19.1	53.4	23.9 + 27.5	31.7 + 23.0
J overall	(A/mm^2)	418	411/603	348	299/438	326/346
J superconductor	(A/mm^2)	1204	1205/2129	967	875/1968	933/982
J copper	(A/mm^2)	1337	1339/1774	1074	973/1093	1037/909
Stored energy†	(MJ)	15.5	22.9	29.5	30.0	31.9
Inductance†	(mH)	64	266	146	692	252
Coil energy density	(J/mm^3)	0.079	0.109	0.089	0.098	0.079

† FalconD & F2D2 designs are single aperture; here stored energy and inductance are scaled to two apertures.

Stress-managed structures may be the only way to reliably reach fields above 15 T. The US-MDP research programme is strongly investing in this direction [573–575], proposing two designs both based on stress management. A stress managed $\cos(\theta)$, where a $\cos(\theta)$ coil is wound on a former that includes the wedges, is being studied at FNAL. A Nb_3Sn coil in mirror configuration has reached 12.7 T at 87% of short sample limit [575].

A fully stress-managed magnet is the CCT (canted cosine theta) configuration, where each turn is supported by a rib integrated to a former. This design, also called tilted solenoid or double helix, dates back to the early 1970s [576] and has been adopted by LBNL since the mid 2000's, aiming to reach fields towards 20 T [577]. A drawback of CCT with respect to the previous option is that the use of conductor is less optimised, since part of it is used to generate a solenoidal field that is cancelled by the other coil. However, the structure is totally mixed with the coil – a kind of endoskeleton – making easier protection and mechanics and possibly allowing higher current densities.

The short model CCT5 built at LBNL reached 8.5 T with a Nb_3Sn winding using a 10 mm cable over a 90 mm aperture [577]. At PSI, using a similar design and the same cable, 10.1 T were reached in a 60 mm aperture short model named CD1 [578]. In both cases the overall current densities (over the insulated coil) are very large (800 and 1000 A/mm^2 respectively): a field of 8-10 T is reached with an equivalent coil width of the order of 17 mm; see Fig. 10.33. PSI is currently pursuing a stress-managed asymmetric common coil as a candidate for 14 T (SMACC1) [571].

Hybrid Nb-Ti/Nb$_3$Sn magnets Material grading is an option that consists of using a cheaper and less performant material in the low field region. It has been used for the D19H magnet [579], and is being used in demonstrators (for instance LPF1 in the IHEP programme [567]). Unlike the current grading, where higher current density is used for low field regions (as in CERN Elin, MSUT, D20, and in the LHC dipole), here similar current densities are used in the inner and outer layer, but the outer layer is made with Nb-Ti. Nb-Ti at 1.9 K with an overall current density of the order of 400 A/mm^2 can be used in coil regions not exceeding 8 T; this could lead to a significant reduction of the mass of Nb_3Sn conductor (>30%); however, this prevents operating at 4.5 K, since the temperature margin of Nb-Ti at 80% of the loadline at 1.9 K is only about 2 K.

10.4.4 High temperature superconductor: perspectives and challenges

High temperature superconductor: opportunities High Temperature Superconductor (HTS), discovered in the mid 80's in the family of cuprates, has many interesting features that make it a game changer in superconducting technology, see Fig. 10.35 [580]: (i) high values of critical current density (>2000 A/mm^2) also above 20 T, opening the way to high fields, (ii) the ability of sustaining high current densities and fields at and above 20 K, opening the path to cheaper cooling systems (even though liquid nitrogen cooling is still considerably out of reach for high field magnets), and (iii) a much higher stability versus thermo-mechanical perturbation due to the increase in enthalpy margin at higher operating temperatures. The HFM programme is exploring the options of dipole magnets in the 14 to 20 T range, at temperatures between 4.5 K and 20 K, thus covering a COM energy in the range of 85 to 120 TeV.

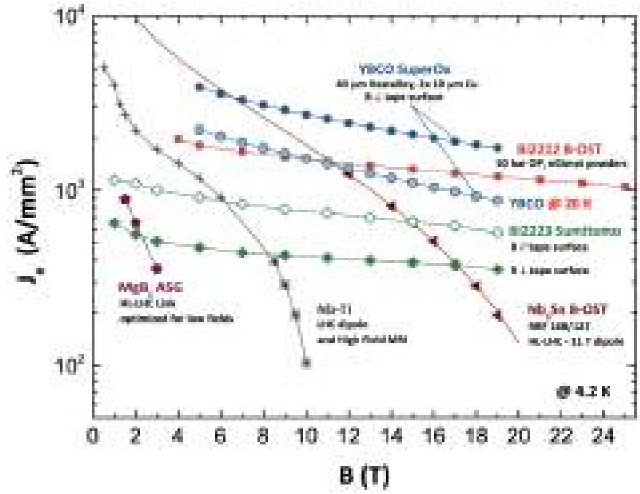

Fig. 10.35 Critical (engineering) current densities of different HTS conductors, Nb_3Sn, and Nb-Ti. Reproduced from [580]

Two types of high-temperature superconductors are commercially available: BSCOO and REBCO. BSCOO [581], produced mainly by one company in the US, has the advantage of being available as round wire with small filaments. Its use is complex since, like Nb_3Sn, it needs a reaction after winding, but at 900 °C in oxygen rich ∼50 bar atmosphere. A process-compatible electrical insulation system must be selected. Moreover, BSCOO is brittle and, hence, requires careful handling in coil manufacturing and appropriate mechanical structures to respect stress limitations. Several short magnet models have successfully been built in the US; see Sect. 10.4.4.

REBCO [582] is produced by multiple suppliers worldwide; this conductor is produced in the geometry of a tape, and its industrialisation recently profited from large private investments aiming at ultra-compact magnet systems for fusion (solenoids and toroidal field coils) with ∼20 T coil field. This has reduced the price in the past ten years by a factor three. The conductor does not require a heat treatment after winding. On the other hand, (i) unit lengths are still typically short (300 m) and longer lengths today affect the cost, (ii) REBCO is a highly anisotropic conductor (anisotropy factor of ∼5). The challenge is not only to make a fully transposed (Rutherford-like) cable from tape to wind a coil, but also to deal with mechanical properties: while very robust against tension and transverse compressive stress, delamination of the tape under tensile transverse stress causes degradation. Another challenge is to control hysteresis losses and field quality as the equivalent filament size is very large in the plane of the tape (typically 4-12 mm).

Development of iron-based superconductors [583, 584], is being strongly pursued in China. The critical current density achieved is still lagging a factor 2-3 behind the expectations set ten years ago, but based on raw-material prices the material has the potential of a very low cost; this could become a significant advantage for a high-field collider magnet, where about half of the price is the superconductor.

Given their potential, the HFM Programme is investing in REBCO tape technology development in the KIT/CERN Collaboration on Coated Conductor (KC4), as well as in iron-based superconductor technology (CNR-SPIN/CERN), aiming at a round wire with powder-in-tube layout [585].

Fields achieved in EuCARD2 and US-MDP dipole models Between 2015 and 2020, three dipole magnets based on REBCO were built within the framework of FP7-Eucard2 programme [586]. In CEA, a dipole technology demonstrator based on double REBCO ribbons and three racetrack coils, without aperture, reached 5.4 T [582]. In the same period, two magnets were built with Roebel cable: in CEA a 40 mm aperture dipole was manufactured with a $\cos(\theta)$ configuration, 12 mm coil width, reached 1.16 T due to one degraded coil [587]. This magnet will be re-tested with a replacement coil. At CERN a dipole was built with the same cable, with an aligned block dipole configuration in a 40 mm aperture, reaching 3.35 T at 5 K and 4.3 T at 4.5 K (FeatherM2.12 and 2.34 [586, 588]).

More recently, the US programme, US-MDP, has developed several Bi-2212 racetrack coils and a CCT magnet (Bin5) which reached 1.6 T in a 31 mm aperture [589]. A CCT with a CORC® cable based on a REBCO tape reached 2.9 T in a 65 mm aperture [590], with a more recent test exceeding 5 T.

Plans for 20 T: hybrid or full-HTS? The FP-7 Eucard2 programme aimed at an HTS insert for a Nb_3Sn external coil [586]; the same strategy has been adopted by US-MDP and IHEP. US-MDP proposes to achieve 20 T via a magnet using different designs [574]: on the one hand an all-CCT hybrid, and on the other hand a COMB (Conductor on Molded Barrel) HTS part, and stress managed $\cos(\theta)$ for the inner Nb_3Sn layer and a classical $\cos(\theta)$ for the outer layer. The IHEP common coil design is also based on an HTS inner coil and Nb_3Sn outer coils [568], with HTS contributing 5 T to the field.

The hybrid option HTS/Nb_3Sn does not allow the higher operational temperature that would be possible with a full-HTS magnet (e.g., 20 K). For the time being, Nb_3Sn is still much better mastered than HTS, and therefore both US and China are working on the hybrid option, at least to make technology demonstrators. It must be noted, though, that the performance-related cost for HTS at 20 K is today two to three times larger than at 4.5 K, and since the conductor is the driving parameter of the estimated magnet cost, this can be a showstopper for the 20 K option. Improved performance at 20 K is a development objective for REBCO conductor.

Challenges: field reproducibility, mechanics, hysteresis losses, protection A stringent requirement for accelerator main magnets is the *precision and reproducibility of the transfer function* not only at high field, but also at injection and during the ramp (10^{-4} to 10^{-5} needed relative to main field). This aspect is strongly related also to the design of insulation and protection: some HTS coils that are being made for fusion operate in DC mode and make use of non-insulated coils, allowing current redistribution that eases reaching higher fields. This option is not suitable for accelerator magnets, which require a dielectric insulation. Metal insulations are also being studied, but these are not yet proven to be suitable for accelerator magnets in terms of field control, ramp losses, and protection.

Another issue is related to transverse (to the tape surface) tensile stress in the winding that causes delamination of the superconducting layer from the supporting substrate, degrading the cable performance. Careful design may control this effect.

The high temperature margins of HTS have the drawback that quench velocities are slow, and the voltage rise that is monitored to detect the quench can take too long. Consequently, quench protection and detection strategies need to significantly different from those of LTS magnets. Moreover, at 20 T the energy density to be absorbed by the coil is well above the enthalpy limit: detection of, and protection from, quenches in HTS coils are still major challenges, and coils that reached 20 T for fusion applications were lost during quenches. Systems that can provide a partial extraction of the stored energy for long magnets are being studied. Another possibility would be to avoid quenches, i.e., having a system that, once a temperature increase is detected, manages to prevent a resistive transition or at lest a thermal runaway.

Finally, stability can be achieved by very large filaments: HTS tapes used for fusion have a width of 4 to 12 mm. This width leads to a large magnetisation, giving rise to hysteresis losses, field quality distortions, and field drifts, that are expected to be larger than for LTS, with long field quality drifts expected in simple tape-stack cables. These effects should be included in the conception of a novel cable that could make REBCO compatible with HEP requirements.

In conclusion, it can be said that the technological readiness level (TRL) of HTS technology for accelerators lags considerably behind that of LTS conductors. Vigorous R&D is therefore needed, also in concert with other fields and applications, over the coming years to demonstrate how HEP can benefit from the potential advantages of HTS technology.

10.5 FCC-hh accelerator systems and technical infrastructures

10.5.1 Cryogenics requirements with 1.9 K Nb_3Sn magnets

In the latest accelerator baseline, the tunnel length has been reduced to 90.7 km with eight access points, requiring an update of the layout of the cryogenic system, which is proposed and described in Fig. 10.36. The current cross-sectional view of the cryogenic distribution line (QRL), and the layout of the individual pipes (lines) can be found in Fig. 10.37. Both figures refer to an FCC-hh operation scenario with 14 T dipole magnets [591].

The layout of the cryogenic system seen in the figure consists of two accelerator cryoplants at points PB, PD, PF, PH, PJ, and PL. Each of these cryoplants has a cooling capacity of 53.1 kW at 4.5 K_{eq}, including 9.9 kW at 1.9 K.

Two cryoplants are foreseen in the high-luminosity insertion region at points PA and PG, each of them with a capacity of 78.9 kW at 4.5 K_{eq}, including 17.6 kW at 1.9 K. Detector cryoplants will be installed in PA, PD, PG and PJ, with a 1.5 kW at 4.5 K_{eq}, similar to the existing helium cryoplant of the CMS experiment. The cryogenic system also includes twenty-four boil-off re-liquefiers.

Without considering detector cryoplants and the boil-off re-liquefiers, this represents a total cryogenic cooling capacity required of 950 kW at 4.5 K_{eq}. It includes 100 kW at 4.5 K_{eq} for the cryogenics of the 2 high-luminosity insertion regions (inner triplets).

This translates into a total electrical power requirement of about 210 MW to operate the cryogenic systems. Neglecting the two high-luminosity insertion regions, the total electrical power required for the FCC-hh cryogenic system decreases to 186 MW.

The advantage of this layout is the reduced cryogenic sector length, decreasing to 4.8 km of cooling length per cryoplant compared to 8.4 km in the CDR. This reduction directly translates into a smaller pumping line. Consequently, the cryogenic distribution line is reduced from DN1350 to DN1100 type. The total helium inventory for the cryogenic system is estimated at 820 t.

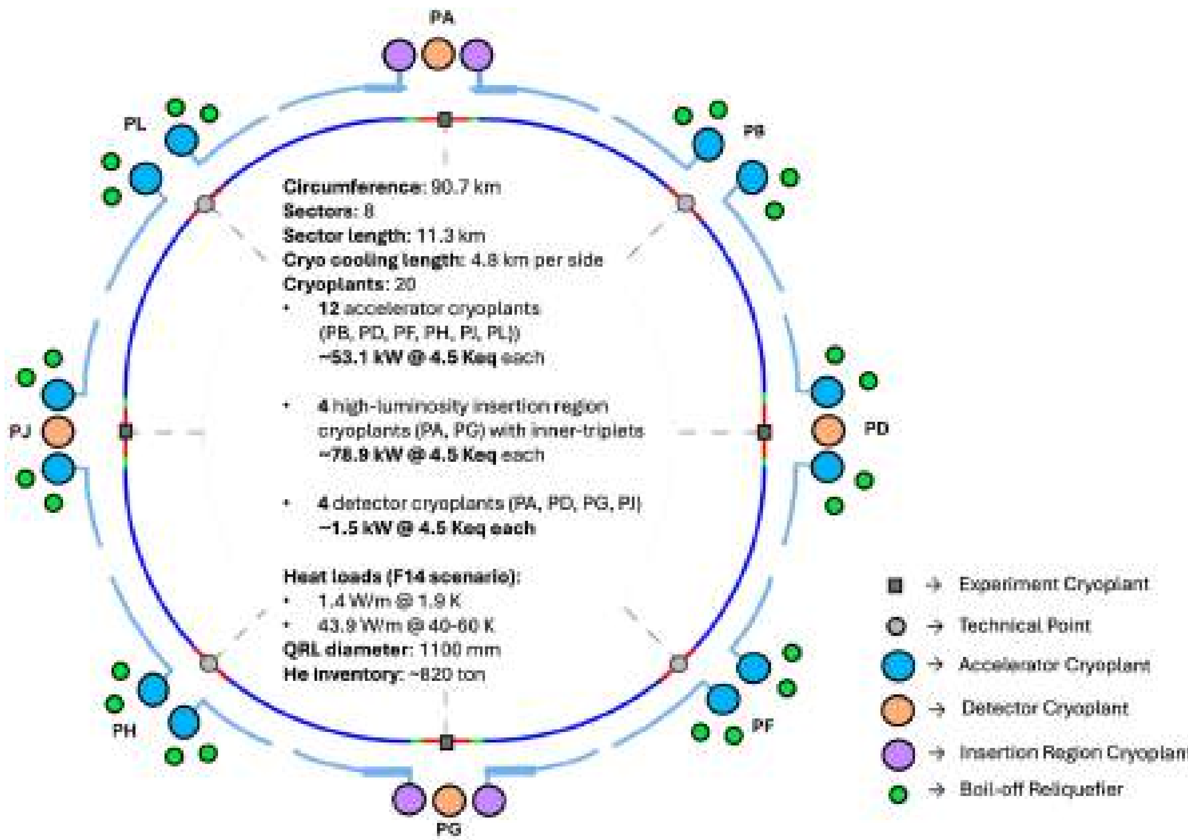

Fig. 10.36 Updated layout of the FCC-hh cryogenic system layout

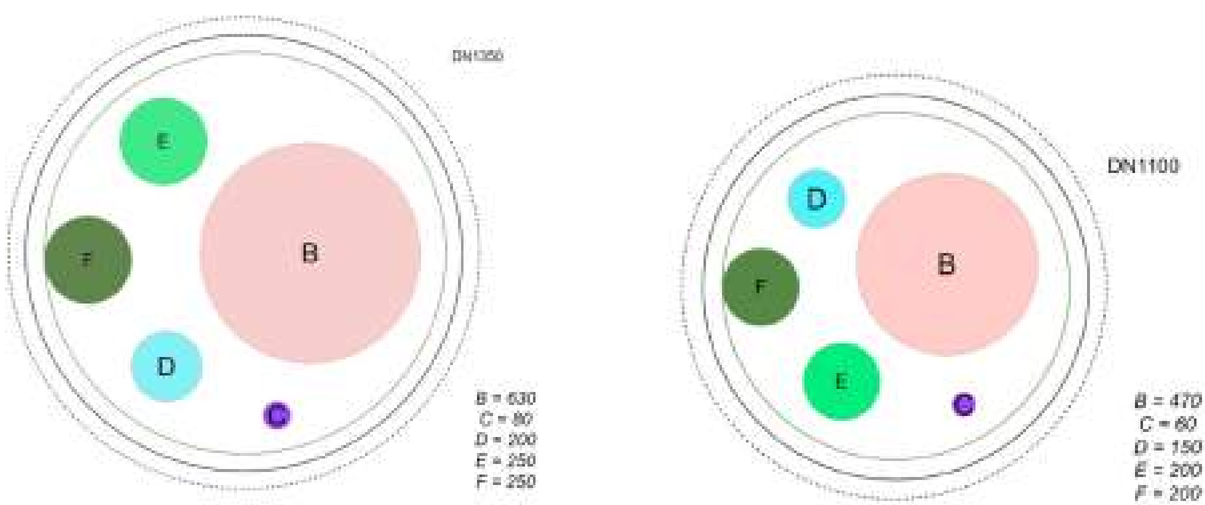

Fig. 10.37 Layout of the cross section of the FCC-hh QRL as of the CDR (left) and in the current configuration (right). The line B represents the very low pressure helium return line; the line C represents the supercritical helium supply line; the line D represents the low pressure helium return line; the line E represents the helium thermal shield supply line; the line F represents the helium thermal shield return line

The key parameters for the FCC-hh accelerator cryogenic system discussed above are summarised in Table 10.20 and neglect the detector needs and cryogenics associated with the high-luminosity insertion regions in PA and PG.

Table 10.20 Key parameters for the cryogenic system of the FCC-hh. A safety factor of 1.2 is included in the helium cryogenic capacity. These figures do not include the high-luminosity insertion regions with the triplet quadrupoles, or the requirements of the experiment detectors

FCC-hh Parameters	CDR [2018]	FSR [2025]
Circumference [km]	97.75	90.7
Dipole field [T]	16	14
Centre of mass energy [TeV]	100	85
Synchr. radiation for two beams [MW]	4.8	2.4
Magnet temperature [K]	1.9	1.9
Beam screen temperature [K]	[40 - 60]	[40 - 60]
Helium cryogenic capacity at 4.5 K equivalent [kW]	1214	947
Number of cryo islands	6	8
Total number of cryoplants	10	16
Arc cooling length [km]	84	76.8
Electrical consumption [MW]	266	208
Helium inventory [t]	880	820

10.5.2 Power converters

A preliminary study has been conducted to assess power converter requirements, focusing on the necessary footprints and volumes in alcoves and surface areas.

The study specifically examines the powering of the superconducting magnets. To stabilise power consumption from the utility grid and minimise the sizing of upstream electrical components (e.g., transformers, cables), energy storage systems integrated with the power converters are required. These systems store energy during the accelerator's ramp-down phase and supply it during beam acceleration. Given their substantial space requirements, these storage elements must be placed in alcoves to minimise power losses from long cable runs.

Preliminary findings, based on FCC-hh magnet specifications, suggest that the space allocated for FCC-ee power converters (in terms of footprint and volume) is comparable to what is needed for the FCC-hh magnet powering including energy storage.

10.5.3 Technical systems

The technical infrastructures described in this section, designed to meet the needs of the FCC-ee, also already incorporate the requirements for FCC-hh.

Electrical networks The electrical connections to the 400 kV lines of RTE (France's Transmission System Operator) have been designed to accommodate the power demands of both FCC-ee and FCC-hh, with the latter requiring about the same power as the FCC-ee in the $t\bar{t}$ mode. Three connection points are planned, each rated at 220 MVA, and will be interconnected through an internal high-voltage network.

For FCC-ee, the estimated peak power demand for $t\bar{t}$ operation is approximately 360 MW, which is well below the 660 MVA capacity of the grid connection. This setup provides redundancy in the power sources, ensuring reliable operation. However, the power demand is not evenly distributed between all points. Specifically, PH, which houses the RF systems, has a substantial power requirement of 200 MW. To address this, a dedicated 400 kV substation will be allocated for the RF power supply. The two remaining connection points, PA and PD, will handle all other loads via the internal high-voltage network and can operate redundantly.

For FCC-hh, the primary power consumers will be the cryogenic systems, with their load more evenly distributed across all three connection points. The eight points of the FCC-hh ring will require a power rating between 40 and 60 MW each.

Unlike FCC-ee, all three grid connections will be essential for powering FCC-hh, leaving no redundancy in power sources. In the event of a power source failure, accelerator operation would not be possible. However, critical systems could continue running in a degraded mode to maintain minimum cryogenic conditions.

Cooling and ventilation The redistribution of thermal loads from FCC-ee to FCC-hh will require the installation of some additional cooling towers at most points, except for PH, where a lower capacity will suffice. However, the overall thermal load in the tunnel will be reduced as the new loads will be located mainly in service caverns and surface buildings.

These adjustments will be limited to designated service areas, ensuring that modifications to cooling networks remain localised. In addition, the tunnel ventilation systems will remain unchanged, with only minor adaptations required for specific service and experiment caverns.

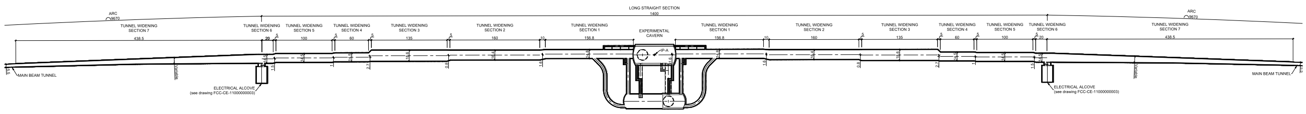

Fig. 10.38 FCC underground - civil engineering in point PA

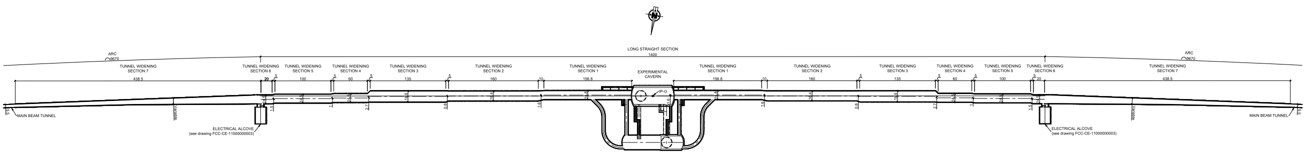

Fig. 10.39 FCC underground - civil engineering in point PG

Fig. 10.40 FCC-hh point PA - experiment cavern cross-section

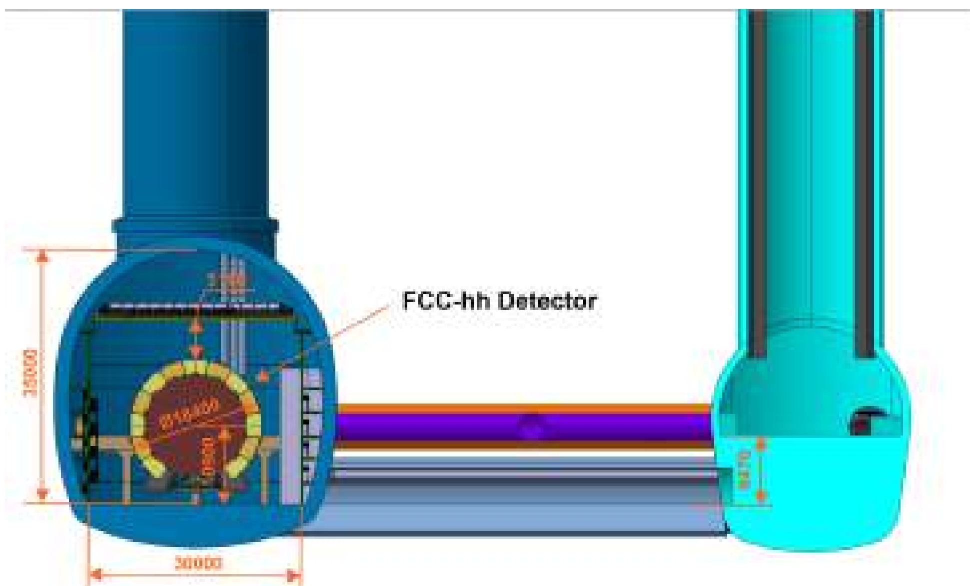

Safety systems For FCC-hh, additional safety measures will be necessary. Unlike FCC-ee, where oxygen deficiency is not a concern in the arc tunnel, the presence of cryogenic systems in FCC-hh requires dedicated monitoring and protective measures. Consequently, oxygen deficiency hazard detection systems will be installed in the tunnel, alcoves, and service caverns to maintain a safe working environment.

10.5.4 3D integration studies

The 3D integration studies of the FCC-hh have been detailed for all areas of the underground tunnels and caverns, fitting the requirements from the work packages. This section presents the results of the configuration and layout of the accelerators and infrastructure systems that were studied for the feasibility study report. This is an evolution of the previous studies made for the conceptual design report [13, 306].

The 3D integration studies take into account both of the configurations of the FCC-ee and FCC-hh to ensure space compatibility.

Integration of point PA and point PG Point PA and point PG will serve as large experiment points, hosting detectors in the cavern in both the FCC-ee and the FCC-hh phases of operation. The cavern size and extent meet the needs of the detectors for both FCC-ee and FCC-hh. In addition, for the FCC-ee, the long straight sections (LSS) on either side of point PA and point PG will host the beamstrahlung dumps and the polarimeter system (see Fig. 10.38 and Fig. 10.39). The LSS of point PA will also host the end of the transfer line from the injector linac, into the booster.

Figures 10.40 and 10.41 present the results of the 3D integration studies for point PA and point PG.

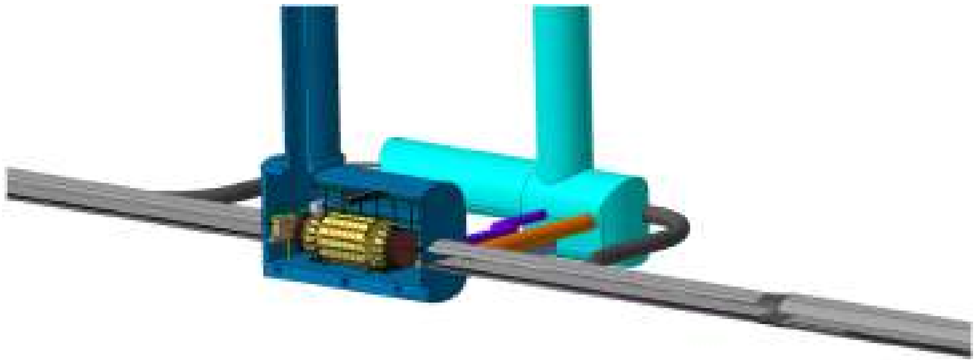

Fig. 10.41 FCC-hh point PA - experiment cavern iso view

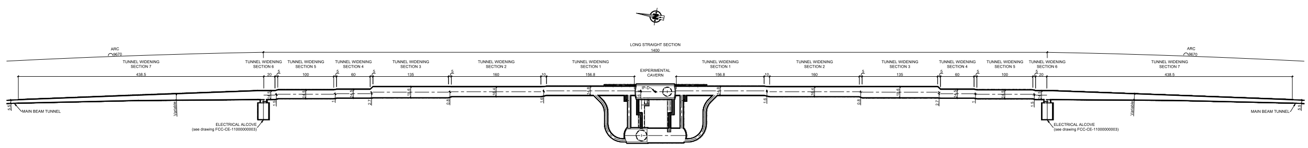

Fig. 10.42 FCC underground - civil engineering in point PD

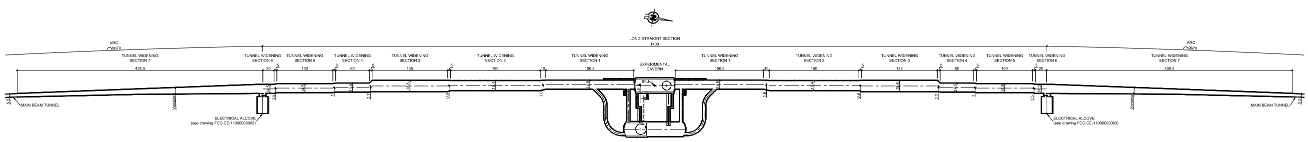

Fig. 10.43 FCC underground - civil engineering in point PJ

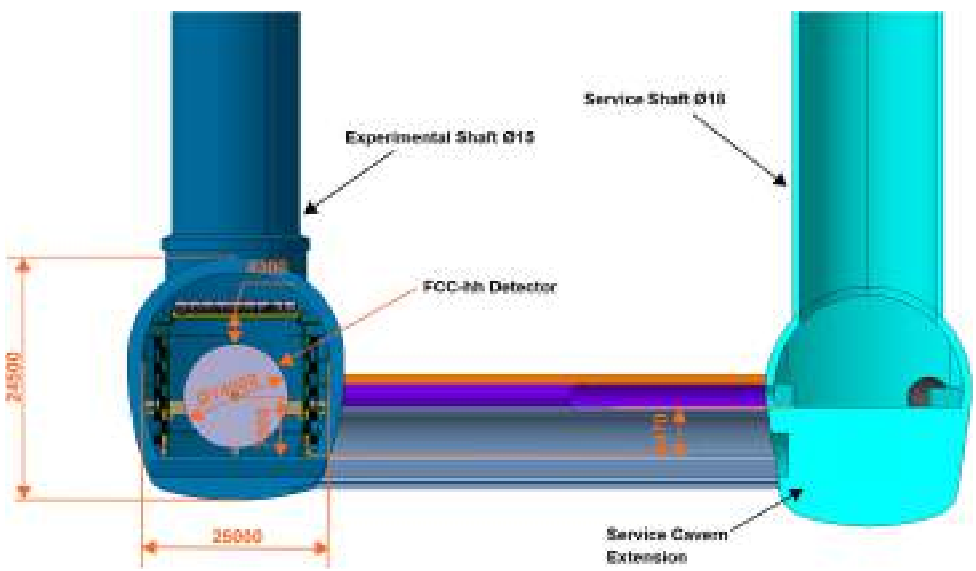

Fig. 10.44 FCC-hh point PD and PJ - experiment cavern cross-section

Integration of point PD and point PJ Point PD and point PJ will serve as small experiment points, hosting detectors in the cavern in both the FCC-ee and the FCC-hh phases of operation (see Fig. 10.42 and Fig. 10.43). The cavern size and extent meet the needs of the detectors for both FCC-ee and FCC-hh. In addition, for the FCC-ee, the long straight section (LSS) on either side of point PD and point PJ will host the beamstrahlung dumps.

Figures 10.44 and 10.45 present the results of the 3D integration studies for the point D and the point J.

Integration of the arcs The FCC-hh superconducting magnets will have a maximum diameter of 1.2 m, regardless of the technology used (Nb_3Sn, HTS, etc.), resulting in the tunnel cross section shown in Fig. 10.46. For the

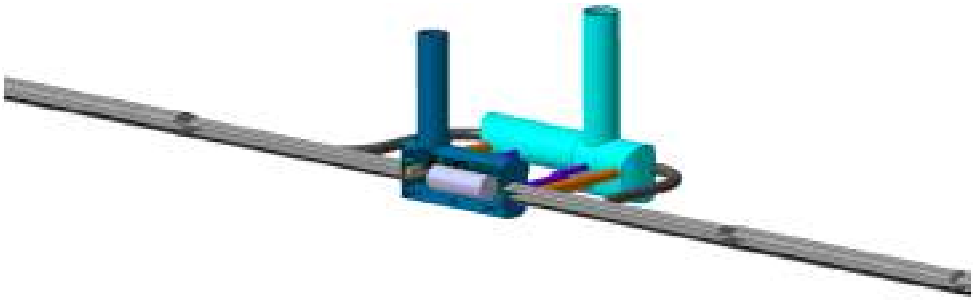

Fig. 10.45 FCC-hh point PD and PJ - experiment cavern iso view

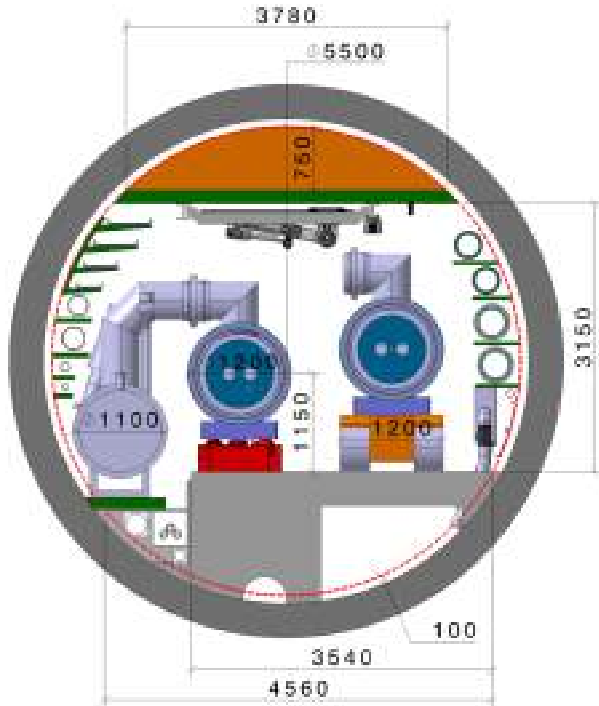

Fig. 10.46 Cross section of the tunnel for the FCC-hh layout in the arcs

FCC-ee ring, the transport area is 2.2 m wide, allowing personal vehicles to pass each other freely throughout the tunnel. In contrast, for FCC-hh, this area may be reduced to 2 m, restricting vehicle crossings to designated alcove lay-bys spaced out every 1.6 km. Consequently, traffic control will require a different approach compared to FCC-ee.

The figures included in this chapter represent the results of the 3D integration studies in the arcs.

Next phase for the integration studies The integration studies have been made with pre-design of volumes and will evolve with detailed technical design in the next phase of the FCC studies. Optimisation of the 3D integration studies with respect to the requirements from work packages will continue for all the areas following the identified technical and space needs:

- Optimisation of the large experiment points PA and PG [374, 375] and small experiment points PD and PJ [376], integrating more detailed detectors design in the experiment caverns,
- Optimisation of the arc half-cell [381].

10.5.5 FCC-hh power demand

In FCC-ee, the primary power-consuming systems are the RF systems, which compensate for synchrotron radiation losses. These systems must supply approximately 100 MW to the beams across different operating modes. In Z mode, RF power accounts for 65% of the total power demand, while in $t\bar{t}$ mode, it represents 37.5%. These values reflect the energy requirements necessary to sustain beam stability and luminosity performance.

For FCC-hh, the dominant power consumer will be the cryogenic systems required for magnet cooling. The cryogenic capacity is determined primarily by two factors: the static heat load of the magnets and the synchrotron

Table 10.21 FCC-hh power demand by technical systems at 85 TeV beam centre-of-mass energy

System	85 TeV
Radio frequency [MW]	17
Cryogenics [MW]	207.5
Cooling & ventilation [MW]	40
Magnet powering [MW]	33
Experiments [MW]	24
Data centre [MW]	8
General services [MW]	26
Total power [MW]	**355**

Table 10.22 FCC-hh power demand during different operational periods

Period	85 TeV
Shutdown [MW]	122
Technical stop [MW]	122
Downtime [MW]	122
Commissioning [MW]	324
Machine development [MW]	324
Beam operation [MW]	355

radiation deposited on the beamscreen. The cryogenic power demand varies depending on the operating temperature of the magnets and the beamscreen. Table 10.21 presents the power demand for the baseline scenario where 14 T Nb_3Sn magnets are cooled to 1.9 K, with a total synchrotron radiation power of 2.4 MW and a beamscreen temperature ranging in the interval 40–60 K.

The cryogenic systems for the arc magnets alone require 185 MW of electrical power, with an additional 22.5 MW needed for the high-luminosity insertions inner-triplet magnets (two sets for two experiments). The RF power requirement is estimated at 23 MW during the energy ramp and decreases to 12 MW at flat top, during beam collisions.

Magnet powering will be managed from alcoves with interconnection boxes, and power losses will be minimised through short cable sections, reducing demand to 33 MW. The estimated power needs for experiments are based on the LHC experiments (ATLAS and CMS), while general services power requirements have been extrapolated from LHC operations. Although some figures require further refinement, these estimates align with expected scaling from the LHC.

For a configuration using Nb_3Sn magnets cooled to 1.9 K and generating 2.4 MW of synchrotron radiation, the total power demand is approximately 360 MW, comparable to that of FCC-ee. The FCC-hh power demand might further be reduced to below 300 MW, if the magnet temperature can be raised to 4.5 K.

Operational model The accelerator operational model determines the energy consumption. The power demand varies depending on the time of year and the operational state of the machine. The machine schedule defines six operational periods: (1) Shutdown; (2) Commissioning; (3) Physics operation; (4) Short downtime (without machine access); (5) Technical stops (longer downtimes); and (6) Machine development. The power demand for each period is shown in Table 10.22.

The introduction of a *eco-mode* for the cryogenic systems during shutdown, reducing power consumption to 83 MW, significantly decreases the power demand during non-operational periods. The annual schedule consists of:

- 120 days of shutdown,
- 30 days of commissioning,
- 20 days of machine development,
- 10 days of technical stops, and
- 185 days of physics (beam operation).

The FCC-hh machine availability is expected to be similar to that of LHC, with an operational efficiency of approximately 80%, corresponding to an expected period of beam collisions of 1700 hours.

Table 10.23 FCC-hh annual energy consumption at 85 TeV collision energy

Beam Energy	42.3 TeV
Annual energy consumption [TWh/y]	2.34

Energy consumption Based on the operational schedule and the expected power demand throughout the FCC-hh programme, the estimated annual energy consumption at 85 TeV is shown in Table 10.23.

For FCC-hh, total annual energy consumption is slightly higher compared to the energy consumption of FCC-ee because of the continuous operation of cryogenic systems. Furthermore, power demand remains relatively high even during shutdown periods. However, introducing an *eco-mode* has significantly reduced cryogenic power consumption during non-operational phases.

10.5.6 Other systems

Other accelerator systems for the FCC-hh, e.g., beam-transfer systems, the cryogenic beam vacuum system, beam diagnostics, etc., are described in the Conceptual Design Report (CDR) [592].

10.5.7 On-going studies

A key feature highlighted during the CDR phase is the potential application of an HTS coating to the beam screen. This approach was explored as a mitigation measure to address the increased resistivity of the beam screen due to its higher operating temperature (around 50 K), which was chosen to reduce the demands of cooling power.

Following the publication of the FCC CDR, extensive research has focused on conducting comprehensive analyses of the coating's performance, examining its electromagnetic properties and other related factors.

A prototype beam screen incorporating the suggested HTS coating is currently under construction. This will facilitate a comprehensive examination of its magnetic characteristics, such as the overall field quality of both the beam screen and the HTS coating. The tests will include dipole and quadrupole external magnetic fields. Impedance measurements will also be attempted, if feasible, to fully characterise the HTS coating.

The application of an amorphous carbon coating to the HTS presents an opportunity to elevate the beam screen's operating temperature, as it inherently resolves vacuum instability issues. The optimal operating temperature will be determined by balancing multiple factors, including HTS performance, beamscreen resistivity, effects on beam dynamics, and benefits for the cryogenic system. These aspects will be further studied in the next project phase to identify the optimum operating temperature.

Finally, FCC-hh will require the installation of the cryogenic distribution line (QRL) that has a diameter below 1.1 m regardless of the operational temperature of the magnets (1.9 K, or 4.5 K).

Appendix A

Costs

A.1 FCC-ee construction

The capital cost for construction of the FCC-ee is summarised in Table A.1. This cost includes construction of the entire new infrastructure and all equipment for operation at the Z, WW and ZH working points. Operation of the FCC collider at the $t\bar{t}$ working point will require later installation of additional RF cavities and associated cryogenic cooling infrastructure with a corresponding total cost of 1260 MCHF.

The costs indicated include materials and personnel costs of contractors and suppliers. They do not include the cost of scientific, engineering, technical and administrative personnel at the host organisation or at the collaborating institutes.

The total construction cost for CERN amounts to 14,020 MCHF (covering Z, WW and ZH working points), dominated by 45% or 6160 MCHF by civil engineering, which also comprises all site-related investments. The capital cost for the technical infrastructures, including site-external connections, is 2840 MCHF, corresponding to 20% of the total construction cost. Another 30%, or 4140 MCHF, corresponds to the collider and full-energy booster construction. The cost estimate for the injector complex and transfer lines is 590 MCHF. In addition, the CERN contribution to the four experiments is estimated at 290 MCHF, while the non-CERN part of the total cost of these four experiments would amount to approximately 1300 MCHF, as shown in Table A.1. The investments are distributed over a time frame of about 15 years.

Table A.1 Estimated investment costs for different construction domains in 2024 Swiss Francs

Domain	Cost [MCHF]
Civil engineering	6160
Technical infrastructures	2840
Injectors and transfer lines	590
Booster and collider	4140
CERN contribution to four experiments	290
FCC-ee total	**14,020**
+ Four experiments (non-CERN part)	1300
FCC-ee total, including four experiments	**15,320**

Table A.2 Estimated investment costs for different construction domains in 2024 Swiss Francs

Domain	Cost (MCHF)
Civil engineering	520
Technical infrastructures	3960
Injectors and transfer lines	1000
Collider	13,400
FCC-hh total	**18,880**

The indicated figures include materials and personnel costs of contractors and suppliers. They do not include the cost of scientific, engineering, technical and administrative personnel at the host organisation or the collaborating institutes. The engagement of this personnel directly leads to the generation of noteworthy socio-economic benefits via the pathways of education, training, direct, indirect and induced economic value added.

A.2 FCC-ee operation costs

A.2.1 Annual cost of operations of each stage

A material cost of 200 MCHF has been estimated by individually categorising each item of equipment according to its nature: fixed installation (1% OPEX), technical infrastructure (5% OPEX), and consumables (3% OPEX). The 200 MCHF figure represents the weighted sum of these categories across all subsystems. Adding an annual electricity cost of 100 MCHF (with some variation depending on the collision energy point) and approximately 300 MCHF for personnel (1400 FTEs), the total average annual operating cost of FCC-ee across all stages amounts to around 600 MCHF.

A.3 FCC-hh construction and operational costs

A.3.1 FCC-hh construction

Table A.2 splits the construction costs into the creation of the infrastructures (subsurface, surface and territorial developments), the enabling technical infrastructures, and the accelerators.

The total construction cost amounts to 18,880 MCHF. It is dominated by the cost for the collider magnets, amounting to about 10,000 MCHF. This cost, however, will need to be reviewed in light of ongoing R&D efforts. In particular, further research into novel types of superconducting materials is essential—not only to potentially reduce costs, but also to unlock broader technological benefits and cross-sectoral applications.

The cost of the four FCC-hh experiments can be estimated only at a later stage, once more detailed designs of the detectors exist. The construction investments are distributed over a time frame of about 15 years.

The costs indicated include materials and personnel costs of contractors and suppliers. They do not include the cost of scientific, engineering, technical and administrative personnel at the host organisation or at the collaborating institutes.

A.3.2 FCC-hh operation

Operational costs for the FCC-hh phase foreseen as a second step in 2070 have not yet been determined.

Appendix B

Installation

B.1 Installation planning

B.1.1 The technically-limited timeline for FCC-ee construction

Preparatory placement studies for the FCC are well advanced. The further timeline is mainly determined by the preparation of the civil engineering (subsurface investigations, civil engineering design and tendering, and the project authorisation processes with the host states, planned to advance in parallel), and, afterwards, by the civil construction and the subsequent installation of technical infrastructure and accelerator components. The timeline of FCC-ee in Table B.1, including work already accomplished. More details on the construction and installation aspects are discussed below.

B.1.2 FCC-ee technical infrastructure and machine

This section outlines a high-level schedule for installing the FCC-ee machine and its supporting infrastructure. Based on the feasibility study, it adopts a 90.7 km circumference layout with eight surface sites. The timeline extends from the start of civil engineering excavation scheduled for January 2033 to the anticipated readiness for beam commissioning in July 2046. The plan is divided into two main phases:

- Civil construction phase 2033-2041
- Installation phase 2038-2046

Civil engineering strategy integration

Synergies found between installation planning and civil engineering phase and updated civil engineering strategy The baseline presented in the midterm review outlined eight handovers of individual shaft sectors. Initially, all installation work within an arc could only commence after the release of a single designated point (see Fig. B.1).

To enhance coordination, synergies between civil engineering and installation planning were explored. As a result, the civil engineering team restructured the handover process, breaking down the singular shaft-sector handover into multiple phased handovers. The revised civil engineering strategy (see Fig. B.2) involves removing the TBMs through the experiment shaft (PX), which allows an earlier release of the machine shaft (PM) at a technical point.

Additionally, a gradual handover approach for arc installation was introduced. The tunnel floor and smoke extraction duct will be the final construction activity completed by civil engineering along the tunnel arc. To coordinate with the machine installation, the tunnel arc is split into sectors corresponding to the alcove locations. Therefore, once civil engineering has completed construction activities up to an alcove, the sector can be released for the installation of machine infrastructure.

For each shaft sector, the following elements now have distinct release dates:

1. PM of the experiment point
2. PM of the technical point
3. Staged release of the arc done alcove by alcove. 5 to 7 staged handovers are foreseen for one arc sector going from the technical point to the experiment point. A separating door will be moved at every handover to separate the two worksites
4. PX of the experiment point

The civil engineering construction durations across each of the sites vary primarily due to the different structural layouts, depths and construction methods.

Table B.1 Timeline for FCC-ee design, construction, and operation

Milestone / phase	years
Conceptual Design Study	2014 – 2018
Territorial implementation studies	2016 – 2025
Definition of the placement scenario	2022
Feasibility Report ready	2025
Earliest Project Approval by CERN Council	2027/28
Environmental evaluation & project authorisation processes	2026 – 2031
Main technologies R&D completion	2031
Technical Design Report ready	2032
Civil engineering - Collider	2033 – 2041
TI Installation – Collider	2039 – 2043
Accelerator Installation – Collider	2041 – 2045
HW Commissioning – Collider	2042 – mid 2046
Start Beam Operation – Collider	mid 2046 – 2047
Nominal Beam Operation – Collider	2048 – 2062

Impact on installation organisation and planning Breaking down the handover process of civil engineering enables an earlier start for installation activities. The early handover of the PM technical points allows for the installation of essential shaft components, including lifts, cranes, and technical infrastructure. Each staged release of the arc facilitates the progressive installation of technical infrastructure in the tunnel, shifting part of the work into the shadow of the critical path.

The staged release of a sector between two access points means that, on the technical point side, technical infrastructure installation will be underway, while civil engineering work will still be ongoing on the opposite side of the separating doors. Safety regulations require two evacuation routes in case of an emergency, which is ensured by the separating door between the two worksites. This door is exclusively for emergency evacuation. In such an event, personnel from the civil engineering side will be responsible for assisting in the evacuation of those from the installation side.

Since the overall arc and final ventilation equipment will not yet be in place during the staged release, the installation of technical infrastructure will be carried out using a temporary ventilation system.

Handover dates The handover dates (Table B.2) were provided by the civil engineering team based on the TBMs advancing at a rate of 16 m/day, which is 10% less than the previous civil engineering baseline.

Installation phase

Installation phase for a sector The installation planning was developed through a bottom-up approach, beginning with a detailed analysis of the sequence and duration required for each sector. The installation process for each of the eight sectors will be carried out in four distinct phases. First, the installation of technical infrastructure and lifting equipment inside the shaft. Second, the installation of the technical infrastructures in the tunnel. Third, the installation of the accelerator itself. Fourth, the commissioning period of the technical infrastructures and the accelerators (see Fig. B.3).

The technical infrastructure must be installed before the accelerator to ensure unobstructed access to the walls and floors and to prevent potential damage from heavy construction activities. Furthermore, most of this infrastructure will remain in place throughout the entire lifespan of the FCC, from the electron collider to the hadron machine. While the installation of technical infrastructure does not require immediate ease of access, all maintenance constraints must be carefully considered.

The installation starts with the shaft which has to be equipped with all services (lifts, crane, ventilation, electricity, pipes ...). This phase is quite slow due to the limited number of workers (expected to be around 30) who can work inside the shaft, because they all depend on the shaft crane. The shaft installation is expected to last for close to 12 months for a 250 m deep shaft. The duration of shaft installation works depends on the shaft depth.

During the installation phase, certain technical infrastructure elements, such as lighting and power supply, will be commissioned progressively. However, a dedicated six-month period will be required at the end of the installation phase to conduct comprehensive testing and final commissioning of all systems.

Once the technical infrastructure of an arc is fully completed, a thorough cleaning will be carried out before the installation of accelerator components begins. The magnet installation process is organized into three shifts, with

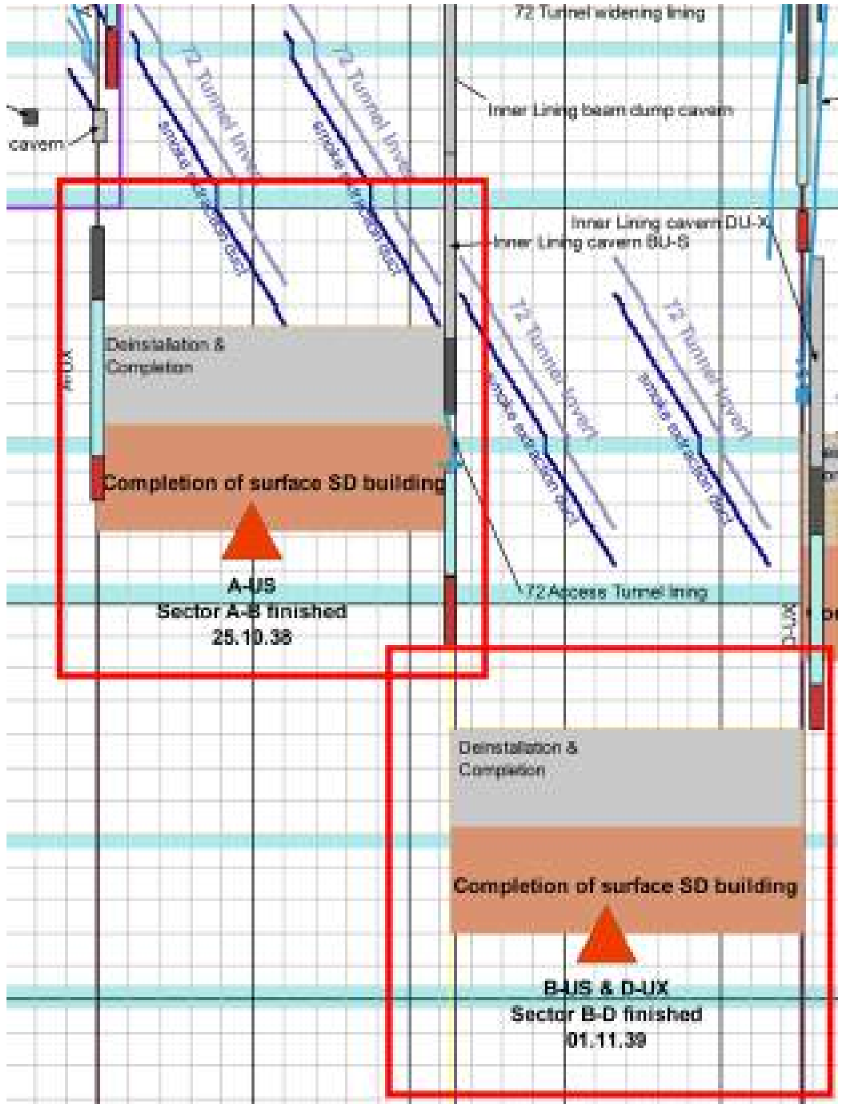

Fig. B.1 Civil engineering previous baseline: one shaft-sector release

the shaft crane serving as the primary bottleneck, as each magnet requires 90 minutes to be lowered. To complete magnet installation within a year, at least two trailers will be necessary.

All cabling will be pre-installed, allowing for system connections to take place after the installation of magnets and vacuum systems. Fire safety doors will be installed at the final stage once all magnets and cavities at points PH and PL are in place. As a result, the final safety systems will only become operational after the full installation of the accelerator. Until then, only temporary safety systems will be in place during the installation phase.

Once all accelerator systems are installed, the commissioning phase will begin, starting with the technical infrastructure. The safety systems will be the first to undergo commissioning, with this phase expected to take approximately six months. Following this, the accelerator commissioning will commence, which is also estimated to last around six months, after which the system will be ready for the first beam tests.

Experiment point installation Experiment shaft installation mainly comprises the installation of the ventilation duct. The installation is expected to be completed within six months. The installation of the experiments is scheduled to take place after the overall accelerator hardware commissioning. A minimum of two years has been allocated for installing each experiment within the cavern. The total available time for the installation of each experiment ranges between four and five years. Table B.3 provides an overview of the start dates and duration of the experiment installations.

Installation at points with radiofrequency systems Radiofrequency equipment will be installed in point PH and in point PL. The installation planning focuses on two main areas: the klystron galleries and the long straight section

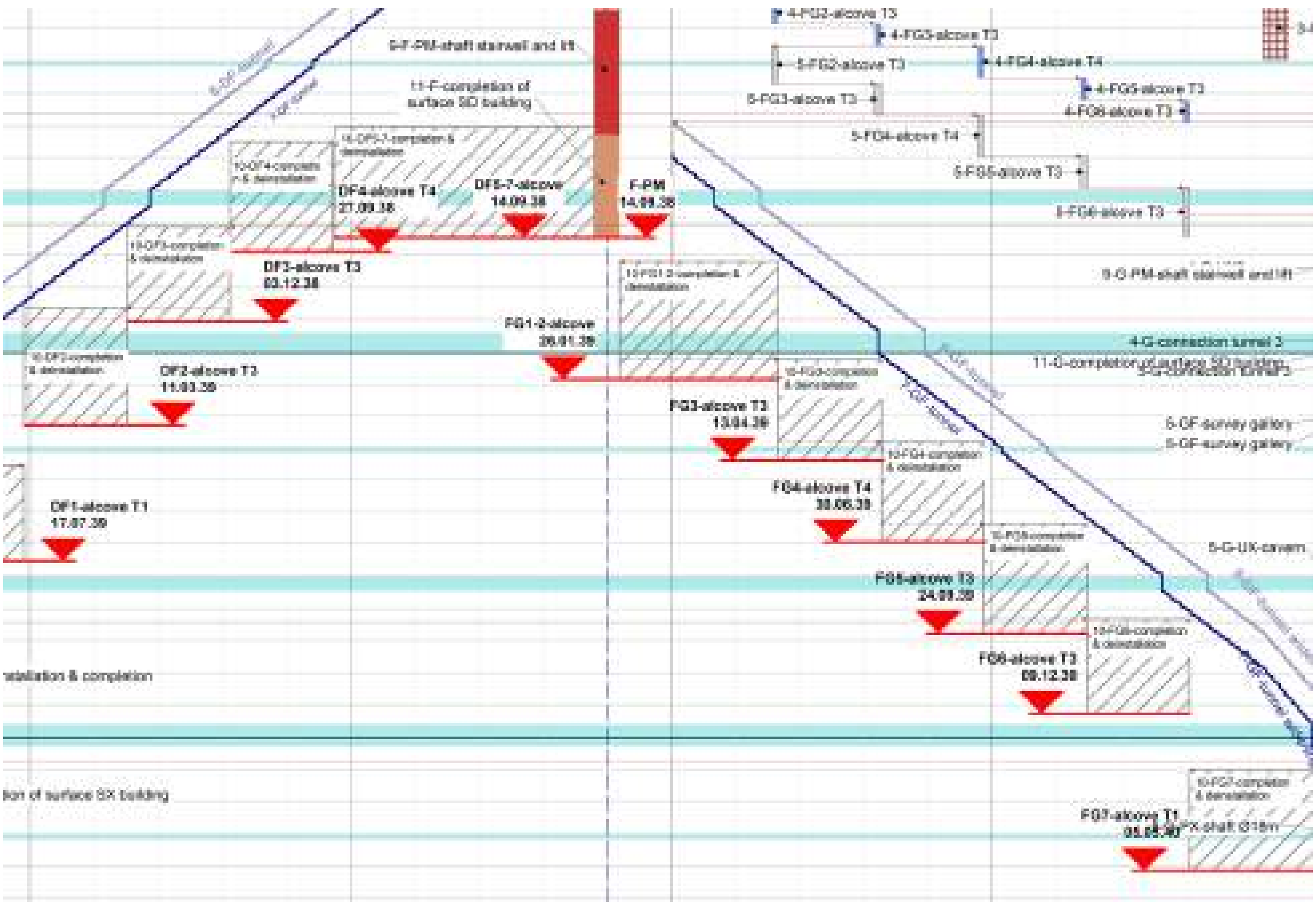

Fig. B.2 Civil engineering current baseline: the staged handover of the arc

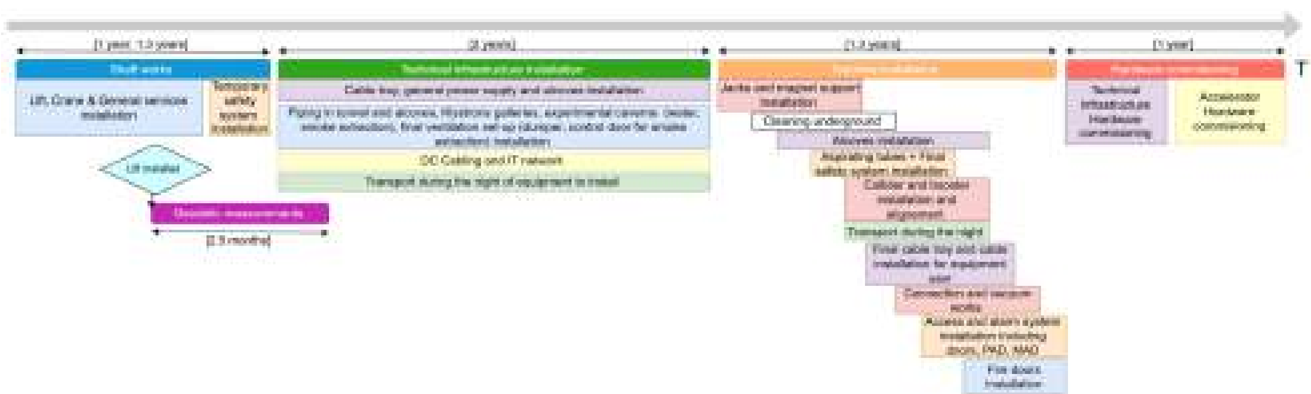

Fig. B.3 Sector sequence for installation

(LSS). Cavities and klystrons will be installed to support all stages of FCC-ee operation, ensuring readiness for the full accelerator lifecycle.

In the klystron gallery, the technical infrastructure will be installed first to ensure the availability of general services in this area. The rate of installation is assumed to be the same as in the tunnel. Following this, the cores will be equipped with waveguides and cable trays using the space from the centre of the galleries to the edges. Two months after the start of core installation, klystron and the low-level RF and control installation will commence.

In the LSS, once the technical infrastructure has been installed, the cryogenic distribution line (QRL) installation can start. Since the cavities will be delivered from point PJ and that the sector H-J is being installed from PH to PJ with magnets, the cavity installation will therefore only start when the transport of magnets has been completed

Table B.2 Handover dates from civil engineering for the machine shaft (PM), experiment shaft (PX) and first alcove

Location	Handover to CERN (2025 update)
PA PX	Mar - 41
PA PM	Feb - 39
A - B Alcove	Jan - 39
PB PM	Nov - 38
B - D Alcove	Nov - 38
PD PX	May - 40
PD PM	April - 38
D - F Alcove	Sep - 38
PF PM	Sep - 38
F - G Alcove	Jan - 39
PG PX	Apr - 41
PG PM	Feb - 39
G - H Alcove	May - 40
PH PM	Dec - 39
H - J Alcove	Sep - 39
PJ PX	Sep - 40
PJ PM	Jun - 38
J - L Alcove	Jun - 39
PL PM	Jun - 39
L - A Alcove	Jun - 39

Table B.3 Experiment installation start date and duration

Point	Start date	Duration in years
PA	11/09/2041	4.4
PD	11/11/2040	5.2
PG	12/10/2041	4.2
PJ	14/03/2041	4.8

for space reasons. Once the cavities have been placed, the connection under clean room conditions between the cavities will take place and two weeks later, other general connection work for the waveguides and controls will be done. Then, cryogenic hardware commissioning will be carried out. After the sector hardware commissioning of the technical infrastructure is completed, a one-year period is planned for cavity conditioning. The sequence is shown in Fig. B.4. The duration depends on the number of systems to be installed at each point.

Strategy for global installation schedule phase The installation strategy involves deploying a maximum of four teams working in parallel on the same type of task, such as shaft works, technical infrastructure, and machine installation. As a result, the start of certain activities may be delayed until the necessary resources become available.

In the previous baseline, the resource usage was organised on a first ready, first installed basis. Including the radiofrequency sequence into the overall schedule has an impact on the critical path and to optimise the latter, resources were allocated in priority to points PH, PJ and PL which will host radiofrequency installation or its transport.

For most sectors benefiting from the staged release for the installation of technical infrastructure, the installation will proceed in the same direction as the civil engineering handover, moving from the technical point to the experiment point. The machine installation follows a sequential 'train' approach to streamline transport logistics, adhering to the same direction—from the technical point to the experiment point.

Overall planning installation Figure B.5 shows overall planning for FCC-ee with the location in the machine indicated across the top and the timeline on each side. Main blocks of activities shown are:

- Civil engineering works.

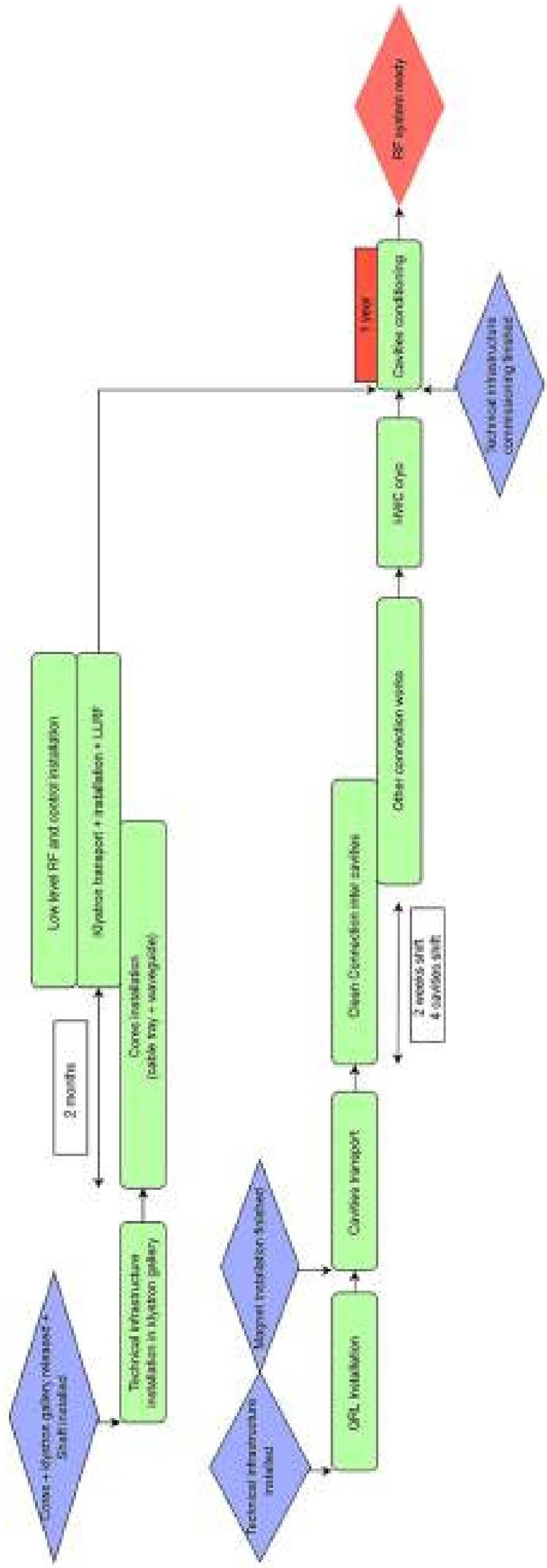

Fig. B.4 Radiofrequency equipment installation sequence

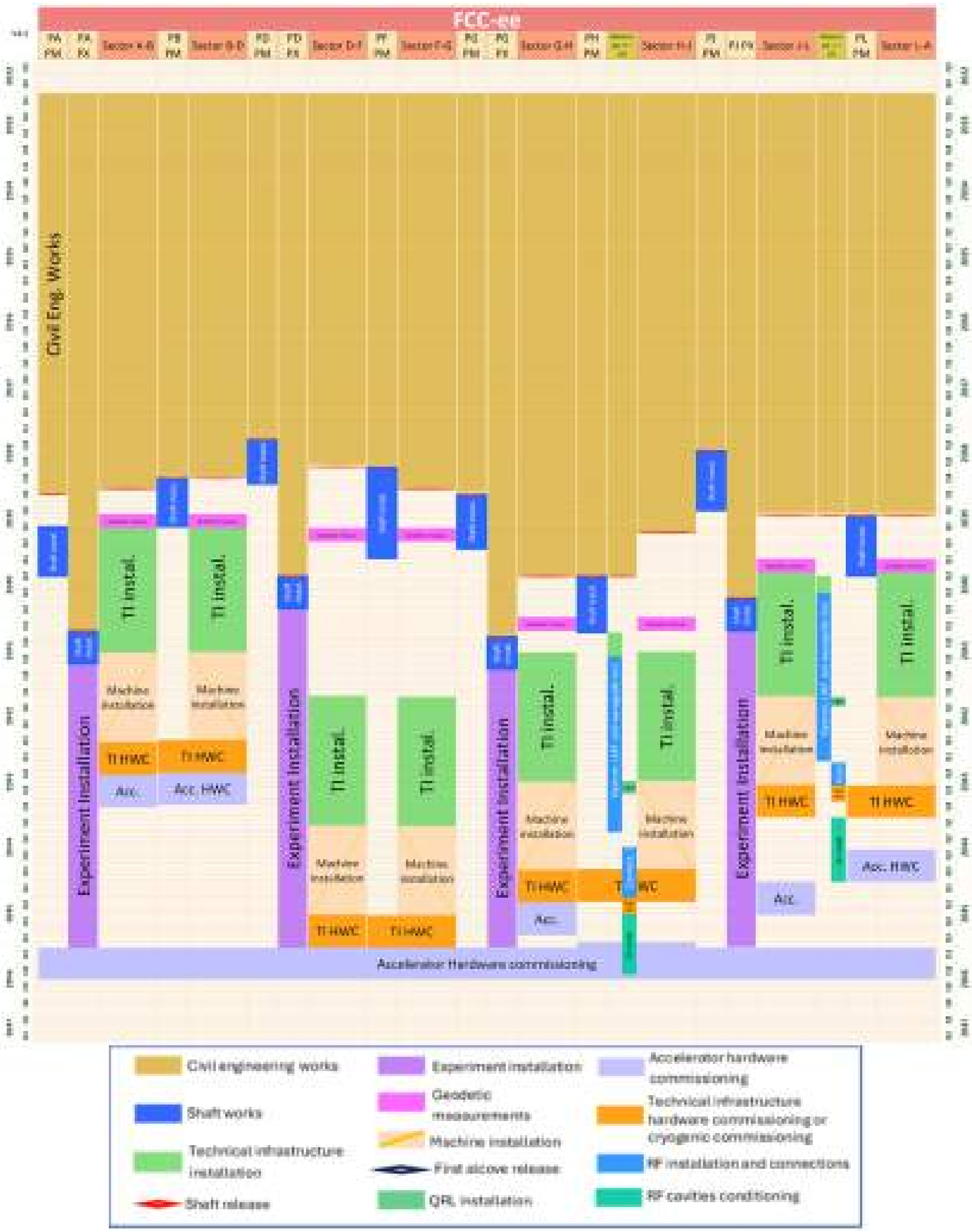

Fig. B.5 Overall linear planning for FCC-ee. The durations of all activities are counted as calendar days. PM is the machine shaft and PX, the experiment shaft

- Shaft and sector civil engineering release date.
- Shaft works, technical infrastructure installation, machine installation and hardware commissioning depicted with a direction line.

The critical path is driven by two sequences:

- The resource levelling from sectors J-L and L-A to sectors D-F and F-G
- The handover date of PH PM and the RF installation at point PH

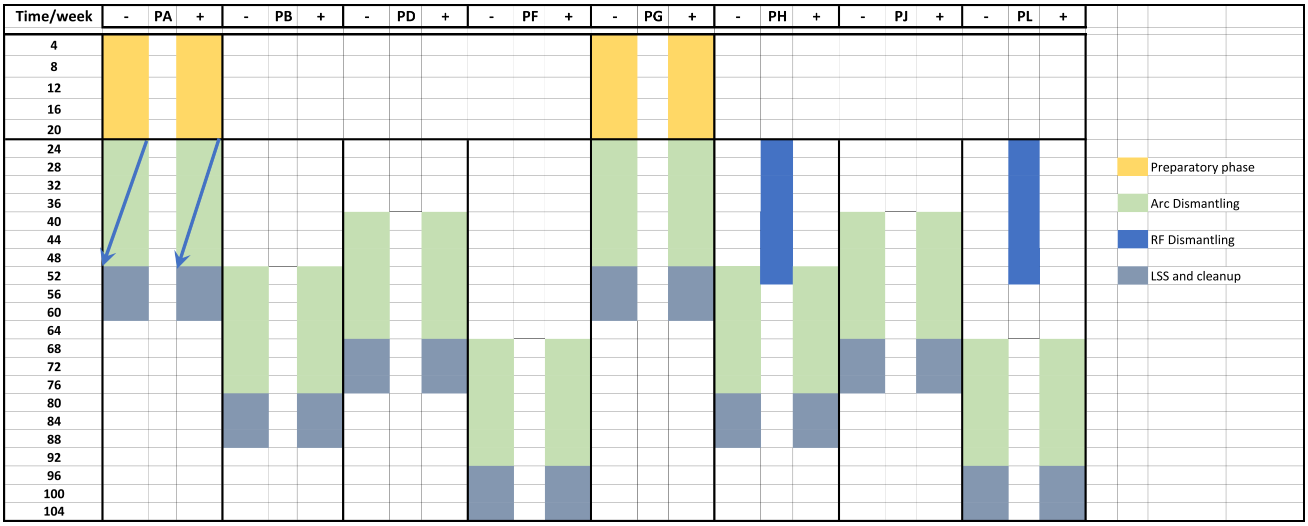

Fig. B.6 Planning for dismantling FCC-ee

The current schedule gives the overall machine readiness for beam in **July 2046**. The durations of all activities are provided as calendar days.

B.1.3 Dismantling FCC-ee

Introduction This section presents a high-level schedule for the period covering the dismantling of FCC-ee to the installation of the FCC-hh machine and its related infrastructure. The time period covered is from the stop of the beam at the end of 2062 to the readiness for beam commissioning in 2073. The key phases are the following:

- Stop of FCC-ee beam at the end of 2062
- Dismantling activities end 2063 – end 2065
- Installation phase 2066 - 2073

Dismantling FCC-ee Since the FCC-ee and FCC-hh machines are different in terms of equipment inside the machine, the whole machine in the arc, the LSS and the experiment will be dismantled. A specific study [323] addressed the dismantling activities foreseen to transition from FCC-ee to FCC-hh. Figure B.6 from this study indicates that it is possible to complete the dismantling of FCC-ee in 2-years. The study also found that it should be possible to dismantle the experiments within this time frame as well.

For the overall planning, a 2-year duration for dismantling was considered independently of the study. In the arc, most of the equipment will be removed from the tunnel: instrumentation, collider and booster magnets, vacuum equipment, cabling for magnets, magnet supports and alignment structures, power converters and related cabling located in the alcoves and the cooling circuit for magnets. In the FCC-ee RF points, point PH and PL, the cavities and QRL will be dismantled.

Civil engineering construction To support the operation of FCC-hh, additional civil engineering constructions will be undertaken.

- Transfer lines
- Beam dump at point PF

Civil engineering has not yet conducted a detailed study of the durations, but the beam dump at point PF has been identified as the most time-critical. As long as the beam dump at point PF is completed within 3.5 years—starting concurrently with dismantling at the end of 2063—it will not impact the schedule.

B.1.4 Installation of FCC-hh

Equipment kept and updated from FCC-ee The technical infrastructures (ventilation, power, network) from FCC-ee will remain for FCC-hh.

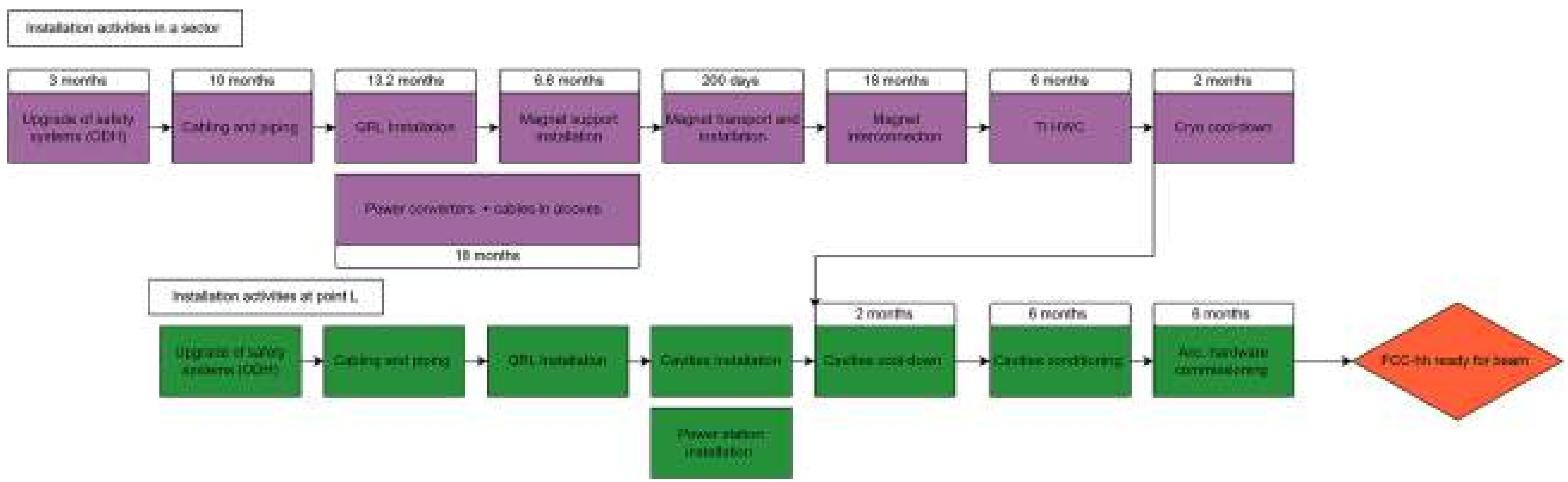

Fig. B.7 Installation sequence for FCC-hh

Installation of a sector Given the long operational lifetime of FCC-ee, an upgrade of the safety systems will be required. This will be followed by installation of specific cabling and piping for FCC-hh. Next the Quench Recovery Line (QRL) will be installed, to provide cryogenics for the superconducting magnets of the machine. The magnet supports will be installed next, followed by the magnets and their interconnection.

Installation at an RF point In point PL, which will be the point where the radiofrequency equipment will be installed, there will also be an upgrade of safety systems, cabling and piping and then QRL installation followed by installation of the cavities.

There will be technical infrastructure hardware commissioning, cryogenic cool down in each sector and in point PL cavity conditioning.

To finish installation activities, each sector will have accelerator hardware commissioning and finally there will be global hardware commissioning for the whole machine.

General strategy for installation (priorities concerning civil engineering works) Similar to the FCC-ee machine, a maximum of four teams can work on the same type of activity simultaneously. The planning (Fig. B.7) is, therefore, driven by the resource levelling and the shift pattern it implies.

Priorities for resource usage have been determined considering the radiofrequency equipment to be installed in point PL and the beam dump (the most critical construction) in point PF. The first sectors to start installation activities are A-B, B-D, J-L and L-A, allowing point PL to be installed as soon as possible. Then sectors D-F, F-G, G-H and H-J can be installed once the resources are available.

This plan creates some contingency for civil engineering to build the beam dump at point PF and limits its potential impact on the readiness for beam commission.

There are 3.5 years starting from the dismantling activities at the end of 2063 which are idle time as a result of the resource levelling in point PF. These 3.5 years can be used to build the beam dump at point PF without having an impact on the beam commissioning date.

The overall planning is divided into two phases:

- Dismantling activities for 2 years
- Installation activities for 8 years

The transition from FCC-ee to FCC-hh is planned to be completed within 10 years, ensuring a timely and efficient upgrade process.

The FCC-hh would be ready for beam commissioning in **2073**.

Funding information Open access funding provided by CERN (European Organization for Nuclear Research).

Data availability The authors declare that the data supporting the findings of this study are available within the paper and/or its supplementary information files.

References

1. D. Shatilov, How to increase the physics output per MW.h for FCC-ee? - Parameter optimization for maximum luminosity. Eur. Phys. J. Plus **137**(1), 159 (2022). https://doi.org/10.1140/epjp/s13360-022-02346-x
2. M.A. Valdivia Garcia, F. Zimmermann, Beam blow up due to beamstrahlung in circular e^+e^- colliders. Eur. Phys. J. Plus **136**(5), 501 (2021). https://doi.org/10.1140/epjp/s13360-021-01485-x
3. K. Ohmi, N. Kuroo, K. Oide, D. Zhou, F. Zimmermann, Coherent beam-beam instability in collisions with a large crossing angle. Phys. Rev. Lett. **119**, 134801 (2017). https://doi.org/10.1103/PhysRevLett.119.134801
4. F. Bordry, M. Benedikt, O. Bruning, J. Jowett, L. Rossi, D. Schulte, S. Stapnes, F. Zimmermann, Machine Parameters and Projected Luminosity Performance of Proposed Future Colliders at CERN. Tech. Rep. CERN, Geneva (2018). https://cds.cern.ch/record/2645151
5. M. Schaumann, Potential performance for pb-pb, *p*-pb, and *p*-*p* collisions in a future circular collider. Phys. Rev. Spec. Top., Accel. Beams **18**, 091002 (2015). https://doi.org/10.1103/PhysRevSTAB.18.091002. https://link.aps.org/doi/10.1103/PhysRevSTAB.18.091002

6. J. Jowett, in *Proc. 9th International Particle Accelerator Conference (IPAC'18)*, Vancouver, BC, Canada, April 29–May 4, 2018, International Particle Accelerator Conference, vol. 9 (JACoW Publishing, Geneva, 2018), pp. 584–589. https://doi.org/10.18429/JACoW-IPAC2018-TUXGBD2
7. M. Schaumann, J.M. Jowett, C. Bahamonde Castro, R. Bruce, A. Lechner, T. Mertens, Bound-free pair production from nuclear collisions and the steady-state quench limit of the main dipole magnets of the cern large hadron collider. Phys. Rev. Accel. Beams **23**, 121003 (2020). https://doi.org/10.1103/PhysRevAccelBeams.23.121003. https://link.aps.org/doi/10.1103/PhysRevAccelBeams.23.121003
8. O. Brüning, L. Rossi, The high-luminosity large hadron collider. Nat. Rev. Phys. **1**(4), 241–243 (2019). https://doi.org/10.1038/s42254-019-0050-6
9. I. Béjar Alonso, O. Brüning, P. Fessia, L. Rossi, L. Tavian, M. Zerlauth, *High-Luminosity Large Hadron Collider (HL–LHC): Technical Design Report*. CERN Yellow Reports: Monographs (CERN, Geneva, 2020). https://doi.org/10.23731/CYRM-2020-0010
10. A. Abada, et al., FCC-hh: the hadron collider: future circular collider conceptual design report volume 3. Eur. Phys. J. Spec. Top. **228**, 755–1107 (2019). https://doi.org/10.1140/epjst/e2019-900087-0
11. M. Zobov, D. Alesini, M.E. Biagini, C. Biscari, A. Bocci, et al., Test of "crab-waist" collisions at the DAΦNE Φ factory. Phys. Rev. Lett. **104**, 174801 (2010). https://doi.org/10.1103/PhysRevLett.104.174801
12. D. Zhou, K. Ohmi, Y. Funakoshi, Y. Ohnishi, Y. Zhang, Simulations and experimental results of beam-beam effects in superkekb. Phys. Rev. Accel. Beams **26**, 071001 (2023). https://doi.org/10.1103/PhysRevAccelBeams.26.071001
13. A. Abada, et al., FCC-ee: the lepton collider: future cirular collider conceptual design report volume 2. Eur. Phys. J. Spec. Top. **228**(2), 261–623 (2019). https://doi.org/10.1140/epjst/e2019-900045-4
14. D. Shatilov, FCC-ee parameter optimization. ICFA Beam Dyn. Newsl. **72**, 30–41 (2017). https://cds.cern.ch/record/2816655
15. P. Kicsiny, D. Zhou, X. Buffat, T. Pieloni, M. Seidel, Incoherent horizontal emittance growth due to the interplay of beam-beam and longitudinal wakefield in crab-waist colliders (2025). arXiv:2501.04609 [physics.acc-ph]
16. D. Shatilov, Fcc-ee parameter optimization. ICFA Beam Dyn. Newsl. **72**, 30–41 (2017)
17. M.H.R. Donald, J.M. Paterson, An investigation of the 'flip-flop' beam-beam effect in SPEAR, in *Proc. PAC'79*, San Francisco, CA, USA (1979)
18. P. Kicsiny, X. Buffat, K. Le Nguyen Nguyen, T. Pieloni, M. Seidel, Impact of beam asymmetries at the future circular collider e^+e^-. Phys. Rev. Accel. Beams **27**, 121001 (2024). https://doi.org/10.1103/PhysRevAccelBeams.27.121001
19. M. Boscolo, H. Burkhardt, M. Sullivan, Machine detector interface studies: layout and synchrotron radiation estimate in the future circular collider interaction region. Phys. Rev. Accel. Beams **20**, 011008 (2017). https://doi.org/10.1103/PhysRevAccelBeams.20.011008
20. K. Oide, M. Aiba, S. Aumon, M. Benedikt, A. Blondel, et al., Design of beam optics for the future circular collider e^+e^- collider rings. Phys. Rev. Accel. Beams **19**, 111005 (2016). https://doi.org/10.1103/PhysRevAccelBeams.19.111005
21. T. Charles, et al., Alignment & stability Challenges for FCC-ee. EPJ Tech. Instrum. **10** (2023). https://doi.org/10.1140/epjti/s40485-023-00096-3
22. R. Tomas, et al., Progress of the fcc-ee optics tuning working group (2023) Paper presented at IPAC 2023, Venezia, Italy. https://doi.org/10.18429/JACoW-IPAC2023-WEPL023
23. R. Tomás, et al., CERN large hadron collider optics model, measurements, and corrections. Phys. Rev. Accel. Beams **13**, 121004 (2010). https://doi.org/10.1103/PhysRevSTAB.13.121004
24. B. Dehning, J. Matheson, G. Mugnai, I. Reichel, R. Schmidt, F. Sonnemann, F. Tecker, Beam based alignment at lep. Nucl. Instrum. Methods Phys. Res., Sect. A, Accel. Spectrom. Detect. Assoc. Equip. **516**(1), 9–20 (2004). https://doi.org/10.1016/j.nima.2003.07.039
25. R. Assmann, P. Raimondi, G. Roy, J. Wenninger, Emittance optimization with dispersion free steering at lep. Phys. Rev. Spec. Top., Accel. Beams **3**, 121001 (2000). https://doi.org/10.1103/PhysRevSTAB.3.121001. https://link.aps.org/doi/10.1103/PhysRevSTAB.3.121001
26. P. Raimondi, P. Emma, N. Toge, N. Walker, V. Ziemann (2025). C.U.S. Stanford Linear Accelerator Center, Menlo Park. Beam based alignment of the SLC final focus superconducting final triplets
27. R.W. Assmann, Beam dynamics in SLC. Conf. Proc. C **970512**, 1331 (1997)
28. E. Musa, I. Agapov, T. Charles, Optics tuning simulations for FCC-ee using Python Accelerator Toolbox (2024). https://arxiv.org/abs/2410.24129
29. N. Toge, et al., New final focus system for the SLAC linear collider. Conf. Proc. C **910506**, 2152–2154 (1991)
30. P. Raimondi, P.J. Emma, N. Toge, N.J. Walker, V. Ziemann, in *1993 IEEE Particle Accelerator Conference (PAC 93)* (1993), pp. 100–101
31. K. Oide, in *Proceedings of the FCC Week 2024* (San Francisco, California, U.S.A., 2024). Presentation slides available at https://indico.cern.ch/event/1298458/contributions/5977859/attachments/2873388/5034194/Optics_Oide_240611.pdf
32. P. Raimondi, S.M. Liuzzo, M. Hofer, L. Farvacque, S. White, Local chromatic correction optics for future circular collider e+e. Phys. Rev. Accel. Beams (2024). Submitted October 2024
33. K. Skoufaris, Sextupolar phase advance tolerances and impact of GM waves on DA (2024). Presentation at the FCC-ee Tuning Working Group Meeting. https://indico.cern.ch/event/1421227/
34. J. Keintzel, Phase advance errors between crab sextupoles in GHC (2024). Presentation at the FCC-ee Tuning Working Group Meeting. https://indico.cern.ch/event/1477971/

35. M. Bai, in *Proc. 1999 Particle Accelerator Conference (Cat. No. 99CH36366)*, vol. 1 (IEEE, 1999), pp. 387–391
36. S. Peggs, C. Tang, Nonlinear diagnostics using an AC dipole. Report No. RHIC/AP/159, Brookhaven National Laboratories (1998). https://www.rhichome.bnl.gov/RHIC/RAP/rhic_notes/RHIC-AP-1-177/RHIC-AP-159.pdf
37. R. Tomás, Adiabaticity of the ramping process of an ac dipole. Phys. Rev. Spec. Top., Accel. Beams **8**, 024401 (2005). https://doi.org/10.1103/PhysRevSTAB.8.024401
38. S. White, E. Maclean, R. Tomás, Direct amplitude detuning measurement with ac dipole. Phys. Rev. Spec. Top., Accel. Beams **16**, 071002 (2013). https://doi.org/10.1103/PhysRevSTAB.16.071002
39. F. Carlier, R. Tomás, E. Maclean, T. Persson, First experimental demonstration of forced dynamic aperture measurements with LHC ac dipoles. Phys. Rev. Accel. Beams **22**, 031002 (2019). https://doi.org/10.1103/PhysRevAccelBeams.22.031002
40. N. Biancacci, R. Tomás, Using ac dipoles to localize sources of beam coupling impedance. Phys. Rev. Accel. Beams **19**, 054001 (2016). https://doi.org/10.1103/PhysRevAccelBeams.19.054001
41. R. Tomás, Normal form of particle motion under the influence of an ac dipole. Phys. Rev. Spec. Top., Accel. Beams **5**, 054001 (2002). https://doi.org/10.1103/PhysRevSTAB.5.054001
42. K. Skoufaris, Beam dynamics in FCC-ee with reduced sextupole strength, in *Presentation at the 200th FCC-ee Accelerator Design Meeting and 71st FCCIS WP2.2 Meeting* (2025). https://indico.cern.ch/event/1497833/
43. R. Tomas, Status of optics correction studies. Presentation at the FCC-Week 2024 (2024). https://indico.cern.ch/event/1298458/
44. C. Garcia-Jaimes, Update of the ballistic optics for FCC-ee. Presentation at the FCC-ee Tuning Working Group Meeting (2024). https://indico.cern.ch/event/1477971/
45. L. van Riesen-Haupt, et al., Relaxed insertion region optics and linear tuning knobs for the Future Circular Collider. JACoW IPAC **2024**, WEPR04.pdf (2024). https://doi.org/10.18429/JACoW-IPAC2024-WEPR04
46. D. Shatilov, Tolerances on the Vertical Dispersion at the IP, in *74th FCC-ee Optics Design Meeting*. https://indico.cern.ch/event/742015/contributions/3065805/attachments/1682394/2703323/dispy_IP.pdf (2018)
47. R. Tomas, M. Aiba, A. Franchi, U. Iriso, Review of linear optics measurement and correction for charged particle accelerators. Phys. Rev. Accel. Beams **20**, 054801 (2017). https://doi.org/10.1103/PhysRevAccelBeams.20.054801
48. M. Hofer, R. Tomás, Coupling levels in the fcc-ee (2023). https://indico.cern.ch/event/1274521/
49. A. Hussain, Progress with multipolar tolerances. FCC-ee optics tuning working Group meeting May 2024. https://indico.cern.ch/event/1421227/. Accessed: 2025-02-05
50. L. van Riesen-Haupt, A. Franchi, A. Faus-Golfe, A. Chance, B. Dalena, et al., The status of the FCC-ee optics tuning. JACoW IPAC **2024**, WEPR02 (2024). https://doi.org/10.18429/JACoW-IPAC2024-WEPR02
51. J. Bauche, et al., Field corrections for FCC-ee magnets. Presented at the Optics Tuning and Corrections for future colliders workshop. CERN (2023). https://indico.cern.ch/event/1242395/
52. J. Bauche, C. Eriksson, F. Saeidi, FCC-ee Collider Magnets. Presented at the 2023 FCCIS WP2 Workshop. https://indico.cern.ch/event/1326738/
53. L. Deniau, et al., The magnetic model of the lhc during commissioning to higher beam intensities. IPAC 2011 (2011). https://accelconf.web.cern.ch/ipac2011/papers/wepo031.pdf
54. E.H. Maclean, et al., First measurement and correction of nonlinear errors in the experimental insertions of the cern large hadron collider. Phys. Rev. Spec. Top., Accel. Beams **18**, 121002 (2015). https://indico.cern.ch/event/1217778/contributions/5122924/attachments/2543790/4380178/221108_BoosterSupportDesign.pdf
55. Y. Wu, Spin tune shifts. Presented at the 8th FCC Physics Workshop, CERN (2025). https://indico.cern.ch/event/1439509/
56. N. Mounet, The LHC transverse coupled bunch instability. Ph.D. thesis, École Polytechnique Fédérale de Lausanne, Lausanne, Switzerland (2012). https://doi.org/10.5075/epfl-thesis-5305
57. A. Rajabi, Precise resistive-wall impedance calculation in vacuum chambers with general cross-sections, in *Proc. of the 14th International Particle Accelerator Conf. (IPAC'23)*, Venice, Italy (2023). https://doi.org/10.18429/jacow-ipac2023-wepl124
58. PyHEADTAIL. https://github.com/PyCOMPLETE/PyHEADTAIL. Accessed: 2023-06-05
59. M. Migliorati, L. Palumbo, Multibunch and multiparticle simulation code with an alternative approach to wakefield effects. Phys. Rev. Spec. Top., Accel. Beams **18**, 031001 (2015). https://doi.org/10.1103/PhysRevSTAB.18.031001
60. M. Migliorati, S. Persichelli, H. Damerau, S. Gilardoni, S. Hancock, L. Palumbo, Beam-wall interaction in the CERN proton synchrotron for the LHC upgrade. Phys. Rev. Spec. Top., Accel. Beams **16**, 031001 (2013). https://doi.org/10.1103/PhysRevSTAB.16.031001
61. E. Métral, M. Migliorati, Longitudinal and transverse mode coupling instability: Vlasov solvers and tracking codes. Phys. Rev. Accel. Beams **23**, 071001 (2020). https://doi.org/10.1103/PhysRevAccelBeams.23.071001
62. Y. Zhang, N. Wang, M. Migliorati, E. Carideo, M. Zobov, in *Proc. IPAC'21* (JACoW Publishing, Geneva, 2021), pp. 25–30. https://doi.org/10.18429/JACoW-IPAC2021-MOXC01
63. Y. Zhang, K. Ohmi, L. Chen, Simulation study of beam-beam effects. Phys. Rev. Spec. Top., Accel. Beams **8**, 074402 (2005). https://doi.org/10.1103/PhysRevSTAB.8.074402
64. Y. Zhang Private communication (2024)
65. Xsuite. https://xsuite.readthedocs.io/
66. S. White, X. Buffat, N. Mounet, T. Pieloni, Transverse mode coupling instability of colliding beams. Phys. Rev. Spec. Top., Accel. Beams **17**, 041002 (2014). https://doi.org/10.1103/PhysRevSTAB.17.041002

67. Y. Zhang, N. Wang, K. Ohmi, D. Zhou, T. Ishibashi, C. Lin, Combined phenomenon of transverse impedance and beam-beam interaction with large piwinski angle. Phys. Rev. Accel. Beams **26**, 064401 (2023). https://doi.org/10.1103/PhysRevAccelBeams.26.064401
68. R. Soos, X. Buffat, in *Proceedings of the ICFA Mini Workshop on Beam-Beam Effects in Circular Colliders*, ed. by W. Herr, L. van Riesen-Haupt (CERN, Geneva, 2024)
69. K. Ohmi, Beam-photoelectron interactions in positron storage rings. Phys. Rev. Lett. **75**, 1526–1529 (1995). https://doi.org/10.1103/PhysRevLett.75.1526
70. G. Rumolo, F. Ruggiero, F. Zimmermann, Simulation of the electron-cloud build up and its consequences on heat load, beam stability, and diagnostics. Phys. Rev. Spec. Top., Accel. Beams **4**, 012801 (2001). https://doi.org/10.1103/PhysRevSTAB.4.012801
71. F. Zimmermann, Review of single bunch instabilities driven by an electron cloud. Phys. Rev. Spec. Top., Accel. Beams **7**, 124801 (2004). https://doi.org/10.1103/PhysRevSTAB.7.124801
72. O. Domínguez, K. Li, G. Arduini, E. Métral, G. Rumolo, F. Zimmermann, H.M. Cuna, First electron-cloud studies at the large hadron collider. Phys. Rev. Spec. Top., Accel. Beams **16**, 011003 (2013). https://doi.org/10.1103/PhysRevSTAB.16.011003
73. PyECLOUD. https://github.com/PyCOMPLETE/PyECLOUD. Accessed: 2025-02-05
74. L. Sabato, T. Pieloni, G. Iadarola, L. Mether, J. Phys. Conf. Ser. **2687**, 062029 (2024). https://doi.org/10.1088/1742-6596/2687/6/062029
75. R. Cimino, I.R. Collins, M.A. Furman, M. Pivi, F. Ruggiero, G. Rumolo, F. Zimmermann, Can low-energy electrons affect high-energy physics accelerators? Phys. Rev. Lett. **93**, 014801 (2004). https://doi.org/10.1103/PhysRevLett.93.014801
76. V. Baglin, I. Collins, B. Henrist, N. Hilleret, G. Vorlaufer, A summary of main experimental results concerning the secondary electron emission of copper. Tech. Rep. LHC-Project-Report-472, CERN, Geneva (2001). https://cds.cern.ch/record/512467
77. B. Henrist, N. Hilleret, M. Jiménez, C. Scheuerlein, M. Taborelli, G. Vorlaufer, Secondary electron emission data for the simulation of electron cloud, in *Proc. of ECLOUD'02* (CERN, Geneva, 2002). https://cds.cern.ch/record/585565
78. R. Cimino, I. Collins, Vacuum chamber surface electronic properties influencing electron cloud phenomena. Appl. Surf. Sci. **235**(1), 231–235 (2004). https://doi.org/10.1016/j.apsusc.2004.05.270
79. M.A. Furman, M.T.F. Pivi, Probabilistic model for the simulation of secondary electron emission. Phys. Rev. Spec. Top., Accel. Beams **5**, 124404 (2002). https://doi.org/10.1103/PhysRevSTAB.5.124404
80. F. Yaman, G. Iadarola, R. Kersevan, et al., Mitigation of electron cloud effects in the FCC-ee collider. EPJ Tech. Instrum. **9** (2022). https://doi.org/10.1140/epjti/s40485-022-00085-y
81. E. Belli, P.C. Pinto, G. Rumolo, A. Sapountzis, T. Sinkovits, M. Taborelli, B. Spataro, M. Zobov, G. Castorina, M. Migliorati, Electron cloud buildup and impedance effects on beam dynamics in the future circular e^+e^- collider and experimental characterization of thin TiZrV vacuum chamber coatings. Phys. Rev. Accel. Beams **21**, 111002 (2018). https://doi.org/10.1103/PhysRevAccelBeams.21.111002
82. Y. Suetsugu, K. Kanazawa, K. Shibata, H. Hisamatsu, Continuing study on the photoelectron and secondary electron yield on TiN coating and NEG (Ti-Zr-V) coating under intense photon irradiation at the KEKB positron ring. Nucl. Instrum. Meth. A **556**, 399–409 (2006). https://doi.org/10.1016/j.nima.2005.10.113
83. B. Humann, F. Cerutti, R. Kersevan, Synchrotron radiation impact on the FCC-ee arcs, in *Proc. 13th International Particle Accelerator Conference (IPAC'22)*, Bangkok, Thailand (2022). https://doi.org/10.18429/JACoW-IPAC2022-WEPOST002
84. G.Y. Hsiung, C.M. Cheng, R. Valizadeh, Measurement of the photoelectron yield from the synchrotron radiation for the neg-coated tubes. J. Phys. Conf. Ser. **2687**(8), 082027 (2024). https://doi.org/10.1088/1742-6596/2687/8/082027
85. M. Morrone, et al., Preliminary design of the fcc-ee vacuum chamber absorbers. J. Phys. Conf. Ser. **2687**, 022011 (2024). https://doi.org/10.1088/1742-6596/2687/2/022011
86. G. Rumolo, et al., Electron cloud simulations: beam instabilities and wakefields. Phys. Rev. Accel. Beams **5**, 121002 (2002). https://doi.org/10.1103/PhysRevSTAB.5.121002
87. K. Ohmi, F. Zimmermann, Head-tail instability caused by electron clouds in positron storage rings. Phys. Rev. Lett. **85**, 3821–3824 (2000). https://doi.org/10.1103/PhysRevLett.85.3821
88. K. Ohmi, F. Zimmermann, E. Perevedentsev, Wake-field and fast head-tail instability caused by an electron cloud. Phys. Rev. E **65**(1), 016502 (2001). https://doi.org/10.1103/PhysRevE.65.016502
89. K. Ohmi, Beam–beam and electron cloud effects in CEPC/FCC-ee. Int. J. Mod. Phys. A **31**(33), 1644014 (2016). https://doi.org/10.1142/S0217751X16440140
90. G. Iadarola, E. Belli, K.S.B. Li, L. Mether, A. Romano, G. Rumolo, Evolution of Python tools for the simulation of electron cloud effects, in *Proc. 8th Int. Particle Accelerator Conf. (IPAC'17)*, Copenhagen, Denmark (2017). https://doi.org/10.18429/JACoW-IPAC2017-THPAB043
91. M. Migliorati, et al., Studies of fcc-ee single bunch instabilities with an updated impedance model. J. Phys. Conf. Ser. **2687**, 062010 (2024). https://doi.org/10.1088/1742-6596/2687/6/062010
92. G. Iadarola, B. Bradu, P. Dijkstal, L. Mether, G. Rumolo, Impact and mitigation of electron cloud effects in the operation of the large hadron collider, in *Proc. 8th Int. Particle Accelerator Conf. (IPAC'17)*, Copenhagen, Denmark (2017). https://doi.org/10.18429/JACoW-IPAC2017-TUPVA019

93. F.J. Decker, M.H.R. Donald, R.C. Field, A. Kulikov, J.T. Seeman, M. Sullivan, U. Wienands, W. Kozanecki, Complicated bunch pattern in PEP-II, in *Proc. Particle Accelerator Conference, PAC'01*, Chicago, IL, USA (2001). https://jacow.org/p01/PAPERS/TPPH126.PDF
94. S.A. Antipov, V. Gubaidulin, I. Agapov, E.C. Cortés García, A. Gamelin, Space charge effects in fourth-generation light sources: the petra iv and soleil ii cases. Phys. Rev. Accel. Beams **28**, 024401 (2025). https://doi.org/10.1103/PhysRevAccelBeams.28.024401
95. V.L. Highland, Some practical remarks on multiple scattering. Nucl. Instrum. Methods **129**(2), 497–499 (1975). https://doi.org/10.1016/0029-554X(75)90743-0
96. C. Benvenuti, R. Calder, O. Gröbner, Vacuum for particle accelerators and storage rings. Vacuum **37**(8–9), 699–707 (1987). https://doi.org/10.1016/0042-207X(87)90057-1
97. P. Møller, Beam-residual gas interactions. Tech. Rep. OPEN-2000-277, CERN (1999). https://doi.org/10.5170/CERN-1999-005.155
98. A.G. Mathewson, S. Zhang, Beam-gas ionisation cross sections at 7.0 TeV (1996). Tech. Rep. CERN, Geneva. https://cds.cern.ch/record/1489148
99. G. Brianti, The stability of ions in bunched-beam machines (1984). https://doi.org/10.5170/CERN-1984-015.369
100. Y. Ohnishi, et al., Accelerator design at SuperKEKB. PTEP **2013**, 03A011 (2013). https://doi.org/10.1093/ptep/pts083
101. K. Akai, K. Furukawa, H. Koiso, Superkekb collider. Nucl. Instrum. Methods Phys. Res., Sect. A, Accel. Spectrom. Detect. Assoc. Equip. **907**, 188–199 (2018)
102. T. Ishibashi, S. Terui, Y. Suetsugu, K. Watanabe, M. Shirai, Movable collimator system for SuperKEKB. Phys. Rev. Accel. Beams **23**, 053501 (2020). https://doi.org/10.1103/PhysRevAccelBeams.23.053501
103. H. Ikeda, Observation of sudden beam loss in SuperKEKB, in *Proc. 14th International Particle Accelerator Conference IPAC'23*, Venezia, Italy (2023). https://doi.org/10.18429/jacow-ipac2023-mopl072
104. M. Hofer, et al., Design of a collimation section for the FCC-ee, in *Proc. IPAC'22 - 13th International Particle Accelerator Conf*, Bangkok, Thailand (2022). https://doi.org/10.18429/JACoW-IPAC2022-WEPOST017
105. G. Broggi, et al., Optimizations and updates of the FCC-ee collimation system design, Proc. of the 15th International Particle Accelerator Conf. (IPAC'24), Nashville, TN, USA. https://doi.org/10.18429/JACoW-IPAC2024-TUPC76
106. G. Broggi, et al., Including beam-beam effects in collimation studies for the FCC-ee, in *Proc. 5th ICFA mini workshop on Beam-Beam Effects in Circular Colliders (BB'24)* (EPFL, Lausanne). To be published https://doi.org/10.18429/JACoW-IPAC2024-TUPC76
107. M. Moudgalya, First studies of the halo collimation needs in the FCC-ee. Master's thesis, Department of Physics, Imperial College, London (2021)
108. M. Aiba, B. Goddard, K. Oide, Y. Papaphilippou, À. Saà Hernàndez, D. Shwartz, S. White, F. Zimmermann, Top-up injection schemes for future circular lepton collider. Nucl. Instrum. Methods. Phys. Res. A **880**, 98–106 (2018). https://doi.org/10.1016/j.nima.2017.10.075
109. R. Bruce, C. Bracco, R. De Maria, M. Giovannozzi, A. Mereghetti, D. Mirarchi, S. Redaelli, E. Quaranta, B. Salvachua, Reaching record-low β^* at the cern large hadron collider using a novel scheme of collimator settings and optics. Nucl. Instrum. Methods. Phys. Res. A **848**, 19–30 (2017). https://doi.org/10.1016/j.nima.2016.12.039
110. R. Bruce, R.W. Assmann, S. Redaelli, Calculations of safe collimator settings and β^* at the CERN large hadron collider. Phys. Rev. Spec. Top., Accel. Beams **18**, 061001 (2015). https://doi.org/10.1103/PhysRevSTAB.18.061001
111. J.B. Jeanneret, Optics of a two-stage collimation system. Phys. Rev. Spec. Top., Accel. Beams **1**, 081001 (1998). https://doi.org/10.1103/PhysRevSTAB.1.081001
112. J. Guardia-Valenzuela, A. Bertarelli, F. Carra, N. Mariani, S. Bizzaro, R. Arenal, Development and properties of high thermal conductivity molybdenum carbide - graphite composites. Carbon **135**, 72–84 (2018). https://doi.org/10.1016/j.carbon.2018.04.010
113. G. Broggi, First study of collimator design for the FCC-ee. Master's thesis, Politecnico di Milano (2022)
114. G. Broggi, A. Abramov, R. Bruce, Beam dynamics studies for the FCC-ee collimation system design, Proc. of the 14th International Particle Accelerator Conf. (IPAC'23), Venice, Italy. https://doi.org/10.18429/jacow-ipac2023-mopa129
115. G. Broggi, Tracking studies for the FCC-ee collimation system design. Nuovo Cimento C **47** (2024). https://doi.org/10.1393/ncc/I2024-24273-x
116. O.S. Brüning, P. Collier, P. Lebrun, S. Myers, R. Ostojic, J. Poole, P. Proudlock, *LHC Design Report. CERN Yellow Rep. Monogr* (CERN, Geneva, 2004). https://doi.org/10.5170/CERN-2004-003-V-1
117. A. Abramov, et al., Development of collimation simulations for the FCC-ee, in *Proc. of the 13th International Particle Accelerator Conf. (IPAC'22)*, Bangkok, Thailand (2022). https://doi.org/10.18429/JACoW-IPAC2022-WEPOST016
118. A. Abramov, et al., Collimation simulations for the FCC-ee. J. Instrum. **19**, T02004 (2024). https://doi.org/10.1088/1748-0221/19/02/T02004
119. G. Iadarola, et al., Xsuite: an integrated beam physics simulation framework, in *Proc. of the 68th ICFA Advanced Beam Dynamics Workshop on High-Intensity and High-Brightness Hadron Beams (HB'23)*, Geneva, Switzerland (2023). https://doi.org/10.18429/JACoW-HB2023-TUA2I1
120. L. Nevay, et al., BDSIM: an accelerator tracking code with particle–matter interactions. Comput. Phys. Commun. **252**, 107200 (2020). https://doi.org/10.1016/j.cpc.2020.107200
121. L. Nevay, et al., BDSIM: automatic Geant4 models of accelerators, in *Proc. ICFA Mini-Workshop on Tracking for Collimation* (CERN, Geneva, 2018), p. 45. https://doi.org/10.23732/CYRCP-2018-002.45

122. F.V. der Veken, et al., Recent developments with the new tools for collimation simulations in Xsuite, in *Proc. of the 68th ICFA Advanced Beam Dynamics Workshop on High-Intensity and High-Brightness Hadron Beams (HB'23)*, Geneva, Switzerland (2023). https://doi.org/10.18429/JACoW-HB2023-THBP13
123. R. Bruce, R. Aßmann, V. Boccone, C. Bracco, M. Brugger, et al., Simulations and measurements of beam loss patterns at the CERN large hadron collider. Phys. Rev. Spec. Top., Accel. Beams **17**(8), 081004 (2014). https://doi.org/10.1103/PhysRevSTAB.17.081004
124. G. Broggi, Beam-gas beam losses and MDI collimators, in *FCC Week 2024*, San Francisco, CA, USA, June 2024 (2024)
125. C. Ahdida, D. Bozzato, D. Calzolari, et al., New capabilities of the FLUKA multi-purpose code. Front. Phys. **9** (2022). https://www.frontiersin.org/article/10.3389/fphy.2021.788253
126. G. Battistoni, et al., Overview of the FLUKA code. Ann. Nucl. Energy **82**, 10–18 (2015). https://doi.org/10.1016/j.anucene.2014.11.007
127. CERN. FLUKA Website. https://fluka.cern
128. M. Boscolo, H. Burkhardt, K. Oide, M.K. Sullivan, IR challenges and the machine detector interface at FCC-ee. Eur. Phys. J. Plus **136**(10), 1068 (2021). https://doi.org/10.1140/epjp/s13360-021-02031-5
129. M. Boscolo, F. Palla, F. Bosi, F. Fransesini, S. Lauciani, Mechanical model for the FCC-ee interaction region. EPJ Tech. Instrum. **10**(1), 16 (2023). https://doi.org/10.1140/epjti/s40485-023-00103-7
130. M. Boscolo, The status of the interaction region design and machine detector interface of the FCC-ee, in *Proc. IPAC'23-14th International Particle Accelerator Conference*, Venezia, Italy (2023). https://doi.org/10.18429/jacow-ipac2023-mopa091
131. M. Boscolo, et al., The FCC-ee interaction region, design and integration of the machine elements and detectors, machine induced backgrounds and key performance indicators (2023). https://doi.org/10.17181/w4kws-rne05
132. M. Boscolo, F. Palla, A. Abramov, M. Aleksa, K.D.J. Andre, et al., The fcc-ee interaction region, design and integration of the machine elements and detectors, machine induced backgrounds and key performance indicators (2023). https://doi.org/10.17181/p4vnt-2va28
133. A. Novokhatski, Estimated heat load and proposed cooling system in the fcc-ee interaction region beam pipe, in *Proc. IPAC'23 - 14th International Particle Accelerator Conference*, Venezia, Italy (2023). https://doi.org/10.18429/jacow-ipac2023-mopa092
134. Th. Brochard, L. Goirand, J. Pasquaud, Dispositif de raccordement entre tronçons d'anneau de synchrotron. B14959 EP, request number 17160419.2-1211 3223591 claiming priority of patent FR 16-52454, Mar. 22, 2016 (2016)
135. L. Watrelot, FCC-ee Machine Detector Interface Alignment System Concepts. Concepts de systemes pour l'alignement de la MDI du FCC-ee. Ph.D. thesis, HESAM U (2023). https://cds.cern.ch/record/2894663. Thesis presented 19 Sep 2023
136. L. Watrelot, M. Sosin, S. Durand, Frequency scanning interferometry based deformation monitoring system for the alignment of the FCC-ee machine detector interface. Meas. Sci. Technol. **34**(7), 075006 (2023). https://doi.org/10.1088/1361-6501/acc6e3
137. M. Sosin, H. Mainaud-Durand, V. Rude, J. Rutkowski, Frequency sweeping interferometry for robust and reliable distance measurements in harsh accelerator environment. Proc. SPIE **11102**, 111020L (2019). https://doi.org/10.1117/12.2529157
138. H. Mainaud Durand, J.C. Gayde, J. Jaros, V. Rude, M. Sosin, A. Zemanek, The new CLIC main linac installation and alignment strategy, in *Proc. IPAC'18*, Vancouver, BC, Canada, April 29-May 4 (2018). https://doi.org/10.18429/JACoW-IPAC2018-WEPAF066
139. L.J. Nevay, et al., BDSIM: an accelerator tracking code with particle–matter interactions. Comput. Phys. Commun. **252**, 107200 (2020). https://doi.org/10.1016/j.cpc.2020.107200. arXiv:1808.10745 [physics.comp-ph]
140. J. Allison, et al., Recent developments in geant4. Nucl. Instrum. Methods Phys. Res., Sect. A, Accel. Spectrom. Detect. Assoc. Equip. **835**, 186–225 (2016). https://doi.org/10.1016/j.nima.2016.06.125
141. K. André, B. Holzer, M. Boscolo, Status of the synchrotron radiation studies in the interaction region of the FCC-ee. JACoW **IPAC2024**, WEPR09 (2024). https://doi.org/10.18429/JACoW-IPAC2024-WEPR09
142. G. Broggi, A. Abramov, K. André, M. Boscolo, M. Hofer, R. Bruce, S. Redaelli, Optimizations and updates of the FCC-ee collimation system design. JACoW **IPAC2024**, TUPC76 (2024). https://doi.org/10.18429/JACoW-IPAC2024-TUPC76
143. M. Boscolo, A. Ciarma, Characterization of the beamstrahlung radiation at the future high-energy circular collider. Phys. Rev. Accel. Beams **26**(11), 111002 (2023). https://doi.org/10.1103/PhysRevAccelBeams.26.111002. arXiv:2307.15597 [hep-ex]
144. A.A. Zholents, et al., High precision measurement of the PSI and PSI-prime MESON MASSES. Phys. Lett. B **96**, 214–216 (1980). https://doi.org/10.1016/0370-2693(80)90247-6
145. V.E. Blinov, E.B. Levichev, S.A. Nikitin, I.B. Nikolaev, Resonant depolarization technique at VEPP-4M in Novosibirsk. Eur. Phys. J. Plus **137**(6), 717 (2022). https://doi.org/10.1140/epjp/s13360-022-02825-1
146. W.W. MacKay, J.F. Hassard, R.T. Giles, M. Hempstead, K. Kinoshita, F.M. Pipkin, R. Wilson, L.N. Hand, Measurement of the Υ mass. Phys. Rev. D **29**, 2483 (1984). https://doi.org/10.1103/PhysRevD.29.2483
147. D.P. Barber, et al., A precision measurement of the Υ' meson mass. Phys. Lett. B **135**, 498 (1984). https://doi.org/10.1016/0370-2693(84)90323-X
148. R. Aßmann, et al., Calibration of center-of-mass energies at LEP-1 for precise measurements of Z properties. Eur. Phys. J. C **6**, 187–223 (1999). https://doi.org/10.1007/s100529801030

149. G. Abbiendi, et al., Determination of the LEP beam energy using radiative fermion-pair events. Phys. Lett. B **604**, 31–47 (2004). https://doi.org/10.1016/j.physletb.2004.10.046. arXiv:hep-ex/0408130
150. B. Dehning, *The LEP Spectrometer* (1999). https://cds.cern.ch/record/398417
151. N. Muchnoi, in *Proc. of ICFA Advanced Beam Dynamics Workshop on High Luminosity Circular e^+e^- Colliders (eeFACT'16)*, Daresbury, UK, October 24-27, 2016, ICFA Advanced Beam Dynamics Workshop on High Luminosity Circular e^+e^- Colliders, vol. 58 (JACoW, Geneva, 2017), pp. 168–172. https://doi.org/10.18429/JACoW-eeFACT2016-WET1H4
152. Z. Duan, Imperfection spin resonances for FCC-ee Booster lattices. 182nd FCC-ee Optics Design Meeting (2024). & 53rd FCCIS WP2.2 Meeting. https://indico.cern.ch/event/1398060/contributions/5880744
153. A. Blondel, et al., *Polarization and centre-of-mass energy calibration at FCC-ee* (2019). arXiv:1909.12245 [physics.acc-ph]
154. A. Blondel, J. Keintzel, G. Wilkinson, *FCC 2nd EPOL Workshop. Second FCC Workshop on Polarization, Center-of-Mass Energy Calibration and Monochromatization* (2022). https://indico.cern.ch/event/1181966/
155. A. Blondel, J. Keintzel, G. Wilkinson, J. Wenninger (editors), et al., Collision-energy calibration and monochromatisation studies at FCC-ee. Tech. Rep. CERN (2025). https://doi.org/10.17181/y6s2j-dhh22
156. I. Ternov, Y. Loskutov, L. Korovina, Possibility of polarizing an electron beam by relativistic radiation in a magnetic field. Sov. Phys. J. **14**, 921 (1962)
157. Y. Wu, D. Barber, F. Carlier, E. Gianfelice-Wendt, T. Pieloni, L. van Riesen-Haupt, in *Proc. IPAC'23*, International Particle Accelerator Conference, 14, (JACoW Publishing, Geneva, 2023), pp. 670–673. https://doi.org/10.18429/JACoW-IPAC2023-MOPL055
158. Y.W. et al. FCC-ee Orbit Correction and Polarization, in *8th FCC Physics Workshop* (2025). https://indico.cern.ch/event/1439509/contributions/6289602/attachments/2997221/5280674/2025%20Physics%20workshop.pdf
159. Y. Wu, F. Carlier, L. van Riesen-Haupt, M. Hofer, M. Seidel, T. Pieloni, W. Herr, Lattice correction and polarization estimation for the future circular collider e+e. JACoW **IPAC2024**, WEPR06 (2024). https://doi.org/10.18429/JACoW-IPAC2024-WEPR06
160. R. Assmann, et al., Deterministic harmonic spin matching in LEP, in *Proc. EPAC'94*, London, UK (1994). https://jacow.org/e94/PDF/EPAC1994_0932.PDF
161. E. Gianfelice-Wendt, Investigation of beam self-polarization in the future e^+e^- circular collider. Phys. Rev. Accel. Beams **19**, 101005 (2016). https://doi.org/10.1103/PhysRevAccelBeams.19.101005
162. A. Blondel, P. Janot, J. Wenninger, R. Aßmann, S. Aumon, et al., Polarization and Centre-of-mass Energy Calibration at FCC-ee (2019). http://arxiv.org/abs/1909.12245
163. J.M. Jowett, T.M. Taylor, Wigglers for control of beam characteristics in LEP. IEEE Trans. Nucl. Sci. **30**, 2581–2583 (1983). https://doi.org/10.1109/TNS.1983.4332889
164. I. Koop, Comments to RD studies at KARA and ESRF (2023). Presented at the FCC EPOL group and FCCIS WP2.5 meeting 19, 2023. http://indico.cern.ch/event/1252333
165. F. Ewald, Polarization at EBS (2023). Presented at the FCC EPOL group and FCCIS WP2.5 meeting 17, 2023. http://indico.cern.ch/event/1240245
166. I. Koop, Local bump depolarizer review, vol. 34 (2024). Presented at the FCC-FS EPOL group and FCCIS WP2.5 meeting. https://indico.cern.ch/event/1471324/
167. W. Hofle, Considerations for the design of the FCCee depolarizer kicker system. Presented at the 8th FCC Physics Workshop, CERN (2025). https://indico.cern.ch/event/1439509/
168. I. Koop, Resonant depolarization at Z-WW R&D. Presented at the EPOL Workshop at CERN, Geneva, Switzerland, 2022 (2022). http://indico.cern.ch/event/1181966/contributions/5055264/
169. N. Muchnoi (2018). FCC-ee polarimeter. arXiv:1803.09595 [physics.ins-det]
170. N. Muchnoi, Electron beam polarimeter and energy spectrometer. J. Instrum. **17**(10), P10014 (2022). https://doi.org/10.1088/1748-0221/17/10/P10014
171. E. Carideo, Energy loss due to impendance and impact on local energy and on energy differences of colliding and non-colliding bunches. Presented at the EPOL Workshop at CERN, Geneva, Switzerland, 2022 (2022). http://indico.cern.ch/event/1181966/contributions/5055264/
172. K. André, Synchrotron Radiation Background Studies @ FCC-ee. PowerPoint presentation (2023). https://indico.cern.ch/event/1202105/contributions/5395363/
173. P. Collier, Synchrotron phase space injection into LEP. Tech. Rep. CERN, Geneva (1995). https://cds.cern.ch/record/90946
174. G. Iadarola, et al., Xsuite: an integrated beam physics simulation framework. JACoW **HB2023**, TUA2I1 (2024). https://doi.org/10.18429/JACoW-HB2023-TUA2I1. arXiv:2310.00317 [physics.acc-ph]
175. A. Lechner, Beam losses and damage potential of the FCC-ee beams (2024). https://indico.cern.ch/event/1420307/
176. A. Lechner (2024). Dump integration/transport at point b. https://indico.cern.ch/event/1359337/
177. Y. Dutheil, *Beam Transfer Systems Feasibility Study Input for FCC-ee* (2024). https://doi.org/10.5281/zenodo.14363733
178. H. Schönbacher, M. Tavlet, Absorbed doses and radiation damage during the 11 years of LEP operation. Nucl. Instrum. Methods Phys. Res. B **217**(1), 77–96 (2004). https://doi.org/10.1016/j.nimb.2003.09.034
179. G. Lerner, et al., HL-LHC Radiation level specification document, Tech. Rep. CERN, Geneva (2024)

180. P. Raimondi, S.M. Liuzzo, Toward a diffraction limited light source. Phys. Rev. Accel. Beams **26**, 021601 (2023). https://doi.org/10.1103/PhysRevAccelBeams.26.021601
181. The CEPC Study Group, *CEPC Conceptual Design Report: Volume 1 - Accelerator* (2018)
182. C. Garcia Jaimes, et al., in *Proc. IPAC'24*. IPAC'24 - 15th International Particle Accelerator Conference, vol. 15 (JACoW Publishing, Geneva, (2024), pp. 2477–2480. https://doi.org/10.18429/JACoW-IPAC2024-WEPR10
183. C. Garcia Jaimes, et al., in *Proc. IPAC'24*, IPAC'24 - 15th International Particle Accelerator Conference, vol. 15 (JACoW Publishing, Geneva, 2024), pp. 2481–2484. https://doi.org/10.18429/JACoW-IPAC2024-WEPR11
184. C. Garcia Jaimes, et al., in *Proc. IPAC'24*, IPAC'24 - 15th International Particle Accelerator Conference, vol. 15 (JACoW Publishing, Geneva, 2024), pp. 2485–2488. https://doi.org/10.18429/JACoW-IPAC2024-WEPR12
185. J.P. Koutchouk, Betatron coupling compensation for LEP v13. Tech. Rep., CERN, Geneva (1983). https://cds.cern.ch/record/446364
186. G. Roy, Can we correct the solenoid coupling better than in 1995? Presented at the 6th LEP Performance Workshop, Chamonix, France (1996). https://cds.cern.ch/record/306386
187. G. Aad, et al., Observation of a new particle in the search for the standard model Higgs boson with the ATLAS detector at the LHC. Phys. Lett. B **716**, 1–29 (2012). https://doi.org/10.1016/j.physletb.2012.08.020. arXiv:1207.7214 [hep-ex]
188. S. Chatrchyan, et al., Observation of a new boson at a mass of 125 GeV with the CMS experiment at the LHC. Phys. Lett. B **716**, 30–61 (2012). https://doi.org/10.1016/j.physletb.2012.08.021. arXiv:1207.7235 [hep-ex]
189. A. Abada, et al., FCC physics opportunities: future circular collider conceptual design report volume 1. Eur. Phys. J. C **79**(6), 474 (2019). https://doi.org/10.1140/epjc/s10052-019-6904-3
190. D. d'Enterria, Higgs physics at the future circular collider. PoS **ICHEP2016** 434 (2017). https://doi.org/10.22323/1.282.0434. arXiv:1701.02663 [hep-ex]
191. W. Altmannshofer, J. Brod, M. Schmaltz, Experimental constraints on the coupling of the Higgs boson to electrons. J. High Energy Phys. **05**, 125 (2015). https://doi.org/10.1007/JHEP05(2015)125. arXiv:1503.04830 [hep-ph]
192. D. d'Enterria, A. Poldaru, G. Wojcik, Measuring the electron Yukawa coupling via resonant s-channel Higgs production at FCC-ee. Eur. Phys. J. Plus **137**(2), 201 (2022). https://doi.org/10.1140/epjp/s13360-021-02204-2. arXiv:2107.02686 [hep-ex]
193. M.A. Valdivia García, A. Faus-Golfe, F. Zimmermann, Towards a monochromatization scheme for direct Higgs production at FCC-ee, in *Proc. 7th International Particle Accelerator Conference, IPAC'16*, Busan, Korea (2016). https://doi.org/10.18429/JACoW-IPAC2016-WEPMW009
194. M.A. Valdivia García, F. Zimmermann, in *CERN-BINP Workshop for Young Scientists in* e^+e^- *Colliders* (2017), pp. 1–12. https://doi.org/10.23727/CERN-Proceedings-2017-001.1
195. M.A. Valdivia García, F. Zimmermann, Optimized monochromatization for direct Higgs production in future circular e^+e^- colliders, in *Proc. 8th International Particle Accelerator Conference, IPAC'17*, Copenhagen, Denmark (2017). https://doi.org/10.18429/JACoW-IPAC2017-WEPIK015
196. H. Jiang, et al., in *FCC-FS EPOL Group and FCCIS WP2.5 Meeting 4* (2022). https://indico.cern.ch/event/1108961/
197. A. Faus-Golfe, M.A. Valdivia García, F. Zimmermann, The challenge of monochromatization: direct s-channel Higgs production: $e^+e^- \rightarrow H$. Eur. Phys. J. Plus **137**(1), 31 (2022). https://doi.org/10.1140/epjp/s13360-021-02151-y
198. H. Jiang, A. Faus-Golfe, K. Oide, Z. Zhang, F. Zimmermann, First optics design for a transverse monochromatic scheme for the direct s-channel Higgs production at FCC-ee collider. JACoW **IPAC2022**, 1878–1880 (2022). https://doi.org/10.18429/JACoW-IPAC2022-WEPOPT017
199. Z. Zhang, et al., Monochromatization interaction region optics design for direct s-channel production at FCC-ee. JACoW **IPAC2023**, MOPL079 (2023). https://doi.org/10.18429/JACoW-IPAC2023-MOPL079
200. Z. Zhang, A. Faus-Golfe, H. Jiang, B. Bai, P. Raimondi, F. Zimmermann, K. Oide, Update in the optics design of monochromatization interaction region for direct Higgs s-channel production at FCC-ee. JACoW **IPAC2024**, WEPR21 (2024). https://doi.org/10.18429/JACoW-IPAC2024-WEPR21
201. A. Faus-Golfe, in *Proc. IPAC'24* (2024). https://indico.jacow.org/event/63/contributions/3067/
202. A. Renieri, Possibility of Achieving Very High-Energy Resolution in electron-Positron Storage Rings. Tech. Rep. LNF-75/6-R, LNF (1975)
203. K. Oide, et al., Design of beam optics for the future circular collider e^+e^- collider rings. Phys. Rev. Accel. Beams **19**(11), 111005 (2016). https://doi.org/10.1103/PhysRevAccelBeams.19.111005. [Addendum: Phys. Rev. Accel. Beams **20**, 049901 (2017)]. arXiv:1610.07170 [physics.acc-ph]
204. K. Oide, in *Proc. FCC-EIC Joint & MDI Workshop* (2022). https://indico.cern.ch/event/1186798/contributions/5062582/
205. J. Keintzel, A. Abramov, M. Benedikt, M. Hofer, P. Hunchak, K. Oide, T. Raubenheimer, R. Tomás García, F. Zimmermann, FCC-ee lattice design. JACoW **eeFACT2022**, 52–60 (2023). https://doi.org/10.18429/JACoW-eeFACT2022-TUYAT0102
206. CERN optics repository. https://acc-models.web.cern.ch/acc-models/fcc/
207. P. Ramondi, in *Proc. FCCIS 2022 Workshop* (2022). https://indico.cern.ch/event/1203316/contributions/5156515/
208. P. Ramondi, in *Proc. FCCIS 2023 WP2 Workshop* (2023). https://indico.cern.ch/event/1326738/contributions/5654524/
209. A. Ciarma, H. Burkhardt, M. Boscolo, P. Raimondi, Alternative solenoid compensation scheme for the FCC-ee interaction region. JACoW **IPAC2024**, TUPC68 (2024). https://doi.org/10.18429/JACoW-IPAC2024-TUPC68
210. MAD - Methodical Accelerator Design. https://mad.web.cern.ch/mad/

211. Z. Zhang, A. Faus-Golfe, A. Korsun, B. Bai, H. Jiang, et al., Monochromatization interaction region optics design for direct s-channel Higgs production at FCC-ee (2024). arXiv:2411.04210v1 [physics.acc-ph]
212. D. Schulte, Beam-beam simulations with Guinea-pig. eConf C **980914**, 127–131 (1998)
213. Institute of High Energy Physics, Beijing (2009). BEPCII Design Report
214. C. Milardi, M. Preger, P. Raimondi, The DAFNE interaction region for the KLOE-2 run (2010)
215. E. Wang, O. Rahman, J. Skaritka, W. Liu, J. Biswas, et al., High voltage dc gun for high intensity polarized electron source. Phys. Rev. Accel. Beams **25**, 033401 (2022). https://doi.org/10.1103/PhysRevAccelBeams.25.033401
216. I. Koop, A. Otboev, Yu. Shatunov, in **sPIN'16** (2016). https://indico.cern.ch/event/570680/contributions/2309891/8
217. P. Janot, C. Grojean, F. Zimmermann, M. Benedikt, Integrated Luminosities and Sequence of Events for the FCC. Feasibility Study Report (2024). https://doi.org/10.17181/nfs96-89q08
218. J. Bauche, et al., Progress of the FCC-ee optics tuning working group (2023). https://doi.org/10.18429/JACoW-IPAC2023-WEPL023. Presented at the 14th International Particle Accelerator Conf. (IPAC'23), Venice, Italy, May 2023 paper WEPL023
219. X. Huang, BBA simulation for FCC-ee ballistic optics (2024). Presentation at the FCC-ee Tuning Working Group Meeting. https://indico.cern.ch/event/1477971/
220. C. Goffing, Horizontal BBA for FCC (2025). Presentation at the FCC-ee Tuning Working Group Meeting. https://indico.cern.ch/event/1505291/
221. X. Huang, *FCCee BBA Simulations. Presentation at the FCC-ee Tuning Working Group Meeting* (2024). https://indico.cern.ch/event/1403458/
222. R.J. Steinhagen, LHC Beam Stability and Feedback Control - Orbit and Energy. Tech. Rep. CERN, Geneva (2007). https://cds.cern.ch/record/1054826
223. R. Alemany, B. Lindstrom, S. Redaelli Private communications (2025)
224. V. Schlott, M. Böge, B. Keil, P. Pollet, T. Schilcher, Fast orbit feedback and beam stability at the Swiss light source. AIP Conf. Proc. **732**(1), 174–181 (2004). https://doi.org/10.1063/1.1831145
225. K. Oide, Optics performance, beam lifetime, injection rate, and vibration, Rome (2023). FCCIS 2023 WP2 Workshop. https://indico.cern.ch/event/1326738/contributions/5650144
226. D. Shatilov, Large footprint with 4 IP, discussion and mitigation. 100th FCC-ee Optics Design Meeting, 19 July 2019 (2019). https://indico.cern.ch/event/835526/
227. J. Salvesen, F. Zimmermann, P. Burrows, First studies on error mitigation by interaction point fast feedback systems for FCC-ee, in *Proc. 15th International Particle Accelerator Conference, IPAC'24*, Nashville, TN (2024). https://doi.org/10.18429/JACoW-IPAC2024-THPG31
228. Y. Funakoshi, et al., Interaction point orbit feedback system at SuperKEKB, in *Proc. 6th International Particle Accelerator Conference (IPAC'15)*, Richmond, VA (2015). https://doi.org/10.18429/JACoW-IPAC2015-MOPHA054
229. Y. Funakoshi, M. Masuzawa, K. Oide, J. Flanagan, M. Tawada, et al., Orbit feedback system for maintaining an optimum beam collision. Phys. Rev. Spec. Top., Accel. Beams **10**, 101001 (2007). https://doi.org/10.1103/PhysRevSTAB.10.101001
230. M. Masuzawa, et al., 7th International Beam Instrumentation Conference, JACoW, 2019 p. TUPC13. https://doi.org/10.18429/JACoW-IBIC2018-TUPC13
231. P. Collier, Transfer and injection into LEP, France (1997). Presented at the 7th LEP Performance Workshop, Chamonix. https://cds.cern.ch/record/348081
232. N. Iida, Injection tuning of superkekb towards its luminosity goal. https://indico.cern.ch/event/1242395/contributions/5419166/attachments/2673309/4634903/FCC-WS_Injection-SuperKEKB_20230626_Iida.pdf (2023). Accessed: 2024-12-22
233. K. Andre, DA studies with Xsuite. Presentation at the 189th FCC-ee Accelerator Design Meeting & 60th FCCIS WP2.2 Meeting (2024). https://indico.cern.ch/event/1440349/#5-da-studies-with-xsuite
234. CERN. Accelerator Fault Tracking (AFT). Online tool https://aft.cern.ch/
235. M. Blaszkiewicz, J.W. Heron, A. Apollonio, T. Buffet, T. Cartier-Michaud, L. Felsberger, J. Uythoven, D. Wollmann, in *European Safety and Reliability Conference (ESREL); Advances in Reliability, Safety and Security, Part 4*, Krakow, Poland (2024), pp. 29–38
236. J. Heron, et al., Update of availability studies (2025). ATDC #16 Availability & Operation model
237. D. Anderson, M. Audrain, K. Fuchsberger, J. Garnier, R. Gorbonosov, et al., The acctesting framework: an extensible framework for accelerator commissioning and systematic testing, in *Proc. ICALEPCS'13*, San Francisco (2013). https://jacow.org/ICALEPCS2013/papers/thppc001.pdf
238. Y. Tanimoto, Photodesorption and Photoelectron Yields from 150 nm Thin NEG Coatings, Brussels (2019). Presented at the FCC Week. https://indico.cern.ch/event/727555/contributions/3427952/attachments/1867220/3070875/FCCWeek2019_poster.pdf
239. T. Sinkovits, Minimum effective thickness for activation and low total electron yield of TiZrV non-evaporable getter coatings, Amsterdam (2018). Presented at the FCC Week. https://indico.cern.ch/event/656491/contributions/2938832/
240. R.M. Manglik, A.E. Bergles, Heat transfer and pressure drop correlations for twisted-tape inserts in isothermal tubes: part ii—transition and turbulent flows. J. Heat Transf. **115**(4), 890–896 (1993). https://doi.org/10.1115/1.2911384
241. E. Belli, Coupling impedance and single beam collective effects for the future circular collider (lepton option). Ph.D. thesis, Rome U (2018). https://cds.cern.ch/record/2669366. Presented 08 Feb 2019

242. S. Gorgi Zadeh, Accelerating cavity and higher order mode coupler design for the Future Circular Collider. Ph.D. thesis, Universität Rostock (2021). https://cds.cern.ch/record/2776785. Presented 15 Mar 2021
243. S.G. Zadeh, U. van Rienen, R. Calaga, F. Gerigk, FCC-ee hybrid RF scheme, in *Proc. IPAC'18*, Vancouver, Canada (2018). https://doi.org/10.18429/JACoW-IPAC2018-MOPMF036
244. Y. Morita, et al., in *Proc. SRF'09* (JACoW Publishing, Geneva, 2009), pp. 236–238. https://jacow.org/SRF2009/papers/TUPPO022.pdf
245. Y. Morita, et al., *KEKB Superconducting Accelerating Cavities and Beam Studies for Super-KEKB* (2010). http://accelconf.web.cern.ch/IPAC10/papers/TUPEB011.pdf
246. T. Abe, K. Akai, N. Akasaka, K. Ebihara, E. Ezura, et al., Performance and operation results of the rf systems for the kek b-factory. Prog. Theor. Exp. Phys. **2013**(3), 03A006 (2013). https://doi.org/10.1093/ptep/ptt020
247. F. Willeke, J. Beebe-Wang, Electron Ion Collider Conceptual Design Report 2021, Upton, NY; Thomas Jefferson National Accelerator Facility (TJNAF), Newport News, VA (2021). https://doi.org/10.2172/1765663. Tech. Rep. Brookhaven National Lab. (BNL)
248. A. Blednykh, M. Blaskiewicz, R. Lindberg, Simulation of the RF system with reversed phasing, Upton, NY (2022). https://doi.org/10.2172/1888292. Tech. Rep. Brookhaven National Laboratory (BNL)
249. D. Boussard, Control of cavities with high beam loading. IEEE Trans. Nucl. Sci. **32**(5), 1852–1856 (1985). https://doi.org/10.1109/TNS.1985.4333745
250. P. Baudrenghien, T. Mastoridis, Fundamental cavity impedance and longitudinal coupled-bunch instabilities at the high luminosity large hadron collider. Phys. Rev. Accel. Beams **20**, 011004 (2017). https://doi.org/10.1103/PhysRevAccelBeams.20.011004
251. F. Pedersen, RF cavity feedback. CERN-PS-92-59-RF p, vol. 17 (1992). https://cds.cern.ch/record/244817
252. J. Tückmantel, Cavity-Beam-Transmitter Interaction Formula Collection with Derivation. CERN-ATS-Note-2011-002 TECH pp. 1–18 (2011). https://cds.cern.ch/record/1323893/files/CERN-ATS-Note-2011-002
253. I. Karpov, P. Baudrenghien, Transient beam loading and rf power evaluation for future circular colliders. Phys. Rev. Accel. Beams **22**, 081002 (2019). https://doi.org/10.1103/PhysRevAccelBeams.22.081002
254. J.D. Fox, L. Beckman, D. Teytelman, D.V. Winkle, A. Young, in *Proc. EPAC'04*, European Particle Accelerator Conference, vol. 9 (JACoW Publishing, Geneva, (2004), pp. 2822–2824. http://accelconf.web.cern.ch/e04/papers/THPLT155.pdf
255. D. Teytelman, J.D. Fox, D.V. Winkle, Operating performance of the low group delay woofer channel in PEP-II, in *Proc. PAC'05*, Knoxville, TN (2005). https://jacow.org/p05/papers/MPPP007.pdf
256. E. Shaposhnikova, RF system for FCC-hh. Presented at the FCC-hh impedance and beam screen workshop, CERN, 30.03.2017 (2017). https://indico.cern.ch/event/619380/contributions/2527389/attachments/1436914/2210174/RFforFCChh_v3.pdf
257. L. Zhang, H. Damerau, I. Karpov, A. Vanel, Fcc circumference studies based on rf synchronization. J. Instrum. **19**(02), T02007 (2024). https://doi.org/10.1088/1748-0221/19/02/T02007
258. H. Damerau, Optimization of FCC circumference for hh, Presented at the FCC Week 2024, San Francisco, USA, June 10–14 (2024). https://indico.cern.ch/event/1298458/contributions/5987294/
259. D. Boussard, et al., The LHC superconducting cavities, in *Proc. of PAC'99*, New York, USA (1999). https://jacow.org/p99/papers/mop120.pdf
260. C. Wyss, *LEP Design Report, v. 3: LEP2* (CERN, Geneva, 1996). https://cds.cern.ch/record/314187. Vol. 1-2 publ. in 1983-84
261. M. Champion, et al., Progress on the proton power upgrade at the spallation neutron source, in *Proc. IPAC'12*, Campinas, SP, Brazil (2021). https://doi.org/10.18429/JACoW-IPAC2021-TUPAB199
262. B. Autin, A. Blondel, K. Bongardt, et al., *Conceptual Design of the SPL, a High-Power Superconducting H^- Linac at CERN*. CERN Yellow Reports: Monographs (CERN, Geneva, 2000). https://doi.org/10.5170/CERN-2000-012
263. E. Cenni, et al., Vertical test results on ESS medium and high beta elliptical cavity prototypes equipped with helium tank, in *Proc. of IPAC'17*, Copenhagen, Denmark, 14–19 May (2017), pp. 14–19. https://doi.org/10.18429/JACoW-IPAC2017-MOPVA041
264. M. Martinello, et al., Q-factor optimization for high-beta 650 MHz cavities for PIP-II. J. Appl. Phys. **130**, 174501 (2021). https://doi.org/10.1063/5.0068531
265. F. Marhauser, Recent results on a multi-cell 800 MHz bulk Nb cavity. Presentation at FCC Week 2018, Amsterdam, the Netherlands, 9–13 April (2022). https://indico.cern.ch/event/656491/contributions/2932251/
266. Z. Un Nisa, Two stage klystron for FCCee. 2nd Workshop on Efficient RF sources, 23-25 September 2024, Toledo, Spain (2024). https://indico.cern.ch/event/1407353/contributions/6015160/
267. Z. Zusheng, RF power sources for CEPC. 2nd Workshop on Efficient RF sources, 23-25 September 2024, Toledo, Spain. (2024). https://indico.cern.ch/event/1407353/contributions/6013275/
268. M. Jensen, Status of the 1.2 MW MB-IOT for ESS. CLIC Workshop 2016, 18-22 January, CERN. https://indico.cern.ch/event/449801/contributions/1945285/
269. I. Syratchev, Ultimate efficiency in linear beam devices. 2nd Workshop on Efficient RF sources. 23-25 September 2024, Toledo, Spain (2024). https://indico.cern.ch/event/1407353/contributions/6013297/
270. T. Kole, RF GaN/SiC Technology from Integra. 2nd Workshop on Efficient RF sources. 23-25 September 2024, Toledo, Spain. https://indico.cern.ch/event/1407353/contributions/6015174/

271. W. Venturini Delsolaro, et al., Progress and R/D challenges for FCC-ee SRF. EPJ Tech. Instrum. **10**(1), 6 (2023). https://doi.org/10.1140/epjti/s40485-023-00094-5
272. S. Posen, R&D towards an 800 MHz cryomodule, London, UK. Presented at the FCC Week 2023 (2023). https://indico.cern.ch/event/1202105/contributions/5385369/
273. I. Syratchev, F. Peauger, I. Karpov, O. Brunner, A superconducting slotted waveguide elliptical cavity for fcc-ee (2021). https://doi.org/10.5281/zenodo.5031953
274. S.G. Zadeh, O. Brunner, F. Peauger, I. Syratchev, in Proc. IPAC'22, 1323–1326 (2022). https://doi.org/10.18429/JACoW-IPAC2022-TUPOTK048
275. F. Peauger, SWELL and other SRF split cavity development, in *Proc. LINAC'22*, Liverpool, UK (2022). https://doi.org/10.18429/JACoW-LINAC2022-TU1AA04
276. J.F. Fuchs, et al., Survey guidelines and requirements for the alignment of a new accelerator equipment on a beam line at cern. Tech. Rep. EDMS Document No. 2708664, CERN (2023). https://edms.cern.ch/document/2708664/0
277. Pacman. https://pacman.web.cern.ch/pacman/. Accessed: 2023-06-14
278. H.M. Durand, et al., Main achievements of the PACMAN project for the alignment at micrometric scale of accelerator components, in *Proc. IPAC'17*, Copenhagen, Denmark (2017). https://doi.org/10.18429/JACoW-IPAC2017-TUPIK077
279. J.C. Gayde, et al., Introduction to a Structured Laser Beam for alignment and status of the R&D (2023). CERN-BE-2023-013
280. K. Polak, J.C. Gayde, Structured laser beam in non-homogeneous environment (2023). https://cds.cern.ch/record/2849070/files/CERN-BE-2023-014.pdf. CERN-BE-2023-014
281. H.M. Durand, et al., Full Remote Alignment System for the High-Luminosity Large Hadron Collider HL-LHC (2023). https://cds.cern.ch/record/2849056/files/CERN-BE-2023-007.pdf. CERN-BE-2023-007
282. M. Sosin, et al., Design and study of a 6 degree-of-freedom universal adjustment platform for HL-LHC components, in *Proc. International Particle Accelerator Conference IPAC'19*, Melbourne, Australia (2019). https://doi.org/10.18429/JACoW-IPAC2019-THPGW058
283. P. Valentin, J.F. Fuchs, F. Klumb, Development of SMART: a stand-alone software for data acquisition at CERN, FERMILAB, USA (2018). IWAA 2018. https://www.slac.stanford.edu/econf/C1810085/Papers/29_2.pdf
284. P. Sainvitu, P. Dewitte, J.C. Gayde, D. Mergelkuhl, D. Missiaen, TSUNAMI, an unified in-field measurement and alignment software for experiments and accelerators at CERN large scale metrology section, France (2016). IWAA 2016, ESRF. https://www.slac.stanford.edu/econf/C1610034/papers/652.pdf2
285. M. Barbier, Q. Dorléat, M. Jones, LGC: a new revised version, France (2016). IWAA 2016, ESRF. https://indico.cern.ch/event/489498/contributions/2217518/attachments/1350928/2039484/LGC_new_revised_version.pdf
286. A. Krainer, W. Bartmann, M. Calviani, et al., A semi-passive beam dilution system for the FCC-ee collider. EPJ Tech. Instrum. **9**(3) (2022). https://doi.org/10.1140/epjti/s40485-022-00078-x
287. J. Maestre, C. Torregrosa, K. Kershaw, C. Bracco, T. Coiffet, et al., Design and behaviour of the large hadron collider external beam dumps capable of receiving 539 MJ/dump. J. Instrum. **16**(11), P11019 (2021). https://doi.org/10.1088/1748-0221/16/11/P11019
288. L. Porta, FCC Electro-Magnetic Separator - Pre-Design Study. Tech. Rep. EDMS Document No. 3207020, CERN (2024). https://edms.cern.ch/document/3207020/
289. W. Kalbreier, N. Garrel, R. Guinand, R.L. Keizer, K.H. Kissler, Layout, design and construction of the electrostatic separation system of the LEP e+e- collider. Tech. Rep. CERN-SPS-88-20-ABT, CERN (1989). https://cds.cern.ch/record/188920
290. L. Porta, FCC Separator Septa - Pre-Design Study. Tech. Rep. EDMS Document No. 3207017, CERN (2024). https://edms.cern.ch/document/3207017
291. E. Howling, BPM design studies. Presented at the FCC Week 10–14 June (2024). https://indico.cern.ch/event/1298458/contributions/5978885/
292. E. Carideo, D. De Arcangelis, M. Migliorati, D. Quartullo, F. Zimmermann, M. Zobov, Transverse and longitudinal single bunch instabilities in FCC-ee, in *Proc. IPAC'21*, Campinas, Brazil (2021). https://doi.org/10.18429/JACoW-IPAC2021-WEPAB225
293. M. Migliorati, C. Antuono, E. Carideo, Y. Zhang, M. Zobov, Impedance modelling and collective effects in the Future Circular e^+e^- Collider with 4 IPs (2022). https://doi.org/10.1140/epjti/s40485-022-00084-z
294. M. Siano, B. Paroli, M.A.C. Potenza, L. Teruzzi, U. Iriso, A.A. Nosych, E. Solano, Two-dimensional electron beam size measurements with X-ray heterodyne near field speckles. Phys. Rev. Accel. Beams **25**, 052801 (2022). https://doi.org/10.1103/PhysRevAccelBeams.25.052801
295. M. Reissig, et al., Simulations of an electro-optical in-vacuum bunch profile monitor and measurements at KARA for use in the FCC-ee, in *Proc. IPAC'24*, Nashville, TN (2024). https://doi.org/10.18429/JACoW-IPAC2024-WEPG56
296. T. Lefèvre, D. Alves, M. Apollonio, A. Aryshev, M. Bergamaschi, et al., Cherenkov diffraction radiation as a tool for beam diagnostics, in *Proc. IBIC'19*, Malmö, Sweden (2019). https://doi.org/10.18429/JACoW-IBIC2019-THAO01
297. R. Kieffer, L. Bartnik, M. Bergamaschi, V.V. Bleko, M. Billing, L. Bobb, J. Conway, et al., Generation of incoherent Cherenkov diffraction radiation in synchrotrons. Phys. Rev. Accel. Beams **23**, 042803 (2020). https://doi.org/10.1103/PhysRevAccelBeams.23.042803
298. R. Ulrich, Zur Cerenkov-Strahlung von Elektronen dicht über einem Dielektrikum. Z. Phys. **194**(2), 180–192 (1966). https://doi.org/10.1007/BF01326045

299. D.V. Karlovets, A.P. Potylitsyn, Diffraction radiation from a finite-conductivity screen. JETP Lett. **90**(5), 326–331 (2009). https://doi.org/10.1134/S0021364009170032
300. A.P. Potylitsyn, S.Y. Gogolev, Radiation losses of the relativistic charge moving near a dielectric radiator. Russ. Phys. J. **62**(12), 2187–2193 (2020). https://doi.org/10.1007/s11182-020-01965-0
301. K. Łasocha, C. Davut, P. Karataev, T. Lefèvre, S. Mazzoni, C. Pakuza, A. Schlögelhofer, E. Senes, Experimental verification of several theoretical models for ChDR description, in *Proc. IPAC'22* (2022), pp. 2420–2423. https://doi.org/10.18429/JACoW-IPAC2022-THOYGD1
302. A. Aryshev, P. Bambade, D.R. Bett, L. Brunetti, P.N. Burrows, et al. ATF report 2020. Tech. Rep, CERN, Geneva (2020). https://cds.cern.ch/record/2742899
303. J. Storey, et al., First results from the operation of a rest gas ionisation profile monitor based on a hybrid pixel detector, in *Proc. IBIC'17, Grand Rapids, MI* (2017). https://doi.org/10.18429/JACoW-IBIC2017-WE2AB5
304. S. Mazzoni, W. Andreazza, E. Balci, D. Belohrad, E. Bravin, N. Chritin, J. Esteban Felipe, T. Lefèvre, M. Martin Nieto, M. Palm, A new luminosity monitor for the LHC run 3, in *Proc. IBIC'22* (2022), pp. 163–167. https://doi.org/10.18429/JACoW-IBIC2022-MOP45
305. J. Bauche, et al., The status of the energy calibration, polarization and monochromatization of the FCC-ee, in *Proc. IPAC'23* (2023), p. MOPL059. https://doi.org/10.18429/JACoW-IPAC2023-MOPL059
306. F. Valchokova-Georgieva, J.P. Corso, K. Hanke, Challenges and solutions in the integration studies of the future circular collider. JACoW IPAC **2023**, WEPM123 (2023). https://doi.org/10.18429/JACoW-IPAC2023-WEPM123
307. B. Humann, Synchrotron radiation studies for the fcc-ee arc with fluka. Talk presented at FCC Week 2021 (2021). https://indico.cern.ch/event/995850/contributions/4405383/
308. J. Wenninger, Considerations on alignment and vibrations for fccee, in *187th FCC-ee Accelerator Design Meeting and 58th FCCIS WP2.2 Meeting* (2024). Talk presented at. https://indico.cern.ch/event/1427822/
309. T. Raubenheimer, Preliminary budget of alignment tolerances and time scales (2022). Talk presented at FCCIS 2022 Workshop. https://indico.cern.ch/event/1203316/contributions/5153505/
310. M. Guinchard, Fcc vibration stability study - stability demonstrator, edms 2919485 (2022, 2023, 2024). https://edms.cern.ch/document/2919485/LAST_RELEASED
311. C. Collette, K. Artoos, A. Kuzmin, M. Sylte, M. Guinchard, C. Hauviller, Active control of quadrupole motion for future linear particle colliders, in *Proceedings of the IASTED International Conference on Intelligent Systems and Control* (2009). https://cds.cern.ch/record/1268422/files/EuCARD-CON-2009-031.pdf
312. S. Janssens, K. Artoos, C. Collette, M. Esposito, P. Carmona, et al., Stabilization and positioning of clic quadrupole magnets with sub-nanometre resolution, in *Proc. ICALEPCS'11*, Grenoble, France (2011). https://jacow.org/icalepcs2011/papers/mommu005.pdf
313. P. Lersnimitthum, A. Piccini, F. Carra, T. Boonyatee, N. Wansophark, N. Ajavakom, Future circular lepton collider vibrational crosstalk. Vibration **7**(4), 912–927 (2024). https://doi.org/10.3390/vibration7040048
314. K. Artoos, O. Capatina, C. Collette, M. Guinchard, C. Hauviller, et al., Ground vibration and coherence length measurements for the CLIC nano-stabilization studies, in *Proc. PAC'09*, Vancouver, Canada (2010). https://jacow.org/PAC2009/papers/th5rfp081.pdf
315. J. Bauche, C. Eriksson, Status of Collider and Booster Magnets for FCC-ee. Presentation given at the FCC Week, Paris, France (2022). https://indico.cern.ch/event/1064327/contributions/4888487/attachments/2453666/4205725/2022-06-01 -FCC week -FCC-ee Magnets -JBauche.pdf
316. Minutes, Meeting no. 1. FCC-ee Arc Half-Cell Senior advisor Panel Meetings (2022). https://indico.cern.ch/event/1204097/
317. Minutes, Meeting no. 2. FCC-ee Arc Half-Cell Senior Advisor Panel Meetings (2022). https://indico.cern.ch/event/1221522/
318. F. Carra, Arc half-cell configuration project & mock-up, Geneva, Switzerland (2022). Presentation given at the FCCIS Workshop. https://indico.cern.ch/event/1203316/contributions/5125329/attachments/2559895/4415585/Arc Half-cell Project.pdf
319. M. Rouchouse, FCC-ee GHC Arc Half-Cell Sectional Drawing EDMS 3180552 (2025). https://edms.cern.ch/document/FCCLJGU_0001/0
320. M. Rouchouse, FCC-ee Conceptual Layout - V24.3_GHC Arc Half-Cell. EDMS 3180559 (2025). https://edms.cern.ch/document/FCCLSCG_0001/0
321. C. Garcia Jaimes, R. Tomas, T. Pieloni, Exploring FCC-ee optics designs with combined function magnets, in *Proc. 14th International Particle Accelerator Conference* (2023). https://doi.org/10.18429/JACoW-IPAC2023-MOPL066
322. A. Faugier, Bilan de démantlèlement de collisioneur LEP. Tech. Rep. SL-Note-2002-043, MR, CERN, Geneva (2002). https://cds.cern.ch/record/702725
323. M. Benedikt, P. Collier, J. Poole, FCC-ee dismantling (2024). https://doi.org/10.5281/zenodo.14098917. Tech. Rep. CERN
324. B. Auchmann, W. Bartmann, M. Benedikt, et al., Future Circular Collider midterm report. Tech. Rep. Internal report, CERN (2024)
325. P. Collier, J. Poole, Background information concerning FCC-ee dismantling (2024). https://doi.org/10.5281/zenodo.14099160. Tech. Rep. CERN
326. CERN, *CAS - CERN Accelerator School: 5th General Accelerator Physics Course: Jyväskylä, Finland 7 - 18 Sep 1992. CAS - CERN Accelerator School: 5th General Accelerator Physics Course* (CERN, Geneva, 1994). https://doi.org/10.5170/CERN-1994-001. 2 volumes, consecutive pagination

327. A.W. Chao, *Physics of Collective Beam Instabilities in High Energy Accelerators* (Wiley, New York, 1993)
328. A. Rajabi, R. Wanzenberg, Resistive wall impedance of multilayer beam pipes of general cross sections, in *Proc. IPAC'23*, Venice, Italy (2023), pp. 3402–3404. https://doi.org/10.18429/JACOW-IPAC2023-WEPL124
329. K.S.B. Li, H. Bartosik, S.E. Hegglin, G. Iadarola, A. Oeftiger, et al., Code development for collective effects, in *Proc. AABD Workshop HB2016* (2016), pp. 362–367. https://jacow.org/hb2016/papers/weam3x01.pdf
330. C. Ahdida, et al., New Capabilities of the FLUKA Multi-Purpose Code. Front. Phys. **9** (2022). https://doi.org/10.3389/fphy.2021.788253
331. W. Bartmann, Y. Dutheil, S. Yue, P. Arrutia, Transfer lines and booster (2024). https://indico.cern.ch/event/1463503/#22-transfer-lines-and-booster. Accessed: 2024-11-30
332. A. Chance, Booster status and future plans (2024). https://indico.cern.ch/event/1469408/
333. Y. Dutheil, et al., FCC-ee booster, injection and extraction concepts (2023). https://indico.cern.ch/event/1326738/timetable/#19-fccee-booster-injection-and
334. A. Grudiev, A. Latina, A. Chance, P. Craievich, S. Bettoni, W. Bartmann, Y. Dutheil, Trajectory Jitter Specification for the FCC-ee Injector (2024). https://indico.cern.ch/event/1405896/. Accessed: 2024-11-30
335. H. Bartosik, CERN, 2024, Proceedings of the FCC Week 2023. https://indico.cern.ch/event/1298458/timetable/#185-booster-and-collider-filling. Accessed: 2024-12-01
336. H. Timko, S. Albright, T. Argyropoulos, H. Damerau, K. Iliakis, et al., Beam longitudinal dynamics simulation studies. Phys. Rev. Accel. Beams **26**, 114602 (2023). https://doi.org/10.1103/PhysRevAccelBeams.26.114602
337. T.O. Raubenheimer, F. Zimmermann, Fast beam-ion instability. I. Linear theory and simulations. Phys. Rev. E **52**, 5487–5498 (1995). https://doi.org/10.1103/PhysRevE.52.5487
338. G.V. Stupakov, T.O. Raubenheimer, F. Zimmermann, Fast beam-ion instability. II. Effect of ion decoherence. Phys. Rev. E **52**, 5499–5504 (1995). https://doi.org/10.1103/PhysRevE.52.5499
339. R. Cimino, M. Commisso, D.R. Grosso, T. Demma, V. Baglin, R. Flammini, R. Larciprete, Nature of the decrease of the secondary-electron yield by electron bombardment and its energy dependence. Phys. Rev. Lett. **109**, 064801 (2012). https://doi.org/10.1103/PhysRevLett.109.064801
340. M. Aiba, S. Fartoukh, A. Franchi, M. Giovannozzi, V. Kain, M. Lamont, R. Tomás, G. Vanbavinckhove, J. Wenninger, F. Zimmermann, R. Calaga, A. Morita, First β-beating measurement and optics analysis for the CERN large hadron collider. Phys. Rev. Spec. Top., Accel. Beams **12**, 081002 (2009). https://doi.org/10.1103/PhysRevSTAB.12.081002
341. B. Dalena, et al., Definition of tolerances and corrector strengths for the orbit control of the high-energy booster ring of the future electron-positron collider, in *Proc. 14th International Particle Accelerator Conference, IPAC'23*, Venezia, Italy, May 7–12 (2023). https://doi.org/10.18429/JACoW-IPAC2023-MOPL054
342. M. Pentella, Magnetic measurement of the FCC-ee booster dipole. Tech. Rep. EDMS Document No. 3199919, CERN (2024). https://edms.cern.ch/document/3199919/
343. P. Chiggiato, Outgassing properties of vacuum materials for particle accelerators. Tech. Rep., CERN (2020). https://cds.cern.ch/record/2723690. 47 pages
344. M. Ady, Monte Carlo simulations of ultra high vacuum and synchrotron radiation for particle accelerators. Ph.D. thesis, Ecole Polytechnique, Lausanne (2016). https://cds.cern.ch/record/2157666. Presented 03 May 2016
345. F. Zimmermann, Update on booster vacuum system, operation mode and polarisation time estimate in the DR. Presented at the 183rd FCC-ee Optics Design Meeting (2024). & 54th FCCIS WP2.2 Meeting. https://indico.cern.ch/event/1404486/#3-update-on-booster-vacuum-sys
346. Y. Pischalnikov, et al., Design and test of the compact tuner for narrow bandwidth SRF cavities, in *Proc. 6th International Particle Accelerator Conference (IPAC'15)*, Richmond, VA, USA (2015). https://doi.org/10.18429/JACoW-IPAC2015-WEPTY035
347. N.C. Shipman, I. Ben-Zvi, G. Burt, A. Castilla, M.R. Coly, et al., Ferro-electric fast reactive tuner applications for SRF cavities, in *Proc. IPAC'21*, Campinas, SP, Brazil (2021). https://doi.org/10.18429/JACoW-IPAC2021-TUXC03
348. J. Corno, N. Georg, S.G. Zadeh, J. Heller, V. Gubarev, et al., Uncertainty modeling and analysis of the European X-ray free electron laser cavities manufacturing process. Nucl. Instrum. Methods Phys. Res., Sect. A, Accel. Spectrom. Detect. Assoc. Equip. **971**, 164135 (2020). https://doi.org/10.1016/j.nima.2020.164135
349. P. Craievich, et al., FCC-ee Injector Study and P^3 Project at PSI. CHART Scientific Report 2021. Tech. Rep, CHART (Swiss Accelerator Research and Technology) (2022). https://chart.ch
350. P. Craievich, et al., FCC-ee Injector Study and P^3 Project at PSI. CHART Scientific Report 2022. Tech. Rep, CHART (Swiss Accelerator Research and Technology) (2023). http://www.chart.ch
351. P. Craievich, et al., FCC-ee Injector Study and P^3 Project at PSI. CHART Scientific Report 2023. Tech. Rep, CHART (Swiss Accelerator Research and Technology) (2024). http://www.chart.ch
352. P. Craievich, et al., FCC-ee Injector Study and P^3 Project at PSI. CHART Scientific Report 2024. Tech. Rep, CHART (Swiss Accelerator Research and Technology) (2024). http://www.chart.ch
353. Z. Vostrel, S. Doebert, Design of an electron source for the FCC-ee with top-up injection capability. Nucl. Instrum. Methods Phys. Res., Sect. A **1063**, 169261 (2024). https://doi.org/10.1016/j.nima.2024.169261
354. A. Latina, RF-Track Reference Manual. (2024). https://doi.org/10.5281/zenodo.4580369
355. I. Chaikovska, R. Chehab, V. Kubytskyi, S. Ogur, A. Ushakov, et al., Positron sources: from conventional to advanced accelerator concepts-based colliders. J. Instrum. **17**(05), P05015 (2022). https://doi.org/10.1088/1748-0221/17/05/p05015
356. R. Chehab, Positron sources, in *CAS: 5th General Accelerator Physics Course* (1992). https://cds.cern.ch/record/235242/files/CERN-94-01-V2.pdf

357. Y. Enomoto, K. Abe, N. Okada, T. Takatomi, in *12th International Particle Accelerator Conference (IPAC)*, (JACoW, Campinas, 2021), pp. 2954–2956. https://doi.org/10.18429/JACoW-IPAC2021-WEPAB144
358. N. Vallis, P. Craievich, M. Schär, R. Zennaro, B. Auchmann, et al., Proof-of-principle e^+ source for future colliders. Phys. Rev. Accel. Beams **27**, 013401 (2024). https://doi.org/10.1103/PhysRevAccelBeams.27.013401
359. R. Roussel, A.L. Edelen, T. Boltz, D. Kennedy, Z. Zhang, et al., Bayesian optimization algorithms for accelerator physics. Phys. Rev. Accel. Beams **27**, 084801 (2024). https://doi.org/10.1103/PhysRevAccelBeams.27.084801
360. M. Scapin, et al., Effect of strain-rate and temperature on mechanical response of pure tungsten. J. Dyn. Behav. Mater. **5**, 296–308 (2019). https://doi.org/10.1007/s40870-019-00221-y
361. S. Manson, Fatigue: a complex subject—some simple approximations. Exp. Mech. **5**, 193–226 (1965). https://doi.org/10.1007/BF02321056
362. S. Ogur, et al., Overall injection strategy for FCC-ee, in *Proc. 62nd ICFA ABDW on High Luminosity Circular e^+e^- Colliders (eeFACT'18)*, Hong Kong, China (2018). https://doi.org/10.18429/JACoW-eeFACT2018-TUPAB03
363. H. Herminghaus, K.H. Kaiser, Design, construction and performance of the energy compressing system of the Mainz 300 MeV electron linac. Nuclear Instruments and Methods **113**(2) (1973). https://doi.org/10.1016/0029-554X(73)90831-8
364. B. Goddard, M. Gyr, V. Kain, T. Risselada, Geometrical alignment and associated beam optics issues of transfer lines with horizontal and vertical deflection (2004). Tech. Rep. CERN, Geneva. https://cds.cern.ch/record/733786
365. A. Wolski, *Low-Emittance Storage Rings* (2014). https://doi.org/10.5170/CERN-2014-009.245
366. W. Bartmann, Y. Dutheil, P.A. Sota, FCC-ee Transfer Lines Magnet Specifications. Internal report edms3121188, CERN (2024). https://edms.cern.ch/document/3121188. Not publicly available
367. P. Thonet, A. Vorozhtsov, et al., *Tl Meeting on Magnet Design* (2024). https://indico.cern.ch/event/1486332/
368. F. Zimmermann, et al., Other science opportunities beyond the FCC-ee (2024). https://indico.cern.ch/event/1454873/
369. K. Furukawa, M. Akemoto, D. Arakawa, Y. Arakida, Y. Bando, et al., Achievement of 200,000 hours of operation at KEK 7-GeV electron 4-GeV positron injector linac. J. Phys. Conf. Ser. **2420**(1), 012021 (2023). https://doi.org/10.1088/1742-6596/2420/1/012021
370. W. Allen, A. Brachman, W. Colocho, M. Stanek, J. Warren, Availability Performance and Considerations for LCLS X-ray FEL at SLAC (2011). Tech. Rep. SLAC, United States. http://www.slac.stanford.edu/cgi-wrap/getdoc/slac-pub-14422.pdf. SLAC-PUB–14422
371. T. Lucas, et al., Analysis of the RF Conditioning and Operation of the High Gradient C-band Linac in SwissFEL. IEEE Trans. Nucl. Sci. (2024). Accepted
372. K. Hanke, et al., Maximum depth, lateral displacement and slope of FCC access points (2021). https://edms.cern.ch/document/2636185/1
373. P. Saiz, FCC Surface Areas. Tech. Rep. EDMS Document No. 3197124, CERN (2024). https://edms.cern.ch/document/3197124/1.3
374. F. Valchkova-Georgieva, FCC Integration - Requirements for Point A. EDMS **3126003** (2025). https://edms.cern.ch/document/FCC-INF-SPC-0005/1.0
375. F. Valchkova-Georgieva, FCC Integration - Requirements for Point G EDMS 3136745 (2025). https://edms.cern.ch/document/FCC-INF-SPC-0011/1.0
376. F. Valchkova-Georgieva, FCC Integration - Requirements for Point D and J. EDMS 3126007 (2025). https://edms.cern.ch/document/FCC-INF-SPC-0007/1.0
377. F. Valchkova-Georgieva, FCC Integration - Requirements for Point B (2025). EDMS 3126005. https://edms.cern.ch/document/FCC-INF-SPC-0006/1.0
378. F. Valchkova-Georgieva, FCC Integration - Requirements for Point F. EDMS **3126008** (2025). https://edms.cern.ch/document/FCC-INF-SPC-0008/1.0
379. F. Valchkova-Georgieva, FCC Integration - Requirements for Point H. EDMS **3126009** (2025). https://edms.cern.ch/document/FCC-INF-SPC-0009/1.0
380. F. Valchkova-Georgieva, FCC Integration - Requirements for Point L. EDMS **3126010** (2025). https://edms.cern.ch/document/FCC-INF-SPC-0010/1.0
381. F. Valchkova-Georgieva, FCC Integration - Requirements for the Arcs (2025). EDMS 3136748. https://edms.cern.ch/document/FCC-INF-SPC-0012/1.0
382. F. Valchkova-Georgieva, FCC Integration - Requirements for the Alcoves (2025). EDMS 3136752. https://edms.cern.ch/document/FCC-INF-SPC-0013/1.0
383. Report of the feasibility study of installing HV cables in the tunnel (2024). https://edms.cern.ch/document/3170168/1
384. L. Delprat, B. Naydenov, B. Bradu, K. Brodzinski, Status of the FCC cryogenics feasibility study. IOP Conf. Ser., Mater. Sci. Eng. (2024). (Submitted)
385. F. Millet, L. Tavian, U. Cardella, O. Amstutz, P. Selva, A. Kuendig, Preliminary conceptual design of FCC-hh cryoplants: linde evaluation. IOP Conf. Ser., Mater. Sci. Eng. **502**, 012131 (2019). https://doi.org/10.1088/1757-899X/502/1/012131
386. L. Tavian, F. Millet, M. Roig, G. Zick, J. Bernhardt, Preliminary conceptual design of FCC-hh cryo-refrigerators: air liquide study. IOP Conf. Ser., Mater. Sci. Eng. **755**, 012085 (2020). https://doi.org/10.1088/1757-899X/755/1/012085
387. K. Canderan, V. Parma, *SRF System Integration - Cryomodule Functional Specifications and Design* (2024). FCC Week. indico.cern.ch/event/1298458/contributions/5977843
388. B. Naydenov, L. Delprat, B. Bradu, K. Brodzinski, 2 K system exergetic optimisation and helium recovery system for FCC-ee. IOP Conf. Ser.: Mater. Sci. (2024). Eng. (submitted)

389. M. Koratzinos, The FCC-ee HTS4 project: study of superconducting short straight sections for FCC-ee (2023). Tech. rep. CERN, Geneva. https://indico.cern.ch/event/1202105/contributions/5385376/
390. C. Colloca, R. Rinaldesi, FCC Transport Requirements. Tech. Rep. EDMS Document No. 2894421, CERN (2023). https://edms.cern.ch/document/2894421/1
391. Official Journal of the European Union, *Directive 2006/42/EC of the European Parliament and of the Council of 17 May 2006 on machinery*. Tech. Rep., European Union (2006). http://data.europa.eu/eli/dir/2006/42/2019-07-26
392. European Union, Official Journal of the European Union, Directive 2014/30/EU of the European Parliament and of the Council of 26 February 2014 on the harmonisation of the laws of the Member States relating to electromagnetic compatibility (2014). Tech. Rep. http://data.europa.eu/eli/dir/2014/30/oj
393. Official Journal of the European Union, *Directive 2014/35/EU of the European Parliament and of the Council of 26 February 2014 on the harmonisation of the laws of the Member States relating to the making available on the market of electrical equipment designed for use within certain voltage limits*. Tech. Rep., European Union (2014). http://data.europa.eu/eli/dir/2014/35/oj
394. G. Kuhlmann, B. Müller, C. Prasse, L. Schreiber, F. Veit, Future Circular Collider - Vehicle and Logistics Concepts. Tech. Rep. EDMS Document No. 3177470, Fraunhofer Institute for Material Flow and Logistics (2025). https://edms.cern.ch/document/3177470/1
395. Official Journal of the European Union, *Directive 2014/33/EU of the European Parliament and of the Council of 26 February 2014 on the harmonisation of the laws of the Member States relating to lifts and safety components for lifts*. Tech. Rep., European Union (2014). http://data.europa.eu/eli/dir/2014/33/oj
396. G. Nergiz, O. Rios, A. Henriques, Evacuation simulation: Input for size of safe areas in the FCC-ee machine. Tech. Rep. FCC-INF-RPT-0072 v2.0, CERN (2024). https://edms.cern.ch/document/2873143
397. D. Lafarge, Transport of elements in Point A and Point B, Presented at TIWG meeting #71, Geneva, Switzerland, 28 August (2024). https://indico.cern.ch/event/1369411
398. M. Zielinski, Production Simulation of the FCC-ee Magnets Using SIEMENS Plant Simulation. Tech. Rep. EDMS Document No. 3223636, CERN (2024). https://edms.cern.ch/document/3223636/1
399. D. Lafarge, S. Pelletier, R. Rinaldesi, Etude pour un transport lourd vers le site PH. Tech. Rep. EDMS Document No. 3095045, CERN (2024). https://edms.cern.ch/document/3095045/2
400. D. Lafarge, S. Pelletier, Study for heavy transport of 60 t magnets to experimental points A, D G and J. Tech. Rep. EDMS Document No. 3212639, CERN (2024). https://edms.cern.ch/document/3212639/1
401. D. Lafarge, Surface transport study for FCC-ee installation. Tech. Rep. EDMS Document No. 3212644, CERN (2024). https://edms.cern.ch/document/3212644/1
402. CERN Service Portal, Fixed Line Phone Service. https://cern.service-now.com/service-portal?id=service_element&name=fixed-line-phone
403. CERNphone user documentation. https://cernphone.docs.cern.ch
404. CERN mobile phone service. https://mobile-service.docs.cern.ch
405. TETRA Radio Communication Service. https://cern.ch/tetra
406. LPWAN Service Documentation, LoRaWAN at CERN. https://lpwan-service.docs.cern.ch/loracern/
407. K. Bos, N. Brook, D. Duellmann, C. Eck, et al. LHC computing Grid: Technical Design Report. Version 1.06 (20 Jun 2005) (2005). http://cds.cern.ch/record/840543
408. News article: Building work for CERN's new data centre in Prévessin begins. https://home.cern/news/news/computing/building-work-cerns-new-data-centre-prevessin-begins
409. CERN Open Data Policy for the LHC Experiments. https://opendata.cern.ch/docs/cern-open-data-policy-for-lhc-experiments
410. Z. Akopov, et al., Status Report of the DPHEP Study Group: Towards a Global Effort for Sustainable Data Preservation in High Energy Physics (2012). https://arxiv.org/abs/1205.4667
411. H. Gamper, The FCC Robotic System for Safety and Availability, Presented at FCC Week, San Francisco, USA, 11 June (2024). https://indico.cern.ch/event/1298458/contributions/5977742/
412. M. Nas, Emergency Response in FCC, Presented at TIWG meeting #56, Geneva, Switzerland, 31 January (2024). https://indico.cern.ch/event/1369396/contributions/5776554/attachments/2790648/4866535/TIWG%20CFRS%20response%20FCC.pdf
413. H. Gamper, A robotic system for CERN's future circular collider. PhD Thesis, Geneva/Linz, Switzerland/Austria, 06 May (2024). https://cds.cern.ch/record/2923795
414. H. Gamper, Maintenance and Operational Safety Requirements for Robotics (2024). https://edms.cern.ch/document/3220312/1
415. H. Gamper, Emergency Safety Requirements for Robotics (2024). https://edms.cern.ch/document/3220303/1
416. M. Di Castro, Code of practice of remote maintenance for inspection and telemanipulation (2021). https://edms.cern.ch/document/2263542
417. B. Weyer, Definition of the geodetic reference systems, datums and frames for the FCC. Tech. Rep. EDMS Document No. 2885819, CERN (2023). https://edms.cern.ch/document/2885819/0
418. M. Varga, A. Wieser, Conceptual design report for the establishment of a surface geodetic reference network including control baselines. Tech. Rep. IGP-AA-2.2, ETHZ (2024)
419. J. Koch, et al., FCC Geoid: Astro-geodetic and GNSS-levelling profile. Tech. Rep. EDMS Document No. 2890235, ETHZ (2023). https://edms.cern.ch/document/2890235/0

420. M. Varga, A. Wieser, Concept for calibration, checking and testing of the geodetic equipment for the FCC. Tech. Rep. IGP-AA-2.5, ETHZ (2024)
421. HSE Unit, The CERN Safety Policy (2016). https://edms.cern.ch/document/1416908
422. HSE Unit, SR-SO. Responsibilities and organisational structure in matters of Safety at CERN (2016). https://edms.cern.ch/document/1389540
423. HSE Unit, GSI-SO-7. Project Safety Officer - PSO (2021). https://edms.cern.ch/document/1410233
424. SUVA, Connaissez-vous le portefeuille des phénomènes dangereux dans votre entreprise? Tech. Rep., SUVA (2023). SUVA publication 66105.f
425. T. Otto, *Safety for Partice Accelerators* (Springer, Berlin, 2021). https://doi.org/10.1007/978-3-030-57031-6
426. VKFI, *AEAI DPI 27-15 Méthodes de preuves en protection incendie*. Tech. Rep. AEAI DPI 27-15, VKFI (2015)
427. SFPE, *The SFPE Guide to Performance-Based Fire Safety Design* (SFPE, 2015), p. 203
428. S. La Mendola, S. Baird, A. Henriques, FCC Performance-based safety design. Tech. Rep. FCC Week 2017 - contribution n. 2601369, CERN (2017)
429. International Organization for Standardization. ISO 834-1 Fire-resistance tests — Elements of building construction (1999). Part 1: General requirements
430. CEN/TC 127/WG 7 - Classification, EN 13501-2. Fire classification of construction products and building elements - Part 2: Classification using data from fire resistance tests, excluding ventilation services, EU (2023). Tech. rep
431. European Comission, Directive 2004/54/EC of the European Parliament and of the Council of 29 April 2004 on minimum safety requirements for tunnels in the trans-European road network (2004). Tech. Rep. EU. https://eur-lex.europa.eu/legal-content/EN/TXT/?uri=CELEX:02004L0054-20090807
432. European Comission, Commission Regulation (EU) No 1303/2014 of 18 November 2014 concerning the technical specification for interoperability relating to ‘safety in railway tunnels’ of the rail system of the European Union. Tech. Rep., EU (2014). https://eur-lex.europa.eu/legal-content/EN/TXT/?uri=uriserv%3AOJ.L_.2014.356.01.0394.01.ENG
433. Direction du travail - Conditions de travail, Commentaire de l’ordonnance 4 relative à la loi sur le travail. Tech. Rep., Le Conseil fédéral Suisse (2024). https://www.seco.admin.ch/seco/fr/home/Arbeit/Arbeitsbedingungen/Arbeitsgesetz-und-Verordnungen/Wegleitungen/Wegleitung-zur-ArGV-4.html
434. NFPA, NFPA520 Standard on Subterranean Spaces. Tech. Rep., NFPA (2021). https://www.nfpa.org/codes-and-standards/nfpa-520-standard-development/520
435. STUVA, Security and Workplace Safety Concepts for the Construction, Installation and Operation of the XFEL Research Facility. Tech. Rep. (2005)
436. ILC Global Design Effort Team. The international linear collider technical design report | volume 3.ii: Accelerator baseline design (2013). https://linearcollider.org/files/images/pdf/Acceleratorpart2.pdf
437. M. Bettelini, Systems approach to underground safety. Undergr. Space **5**(3), 258–266 (2020). https://doi.org/10.1016/j.undsp.2019.04.005
438. I.M. Melero, G. Peon, Ventilation strategy for FCC, Presented at the FCC Week 2024, San Francisco, USA, USA, June 10–14 (2024). https://indico.cern.ch/event/1298458/contributions/5976113/
439. D. Perovic, S.L. Mendola, R. Froeschl, O. Deschamps, P. Vojtyla, et al. CMS FIRIA (Fire-induced Radiological Analysis) Report. Tech. Rep. EDMS 2758294, CERN (2024). https://edms.cern.ch/document/2758294
440. G. Gai, B.B. Rubio, S. La Mendola, R. Froeschl, V. Kouskoura, et al. ATLAS FIRIA (Fire-induced Radiological Analysis) Report. Tech. Rep. EDMS 2396252, CERN (2021). https://edms.cern.ch/document/2396252/1
441. R. Francaise, Code du travail, articles l1 à l8331-1, France (2024). Tech. Rep. https://www.legifrance.gouv.fr/codes/texte_lc/LEGITEXT000006072050/
442. VKFI, Norme et Directive de Protection Incendie (2015). https://www.bsvonline.ch/fr/prescriptions-de-protection-incendie/prescriptions-2015#c-directives
443. F. Institute FIML Final Report. Tech. Rep, Fraunhofer Institute (2024). https://edms.cern.ch/document/3177470
444. R. Rinaldesi, Transport concept for personnel (normal and evacuation), Presented at the FCC Week 2024, San Francisco, USA, June 10–14 (2024). https://indico.cern.ch/event/1298458/contributions/5976137/
445. CEN, EN 81-20:2020 Safety rules for the construction and installation of lifts - Lifts for the transport of persons and goods - Part 20: Passenger and goods passenger lifts. Tech. rep., CEN (2020)
446. ISO, ISO 8100-1:2019 Lifts for the transport of persons and goods. Tech. Rep., ISO (2019)
447. Le Conseil Fédéral suisse, Le Gouvernement de la République française et le CERN, Accord relatif à l’assistance mutuelle entre les services dans le cadre d’opérations de secours. Tech. Rep. EDMS Document No. 2006013/1, CERN (2016). https://edms.cern.ch/ui/file/2006013/1/ConventionsecoursCERN_alternat_suisse.pdf
448. C. Marcel, Electrical secured network concept description. Tech. Rep. ELG-GENNET-RPT-0031, CERN (2024). https://edms.cern.ch/document/3152176
449. International Electrotechnical Commission. IEC 61511 Functional safety - Safety instrumented systems for the process industry sector (2016)
450. CEN. EN 54: Fire detection and fire alarm systems
451. European Commission, Commission Delegated Regulation (EU) 2024/1681 of 6 March 2024 supplementing Regulation (EU) No 305/2011 of the European Parliament and of the Council by establishing classes of performance in relation to the resistance to fire of construction products. Tech. Rep. Document 32024R1681, European Commission, Directorate-General for Internal Market, Industry, Entrepreneurship and SMEs (2024). https://eur-lex.europa.eu/legal-content/EN/ALL/?uri=CELEX:32024R1681

452. C.S. Guideline, 'SG-EL-0-0-1 Installation d'éclairage de sécurité (2011). Tech. rep. CERN. https://edms.cern.ch/ui/file/1167351/LAST__RELEASED/Safety__Guideline__EL-0-0-1__version__2012.pdf
453. S. Arias, S. La Mendola, J. Wahlqvist, O. Rios, D. Nilsson, E. Ronchi, Virtual reality evacuation experiments on way-finding systems for the future circular collider. Fire Technol. **55**(6), 2319–2340 (2019). https://doi.org/10.1007/s10694-019-00868-y
454. V. Vlachoudis, in *Proceedings of the International Conference on Mathematics, Computational Methods & Reactor Physics (M&C 2009)* (American Nuclear Society, Saratoga Springs, New York, 2009)
455. HSE Unit, Safety Code F – Radiation Protection (2006). https://edms.cern.ch/document/335729
456. D. Forkel-Wirth, T. Otto, Area classification. Tech. Rep. EDMS 810149, CERN (2006). https://edms.cern.ch/document/810149
457. European Union, Official Journal of the European Union, Directive 2006/25/EC on the minimum health and safety requirements regarding the exposure of workers to risks arising from physical agents (artificial optical radiation) (2006). Tech. Rep. Directive 2006/25/EC
458. European Union, Official Journal of the European Union, Directive 2013/35/EU on the minimum health and safety requirements regarding the exposure of workers to the risks arising from physical agents (electromagnetic fields) (2013). Tech. Rep. Directive 2013/35/EC
459. HSE Unit, Protection of persons from exposure to Static Magnetic Fields (2024). https://edms.cern.ch/document/2974732
460. K. Hanke, Residual magnetic field at surface of experimental points. Tech. Rep. FCC-INF-PM-0077, CERN (2024). https://edms.cern.ch/document/2856463
461. International Electrotechnical Commission. IEC 60825 Safety of laser products (2021)
462. International Electrotechnical Commission. IEC 60529 Degrees of protection provided by enclosures (IP Code) (2013)
463. European Union, Official Journal of the European Union, Regulation 2023/1230/EU on machinery (2023). Tech. Rep. Regulation 2023/1230/EU
464. HSE Unit, Protection of workers against noise (2019). https://edms.cern.ch/document/1826633
465. European Committee for Standardization, EN 547: Safety of machinery - Human body measurements - Part 1: Principles for determining the dimensions required for openings for whole body access into machinery, Standard, CEN, Brussels (1996)
466. A. Harrison, Risk analysis of the LHC underground area: fire risk due to faulty electrical equipment. Ph.D. thesis, Leoben University (2007). https://cds.cern.ch/record/1044825. Presented on Sep 2007
467. G. Nergiz, O. Rios, Smoke extraction strategies analysis for FCC-ee tunnel. Tech. Rep. FCC-INF-RPT-0104, CERN (2024). https://edms.cern.ch/document/3169951
468. NIST, National Institute of Standards and Technology, US, Fire dyanmics simulator v6 (2024). Tech. Rep. https://pages.nist.gov/fds-smv/
469. ISO Standard, ISO 13571:2012. Life-threatening components of fire - Guidelines for the estimation of time to compromised tenability in fires. Tech. Rep., ISO (2012)
470. BSI Standards Publication, BS PS-7974-6: Application of fire safety engineering principles to the design of buildings. Part 6: Human factors: Life safety strategies — Occupant evacuation, behaviour and condition (Sub-system 6). Tech. Rep., BSI (2004)
471. O. Rios, Quantitive assessment of Fire Hazzard for FCChh (and FCCee). Tech. Rep. FCC-INF-RPT-0055, CERN (2018). https://edms.cern.ch/document/1975602/1
472. ISO Standard, ISO 16733-1 Fire safety engineering — Selection of design fire scenarios and design fires — Part 1: Selection of design fire scenario. Tech. Rep., ISO (2015)
473. S. Desanghere, E. Cesmat, D. Giuliani, Experimental and numerical studies to assess the benefits of water mist system in Mont-Blanc tunnel, Lombardi, GEIE-TMB (2015). Tech. Rep. https://www.tunnelmb.net/public/files/456/1__b-3-mitigazione-poster-eng.pdf
474. Proceedings, 12th International Conference Tunnel Safety and Ventilation. Tech. Rep., Gratz (2024). https://www.tunnel-graz.at/library/tunnel-2024.html
475. M.J. Hurley, D.T. Gottuk, J.R. Hall Jr., K. Harada, E.D. Kuligowski, et al., *SFPE Handbook of Fire Protection Engineering* (Springer, Berlin, 2015)
476. CEN/TC 127/WG 7 - Classification, EN 13501-1. Fire classification of construction products and building elements - Part 1: Classification using data from reaction to fire tests, Tech. rep., EU (2020)
477. Centre d'Études des Tunnels, CETU, Comportement au feu des tunnels routiers. Tech. rep., Ministère de l'Équipement, des Transports, de l'Aménagement du territoire, du Tourisme et de la Mer. Direction des routes (2005). https://www.cetu.developpement-durable.gouv.fr/IMG/pdf/Guide__comportement__au__feu__cle2f3714.pdf
478. Ministère de l'Équipement, des Transports, de l'Aménagement du territoire, du Tourisme et de la Mer. Direction des routes, Arrêté du 8 novembre 2006 fixant les exigences de sécurité minimales applicables aux tunnels routiers de plus de 500 mètres du réseau transeuropéen, Tech. Rep., France (2006). https://www.legifrance.gouv.fr/loda/id/JORFTEXT000000244062
479. HSE Unit, The use of plastic and other non-metallic materials at CERN with respect to fire safety and radiation resistance (2005). https://edms.cern.ch/document/335806
480. CERN Safety Guidelines, SSI-FS-2-1. Fire Safety and Radiation Resistance requirements for Cables. Tech. Rep., CERN (2024). https://edms.cern.ch/file/2669584/LAST__RELEASED/SSI-FS-2-1__EN.pdf

481. D. Drysdale, *An Introduction to Fire Dynamics* (Wiley, New York, 2011). https://doi.org/10.1002/9781119975465.ch6
482. BSI Standards Publication, Fire safety in the design, management and use of buildings – Code of practice. Tech. Rep., BSI (2017)
483. Ministre des transports, Annex 2. 2000-6: Instruction technique relative aux dispositions de sécurité dans les nouveaux tunnels routiers (conception et exploitation), France (2005). Tech. Rep. https://dtrf.cerema.fr/pdf/pj/Dtrf/0002/Dtrf-0002392/TO2392.pdf
484. Ministre des transports, Arrêté du 22 novembre 2005 relatif à la sécurité dans les tunnels des systèmes de transport public guidés urbains de personnes, France (2005). Tech. Rep. https://www.legifrance.gouv.fr/loda/id/JORFTEXT000000450184/2018-06-08
485. VKFI, AEAI DPI 15-15. Tech. Rep. AEAI DPI 15-15, VKFI (2015)
486. SIA, SIA-197-1: Projet de tunnels - Tunnels ferroviaires. Tech. Rep., SIA (2019). https://connect.snv.ch/en/sn-505197-1-2019
487. SIA, SIA-197-2: Projet de tunnels - Tunnels routiers. Tech. Rep., SIA (2023). https://connect.snv.ch/en/sn-5051972-2023
488. F. De Salvo, Underground design methodology report. Tech. Rep. LHC-K3500-ER-0001, CERN (2017). https://edms.cern.ch/document/1709154
489. K. Canderan, V. Parma, FCC-ee CM Helium safety study. Tech. Rep. FCC-INF-RPT-0098, CERN (2024). https://edms.cern.ch/document/3103096
490. A. Henriques, G. Nergiz, FCC-ee ODH safety study - 3 kg/s scenario. Tech. Rep. FCC-INF-RPT-0096, CERN (2024). https://edms.cern.ch/document/3089983
491. A. Henriques, G. Nergiz, FCC-ee ODH safety study - MCI (20 kg/s) scenario. Tech. Rep. FCC-INF-RPT-0102, CERN (2024). https://edms.cern.ch/document/3153491
492. T. Koettig, J. Casas-Cubillos, M. Chorowski, L. Dufay-Chanat, M. Grabowski, A. Jedrusyna, et al., Controlled cold helium spill test in the LHC tunnel at CERN. Phys. Proc. **67**, 1074–1082 (2015). https://doi.org/10.1016/j.phpro.2015.06.203. https://cds.cern.ch/record/2103418
493. L. Danciu, S. Nandan, C. Reyes, R. Basili, G. Weatherill, et al., The 2020 update of the European Seismic Hazard Model: Model Overview. EFEHR Technical Report 001, v1.0.0. Tech. Rep., EFEHR (2020)
494. European Committee for Standardization (CEN), Eurocode 8: Design of structures for earthquake resistance - Part 1-1: General Rules and Seismic Action (European Commission, 1998). Tech. Rep. prEN 1998-1-1:2022. https://eurocodes.jrc.ec.europa.eu/EN-Eurocodes/eurocode-8-design-structures-earthquake-resistance
495. S. La Mendola, LHC Evacuation assessment for LS1. LHC experiments and machine. Tech. Rep. EDMS 1352807, CERN (2012). https://edms.cern.ch/document/1352807
496. T. Otto, Estimation of Occupancy of LHC Sectors during Long Shutdown 2. Tech. Rep. FCC-INF-RPT-0071, CERN (2023). https://edms.cern.ch/document/2851367
497. VKFI, AEAI DPI 16-15: Signalisation des voies d'évacuation. Éclairage de sécurité. Alimentation de sécurité. Tech. Rep. AEAI DPI 16-15, VKFI (2015)
498. P. Besson, FS-01 Interpretation of Safety Requirements - Evacuation procedure and principles for cern sites on French territory. Tech. Rep. EDMS N. 1815461 v1, CERN (2017). https://edms.cern.ch/document/1815461
499. Th. Otto, M. Nass, O. Rios, Emergency interventions and fire fighting in FCC. Tech. Rep. FCC-INF-PM-0088 v. 1.0, CERN (2024). https://edms.cern.ch/document/2922606
500. Republique Francaise, Loi n^o 93-1418 du 31 décembre 1993. Tech. Rep., France (1994). https://www.legifrance.gouv.fr/loda/id/JORFTEXT000000361975#:~:text=de%20b%C3%A2timent%20...-,Loi%20n%C2%B0%2093%2D1418%20du%2031%20d%C3%A9cembre%201993%20modifiant,date%20du%2024%20juin%201992
501. HSE Unit, SR-SIM. Responsibilities in matters of Safety Incident Management at CERN (2024). https://edms.cern.ch/document/2583792
502. M. Mannelli, in *ALPHA A Compact, Modular Three Solenoid System as a Common Magnet Platform for the sequential staging of an FCC-ee, followed by an FCC-hh Advanced Lepton Photon Hadron Apparatus.* (2020), 4th FCC Physics and Experiments Workshop
503. R. Bruce, J. Molson, Preliminary collimation system design concept and performance estimate: Deliverable D2.6. Tech. Rep., CERN, Geneva (2019). https://cds.cern.ch/record/2665192. On behalf of EuroCirCol WP2
504. R. Van Weelderen (2022). Private communication
505. G. Perez-Segurana, E. Todesco, M. Giovannozzi, Study of the corrector systems for the new lattice of the CERN hadron-hadron future circular collider, in *Proc. IPAC'24*, Nashville, TN, USA (2024). https://doi.org/10.18429/JACoW-IPAC2024-MOPC15
506. M. Giovannozzi, et al., Recent updates of the layout of the lattice of the CERN hadron-hadron future circular collider, in *Proc. IPAC'23*, Venice, Italy (2023). https://doi.org/10.18429/JACoW-IPAC2023-MOPL033
507. W. Bartmann, M. Atanasov, M.J. Barnes, J. Borburgh, F. Burkart, B. Goddard, T. Kramer, A. Lechner, A. Sanz Ull, R. Schmidt, et al., Dump system concepts for the future circular collider. Phys. Rev. Accel. Beams **20**, 031001 (2017). https://doi.org/10.1103/PhysRevAccelBeams.20.031001
508. R. Bruce, R.D. Maria, M. Giovannozzi, N. Mounet, S. Redaelli, Optics configurations for improved machine impedance and cleaning performance of a multi-stage collimation insertion, in *Proc. IPAC'21*, Campinas, SP, Brazil (2021). https://doi.org/10.18429/JACoW-IPAC2021-MOPAB006

509. B. Lindström, et al., Proc. HB'23, in *ICFA Advanced Beam Dynamics Workshop on High-Intensity and High-Brightness Hadron Beams*, (JACoW Publishing, Geneva, 2024), pp. 183–187. https://doi.org/10.18429/JACoW-HB2023-TUC4C2
510. M. Varasteh, R. Bruce, F. Cerutti, M. Crouch, F. Zimmermann, Impact of betatron collimation losses in the high-energy large hadron collider. Phys. Rev. Accel. Beams **24**, 041601 (2021). https://doi.org/10.1103/PhysRevAccelBeams.24.041601
511. D. Amorim, S. Antipov, N. Biancacci, B. Salvant, P. Arpaia, et al., HL-LHC impedance and related effects. Tech. Rep. CERN-ACC-NOTE-2018-0087, CERN (2018). https://cds.cern.ch/record/2652401
512. N.J. Simon, E.S. Drexler, R.P. Reed, *Properties of Copper and Copper Alloys at Cryogenic Temperatures* (National Inst. of Standards and Technology (MSEL), Boulder, 1992). https://doi.org/10.2172/5340308. Final report. Tech. Rep., Materials Reliability Div.
513. J.G. Hust, A.B. Lankford, *Thermal Conductivity of Aluminum, Copper, Iron, and Tungsten for Temperatures from 1 k to the Melting Point* (National Bureau of Standards, Boulder, 1984). Tech. Rep., Chemical Engineering Science Div. https://www.osti.gov/biblio/6225458
514. Xwakes. https://github.com/xsuite/xwakes/. Accessed: 2025-02-05
515. R. Aßmann, et al., Review of the FCC-hh Injection Energy, 16 October 2015. Conclusions and Recommendations. Unpublished
516. M. Giovannozzi, E. Todesco, Combined-function optics for circular high-energy hadron colliders. Eur. Phys. J. Plus **137**(3), 361 (2022). https://doi.org/10.1140/epjp/s13360-022-02583-0
517. E. Todesco, M. Giovannozzi, Optimizing the filling factor in high energy colliders, in *Proc. IPAC'23*, Venice, Italy (2023). https://doi.org/10.18429/JACoW-IPAC2023-WEPM061
518. B. Goddard, W. Bartmann, W. Herr, P. Lebrun, A. Milanese, Main changes to LHC layout for reuse as FCC-hh High Energy Booster. https://cds.cern.ch/record/2002005/files/CERN-ACC-2015-030.pdf
519. L.A. Dyks, D. Posthuma de Boer, A. Ross, M. Backhouse, S. Alden, G.L. D' Alessandro, D. Harryman, The superconducting super proton synchrotron. Tech. Rep., John Adams Institute (2019). https://doi.org/10.17181/CERN.3DI5.3YUS. Student design project as part of the JAI Graduate Accelerator Physics Programme
520. M. Vretenar, J. Vollaire, R. Scrivens, C. Rossi, F. Roncarolo, S. Ramberger, U. Raich, B. Puccio, D. Nisbet, R. Mompo, et al., *Linac4 Design Report*. CERN Yellow Reports: Monographs, vol. 6 (CERN, Geneva, 2020). https://doi.org/10.23731/CYRM-2020-006
521. FASER - LHC experiment. https://faser.web.cern.ch/
522. G. Jackson, The Fermilab recycler ring technical design report. Rev. **1**(2) (1996). https://doi.org/10.2172/16029. Tech. rep., FNAL
523. M. Hu, The fermilab recycler ring, in *Proc. Particle Accelerator Conference (PAC'01)*, Chicago, IL, USA (2001). https://doi.org/10.1109/PAC.2001.987423
524. J.A. Clarke, in *The Science and Technology of Undulators and Wigglers* (Oxford University Press, London, 2004). https://doi.org/10.1093/acprof:oso/9780198508557.003.0007
525. G. Peon (2023). Private communication
526. B. Shepherd, Development of adjustable permanent magnet quadrupoles, Greece (2019). Presented at the ALERT 2019 workshop, Ioanna. https://indico.cern.ch/event/819665/contributions/3494717
527. B. Lindstrom, P. Bélanger, A. Gorzawski, J. Kral, A. Lechner, et al., Dynamics of the interaction of dust particles with the LHC beam. Phys. Rev. Accel. Beams **23**, 124501 (2020). https://doi.org/10.1103/PhysRevAccelBeams.23.124501
528. J. Hunt, Update on R2E and heat load simulations, Brussels, Belgium (2019). Presented at FCC Week. https://indico.cern.ch/event/727555/contributions/3449897/attachments/1870542/3078010/huntFCCweekPresentation_2.pdf
529. A.J. Samin, A review of radiation-induced demagnetization of permanent magnets. J. Nucl. Mater. **503**, 42–55 (2018). https://doi.org/10.1016/j.jnucmat.2018.02.029
530. G. Lefebvre, Le marché des terres rares en 2022 [rare earth mineral market information]. Available from Le portail français des ressources minérales non énergétiques (2022). https://www.mineralinfo.fr/fr/ecomine/marche-des-terres-rares-2022-filieres-dapprovisionnement-aimants-permanents
531. K. Halbach, Application of permanent magnets in accelerators and electron storage rings (invited). J. Appl. Phys. **57**(8), 3605–3608 (1985). https://doi.org/10.1063/1.335021
532. P.A. Thonet, Design and manufacturing of three permanent magnet dipoles for faser experiment (2021). https://indico.cern.ch/event/1010394/. CERN TE-MSC Seminar
533. S. Brooks, G. Mahler, J. Cintorino, J. Tuozzolo, R. Michnoff, Permanent magnets for the return loop of the Cornell-Brookhaven energy recovery linac test accelerator. Phys. Rev. Accel. Beams **23**, 112401 (2020). https://doi.org/10.1103/PhysRevAccelBeams.23.112401
534. https://roxie.docs.cern.ch/
535. D. Tommasini, et al., The 16 T dipole development program for FCC. IEEE Trans. Appl. Supercond. **27**(4), 4000405 (2017). https://doi.org/10.1109/TASC.2016.2634600
536. M. Lamont, Mandate of the hfm program leader (2024). Unpublished document
537. R. Perin, in *Encyclopedia of Applied Superconductivity* (IOP, London, 1998), pp. 919–950
538. L. Rossi, The LHC main dipoles and quadrupoles toward series production. IEEE Trans. Appl. Supercond. **13**(2), 1221–1228 (2003). https://doi.org/10.1109/TASC.2016.814317
539. A. Ballarino, L. Bottura, Targets for R&D on Nb_3Sn conductor for high energy physics. IEEE Trans. Appl. Supercond. **25**(2), 6000906 (2015). https://doi.org/10.1109/TASC.2014.2367105

540. G. Pérez Segurana, et al., A new baseline layout for the FCC-hh ring, in *Proc. International Particle Acelerator Confrence IPAC24* (2024). https://doi.org/10.18429/JACoW-IPAC2024-MOPC14
541. O.S. Brüning, P. Collier, P. Lebrun, S. Myers, R. Ostojic, J. Poole, P. Proudlock, *LHC Design Report. CERN Yellow Reports: Monographs* (CERN, Geneva, 2004). https://doi.org/10.5170/CERN-2004-003-V-1
542. G. Ambrosio, et al., Challenges and lessons learned from fabrication, testing, and analysis of eight MQXFA low beta quadrupole magnets for HL-LHC. IEEE Trans. Appl. Supercond. **33**(5), 4003508 (2023). https://doi.org/10.1109/TASC.2023.3261842
543. S. Izquierdo Bermudez, et al., Status of the MQXFB Nb_3Sn quadrupoles for the HL-LHC. IEEE Trans. Appl. Supercond. **33**(5), 4001209 (2023). https://doi.org/10.1109/TASC.2023.3244445
544. S. Izquierdo Bermudez, Persistent current magnetization effects in the 16 T main dipoles for the future circular collider. Internal Note EDMS 2036614, CERN (2018). https://edms.cern.ch/document/2036614
545. A. Ballarino, et al., *The CERN FCC Conductor Development Program: A Worldwide Effort for the Future Generation of High-Field Magnets* (2019). https://doi.org/10.1109/TASC.2019.2896469
546. X. Xu, et al., Significant reduction in the low-field magnetization of Nb_3Sn superconducting strands using the internal oxidation APC approach. Supercond. Sci. Technol. **36**(8), 085008 (2023). https://doi.org/10.1088/1361-6668/acdf8c
547. F. Meot, T. Tortschanoff, Combined function focusing, combined function superconducting dipole, for large hadron colliders. Technical Report CERN SL-Note-94-97-AP, CERN (1994). https://cds.cern.ch/record/267404
548. M. Giovannozzi, E. Todesco, Combined-function optics for circular high-energy hadron colliders. Eur. Phys. J. **137** (2022). https://doi.org/10.1140/epjp/s13360-022-02583-0
549. G. Ambrosio, et al., Design of Nb_3Sn coils for LARP long magnets. IEEE Trans. Appl. Supercond. **17**(2), 1035–1038 (2007). https://doi.org/10.1109/TASC.2007.898401
550. J. Strait, et al., Tests of full scale SSC R&D dipole magnets. IEEE Trans. Magn. **25**(2), 1455–1458 (1989). https://doi.org/10.1109/20.92570
551. R. Valente, et al., Electromagnetic and mechanical study for the Nb_3Sn cos-theta dipole model for the FCC. IEEE Trans. Appl. Supercond. **30**(4), 4001905 (2020). https://doi.org/10.1109/TASC.2020.2973050
552. A. Den Ouden, et al., Application of Nb_3Sn superconductors in high-field accelerator magnets. IEEE Trans. Appl. Supercond. **7**(2), 733–738 (1997). https://doi.org/10.1109/77.614654
553. D. Dell'Orco, et al., Design of the Nb_3Sn dipole D20. IEEE Trans. Appl. Supercond. **3**(1), 82–86 (1993). https://doi.org/10.1109/77.233469
554. A. McInturff, et al., Test results for a high field (13 T) Nb_3Sn dipole, in *Proc. Particle Accelerator Conference*, Vancouver (1997). https://doi.org/10.1109/PAC.1997.751111
555. G.L. Sabbi, et al., Design of HD2: a 15 Tesla Nb_3Sn dipole with a 35 mm bore. IEEE Trans. Appl. Supercond. **15**(2), 1128–1131 (2005). https://doi.org/10.1109/TASC.2005.849683
556. A. Milanese, et al., Design of the EuCARD high field model dipole magnet FRESCA2. IEEE Trans. Appl. Supercond. **22**(3), 4002604 (2012). https://doi.org/10.1109/TASC.2011.2178980
557. G. Willering, et al., Tests of the FRESCA2 100 mm bore Nb_3Sn block-coil magnet to a record field of 14.6 T. IEEE Trans. Appl. Supercond. **29**(5), 4004906 (2019). https://doi.org/10.1109/TASC.2019.2900938
558. M. Karppinen, et al., Design of 11 T twin-aperture Nb_3Sn dipole demonstrator magnet for LHC upgrades. IEEE Trans. Appl. Supercond. **22**(3), 4901504 (2012). https://doi.org/10.1109/TASC.2011.2178111
559. A. Zlobin, et al., Development and test of a single-aperture 11 T Nb_3Sn demonstrator dipole for LHC upgrades. IEEE Trans. Appl. Supercond. **23**(3), 4000904 (2013). https://doi.org/10.1109/TASC.2013.2244634
560. A. Zlobin, et al., Development and first test of the 15 T Nb_3Sn dipole demonstrator MDPCT1. IEEE Trans. Appl. Supercond. **30**(4), 4000805 (2020). https://doi.org/10.1109/TASC.2020.2967686
561. E. Todesco, et al., The HL-LHC magnets towards series production. Supercond. Sci. Technol. **34**(5), 053001 (2021). https://doi.org/10.1088/1361-6668/abdba4
562. R. Valente, et al., Baseline design of a 16 T $\cos(\theta)$ bending dipole for the future circular collider. IEEE Trans. Appl. Supercond. **29**(5), 4000405 (2019). https://doi.org/10.1109/TASC.2019.2901604
563. J.C. Perez, et al., BOND: a 14 T dipole based on block coils. IEEE Trans. Appl. Supercond. (2025). Accepted for publication
564. H. Felice, et al., F2d2: a block-coil short-model dipole toward FCC. IEEE Trans. Appl. Supercond. **29**(5), 4001807 (2019). https://doi.org/10.1109/TASC.2019.2900937
565. V. Calvelli, et al., R2d2, the CEA graded Nb_3Sn research racetrack dipole demonstrator magnet. IEEE Trans. Appl. Supercond. **31**(5), 4002706 (2021). https://doi.org/10.1109/TASC.2021.3065870
566. R. Gupta, A common coil design for high field 2-in-1 accelerator magnets, in *Proc. Particle Accelerator Conference* (1997). http://jacow.org/pac97/papers/pdf/3P004.PDF
567. C. Wang, et al., Development of superconducting model dipole magnets beyond 12 T with a combined common-coil configuration. Supercond. Sci. Technol. **34**(6), 065006 (2023). https://doi.org/10.1088/1361-6668/abf5d1
568. C. Wang, et al., Design and fabrication of a 13-T twin-aperture superconducting dipole magnet with graded common-coil configuration. IEEE Trans. Appl. Supercond. **34**(5), 4000805 (2024). https://doi.org/10.1109/TASC.2024.3041234
569. J.A. Garcia-Matos, et al., Design of a common coil magnet using existing racetrack model coils (RMC). IEEE Trans. Appl. Supercond. **34**(5), 4300105 (2024). https://doi.org/10.1109/TASC.2024.3045678
570. J.A. García-Matos, C.M. Jardim, F. Toral, J.C. Perez, E. Todesco, Magnetic design of a 14 T common coil demonstrator magnet (DAISY). IEEE Trans. Appl. Supercond. **35**(5), 1–5 (2025). https://doi.org/10.1109/TASC.2025.3537069

571. D. Araujo, et al., Electromechanical design of Nb_3Sn stress managed asymmetric common-coils. IEEE Trans. on Applied SC (2025). Submitted for publication
572. T. Elliot, et al., 16 Tesla Nb_3Sn dipole development at Texas A&M University. IEEE Trans. Appl. Supercond. **7**(2), 555–557 (1997)
573. S. Caspi, et al., Canted–cosine–theta magnet (CCT)—a concept for high field accelerator magnets. IEEE Trans. Appl. Supercond. **24**(3), 4001804 (2014). https://doi.org/10.1109/TASC.2013.2284722
574. P. Ferracin, et al., Conceptual design of 20 T hybrid accelerator dipole magnets. IEEE Trans. Appl. Supercond. **33**(3), 4002007 (2023). https://doi.org/10.1109/TASC.2023.3244446
575. I. Novitski, et al., Development and test of a large-aperture Nb_3Sn cos-theta dipole coil with stress management. IEEE Trans. Appl. Supercond. **34**(5), 4001305 (2023). https://doi.org/10.1109/TASC.2023.3244447
576. D.I. Meyer, R. Flashck, A new configuration for a dipole magnet for use in high energy physics applications. Nucl. Instrum. Methods **80**(2), 339–341 (1970). https://doi.org/10.1016/0029-554X(70)90057-0
577. D. Arbalez, et al., Status of the Nb_3Sn canted-cosine-theta dipole magnet program at Lawrence Berkeley National Laboratory. IEEE Trans. Appl. Supercond. **32**(6), 4003207 (2022). https://doi.org/10.1109/TASC.2022.3155505
578. B. Auchmann, et al., Test results from CD1 short CCT Nb_3Sn dipole demonstrator and considerations about CCT technology for the fcc-hh main dipole. IEEE Trans. Appl. Supercond. **34**(5), 4001305 (2023). https://doi.org/10.1109/TASC.2023.3344425
579. S. Caspi, et al., Design and construction of a hybrid Nb_3Sn Nb-Ti dipole magnet. IEEE Trans. Appl. Supercond. **7**(2), 547 (1997). https://doi.org/10.1109/77.614654
580. N. Mounet (ed.), *2021 European Strategy for Particle Physics – Accelerator R&D Roadmap. CERN Yellow Reports: Monographs* (CERN, Geneva, 2022). https://arxiv.org/abs/2201.07895
581. D.C. Larbalestier, et al., High-Tc superconducting materials for electric power applications. Nature **414**, 368–377 (2002). https://doi.org/10.1038/35104654
582. M. Durante, et al., Realization and first test results of the eucard 5.4-T REBCO dipole magnet. IEEE Trans. Appl. Supercond. **28**(3), 4203805 (2018). https://doi.org/10.1109/TASC.2017.2780080
583. G. Biswal, K.L. Mohanta, A recent review on iron-based superconductor. Mater. Today Proc. **35**, 207–215 (2020). https://doi.org/10.1016/j.matpr.2020.03.211
584. G.R. Stewart, Superconductivity in iron compounds. Rev. Mod. Phys. **83**, 1589 (2011). https://doi.org/10.1103/RevModPhys.83.1589
585. A. Malagoli, et al., Development of a scalable method for the synthesis of high quality (Ba,K)-122 superconducting powders. IEEE Transactions on Applied Superconductivity (2025). Early Access
586. G. Kirby, et al., First cold powering test of REBCO roebel wound coil for the EuCARD2 future magnet development project. IEEE Trans. Appl. Supercond. **27**(4), 1–7 (2017). https://doi.org/10.1109/TASC.2017.2653204
587. M. Durante, et al., Overview of HTS accelerator magnet developments at CEA saclay. IEEE Trans. Appl. Supercond. **34**(5), 4002905 (2024). https://doi.org/10.1109/TASC.2024.3045679
588. L. Rossi, C. Senatore, HTS accelerator magnet and conductor development in Europe. Instruments **5**(1), 8 (2021). https://doi.org/10.3390/instruments5020008
589. T. Shen, et al., Design, fabrication, and characterization of a high-field high-temperature superconducting Bi-2212 accelerator dipole magnet. Phys. Rev. Accel. Beams **25** (2022). https://doi.org/10.1103/PhysRevAccelBeams.25.122401
590. Y.M. Wang, L. Sánchez, J. Ågren, J. Huang, R. Forsberg, et al., Colorado geoid computation experiment: overview and summary. J. Geod. **95**(12) (2021). https://link.springer.com/article/10.1007/s00190-021-01567-9
591. F. Zimmermann, Scenarios for the FCC-hh (2024). Tech. Rep. CERN, Geneva. https://indico.cern.ch/event/1439072/contributions/6106995/attachments/2917946/5120981/FCC_hh_scenarios.pdf
592. The FCC Collaboration, FCC-hh: the Hadron Collider. Eur. Phys. J. Spec. Top. **228** (2019). https://doi.org/10.1140/epjst/e2019-900087-0

Affiliations

[1] CERN, European Organization for Nuclear Research, Geneva, Switzerland
[2] PSI, Paul Scherrer Institute, Villigen, Switzerland
[3] CEA/Irfu, Commissariat à l'Energie Atomique et aux Energies Alternatives, Institut de recherche sur les lois fondamentales de l'Univers, Saclay, France
[4] DESY, Deutsches Elektronen-Synchrotron, Hamburg, Germany
[5] Humboldt-Universität zu Berlin, Berlin, Germany
[6] BNL, Brookhaven National Laboratory, Upton, NY, USA
[7] SLAC National Accelerator Laboratory, Menlo Park, CA, USA
[8] University of Oxford, Oxford, UK
[9] CNRS/IN2P3, Centre National de la Recherche Scientifique, Institut National de Physique Nucléaire et de Physique des Particules, Paris, France
[10] IJCLab, Laboratoire de Physique des 2 Infinis Irène Joliot Curie, Orsay, France
[11] Université Paris-Saclay et Université Paris-Cité, Paris, France

[12] INFN, Istituto Nazionale di Fisica Nucleare, Sezione di Bari, Bari, Italy
[13] Università di Bari, Bari, Italy
[14] IPM, Institute for Research in Fundamental Science, Tehran, Iran
[15] Malayer University, Malayer, Iran
[16] LAPP, Laboratoire d'Annecy de Physique des Particules, Annecy, France
[17] Université Savoie Mont Blanc, Annecy, France
[18] University of Belgrade, Belgrade, Serbia
[19] ICMAB/CISC, Institut de Ciència de Materials de Barcelona, Consejo Superior de Investigaciones Científicas, Barcelona, Spain
[20] INFN, Istituto Nazionale di Fisica Nucleare, Sezione di Roma Tor Vergata, Rome, Italy
[21] Università Roma Tor Vergata, Rome, Italy
[22] Yozgat Bozok Üniversitesi, Yozgat, Türkiye
[23] Texas Tech University, Lubbock, TX, USA
[24] TOBB ETU, TOBB Ekonomi ve Teknoloji Üniversitesi, Ankara, Türkiye
[25] INFN, Istituto Nazionale di Fisica Nucleare, Sezione di Bologna, Bologna, Italy
[26] Università di Bologna, Bologna, Italy
[27] CIEMAT, Centro de Investigaciones Energéticas, Medioambientales y Tecnológicas, Madrid, Spain
[28] KACST, King Abdulaziz City for Science and Technology, Riyadh, Saudi Arabia
[29] Università Roma Tre, Rome, Italy
[30] INFN, Istituto Nazionale di Fisica Nucleare, Sezione di Milano-Bicocca, Milan, Italy
[31] Università di Milano-Bicocca, Milan, Italy
[32] University of Cambridge, Cambridge, UK
[33] İstanbul Üniversitesi, Istanbul, Türkiye
[34] Eskişehir Teknik Üniversitesi, Eskişehir, Türkiye
[35] INFN, Istituto Nazionale di Fisica Nucleare, Sezione di Napoli, Naples, Italy
[36] Università di Napoli Federico II, Naples, Italy
[37] FNAL, Fermi National Accelerator Laboratory, Batavia, IL, USA
[38] University of Tehran, Tehran, Iran
[39] FUM, Ferdowsi University of Mashhad, Mashhad, Iran
[40] INFN, Istituto Nazionale di Fisica Nucleare, Sezione di Pisa, Pisa, Italy
[41] University of Texas Austin, Austin, TX, USA
[42] IPHC, Institut Pluridisciplinaire Hubert Curien, Strasbourg, France
[43] Université de Strasbourg, Strasbourg, France
[44] INFN, Istituto Nazionale di Fisica Nucleare, Sezione di Milano, Milan, Italy
[45] Università di Milano, Milan, Italy
[46] PIBG, Pôle Invertébrés du Basin Genevois, Geneva, Switzerland
[47] UFRN, Universidade Federal do Rio Grande do Norte, Natal, Brazil
[48] INFN, Istituto Nazionale di Fisica Nucleare, Laboratori Nazionali di Frascati, Frascati, Italy
[49] UNIBAS, University of Basel, Basel, Switzerland
[50] Politecnico di Bari, Bari, Italy
[51] LIP, Laboratório de Instrumentação e Física Experimental de Partículas, Lisbon, Portugal
[52] University of Manchester, Manchester, UK
[53] CI, Cockcroft Institute, Warrington , UK
[54] Brandeis University, Waltham, MA, USA
[55] A. Alikhanyan National Laboratory, Yerevan, Armenia
[56] IP2I, Institut de Physique des 2 Infinis de Lyon, Lyon, France
[57] Université Claude Bernard Lyon 1, Lyon, France
[58] Ankara Üniversitesi, Ankara, Türkiye
[59] Lund University, Lund, Sweden
[60] INFN, Istituto Nazionale di Fisica Nucleare, Sezione di Torino, Turin, Italy
[61] New York University Abu Dhabi, Abu Dhabi, United Arab Emirates
[62] Stony Brook University, Stony Brook, NY, USA
[63] INFN, Istituto Nazionale di Fisica Nucleare, Sezione di Perugia, Perugia, Italy
[64] Università di Perugia, Perugia, Italy
[65] Technische Universität München, Munich, Germany
[66] Hatay Mustafa Kemal Üniversitesi, Hatay, Türkiye

[67] Doğuş Üniversitesi, Istanbul, Türkiye
[68] INFN, Istituto Nazionale di Fisica Nucleare, Sezione di Padova, Padua, Italy
[69] Harbin Institute of Technology, Harbin, People's Republic of China
[70] University of Wisconsin-Madison, Madison, WI, USA
[71] RAL, Rutherford Appleton Laboratory, Science and Technology Facilities Council, Didcot, UK
[72] IMSc, Institute of Mathematical Sciences, Chennai, India
[73] Universität Zürich, Zurich, Switzerland
[74] University of New Mexico, Albuquerque, NM, USA
[75] CPPM, Centre de Physique des Particules de Marseille, Marseille, France
[76] Aix-Marseille Université, Marseille, France
[77] Università di Pisa, Pisa, Italy
[78] HUN-REN Wigner Research Centre for Physics, Budapest, Hungary
[79] Catholic University of America, Washington, DC, USA
[80] Duke University, Durham, NC, USA
[81] LLR, Laboratoire Leprince-Ringuet, Palaiseau, France
[82] École Polytechnique, Institut Polytechnique de Paris, Palaiseau, France
[83] TRIUMF, Canada's National Laboratory for Particle and Nuclear Physics, Vancouver, Canada
[84] Simon Fraser University, Burnaby, Canada
[85] FEEM, Fondazione Ente Nazionale Idrocarburi (ENI) Enrico Mattei, Milan, Italy
[86] BRGM, Bureau de Recherches Géologiques et Minières, Orléans, France
[87] Işık Üniversitesi, Istanbul, Türkiye
[88] İstanbul Teknik Üniversitesi, Istanbul, Türkiye
[89] UNIBE, University of Bern, Bern, Switzerland
[90] Università di Roma la Sapienza, Rome, Italy
[91] CNR-SPIN, Consiglio Nazionale delle Ricerche, Genoa, Italy
[92] Expert naturaliste et entomologiste, Rumilly, France
[93] ORNL, Oak Ridge National Laboratory, Oak Ridge, TN, USA
[94] HEPHY, Institut für Hochenergiephysik, Vienna, Austria
[95] Geos, Bureau d'ingénieurs conseils en géotechnique, génie civil, hydraulique et environnement, Geneva, Switzerland
[96] APC, Laboratoire AstroParticule et Cosmologie, Paris, France
[97] Université Paris Cité, Paris, France
[98] TUWIEN, Technische Universität Wien, Vienna, Austria
[99] HEPIA, Haute École du Paysage, d'Ingénierie et d'Architecture de Genève, Geneva, Switzerland
[100] HES-SO University of Applied Sciences and Arts Western Switzerland, Geneva, Switzerland
[101] UNIGE, Université de Genève, Geneva, Switzerland
[102] SETEC ALS, Société d'ingénierie conseil en infrastructures de transport, génie civil et environnement, Lyon, France
[103] East Texas A&M University, Commerce, TX, USA
[104] Amberg Engineering Ltd, Regensdorf-Watt, Switzerland
[105] ECOTEC Environnement SA, Bureau d'études et de conseil en environnement, Geneva, Switzerland
[106] Southern Methodist University, Dallas, TX, USA
[107] IFJ PAN, Institute of Nuclear Physics, Polish Academy of Sciences, Kraków, Poland
[108] Cerema, établissement public pour l'élaboration, le déploiement et l'évaluation de politiques publiques d'aménagement et de transport, Lyon, France
[109] Rendel Ltd, Engineering design consultancy firm, London, UK
[110] INFN, Istituto Nazionale di Fisica Nucleare, Sezione di Roma Tre, Rome, Italy
[111] İstanbul Beykent Üniversitesi, Istanbul, Türkiye
[112] University of Iowa, Iowa City, IA, USA
[113] Indian Institute of Technology Kanpur, Kanpur, India
[114] EPFL, École Polytechnique Fédérale de Lausanne, Lausanne, Switzerland
[115] Fakultät für Mathematik, Informatik und Naturwissenschaften, Universität Hamburg, Hamburg, Germany
[116] VUB, Vrije Universiteit Brussel, Brussels, Belgium
[117] LPNHE, Laboratoire de Physique Nucléaire et de Hautes Énergies, Paris, France
[118] Scuola Superiore Meridionale, Naples, Italy
[119] Affiliated with an institute formerly covered by a cooperation agreement with CERN, Geneva, Switzerland
[120] University of Saskatchewan and the Canadian Light Source, Saskatoon, Canada
[121] University of Bristol, Bristol, UK

[122] Northwestern University, Evanston, IL, USA
[123] University of Florida, Gainesville, FL, USA
[124] York University, Toronto, Canada
[125] INFN, Istituto Nazionale di Fisica Nucleare, Sezione di Cagliari, Cagliari, Italy
[126] Università di Cagliari, Cagliari, Italy
[127] INFN, Istituto Nazionale di Fisica Nucleare, Sezione di Pavia, Pavia, Italy
[128] Queen's University, Kingston, Canada
[129] CFTP-IST, Centro de Física Téorica de Partículas, Instituto Superior Tecnico, Universidade de Lisboa, Lisbon, Portugal
[130] Uppsala University, Uppsala, Sweden
[131] MPP, Max-Planck-Institut für Physik Garching, Garching, Germany
[132] KIT, Karlsruher Institut für Technologie, Karlsruhe, Germany
[133] NSC KIPT, National Science Center Kharkiv Institute of Physics and Technology, Kharkiv, Ukraine
[134] Università degli Studi dell'Insubria, Como, Italy
[135] Albert-Ludwigs-Universität Freiburg, Freiburg im Breisgau, Germany
[136] JAI, John Adams Institute for Accelerator Science, University of Oxford, Oxford, UK
[137] CNRS/INP, Centre National de la Recherche Scientifique, Institut de Physique, Paris, France
[138] LPTHE, Laboratoire de Physique Théorique et Hautes Energies, Paris, France
[139] Sorbonne Université, Paris, France
[140] INFN, Istituto Nazionale di Fisica Nucleare, Sezione di Genova, Genoa, Italy
[141] LBNL, Lawrence Berkeley National Laboratory, Berkeley, CA, USA
[142] IIT, Instituto Italiano di Tecnologia, Genoa, Italy
[143] Gümüşhane Üniversitesi, Gümüşhane, Türkiye
[144] WSP Ingénieurs Conseils SA, Geneva, Switzerland
[145] UADY, Autonomous University of Yucatan, Mérida, Mexico
[146] INFN, Istituto Nazionale di Fisica Nucleare, Sezione di Ferrara, Ferrara, Italy
[147] Università di Ferrara, Ferrara, Italy
[148] MARCELEON, Cabinet d'ingénierie juridique et foncière, Chambéry, France
[149] CSIL (Economic Research Institute), Milan, Italy
[150] ETHZ, Swiss Federal Institute of Technology Zurich, Zurich, Switzerland
[151] UAH, Universidad de Alcalá Madrid, Alcalá de Henares, Spain
[152] CIA, Conseil Ingénierie Acoustique, Lyon, France
[153] Evinerude, Bureau d'études environnementales, Lyon, France
[154] LPCA, Laboratoire de Physique de Clermont Auvergne, Clermont-Ferrand, France
[155] Université Clermont Auvergne, Clermont-Ferrand, France
[156] ANSTO, Australian Synchrotron, Melbourne, Australia
[157] Brahmananda Keshab Chandra College, Kolkata, India
[158] ANL, Argonne National Laboratory, Lemont, IL, USA
[159] INFN, Istituto Nazionale di Fisica Nucleare, Sezione di Lecce, Lecce, Italy
[160] Università di Palermo, Palermo, Italy
[161] Wrocław University of Science and Technology, Wrocław, Poland
[162] Rutgers University, New Brunswick, NJ, USA
[163] Princeton University, Princeton, NJ, USA
[164] Università di Padova, Padua, Italy
[165] IUE, İzmir Ekonomi Üniversitesi, Izmir, Türkiye
[166] Ege Üniversitesi, Izmir, Türkiye
[167] INFN, Istituto Nazionale di Fisica Nucleare, Gruppo Collegato di Udine, Udine, Italy
[168] Università di Udine, Udine, Italy
[169] University of Massachusetts Amherst, Amherst, MA, USA
[170] INFN, Istituto Nazionale di Fisica Nucleare, Sezione di Roma, Rome, Italy
[171] CELLS/ALBA, Consortium for the Construction, Equipment and Exploitation of the Synchrotron Light Laboratory, Cerdanyola del Vallès, Spain
[172] LPSC, Laboratoire de Physique Subatomique et de Cosmologie, Grenoble, France
[173] Université Grenoble Alpes, Grenoble, France
[174] Università degli Studi di Napoli Parthenope, Naples, Italy
[175] National High Magnetic Field Laboratory, Tallahassee, FL, USA
[176] Florida State University, Tallahassee, FL, USA

[177] University of Johannesburg, Johannesburg, South Africa
[178] IGFAE, Instituto Galego de Fisica de Altas Enerxías, Universidade de Santiago de Compostela, Santiago de Compostela, Spain
[179] University of Glasgow, Glasgow, UK
[180] LSE, London School of Economics, London, UK
[181] Universidade de Santiago de Compostela, Santiago de Compostela, Spain
[182] Imperial College London, London, UK
[183] MIT, Massachusetts Institute of Technology, Cambridge, MA, USA
[184] CETU, Centre d'Etude des Tunnels, Lyon, France
[185] University of Liverpool, Liverpool, UK
[186] Linde Kryotechnik AG, Pfungen, Switzerland
[187] ILF Consulting Engineers, Zurich, Switzerland
[188] NBI, Niels Bohr Institute, Copenhagen, Denmark
[189] Hokkaido University, Sapporo, Japan
[190] CUNI, Charles University, Prague, Czech Republic
[191] Universidad de Granada, Granada, Spain
[192] INFN, Istituto Nazionale di Fisica Nucleare, Sezione di Firenze, Florence, Italy
[193] University of Malta, Msida, Malta
[194] BU, Boston University, Boston, MA, USA
[195] IBU, Bolu Abant İzzet Baysal Üniversitesi, Bolu, Türkiye
[196] Julius-Maximilians-Universität Würzburg, Würzburg, Germany
[197] University of Adelaide, Adelaide, Australia
[198] HIP, Helsinki Institute of Physics, University of Helsinki, Helsinki, Finland
[199] ULB, Université Libre de Bruxelles, Brussels, Belgium
[200] IMA, Institut für Maschinenelemente, Universität Stuttgart, Stuttgart, Germany
[201] CP3, Centre de Cosmologie, de Physique des Particules et de Phénoménologie, Université Catholique de Louvain, Louvain-la-Neuve, Belgium
[202] NIKHEF, Nationaal instituut voor subatomaire fysica, Amsterdam, The Netherlands
[203] IHEP, Chinese Academy of Sciences, Beijing, People's Republic of China
[204] UAS, Universidad Autónoma de Sinaloa, Culiacán, Mexico
[205] BOKU, Universität für Bodenkultur Wien, Vienna, Austria
[206] University of Silesia in Katowice, Katowice, Poland
[207] Purdue University, West Lafayette, IN, USA
[208] University of Delhi, Delhi, India
[209] Ginger BURGEAP, bureau d'études en environnement, Lyon, France
[210] King's College London, London, UK
[211] University of Maryland, College Park, MD, USA
[212] KEK, High Energy Accelerator Research Organization, Tsukuba, Japan
[213] Geoenergy, Reservoir Geology and Basin Analysis Group, Geneva, Switzerland
[214] SETEC International, Société d'ingénierie en charge des transports et des infrastructures, Lyon, France
[215] KKU, Kırıkkale Üniversitesi, Kırıkkale, Türkiye
[216] SETEC LERM, Société d'ingénierie conseil en matériaux de construction, Lyon, France
[217] BUAP, Benemérita Universidad Autónoma de Puebla, Puebla, Mexico
[218] Stanford University, Stanford, CA, USA
[219] University of Pittsburgh, Pittsburgh, PA, USA
[220] MUL, Montanuniversität Leoben, Lehrstuhl für Subsurface Engineering, Geotechnik und unterirdisches Bauen, Leoben, Austria
[221] MUL-ZaB, Underground Research Center, Zentrum am Berg, Leoben, Austria
[222] IFAE, Institut de Física d'Altes Energies, Barcelona, Spain
[223] FHNW, University of Applied Sciences Northwestern Switzerland, Windisch, Switzerland
[224] UPES, University of Petroleum and Energy Studies, Dehradun, India
[225] GANIL, Grand Accélérateur National d'Ions Lourds, Caen, France
[226] Université Caen Normandie, Caen, France
[227] UFRGS, Universidade Federal do Rio Grande do Sul, Porto Alegre, Brazil
[228] Technische Universität Darmstadt, Darmstadt, Germany
[229] Universidade de Coimbra, Coimbra, Portugal

[230] UFPel, Universidade Federal de Pelotas, Pelotas, Brazil
[231] University of California Santa Cruz, Santa Cruz, CA, USA
[232] Università del Salento, Lecce, Italy
[233] Brown University, Providence, RI, USA
[234] University of California Berkeley, Berkeley, CA, USA
[235] Università di Torino, Turin, Italy
[236] Johns Hopkins University, Baltimore, MD, USA
[237] Fudan University, Shanghai, People's Republic of China
[238] LAPTh, Laboratoire d'Annecy-le-Vieux de Physique Théorique, Annecy-le-Vieux, France
[239] Dongguan University of Technology, Dongguan, People's Republic of China
[240] Kahramanmaraş Sütçü İmam Üniversitesi, Kahramanmaraş, Türkiye
[241] UNACH, Universidad Autónoma de Chiapas, Tuxtla Gutiérrez, Mexico
[242] MCTP, Mesoamerican Centre for Theoretical Physics, Tuxtla Gutiérrez, Mexico
[243] UAZ, Universidad Autónoma de Zacatecas, Zacatecas, Mexico
[244] University of Jyväskylä, Jyväskylä, Finland
[245] Technische Universität Dortmund, Dortmund, Germany
[246] Overleaf, London, UK
[247] University of Virginia, Charlottesville, VA, USA
[248] Cornell University, Ithaca, NY, USA
[249] FIT, Florida Institute of Technology, Melbourne, FL, USA
[250] Shirokuma GmbH, Zurich, Switzerland
[251] National Centre for Physics, Islamabad, Pakistan
[252] Johannes Gutenberg Universität Mainz, Mainz, Germany
[253] PAEC, Pakistan Atomic Energy Commission, Islamabad, Pakistan
[254] Mathabhanga College, Mathabhanga, India
[255] Harish-Chandra Research Institute, Prayagraj, India
[256] MPIK, Max-Planck-Institut für Kernphysik Heidelberg, Heidelberg, Germany
[257] European Spallation Source ERIC, Lund, Sweden
[258] Centre de calcul de l'IN2P3, Villeurbanne, France
[259] GSI, Helmholtzzentrum für Schwerionenforschung GmbH, Darmstadt, Germany
[260] IBS, Institute for Basic Science, Center for Theoretical Physics of the Universe, Daejeon, Republic of Korea
[261] University of Warsaw, Warsaw, Poland
[262] University of Ljubljana, Ljubljana, Slovenia
[263] Jozef Stefan Institute, Ljubljana, Slovenia
[264] Microhumus, Bureau d'étude et d'ingénierie spécialisé dans la gestion des sols dégradés, Nancy, France
[265] Fakultät für Physik und Astronomie, Universität Heidelberg, Heidelberg, Germany
[266] Niğde Ömer Halisdemir Üniversitesi, Niğde, Türkiye
[267] Giresun Üniversitesi, Giresun, Türkiye
[268] University of Miskolc, Miskolc, Hungary
[269] NTUA, National Technical University of Athens, Athens, Greece
[270] Transmutex SA, Geneva, Switzerland
[271] DIAS, Dublin Institute for Advanced Studies, School of Theoretical Physics, Dublin, Ireland
[272] AGH, University of Science and Technology, Kraków, Poland
[273] University of Science and Technology of Mazandaran, Behshahr, Iran
[274] IPPP, Institute for Particle Physics Phenomenology, Durham University, Durham, UK
[275] Bursa Uludağ Üniversitesi, Bursa, Türkiye
[276] YU, Yonsei University, Seoul, Republic of Korea
[277] Affiliated with an international laboratory covered by a cooperation agreement with CERN, Geneva, Switzerland
[278] CPT, Centre de Physique Théorique, Marseille, France
[279] Aix-Marseille Université et Université du Sud Toulon Var, Marseille, France
[280] KIAS, Korea Institute for Advanced Study, Seoul, Republic of Korea
[281] Carleton University, Ottawa, Canada
[282] FEAC Engineering P.C., Patras, Greece
[283] UPATRAS, University of Patras, Patras, Greece
[284] University of Kansas, Lawrence, KS, USA
[285] AUTH, Aristotle University of Thessaloniki, Thessaloniki, Greece

[286] IML, Fraunhofer-Institut für Materialfluss und Logistik, Dortmund, Germany
[287] RWTH Aachen, Rheinisch-Westfälische Technische Hochschule Aachen, Aachen, Germany
[288] ZHAW, Zurich University of Applied Sciences, Winterthur, Switzerland
[289] Universität Münster, Münster, Germany
[290] University of the Witwatersrand, Johannesburg, South Africa
[291] Fachhochschule Technikum Wien, Vienna, Austria
[292] University of California Irvine, Irvine, CA, USA
[293] Northeastern University, Boston, MA, USA
[294] ESI, European Scientific Institute, Archamps, France
[295] UOS, University of Seoul, Seoul, Republic of Korea
[296] KNU Kyungpook National University, Daegu, Republic of Korea
[297] KU, Korea University, Seoul, Republic of Korea
[298] Tampere University, Tampere, Finland
[299] University of Edinburgh, Edinburgh, UK
[300] BG Ingénieurs Conseils, Lausanne, Switzerland
[301] T.-D. Lee Institute, Shanghai, People's Republic of China
[302] Shanghai Jiao Tong University, Shanghai, People's Republic of China
[303] CNR, Consiglio Nazionale delle Ricerche, Rome, Italy
[304] University of Michigan, Ann Arbor, MI, USA
[305] University of Pennsylvania, Philadelphia, PA, USA
[306] University of Minnesota, Minneapolis, MN, USA
[307] ESRF, European Synchrotron Radiation Facility, Grenoble, France
[308] SUSSEX, University of Sussex, Brighton, UK
[309] Università di Bari Aldo Moro, Bari, Italy
[310] University of Bath, Bath, UK
[311] Scuola Normale Superiore di Pisa, Pisa, Italy
[312] Universidade de São Paulo, São Paulo, Brazil
[313] Universität Graz, Graz, Austria
[314] Center for High Energy Physics, Fayoum University, Fayoum, Egypt
[315] Center of Theoretical Physics, British University in Egypt, Cairo, Egypt
[316] Cairo University, Cairo, Egypt
[317] Sorbonne Université et Université Paris Cité, Paris, France
[318] Università di Genova, Genoa, Italy
[319] IFIC-CSIC/UV, Instituto de Física Corpuscular, Consejo Superior de Investigaciones Científicas/Universidad de Valencia, Valencia, Spain
[320] Service de géologie, sols et déchets du canton de Genève, Geneva, Switzerland
[321] NICPB, National Institute for Chemical Physics and Biophysics, Tallinn, Estonia
[322] UT, University of Tartu, Tartu, Estonia
[323] Universidad de Salamanca, Salamanca, Spain
[324] UGTO, Universidad de Guanajuato, Guanajuato, Mexico
[325] Edaphos Engineering, Geneva, Switzerland
[326] Helmholtz-Zentrum Dresden-Rossendorf, Dresden, Germany
[327] Tata Institute of Fundamental Research Mumbai, Mumbai, India
[328] Universiteit Gent, Ghent, Belgium
[329] CNR-IOM, Consiglio Nazionale delle Ricerche, Trieste, Italy
[330] JKU, Johannes Kepler Universität Linz, Linz, Austria
[331] University of Stavanger, Stavanger, Norway
[332] Universidad Nacional de Colombia, Bogotá, Colombia
[333] Trento Institute for Fundamental Physics and Applications, Trento, Italy
[334] Caltech, California Institute of Technology, Pasadena, CA, USA
[335] Università della Calabria, Rende, Italy
[336] IFT, Instituto de Física Teórica, Universidad Autónoma de Madrid, Madrid, Spain
[337] UPC, Universitat Politècnica de Catalunya, Barcelona, Spain
[338] Departamento de Física, Universidade do Minho, Braga, Portugal
[339] Centro de Física das Universidades do Minho e do Porto, Porto, Portugal
[340] LaPMET, Laboratory of Physics for Materials and Emergent Technologies, Porto, Portugal

[341] University of Bergen, Bergen, Norway
[342] SAPHIR, Instituto Milenio de Física Subatómica en la Frontera de Altas Energías, Santiago, Chile
[343] Universidad Andres Bello, Santiago, Chile
[344] IIP, International Institute of Physics, Natal, Brazil
[345] Tokyo International University, Tokyo, Japan
[346] Izmir Bakırçay Üniversitesi, Izmir, Türkiye
[347] INFN, Istituto Nazionale di Fisica Nucleare, Laboratori Nazionali del Gran Sasso, Assergi, Italy
[348] Universitá degli Studi di Cassino e del Lazio Meridionale, Cassino, Italy
[349] Vinča Institute of Nuclear Sciences, Belgrade, Serbia
[350] Kennesaw State University, Kennesaw, GA, USA
[351] Università di Pavia, Pavia, Italy
[352] Columbia University, New York, NY, USA
[353] Department of Energy of the United States of America, DOE, Washington, DC, USA
[354] IPSA, Institut Polytechnique des Sciences Avancées, Ivry-sur-Seine, France
[355] Università degli Studi del Sannio, Benevento, Italy
[356] UJ, Jagiellonian University, Kraków, Poland
[357] Universität Wien, Vienna, Austria
[358] Goethe-Universität Frankfurt, Institut für Angewandte Physik, Frankfurt am Main, Germany
[359] HFFH, Helmholtz Forschungsakademie Hessen für FAIR, Frankfurt am Main, Germany
[360] INCDTIM, National Institute for Research and Development of Isotopic and Molecular Technologies, Cluj-Napoca, Romania
[361] University of Arizona, Tucson, AZ, USA
[362] Technische Universität Dresden, Dresden, Germany
[363] RTU, Riga Technical University, Riga, Latvia
[364] Lancaster University, Lancaster, UK
[365] University of Cyprus, Nicosia, Cyprus
[366] Cosmos Open University, Nicosia, Cyprus
[367] CBPF, Centro Brasileiro de Pesquisas Físicas, Rio de Janeiro, Brazil
[368] Universität Bonn, Bonn, Germany
[369] CMU, Chiang Mai University, Chiang Mai, Thailand
[370] JLAB, Thomas Jefferson National Accelerator Facility, Newport News, VA, USA
[371] ESPOL, Escuela Superior Politécnica del Litoral, Guayaquil, Ecuador
[372] IRB, Rudjer Boskovic Institute, Zagreb, Croatia
[373] Air Liquide Advanced Technologies, Grenoble, France
[374] VU Amsterdam, Amsterdam, The Netherlands
[375] INGÉROP, Groupe d'ingénierie et de conseil en mobilité durable, transition énergétique et cadre de vie, Lyon, France
[376] Warsaw University of Technology, Warsaw, Poland
[377] IFCA, Instituto de Física de Cantabria, Santander, Spain
[378] Institut für Beschleunigerphysik und Technologie, Eggenstein-Leopoldshafen, Germany
[379] Uşak Üniversitesi, Uşak, Türkiye
[380] ICEPP, International Center for Elementary Particle Physics, University of Tokyo, Tokyo, Japan
[381] Rudolf Peierls Centre for Theoretical Physics, University of Oxford, Oxford, UK
[382] All Souls College, University of Oxford, Oxford, UK
[383] Akdeniz Üniversitesi, Antalya, Türkiye
[384] Latitude Durable SARL, Geneva, Switzerland
[385] USAL, Universidad de Salamanca, Salamanca, Spain
[386] PRISMA+ Cluster of Excellence, Mainz, Germany
[387] Michigan State University, East Lansing, MI, USA
[388] Universidad Complutense Madrid, Madrid, Spain
[389] scMetrology SARL, Geneva, Switzerland
[390] IST, Instituto Superior Tecnico, Universidade de Lisboa, Lisbon, Portugal
[391] CeFEMA, Center of Physics and Engineering of Advanced Materials, Lisbon, Portugal
[392] Indian Institute of Science Education and Research Mohali, Mohali, India
[393] NIU, Northern Illinois University, DeKalb, IL, USA
[394] Banaras Hindu University, Varanasi, India
[395] Comenius University, Bratislava, Slovakia

[396] Monash University, Melbourne, Australia
[397] Slovak Academy of Sciences, Bratislava, Slovakia
[398] KAIST, Korea Advanced Institute of Science and Technology, Daejeon, Republic of Korea
[399] Amberg Engineering Chambéry, Chambéry, France
[400] Khalifa University of Science and Technology, Abu Dhabi, United Arab Emirates
[401] University of Tennessee, Knoxville, TN, USA
[402] IFIC-CSIC/UV, Instituto de Física Corpuscular, Consejo Superior de Investigaciones Científicas/Universidad de Valencia, Valencia, Spain
[403] WIFO, Österreichisches Institut für Wirtschaftsforschung, Vienna, Austria
[404] Universidade do Estado do Rio de Janeiro, Rio de Janeiro, Brazil
[405] Mélica, NATURA SCOP, Études et expertises environnementales, Aubenas, France
[406] Università LUM, Casamassima, Italy
[407] University of Twente, Enschede, The Netherlands
[408] Arak University, Arak, Iran
[409] Università di Trieste, Trieste, Italy
[410] ForestAllia, Cabinet de gestion et d'expertise forestières, Besançon, France
[411] Universität Siegen, Siegen, Germany
[412] University of Oregon, Eugene, OR, USA
[413] Universität Rostock, Rostock, Germany
[414] CEGELEC SA, Geneva, Switzerland
[415] KTH, Royal Institute of Technology, Stockholm, Sweden
[416] OKC, Oskar Klein Centre for Cosmoparticle Physics, Stockholm, Sweden
[417] Brigham Young University, Provo, UT, USA
[418] Expert foncier et agricole, Chadrat, France
[419] ITSM, Institut für Thermische Strömungsmaschinen und Maschinenlaboratorium, Universität Stuttgart, Stuttgart, Germany
[420] École Normale Supérieure de Lyon, Lyon, France
[421] CTU, Czech Technical University, Prague, Czech Republic
[422] University of Chicago, Chicago, IL, USA
[423] Baylor University, Waco, TX, USA
[424] University of Birmingham, Birmingham, UK
[425] University of Southampton, Southampton, UK
[426] Swisstopo, Federal Office of Topography, Wabern, Switzerland
[427] Daresbury Laboratory, Science and Technology Facilities Council, Daresbury, UK
[428] IZTECH, Izmir Yüksek Teknoloji Enstitüsü, Izmir, Türkiye
[429] City University of Hong Kong, Hong Kong, Hong Kong